12-2022

ANALYSIS OF PHYSICOCHEMICAL PROPERTIES AND TERRESTRIAL DYNAMICS OF MECHANICALLY FORMED MICRO-NANO SCALED PARTICLES FROM AGRICULTURAL PLASTIC MULCHES

Anton Friedrich Astner
aaston@utk.edu

To the Graduate Council:

I am submitting herewith a dissertation written by Anton Friedrich Astner entitled "ANALYSIS OF PHYSICOCHEMICAL PROPERTIES AND TERRESTRIAL DYNAMICS OF MECHANICALLY FORMED MICRO-NANO SCALED PARTICLES FROM AGRICULTURAL PLASTIC MULCHES." I have examined the final electronic copy of this dissertation for form and content and recommend that it be accepted in partial fulfillment of the requirements for the degree of Doctor of Philosophy, with a major in Biosystems Engineering.

Douglas G. Hayes, Major Professor

We have read this dissertation and recommend its acceptance:

Douglas G. Hayes, Sean M. Schaeffer, Barbara R. Evans, Hugh M. O'Neill, Timothy M. Young, David P. Harper

Accepted for the Council:

Dixie L. Thompson

Vice Provost and Dean of the Graduate School

(Original signatures are on file with official student records.)

ANALYSIS OF PHYSICOCHEMICAL PROPERTIES AND TERRESTRIAL DYNAMICS OF MECHANICALLY FORMED MICRO-NANO SCALED PARTICLES FROM AGRICULTURAL PLASTIC MULCHES

A Dissertation Presented for the

Doctor of Philosophy

Degree

The University of Tennessee, Knoxville

Anton Friedrich Astner

December 2022

DEDICATION

To my mom

Maria Theresia Astner

ACKNOWLEDGEMENTS

ABSTRACT

Terrestrial microplastics (MPs) and nanoplastics (NPs) (MNPs, collectively), formed through the fragmentation of agricultural plastics, have the potential to impact soil biota and adjacent waterways severely. Agricultural mulch films, the most abundant agricultural plastic material used in specialty crop production, significantly contribute to MP and NP formation in agricultural soils. However, most environmental fate, transport, and ecotoxicity studies have utilized non-representative MPs and NPs materials, such as monodisperse polystyrene microspheres, resulting in unreliable study outcomes. To address the shortcomings, the overall objective of this dissertation was to investigate the individual life stages of MNPs of conventional polyethylene and biodegradable mulches (BDMs) in soil. Therefore, MNPs were formed from agricultural plastic feedstocks (e.g., polybutylene adipate terephthalate [PBAT] film and pellets) using a laboratory cryogenic cooling procedure (CRYO) that mimicked degradation of agricultural plastics soil and their changes of dimensional and physiochemical properties during the size reduction process were investigated. The resultant MNPs are useful for surrogates in environmental studies and were employed in this dissertation to investigate the MNPs' biodegradation in a soil incubation study. In addition, the agglomeration behavior of NPs at soil-water interfaces was explored using Small Angle Neutron Scattering (SANS) techniques. For the latter, neutron contrast matching allowed isolating the NPs signal in the neutron beam by negating the signal attributable to the soil. As a result, a greater biodegradability was observed for MPs than NPs, a counterintuitive trend reflecting the leaching away of minor components while forming NPs. Agglomeration of larger-sized NPs particles was detected through SANS, whereas smaller NPs remained dispersed in water.

Furthermore, convective transport impacted the NP's particle size, leading to a significant size reduction of larger-scaled NPs. The results of this dissertation demonstrate that MPs form during high mechanical impact as occurring during the tillage into the soil. Furthermore, NPs form from MPs that a longer residence time in the soil than expected is required to achieve complete mineralization and that dispersion of NPs water may promote NPs' transport into groundwater and waterways.

TABLE OF CONTENTS

LIST OF TABLES

LIST OF FIGURES

LIST OF ABBREVIATIONS (NOMENCLATURE LIST)

α:	scale parameter for the two-parameter Weibull model
AIC:	Akaike's information criterion (used to assess the quality of the Weibull model)
β:	shape parameter for the two-parameter Weibull model
BDM(s):	biodegradable plastic mulch(es)
BIC:	Bayesian information criterion (used to assess the quality of the Weibull model)
CRYO:	cryogenic pretreatment of unweathered mulch film
DLS:	dynamic light scattering
DLS:	dynamic light scattering
d_p:	average particle size (diameter)
DSC:	differential scanning calorimetry
DTG:	differential thermogram (DSC analysis)
FTIR:	Fourier transform infrared
FTIR:	Fourier transform infrared spectroscopy
GPC:	gel permeation chromatography
LDPE:	low-density polyethylene
Mn:	number-averaged molecular weight
MNPs:	micro and nanoplastics
MP:	microplastic
MPs:	microplastics
Mt:	million tons
Mw:	weight-averaged molecular weight
NDF:	number density frequency
NMR:	nuclear magnetic resonance
NP:	nanoplastic
NPs -	nanoplastics
PBAT:	polybutylene adipate terephthalate
PBAT:	polybutylene adipate-co-terephthalate
PD:	particle polydispersity
PDI:	polydispersity index (for molecular weight)
PE:	polyethylene
PHA:	polyhydroxyalkanoate
PLA:	polylactic acid
PSD:	particle size distribution
TGA:	thermogravimetric analysis
TGA:	thermogravimetric analysis
UV:	ultraviolet radiation
W:	environmentally weathered
X_c:	mole fraction of crystalline morphology for PBAT

CHAPTER I

INTRODUCTION AND LITERATURE REVIEW

1.1 Plastic in Nature

Global environmental plastic pollution and lack of recycling options result in severe plastic contamination and dispersion within terrestrial and aquatic compartments. The plastic waste generation is predicted for 26,000 Mt by 2050, from which around 45% can enter the waste stream without being recycled (Geyer *et al.*, 2017). As a result, plastics released into terrestrial systems are 4-23 times greater than freshwater systems, raising concerns about the detrimental impacts on soil organisms and microbiomes (Horton *et al.*, 2017; Sobhani *et al.*, 2021). In addition, the environmentally dispersed plastic materials undergo fragmentation due to shear, chemical, and biochemical reactions, leading to the formation of micro- and nanoplastics (MPs and NPs, respectively), resulting in small particles with diameters (d_p) of 0.1–5000 μm and 1–1000 nm. Significant contributors to environmental plastic for dispersion of MPs and NPs (collectively MNPs) are agricultural plastic mulch films, contributing to the deposition of plastic residues and pollution in soil. Mulches are thin polymeric film sheets that control soil temperature, for example, warm or cool the soil with a black or white surface color, conserve soil moisture, and suppress weeds resulting in increased crop yields (Anunciado *et al.*, 2021).

Environmental exposure of mulch films to sunlight, wind, and water leads to embrittlement and defragmentation, resulting in terrestrial MPs and NPs. These small fragments of agricultural plastics that reside in the soil for extended durations and are an emerging environmental pollutant and are currently being investigated for breakdown, agglomeration behavior, and their potential impact on soil dynamics and microorganisms. The continuous development of agricultural plastics for improved vegetable crop production (comprehensively termed "plasticulture, including drip-irrigation tubing and tape) supported the commercial production of specialty crops (Ekebafe *et al.*, 2011; Sanders *et al.*, 1995). As part of the plasticulture system, agricultural mulching became a prominent practice employing plastic films to cover the soil surface and provide conditions that optimize specialty crop yields (Bandopadhyay *et al.*, 2020; Hayes *et al.*, 2019; Menossi *et al.*, 2021). Furthermore, mulch deployment enhances economic viability, allowing drip irrigation for efficient fertilizer and water utilization (Hayes *et al.*, 2017). However, commercially used plastic mulch films are manufactured from low-density polyethylene (LDPE), providing poor biodegradability (Kasirajan & Ngouajio, 2012).

The absence of hydrolyzable bonds makes LDPE films resistant to biodegradation, resulting in additional costs for removal and disposal after the growing season. As a result, plastic film residuals frequently remain in the field or are stockpiled on farms for extended durations (Chen *et al.*, 2020; DeVetter *et al.*, 2021; Sintim *et al.*, 2021; Velandia *et al.*, 2018). Due to poor biodegradability, these smaller fragments can persist for many years in soils and can cause harm to soil-related ecosystems, such as negative impacts on plant growth and soil fertility, and may eventually leach into the groundwater (Rillig *et al.*, 2017). In addition, LDPE is mainly extracted from fossil sources, contributing to CO_2 greenhouse gas emissions through sourcing and manufacturing processes. Fundamental studies investigating the fate, transport, ecotoxicity, and behavior of MPs and NPs in the terrestrial environment require representative MPs and NPs models. Furthermore, it is essential to understand the transformation stages from the film into MPs and NPs formation through mechanical impact, aggregation, and biodegradation characteristics in soil (Lionetto *et al.*, 2021). Currently, most scientific work related to MPs and NPs employ monodisperse polystyrene spheres, which do not represent authentical MP and NP particles for fundamental environmental studies. Hence, the availability of representative MNPs is essential for conducting reliable environmental research studies. Furthermore, it is crucial to understand and characterize the individual transformational stages (life stages) from the film, MPs to NPs, including the dimensional, physiochemical properties as closer described in Chapters II-VI of this dissertation.

1.2 Mulch Films

The use of polymer films in agriculture started in the early 1950s on a significant scale when LDPE was essential in replacing paper for mulching vegetables (Byrdson, 1970; Garnaud, 2000). Polymerized vinyl monomers form PE, which has the simplest structure of any polymer. A monomer is a merely pure material and becomes a macromolecular compound through polymerization. The main attractive features of LDPE are excellent electrical insulation properties, excellent chemical resistance, good processability, and various transparencies at specific grades (Gilbert, 2016). Three polymerization paths describe the formation from the monomer: high-pressure process, middle-pressure process, and low-pressure process, which result in different degrees of crystallinity and density. High-density polyethylene (HDPE) shows low crystallinity

and density, unlike LDPE with high density and crystallinity. As the crystallinity and density increase, the hardness, softening point, strength, toughness, and elongation decrease. PE plastic has excellent chemical stability and water resistance. Even though its tensile strength is not high, it shows excellent flexibility at low temperatures. Carbon Black as an additive increases the aging resistance of PE. Agricultural mulches are frequently composed of LDPE as a feedstock for crop cultivation (Espi *et al.*, 2006).

1.3 Biodegradable Mulches (BDMs)

Biodegradable plastic mulch films (BDMs) were developed and represent a more environmentally friendly alternative to nonbiodegradable LDPE films. BDMs offer similar mechanical properties to LDPE films, enabling good field performance during the growing season, and are intended to be tilled into the soil after the growing season (Serrano-Ruiz *et al.*, 2021; Sintim *et al.*, 2019). In the soil, BDMs biodegrade through soil microorganisms by microbial hydrolysis in aerobic conditions into carbon dioxide, water, and microbial biomass (Goldberger *et al.*, 2019; Hayes *et al.*, 2012). However, besides higher purchase costs, the BDM's unpredictable breakdown during deployment and possible incomplete soil biodegradation, and unknown long-term effects on soil biota such as ecotoxicity, soil properties (impacting plant growth) of incorporated (remaining) plastic fragments in soil have been preventive (barriers for adoption) factors for implementation to the farming communities (Hayes *et al.*, 2019; Miles *et al.*, 2017).

1.3.1 Mulch feedstocks with hydrolyzable backbones

Polymers with hydrolyzable ester bonds in their backbones are more susceptible to biodegradation than polymers consisting of carbon chain backbones like polyethylene. under environmental stress conditions. Hydrolyzable polymers include polyesters, polyamides, polyurethanes, polyureas, Poly (amide-enamine)s, and polyanhydrides (Chandra & Rustgi, 1998; Nair & Laurencin, 2007). In two steps, enzymes and chemical reactions promote polymer biodegradation by chemical deterioration associated with living organisms. The first step includes fragmentation of the polymers into lower molecular mass species utilizing either abiotic reactions, e.g., oxidation, photodegradation, hydrolysis, or biotic reactions, i.e., degradations by microorganisms. In the following, bio assimilation of the polymer fragments by microorganisms and their mineralization occurs. The biodegradability varies based on the origin of the polymer, its

chemical structure, and the degrading environmental conditions, such as ambient temperature and moisture, among other factors.

1.3.2 Aliphatic polyesters

Based on their essential diversity and synthetic versatility, aliphatic polyesters are most extensively researched within biodegradable polymers, including many monomers. However, polycondensation of monomers generally results in low molecular weight polymers. In contrast, ring-opening polymerization promotes the manufacture of high molecular polymers utilizing six or seven-membered lactones (Löfgren *et al.*, 1995). On the contrary, aliphatic polyesters are almost the only high molecular weight biodegradable compounds (Chandra & Rustgi, 1998) and thus have been extensively investigated. In addition, their hydrolyzable ester bonds make them biodegradable.

1.3.3 Aromatic co-polyesters

The development of polyesters and co-polyesters with aliphatic monomeric units of different sizes includes a wide array. However, the mechanical properties of such polyesters are lower than those of non-biodegradable polymers. Aromatic polyesters generally are insensitive to hydrolytic degradation and enzymatic or microbial attack; aliphatic-aromatic polyesters show improved polymer chemical and mechanical properties. Aliphatic-aromatic-polyesters consist of aliphatic and aromatic monomers mixtures and are comprised of terephthalic acid. Shaik *et al.* (2001) presented a broad range of aliphatic-aromatic-polyesters of different sizes. Poly-(butylene adipate-co-terephthalate) is the most frequently studied polyester and represents an environmentally friendly alternative to LDPE. PBAT is a synthetic, biodegradable polyester composed of adipic acid and butanediol as aliphatic units and terephthalic acid as aromatic ones, a component for agricultural mulch manufacture (Figure I–1). In this copolymer, the aromatic monomer contributes to excellent thermal stability and mechanical properties (when using terephthalic acid higher than 35% mol) and provides flexibility and good biodegradability. However, the biodegradation rate decreases rapidly as the concentration becomes higher than 55% (Witt *et al.*, 2001; Witt *et al.*, 1997).

1.3.4 PBAT blends

Biodegradable polymer PBAT blends are selected over individual biopolymers as matrices for composite applications. PBAT polymer blending creates unique materials with specific desired properties by combining the different advantageous qualities of two or more neat polymers.

The application of pure PBAT is limited due to its high costs and lower mechanical properties than PBAT blends (Jian *et al.*, 2020). Therefore, starch, a biopolymer component derived from renewable resources, is frequently used as a filler to control the biodegradability properties of PBAT blends (Wang *et al.*, 2019). For agricultural applications, PBAT blends contain up to 30% starch, which promotes biodegradability due to its hydrophilic nature. In addition, water is an effective starch plasticizer due to its small molecular size allowing hydrogen bonding with starch. Thus, water further facilitates starch recrystallization changing the tensile properties of the bioplastic (Van Soest & Knooren, 1997). The resulting mechanical properties are typically a compromise between the parent polymers. The commercial feedstock blend of PBAT and lignin is currently being explored for their potential use for biodegradable plastics (Xiong *et al.*, 2020). For novel biodegradable polymer PBAT blends, Kraft lignin (KL) represents a biobased antioxidant, which can act as a photo initiator, increasing oxidation based on UV radiation wavelength (Kaur *et al.*, 2021; Xing *et al.*, 2017). The lignin addition increased the oxidation induction time, oxidative degradation, and thermal degradation temperatures of the matrix, suggesting that PBAT/lignin ratios influence the biodegradation rate of polymers (Botta *et al.*, 2022; Tavares & Rosa, 2019). Therefore, the hydrophobic structure of lignin could tune the biodegradability of PBAT (Oyama *et al.*, 2011). Lignin is an abundant natural polymer with a cross-linked and complex phenolic and hydrophobic structure. As a derivative of native lignin, KL is available at a large scale as a by-product of pulping processes such as paper manufacturing by the Kraft process. The by-product lignin ends up as waste; however, high-value applications can utilize lignin as an essential building block. Studies on lignin have reported characteristics as an antioxidant (Domenek *et al.*, 2013), antibacterial (Yang *et al.*, 2016), antimicrobial (Yang *et al.*, 2016), and barrier properties (Shankar *et al.*, 2015) of lignin, which is essential for its potential use in food packaging. It is worth mentioning that industrial lignins, including Kraft and Sulfite processes, have residual sulfur content and inherent odor, which can be a drawback for the manufacture of films. However, edible films derived from fish skin gelatin and sulfite process

lignin proved excellent antioxidant capacity and low cytotoxicity properties (Núñez-Flores *et al.*, 2012). The lignin structure contains many functional groups in different portions, including phenolic and aliphatic hydroxyls, carbonyls, carboxyls, and methoxyl (Tavares *et al.*, 2018). These groups enable interaction and compatibility with polymeric matrices such as PBAT.

Renewable and biodegradable UV-blocking films are in high demand for the increasing need for a sustainable environment. Lignin can offer significant UV absorption, but it deteriorates the mechanical properties of films at a high content. Therefore, biobased 10-undecenoic and oleic acids were successfully grafted onto soda lignin via solvent- and catalyst-free processes, as confirmed by ^{31}P and ^{1}H NMR and Fourier transform infrared (FTIR) (Alzagameem *et al.*, 2018).

The resulting lignin ester derivatives and clean lignin were melt-blended with a biodegradable PBAT to prepare UV-protective films. Incorporating the modified lignins into the PBAT matrix exhibited good dispersion of lignin particles with almost unaffected tensile properties and excellent thermal stability for up to 20 wt % loading of lignin derivatives. In addition, the resulting films showed unique UV-barrier properties with 10 wt % lignin loading and complete protection in the UV-irradiation range (280–400 nm). The study also revealed that UV protection was present even after 50 hours of UV irradiation. This work demonstrates a promising procedure to produce high-performance and biodegradable PBAT–lignin UV-blocking films (Sadeghifar *et al.*, 2017; Xing *et al.*, 2017).

In another study, two developed strategies improved the mechanical properties of PBAT/lignin composites: through (1) modification of lignin via methylation to reduce hydrogen bonding between −OH groups and (2) enhance the intermolecular interactions between PBAT and lignin by adding maleic anhydride-graft-PBAT as a compatibilizer (Xiong *et al.*, 2020). The composites obtained from the two compositions with 60 wt % lignin contents showed an ideal tensile performance meeting standard for packaging. In addition, morphological and thermal analyses investigated the interactions between different composite components. The results showed that the molecular mobility of lignin and the agglomeration size is remarkably impacted by the ductility and mechanical strength of the PBAT/lignin films.

1.3.5 Poly (lactic acid) or polylactide (PLA)

A promising biodegradable polymer is the most extensively researched and frequently used biodegradable and renewable aliphatic polyester (Mathew, 2022) (Figure I–2).

PLA has a proven potential to replace conventional petrochemical-based polymers for industrial applications. Although PLA is an expensive polymer, using cheaper fillers such as vegetable waste materials (spinach stems, tomato pomace) can alleviate the costs (Merino *et al.*, 2022). Furthermore, as a thermoplastic aliphatic polyester, PLA's ability for biodegradation and properties has promoted its commercial applications, e.g., in food packaging (Arrieta *et al.*, 2013) bottles (Lima *et al.*, 2008) biomedicine (Sha *et al.*, 2016), automotive parts (Notta-Cuvier *et al.*, 2015), and mulches for agricultural applications (Hayes *et al.*, 2012). However, although PLA tends to have a high modulus and tensile strength, applications with high strain failures are not well suited due to its brittle character and low elongation at break. (Siegenthaler *et al.*, 2011). Thus, blending and compounding with flexible (ductile) polymers such as PBAT seems reasonable.

Two different methods can synthesize PLA polymers: such as (A) through direct polycondensation of lactic acid or (B) through ring-opening polymerization (ROP) of L-lactide (LA), a cyclic dimer of lactic acid. To achieve a high molecular weight or the polymer, method (A) requires severe conditions involving long reaction times, temperatures between 180–200 °C, and a low pressure (5 mmHg) (Ajioka *et al.*, 1995). In contrast, method (B) can produce PLAs with narrow molecular weight distribution under less severe reaction conditions (low temperature of 130 °C and short reaction times) (Hyon *et al.*, 1997; Kowalski *et al.*, 2000). Consequently, the industrial production of PLA adopted the ROP of L-lactide. PLA biodegradation was evaluated under composting conditions where PLA degradation occurred in two stages: firstly, the abiotic chain scission of the polymer, resulting in a decrease of molecular weight, and secondly, the mineralization stage (Kijchavengkul *et al.*, 2009). For PLA, chain scission occurred during the latter end of the first stage. Both phases are accelerated as the temperature increases (Kyrikou & Briassoulis, 2007).

1.3.6 Polyhydroxyalkanoates (PHAs)

For PHA generation, microorganisms produce natural polymers as a storage material for carbon and energy (Lamont, 2005). PHAs contain over 90 monomers ranging from rigid plastics

to tough elastomers, which predominantly depend on the molecular structure. PHA typically possesses 3-hydroxy butyrate (PHB; the molecular structure displayed in Figure I-3 as its primary monomeric unit. In soil, PHA is readily biodegradable (Rudnik & Briassoulis, 2011) and is a highly crystalline thermoplastic polymer that is susceptible to embrittlement. Furthermore, it is known to undergo secondary crystallization for its amorphous phase under storage, leading to a further increase in crystallinity and embrittlement and a substantial decrease of elongation at break (Briassoulis, 2004). A significant problem is its incompatibility with several other polymers (Briassoulis, 2004). In addition, PHA is susceptible to loss of elongation at the break due to ultraviolet radiation produced by the sun, but with the tensile strength remaining constant over a three-month exposure period (Rudnik & Briassoulis, 2011). Therefore, like PLA, blending PHA with other polymers (e.g., polyvinyl acetate) or plasticizers is necessary to improve its physical properties.

1.4 Plastic Degradation in Agricultural Ecosystems

The definition of degradation is "an irreversible process leading to a significant change of the structure of a material, typically characterized by a loss of properties (e.g., integrity, molecular weight, structure or mechanical strength) and fragmentation," according to the American Society for Testing and Materials (ASTM) and the International Organization for Standardization (ISO). Biodegradable plastics' degradation is generally described by a two-step mechanism involving abiotic factors followed by biotic factors (Figure I-6). The abiotic process involves chemical hydrolysis of biodegradable plastic in the presence of water at elevated temperatures. This step is followed by biotic degradation in which microorganisms decompose polymer break-down products generating carbon dioxide, water, and biomass under aerobic conditions and methane, hydrocarbons, and biomass under anaerobic conditions (Huang *et al.*, 2004). Environmental factors contributing to fragmentation and biodegradation occur above ground exposure (UV radiation) and in the soil (microorganisms).

Depending on the degradation environment, the polymer material breakdown can occur by either photodegradation, chemical degradation, or microbial action. First, the polymeric components will break down, provided water, soil biota, and microorganisms are present. Environmental polymer degradation involves first abiotic factors followed by biotic factors (Figure

I-6) and includes changes in the chemical structure and supramolecular structure of polymers or polymer-based products leading to embrittlement, and thus loss of color, shape, diffusion/permeability, and other physical properties under the influence of chemical and biochemical reactions, or environmental factors (e.g., sunlight, heat, or exposure to chemicals) (Matusinovic & Wilkie, 2014). Such loss can occur by the breakage of polymer molecules leading to MP formation, with similar chemical composition as the original material (Vert *et al.*, 1992). However, for biodegradable polymers, the gradual reduction of polymeric components at a controlled rate is desired (Niaounakis, 2015). Technically, all polymers are degradable; however, this term describes polymers capable of decomposing chemically or biologically within several months or years in the soil. Degradable plastics can utilize biopolymers (polymeric components derived from renewable resources), such as poly (alkyl hydroxy alkanoates), poly (lactic acid), cellulose, and starch, among others.

Furthermore, degradable plastics can also be synthesized from polycaprolactone (PCL) in combination with polyvinyl alcohol (PVA). These can degrade by both abiotic and biodegradation mechanisms (Kawai *et al.*, 1992; Pitt, 1992). Intentional polymer modification triggers some reactions by design, resulting in a material with different desired properties. For example, backbone chain scission degradation can occur via depolymerization, random chain breakage, weak-link or preferential site degradation, or some combinations. In depolymerization, the monomer splits off from an activated end group, which is the opposite of addition polymerization and often referred to as "unzipping." Most polymers show susceptibility to degradation under solar radiation (sunlight) and high temperatures, even in the presence of antioxidants. Thus, LDPE sheets, impregnated with carbon black, became brittle after exposure to weathering for one year in South Florida. Long-term degradation is often signaled for polymer films by changing the surface color, resulting in decreased mechanical properties. In the terrestrial environment, polymers are subject to oxidative degradation in the presence of other factors such as heat, air, high-energy radiation, including ultraviolet (UV) and higher energy visible light, and mechanical impact leading to breakage of bonds resulting in a further breakdown. Abiotic hydrolysis is the most critical reaction for initiating the environmental degradation of synthetic polymers (Domb *et al.*, 1998) such as polycarboxylates (Winursito & Matsumura, 1996), PET (Heidary & Gordon, 1994), PLA and their copolymers (Hiltunen *et al.*, 1997).

1.4.1 Photolysis (Sunlight)

Plastic mulches exposed to sunlight lead to severe physicochemical structural changes of BDM's. Plastic photodegradation is the primary driver of the biodegradation process. Biodegradable mulch films are designed to biodegrade by hydrolysis and microbial breakdown of the polymer chain. Solar exposure during the season affects biodegradation in two ways. In the first step, main chain scission from photodegradation reduces the average molecular weight, increasing the accessibility to the polymer chain influenced by moisture and microorganisms (Domb *et al.*, 1998; Kijchavengkul *et al.*, 2008). The smaller plastic molecules can be easier hydrolyzed and utilized by microbes. Second, in the case of aliphatic-aromatic polyesters, photodegradation can trigger chain scission and crosslink (Osawa, 1992). In abiotic degradation, the action of light radiation is one of the most critical parameters. Photodegradation can result in Norrish reactions and crosslinking reactions or oxidative processes (Nakamura *et al.*, 2006) (Hayes *et al.*, 2019). The Norrish reactions are photodegradations that transform the polymers by photoionization (Norrish I) and chain scission (Norrish II) (Figure I-5).

1.4.2 Oxidization

Two main chemical degradation reactions include oxidation and hydrolysis to indicate a synergism between oxidation and hydrolysis for chain cleavage and the addition of hydroxyl and carbonyl groups. For the oxidation of polymers, O_2 in its natural form or as ozone (O_3) triggers the cleavage of covalent bonds in polymers and releases free peroxy radicals resulting in cross-linking and chain scission. Polymers with unsaturated bonds or branched polymers are more likely to undergo oxidation than others (Tiwari, 2012). For mulch films exposed to environmental conditions, free radicals are formed through the auto-oxidation process followed by a photooxidation process (Kyrikou & Briassoulis, 2007).

1.4.3 Mechanical degradation

Mechanical degradation occurs due to compression, tension, and shear forces. The causes of these forces are numerous, e.g., a range of constraints during material installation, aging due to load, air and water turbulences, snow pressure, and bird damage. So, thermoplastic films can undergo several mechanical degradations under field conditions (e.g., low-tunnel films, and mulches, among others) (Briassoulis, 2007). At the macroscopic level, damages are frequently not

visible immediately (Duval, 2009), but at the molecular level, degradation could be started. Mechanical factors are not predominant during biodegradation, but mechanical damages can activate or accelerate the process (Briassoulis, 2005). In field conditions, mechanical stresses synergize with the other abiotic parameters (temperature, solar radiation, and chemicals).

1.4.4 Biotic Polymeric degradation

Recent research confirmed that biodegradation is influenced by temperature, a major environmental factor affecting biodegradation rates. The observation showed that the biodegradation reaction occurred at 97% within the tested temperature range between 15-28 °C, which indicates a persistence in the metabolic activities of the involved mesophilic microbial communities (Pischedda *et al.*, 2019). Biodegradation of Poly (lactic acid)—PLA—films in soil matrix under mesophilic conditions utilized natural attenuation, bio-augmentation, and bio-stimulation.

In nature, biotic and abiotic factors act synergistically to decompose organic matter. Several studies about the biodegradation of some polymers show that abiotic degradation precedes microbial assimilation (Kister *et al.*, 2000; Proikakis *et al.*, 2006). Consequently, abiotic degradation is also essential to initiating the degradation process. Biodegradation is governed by factors such as polymer characteristics, type of organism, and the nature of pretreatment (Figure I-4). Also, polymer characteristics such as mobility, tactility, crystallinity, molecular weight, type of functional groups present in the structure, and plasticizers or additives in the polymer all play an essential role in degradation (Artham & Doble, 2008). In addition, the rate of biodegradation is governed by the biodegradation environment. Depending on the environment, microbial communities differ significantly between types, such as soil or compost, topographical regions, and management practices. Composting transforms biodegradable components, either bio- or fossil-based, into compost, under aerobic conditions by releasing CO_2 water and minerals through microbial actions. Biodegradation in the soil can be slower than compost operations due to lower temperature, soil moisture level, degree of aeration, and concentration of microorganisms in the soil (Narayan, 2010). Therefore, it is crucial to reference biodegradation to a specific biodegradation environment and its underlying properties (Figure I-4).

In-field conditions, mechanical stresses synergize with the other abiotic parameters (temperature, solar radiation, and chemicals). A recent review lists and describes the main underlying factors that promote the biodegradation of plastics (Vert *et al.*, 2012). Three categories describe biodegradation, such as abiotic (environmental) conditions, microbial requirements, and properties of the mulch material. The products of microbial degradation of BDMs, under aerobic conditions include microbial biomass, soil organic carbon (SOC) water, and carbon dioxide (Figure I-6). Methane is an additional metabolite formed under anaerobic conditions (César 2014; Kasirajan and Ngouajio 2012). SOCs are rich in humic and fulvic acids that may improve soil health (Azios, 2007).

1.4.5 Nanoplastic behavior in suspensions

High colloid stability can be expected in a monodispersed suspension containing a homogenous component (populations) of NPs and water. A uniform particle surface charge across a wide range of pH conditions was observed, maintaining a stable dispersion since the NPs electrostatically repel each other caused by surface charge, as depicted in Figure I-7 (Crutchik *et al.*, 2020).

1.4.6 Ionic strength

Increased ionic strength in solution in the presence of NPs impacts the colloidal stability through cations' electrostatic charge screening effect. Therefore, the addition of metallic cations in the solution will impact the typically negatively charged NPs by limiting the electrostatic effect of each particle and therefore limiting the Debye radius (Singh *et al.*, 2019). Consequently, the aggregation will occur since the energy levels preventing the particle attraction at which van der Waals attractions will occur are diminishing

Increased ionic strength in solution in the presence of NPs impacts the colloidal stability through cations' electrostatic charge screening effect. Therefore, the addition of metallic cations in the solution will impact the typically negatively charged NPs by limiting the electrostatic effect of each particle and therefore limiting the Debye radius (Singh *et al.*, 2019). Consequently, the aggregation will occur since the energy levels preventing the particle attraction at which van der Waals attractions will occur are diminishing (Figure I-7b) resulting in less stable aggregates by increasing the ionic strength in the slurry (Zhang *et al.*, 2019). Therefore, higher ionic strength

generally results in increased aggregation caused by repulsion between particles based on the lower fluid mobility of NPs. Furthermore, metal cations are adsorbed to NPs, decreasing the particles' fluid stability. Cation surface adsorption on negatively charged NPs results in a lower net surface charge of the particles and limits the repulsive effects between NPs by changing their ζ potential closer to zero increasing the effects of van der Waals attraction (Song *et al.*, 2019). Larger NPs particles tend to be more stable in metal cations since higher levels would be required to electrically destabilize the particles, which can be explained by higher levels of free Gibbs free absorption energy of larger particles (Cui *et al.*, 2018). Overall, high ionic strength decreases the NP's mobility in aqueous slurry systems, varying based on the surface functionality and size of the NPs.

1.4.7 Impact of organic matter on nanoparticles

In soil, dissolved organic matter (DOM), including proteins, influence the NPs' mobility based on their surface charges and the solution chemistry. For example, a slurry of elevated DOM (e.g., humic acid) concentrations dispersed NPs with opposite net surface charges may result in increased agglomeration (attachment) effects due to lowering the ζ potential on NP s (Kihara *et al.*, 2019). The aggregation occurs because of lower electrostatic repulsion, leading to larger particle hydrodynamic diameters by as much as two orders of magnitude (Summers *et al.*, 2018). However, with much higher DOM ratios than NPs, organic matter can coat the NPs and cause a reduction in aggregation since the particles repel each other due to a non-zero ζ potential (Kihara *et al.*, 2019). Therefore, less stable NPs solutions can be expected in high metal cations concentrations and DOM compared to dual fractions of either individual solutions of NP-cations or NPs -DOM (Cai *et al.*, 2018). Larger particles of organic matter (POM) generally increase the slurry stability based on steric repulsion. Although organic material naturally tends to be absorbed by positive charges NPs, negatively charged NPs might stay dispersed in solution or possibly form negatively charged heteroaggregates with DOM and metal cations (Song *et al.*, 2019).

Larger-sized NPs with particle diameters (d_p) of around 200 nm are less sensitive to interactions with components suspended in a solution than particles with a d_p of 50 nm. Therefore, the NPs interactions may be primarily influenced by particle size and surface chemistry. In nature, the surface chemistry of particles will be determined by interactions with organic matter (e.g., the presence of DOM) and cations compared to the original material (Brewer *et al.*, 2020).

1.4.8 Inorganic colloids

In soil, destabilization of NPs may occur through inorganic colloids such as minerals in solution, where NPs tend to form unstable heteroaggregates. The respective zeta potential will determine the formation and interaction of inorganic colloids as observed through clay-NPs interactions represented by negatively charged NPs and montmorillonite at low pH values. However, cation bridging between particles can improve the aggregation behavior. Also, positively charged NPs may form heteroaggregates with iron oxide minerals in pure water (Singh *et al.*, 2019). In general, NPs stability was decreased in the presence of DOM-suspended sediments (Li *et al.*, 2019). NPs dispersed in the terrestrial environment will be modified by interactions; sedimentation may occur through the aggregation of NPs and result in particle density causing settling out of suspension in a water column (Figure I-7f) as the settling velocity proportional to the square of the particle size and particle density. Enhanced NPs sedimentation was observed in studies employing high metal cation concentrations and DOM (Dong *et al.*, 2019). Inorganic colloids such as suspended surface soil sediments and POMs may attach to NPs and form heteroaggregates, especially under higher metal cation concentrations which tend to settle out of suspension within days or even minutes. Settled particles can resuspend under the influence of bioturbation in a water column to restore mobility, and therefore sedimentation may be an essential mechanism to consider for controlling the NP's mobility in the aquatic environment.

1.4.9 Nanoplastic attachment to soil and sediments

In a terrestrial environment, NPs transport may attach to surfaces of mineral particles resulting in immobilization. The attachment interactions between NPs and minerals or substrates occur similarly in the aqueous and colloidal environment.

The presence of positively charged NPs in a slurry of negatively charged silica sand results in the attraction and attachment of NPs onto the sand particles (Shaniv *et al.*, 2021). In contrast, negatively charged NPs will result in repulsion and stabilization and may result from enhanced NPs mobility. Cationic Ca^{2+} particles may absorb dissolved DOM through cation or polymer

bridging (Liu *et al.*, 2019). A solution's soil pH and zeta potential are inversely related, where low pH conditions increase the zeta potential on NPs and soil component surfaces. Decreasing repulsive forces, NPs may be retained in the solid phase. Soil minerals play an essential role in

NP's mobility. In particular, iron (Fe) and aluminum (Al) oxides possess a positive charge at pH ranges between 7.5 and 9, and negatively charged NPs will attach to mineral surfaces. Interestingly, at high pH levels (>9), oxide minerals become negatively charged and will contribute to the electrostatic stabilization of NPs in the solution. For clay minerals in the soil, representing functional groups of Al−OH and Si−OH may result in similar aggregation/repulsion behavior based on the protonation and deprotonation of these components at different pH values.

Soil can have only a finite amount of surface sites for NPs aggregation attachment. As these sites become occupied during prolonged exposure to NPs, the soil will begin to approach its retention capacity, and further NP attachment will decrease, with a corresponding increase in NPs transport (Figure I-7e). However, NPs' detection in the soil is challenging due to their small dimensions and concentrations, making them indistinguishable from soil particles. Microscopic techniques offer the detection possible by labeling the particles with fluorescent dyes (Nile red), which makes NPs detectable under the microscope. However, introducing additional chemicals will most likely alter the properties and influence the sample analysis.

Therefore, due to the lack of feasible options, advanced detection techniques are required to investigate the in-situ behavior of size, shape, and agglomeration behavior (particle dynamics and sizes) in the context of NPs in terrestrial environments. Scattering techniques provide valuable information at a wide length scale about sample features such as polydispersity and porosity, among others. Therefore SANS (Small Angle Neutron Scattering) and ULTRA-SANS (USANS) are promising techniques that will help to measure dynamics such as the aggregation behavior of soil particulates. In addition, neutrons are nondestructive to the samples, which allows investigation over extended periods to achieve high experimental resolution. The unique contrast matching methods employed in SANS and USANS techniques allow the investigation of particle dynamics and interactions of two different components (e.g., soil and NPs slurry).

In contrast to microscopy, SANS techniques allow investigation of in situ measurements of size, shape, and agglomeration behavior (particle dynamics and sizes) in context to NPs in terrestrial environments. Contrast variation was achieved by selecting a solvent H_2O/D_2O ratio to match soil scattering, thereby becoming sensitive to NPs only. This research addresses a knowledge gap: fundamental knowledge of NP-based interactions, such as homo and hetero-aggregation of NPs and soil particulates, and their transport effect of terrestrial NPs. Although the

NPs' interaction, aggregation behavior, and association with soil particles are currently unknown on the fate and transport of terrestrial NPs' surface properties, aggregation behavior and association with soil particulates are believed to be altered over time in soil environments.

1.5 Small-Angle Neutron Scattering Techniques (SANS)

For our study, NPs successfully investigated through SANS and Ultra-SANS by using contrast matching techniques presented in Chapters V and VI.

Scattering techniques such as small angle neutron scattering (SANS) provide essential information about complex particle systems at different length scales, which interatomic distances, porosity, aggregation, polydispersity, and morphology. The scattering principle of scattering techniques is based on a neutron beam in which the sample is for a determined runtime. As a result, a series of multi-oriented scattered neutrons are emitted beam's wavelength (λ) and incidence angle ($2\,\theta$). The neutron beam enters the sample (generally transferred into a cell). It interacts with the sample's structural features at varying scales, generating multi-length scale scattered beams monitored and recorded on 2D detectors.

The beam energy is inversely proportional to its wavelength, so the high-energy waves penetrate smaller-scale structures. The interaction between the sample and neutron source will result in either an elastic (constructive interchange) or inelastic (destructive interference) scattering behavior. The collected signals on the 2d detectors are being averaged, normalized, and integrated to generate a 2 D scattering image with characteristic ring patterns (Figure I-8). Finally, a Fourier transformation converts the scattering image to a 1D wavenumber profile, representing the I (q) vs. q (=Q) relationship, which can be analyzed through curve fitting, and conclusions can be drawn from the sample.

For nanoparticle (NPs) detection, scattering methods, such as light scattering (LS), X-ray scattering, and neutron scattering, successfully contributed to the structural characterization of polymeric systems. For example, LS has been used to characterize polymers in solutions since the 1940s (Chu, 2007; Doty, 1945; Zimm, 1948).

Historically, polymer science has employed SANS techniques since the early 1970s (Kirste *et al.*, 1972; Schelten *et al.*, 1974). SANS is a suited technique for polymer characterization—in particular, polymer solutions, crystalline morphology structure, polymer blends, block

copolymers, and polymer slurries use a deuterated solvent which lowers the incoherent scattering arising from H-containing materials. Furthermore, SANS techniques allow individual measurements under different sample environments, such as under high-pressure, shear deformation, temperature, and humidity control (Borsali & Pecora, 2008). Typical examples are presented in a Guinier plot, Zimm plot, and Kratky plot analyses, from which the weight-average molecular weight and the radius of gyration can be evaluated (Borsali & Pecora, 2008). The analysis allows for the quick and accurate determination of the above-mentioned molecular parameters. X-ray scattering techniques have advanced after synchrotron sources became available in the 1980s. Neutron scattering has several characteristic features useful to X-ray scattering: (Squires, 1996).

The benefits of SANS are (1) wavelength suitable for structural analysis in nanometer-scales (diffraction), (2) sensitivity to elements and their isotopes (nuclear scattering), (3) high penetration power (radiography), (4) capability of labeling without changing the chemical/physical properties, that is, isotopic labeling (H/D substitution for neutron scattering), (5) sensitivity to the magnetic structure of the sample (magnetic scattering) and (6) energy exchange between neutron and nucleus in the sample due to the finite (that is, non-zero) mass of the neutron (inelastic scattering). The use of neutron scattering allows characterization, material structure, magnetic structure, excitation states of condensed matter, and the dynamics of soft matter (Higgins & Benoit, 1994).

Besides the numerous types of neutron scattering methodologies, small-angle neutron scattering (SANS) uses only low scattering angles, θ, up to 5 or 10 degrees. SANS used the typical wavelength of $\lambda_N \approx 0.6$–1 nm derived from a neutron beam. Furthermore, SANS is very useful for the structural characterization of different materials, and the detection of density/concentration changes of media within a spatial range up to 100 nm ($\approx (4\pi/\lambda_N) \sin (\theta/2)$) can be conducted by SANS. SANS is also frequently used as a complementary technique to small-angle X-ray scattering (Ezquerra *et al.*, 2009).

Scattering techniques provide valuable information at various length scales, from atomic size (nanometers) to macroscopic (micrometer) sizes, about morphology, polydispersity porosity, agglomeration behavior interatomic distances. The principle of scattering techniques employs sources of light, x-ray, or neutron to irradiate a sample over a specific duration. The emitted beam

interacts with the sample structural features as a function of the wavelength (λ) and scattering angle (θ). These parameters determine the probed length scale through the relationship:

$$d \approx \frac{\lambda}{\theta} \quad \frac{\text{(wavelength)}}{\text{(scattering angle)}} \tag{1}$$

These interactions between the radiation source and sample can result in either elastic (pure constructive-interference interaction) or inelastic (destructive interference) scattering. A 2D detection system measures the scattered signals, integrated over time, and normalizes the count per time unit and pixels, generating a 2D scattering image with characteristic ring patterns representing (electron) densities. The rings reflect the wave vectors produced by reflections which can be associated with the structural features of the sample material.

Fourier transformations generate the relationship vs. wavenumber (I(q) vs. q). The relationships between the length scale wavenumber and emitted beam are described as follows:

$$q = \frac{4\pi \sin\theta}{\lambda} \tag{2}$$

$$d = \frac{2\pi}{q} \tag{3}$$

Where q relates to a scattering wave vector and characteristic length d.

Small angle scattering methods such as small angle neutron scattering (SANS) are employed to measure average pore sizes and aggregation behavior of nanoscale regimes ranging between 1-100 nm in length scale. Data processing of collected scattering data involves data reduction and data analysis. The reduction procedures generally depend on the instrument's setup; however, the data analysis, including curve fitting, is independent of the instrument design (Ilavsky & Jemian, 2009; Pro, 2011). Advanced post-processing methods improve the signal-to-noise ratio through background subtraction for data analysis. In addition, several powerful software packages, such as Irena and Nika (designed for IGOR Pro), enable efficient data processing and curve fitting procedures. Scattering intensity profiles are generally analyzed via power-law relationships, which

correspond to the structural features of the particulates investigated. The Guinier analysis is ideal for low and intermediate q ranges to characterize polydispersity and aggregations and determine the gyration's radius and particle diameter (Li *et al.*, 2016; Sorensen & Wang, 1999). The Porod fit represents another suitable method for the characterization of low q regions, where surface correlations follow a 'Q^{-n}' relationship:

$$I(Q) = \alpha \, S \, q^{-\beta} \tag{4}$$

Where β is the Porod exponent and S represents the surface-related factor. Sharp interfaces reflect a value of n=4, which refer to abrupt variations in the domain length. Scaling may occur in the case of surface fractals present in the sample. The Porod law for fractal structures is:

$$I(q) = \alpha \, S' \, q^{-(6-\beta)} = S' \, q^{-d}{}_f \tag{5}$$

This form can be used to determine the surface fractal dimensionality as $d_f = (6 - n)$ where $2 \le d_f \le 3$ and $n = 4$, equally $d_f = 2$, representing smooth surfaces as n approaches a value of 2. Rough surfaces result in $d_f = 3$ values. A scattering curve can obtain multiple sections showing features, reflecting Porod fits.

The objectives of this study aimed to investigate the effects of ex-situ stirring on the mechanical abrasion and agglomeration behavior of NPs derived from agricultural mulches.

1.6 Research Chapter Objectives

The research described in this dissertation aims to understand the individual life stages of MPs and NPs of nonbiodegradable mulches and BDMs in soil (Figure I-9). The transformation of plastic fragments into MPs and NPs and the dimensional and physicochemical properties of biodegradable and non-biodegradable agricultural mulch feedstocks are described herein. Furthermore, the size reduction of plastic particles on the nanoscale under the mechanical impact (ex-situ stirring, also termed convective transport) and the aggregation behavior in the presence of soil aggregates at varying plastic concentrations was evaluated. Hence, four specific objectives are addressed in this dissertation:

- Mechanically form MPs and NPs derived from agricultural plastic mulch films and pellets feedstocks that are representative of MNPs occurring in the agricultural field for employment in environmental studies (Chapters II-IV)

- Determine how MPs form from fragments and how NPs form from MPs in soil and their dimensional, physicochemical, and biodegradability-related properties (Chapter III)

- Determine how environmental weathering affects the formation of MPs and NPs derived from agricultural mulch films (Chapter IV)

- Evaluate the effects of convection on the colloidal and agglomeration behavior of NPs derived from agricultural plastics dispersed in water in the presence of soil particles (Chapters V & VI)

1.7 Description of Chapters

- **Chapter II:** The principal objective of this study was to compare and evaluate the breakdown of a PBAT-rich BDM film and PBAT pellets by calculating d_p's for MPs and NPs.

- **Chapter III:** This chapter describes the mechanical formation of realistic MPs and NPs using biodegradable (PBAT) and non-biodegradable mulch materials (LDPE) that mimics their exposures and interactions with the soil environment (conditions) in the soil, represented in Figure I-9. After the growing season, BDMs fragments (what is left after environmental weathering) on the soil surface are being plowed into the soil and further fragment into NPs due to mechanical impact in soil. LDPE is not biodegradable and requires removal from the soil surface at the end of the growing season.

  Hypothesis: To investigate if the particle size distribution and thermal properties of cryogenically treated PBAT were significantly different compared to LPDE feedstocks

- **Chapter IV:** The primary objective of this study was to determine if cryogenic treatment of two biodegradable mulch films (PBAT and PLA/PHA) effectively mimicked the embrittlement caused by environmentally weathering (after one growing season) regarding their dimensional, thermal, chemical, and biodegradability properties of the formed MNPs.

  Hypothesis 1-III: To determine if particle size distribution becomes more uniform as the average particle size (d_p) of MNPs decreases

Hypothesis 2-III: To investigate if the particle size distribution of MNPs formed from environmentally weathered polymers will result in smaller d_ps than cryogenically formed particles.

Hypothesis 3-III: To evaluate if NPs degrade faster under aerobic biodegradation conditions in the presence of soil and compost components.

- **Chapter V:** This study aimed to determine the NPs' (1 wt%) in-situ agglomeration in the presence of soil particles (vermiculite serving as a surrogate soil, 0.5 wt%) dispersed in composite slurries using different D_2O/H_2O solvent ratios. Furthermore, this study was performed to detect the change of d_p for NPs under the impact of convective transport (0h, 24h) using Small Angle Neutron Scattering (SANS) and Ultra-SANS techniques.

- **Chapter VI):** This chapter expands the study described in Chapter V by using higher NPs concentrations (5 wt%) and extended stirring time (168 h) in h presence of soil particles (vermiculite, 0.5 wt%) to investigate the particles' size reduction ad agglomeration behavior.

APPENDIX I
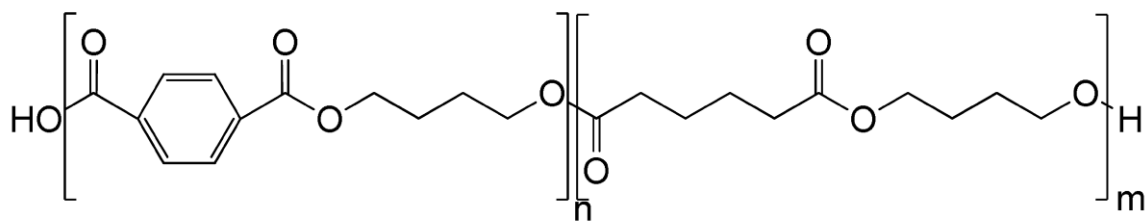
Figure I-1. Chemical structure of Polybutylene adipate terephthalate (PBAT)
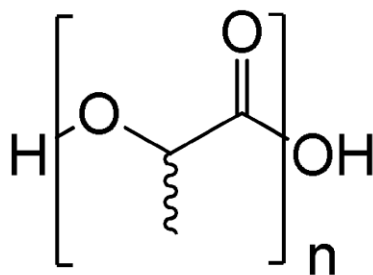
Figure I-2. Chemical structure of Poly-L-Lactic Acid (PLA)
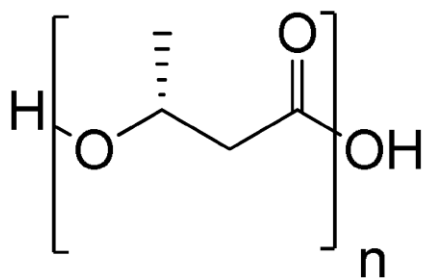
Figure I-3. Chemical structure of Polyhydroxyalkanoate (PHA)
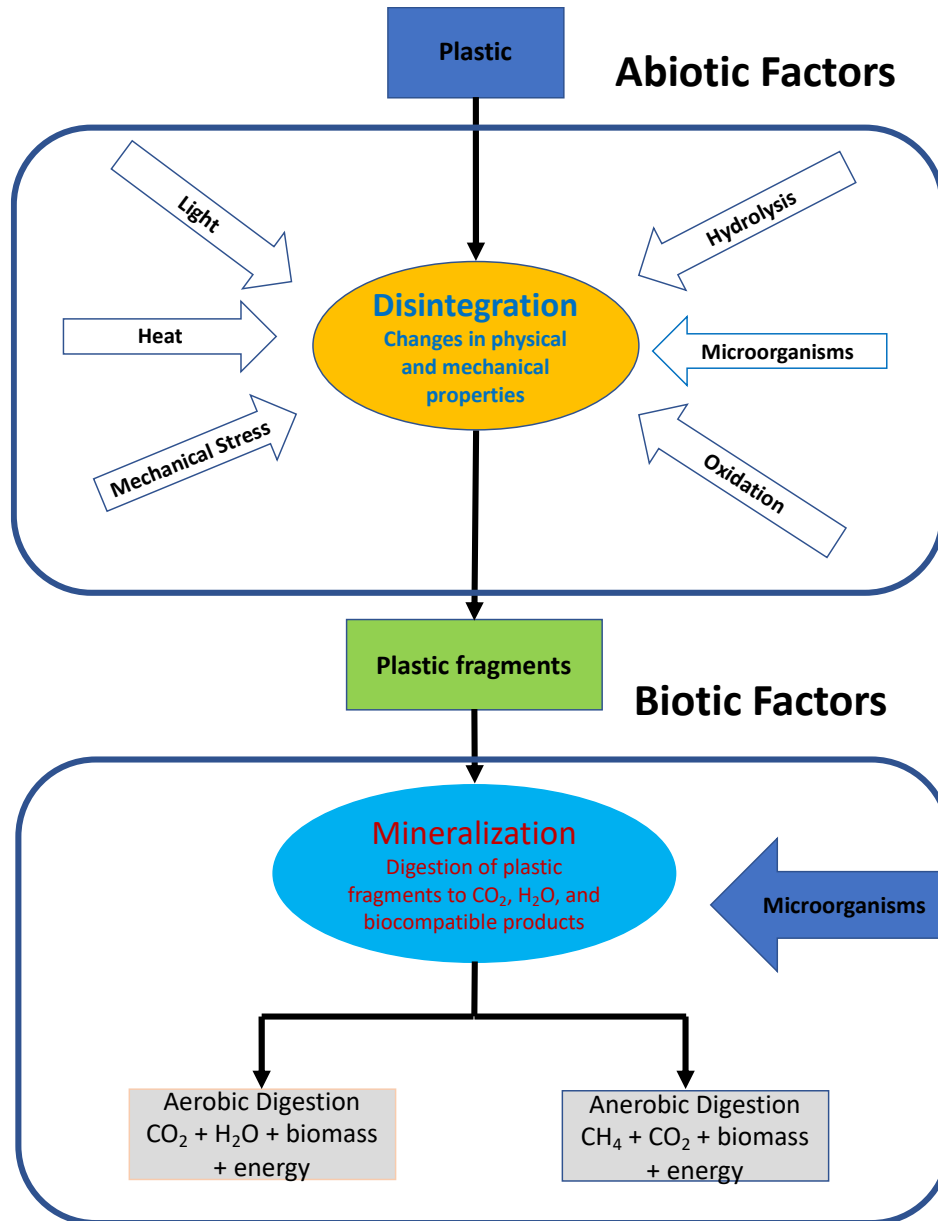
Figure I-4. Scheme of polymer biodegradation in the natural environment adapted from (Lendlein & Sisson, 2011).
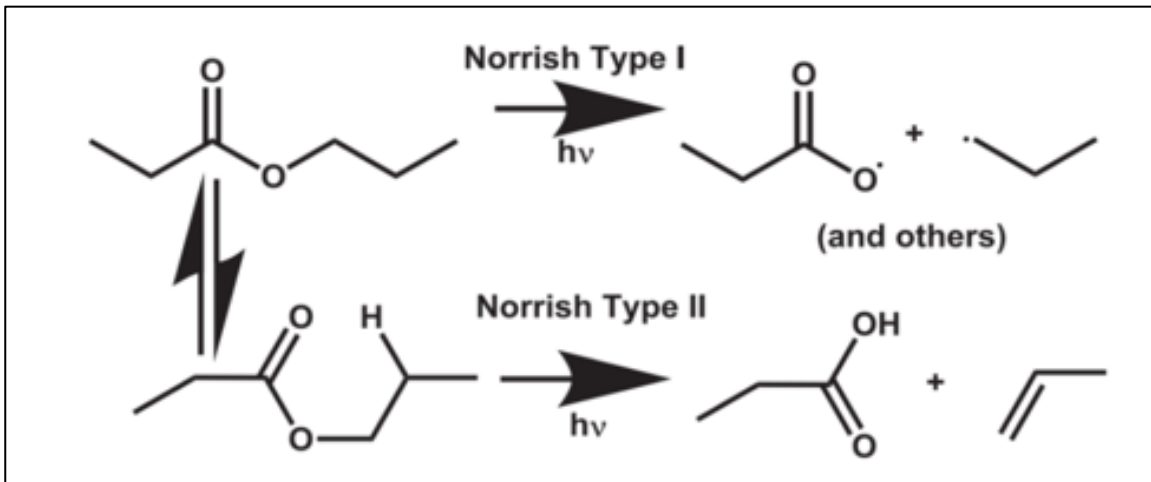
Figure I-5. Norrish-type photochemical reactions for polyesters adapted from (Hayes *et al.*, 2019).
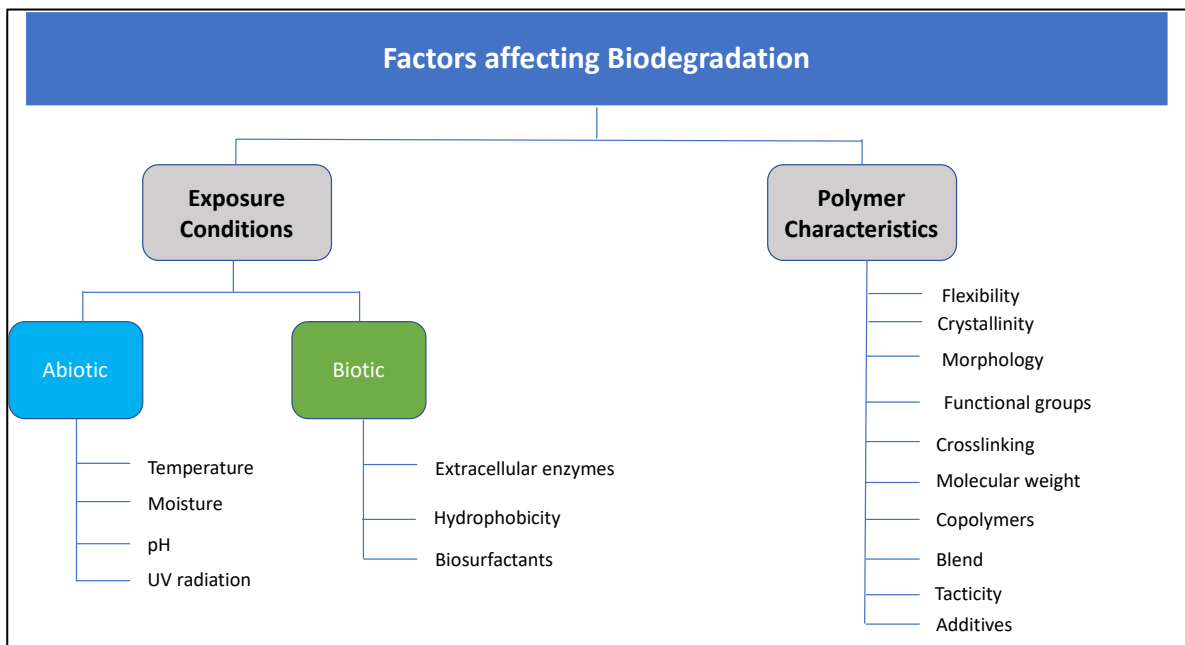
Figure I-6. Factors affecting biodegradation adapted from (Kijchavengkul & Auras, 2008).
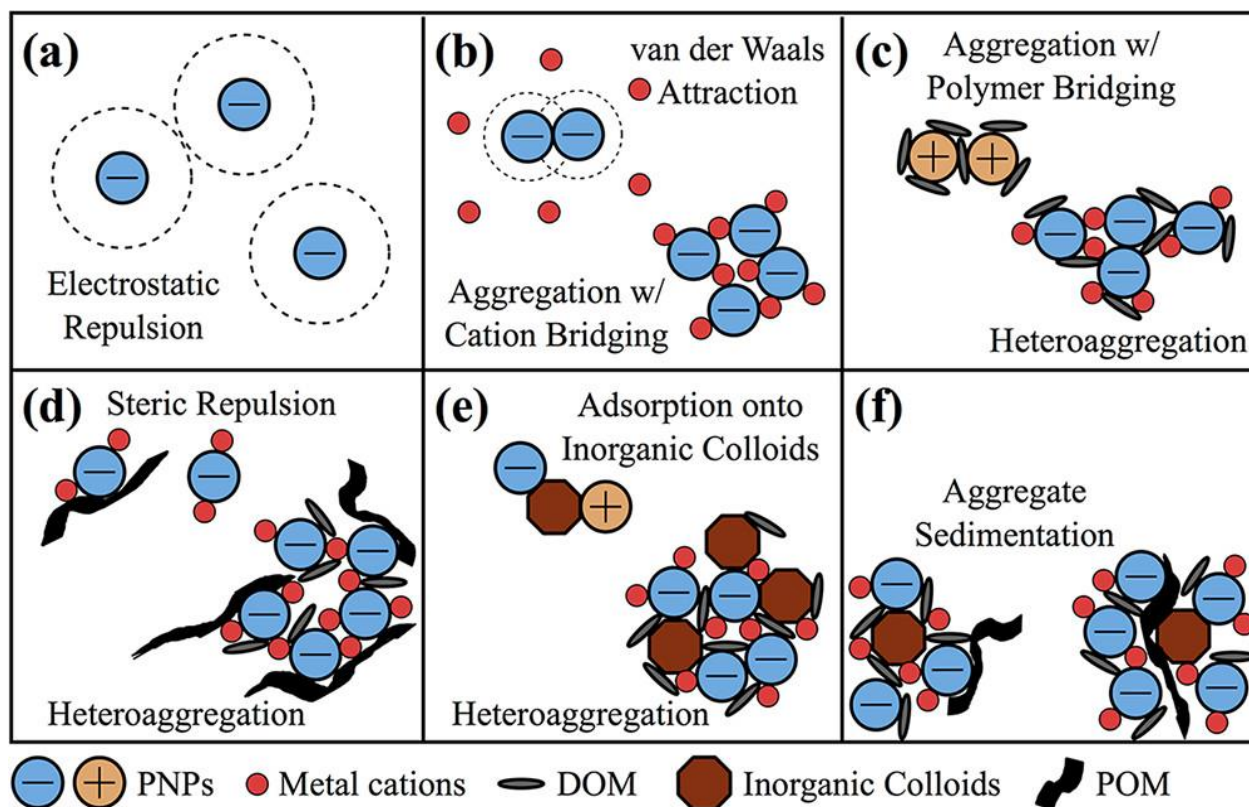
Figure I-7. Interactions of nanoplastics (NPs) suspended in other soil components.

Figure adapted from (Brewer *et al.*, 2020). Interaction effects between suspended NPs in an aqueous solution can occur under various conditions described as follows: (a) Monodisperse suspension: similar electrostatic charge of NPs results in repulsion hindering aggregating, maintaining a monodisperse suspension (b) Aggregation: metal cations increase NPs aggregation through van der Waals attractions or cation bridging. (c) Aggregation: positive charge NPs (=PNPs) in dissolved organic matter (DOM) can result in polymer bridging between the particles. DOM can also be adsorbed by negatively charged NPs in the presence of metal cations, leading to meter aggregation. (d) Heteroaggregation: NPs can absorb particulate organic matter (POM), where these large organic molecules can result in steric repulsion between NPs, minimizing aggregation. However, the same conditions can result in the incorporation of NPs into larger heteroaggregates. (e) Heteroaggregation: Absorption of positively and negatively charged NPs onto inorganic colloids, leading to heteroaggregation with other suspended components. (f) Aggregate sedimentation: Increased aggregation behavior can lead to the sedimentation of NPs in combination with cations, DOM, and POM, by concentration reduction in the mobile fluid phase.
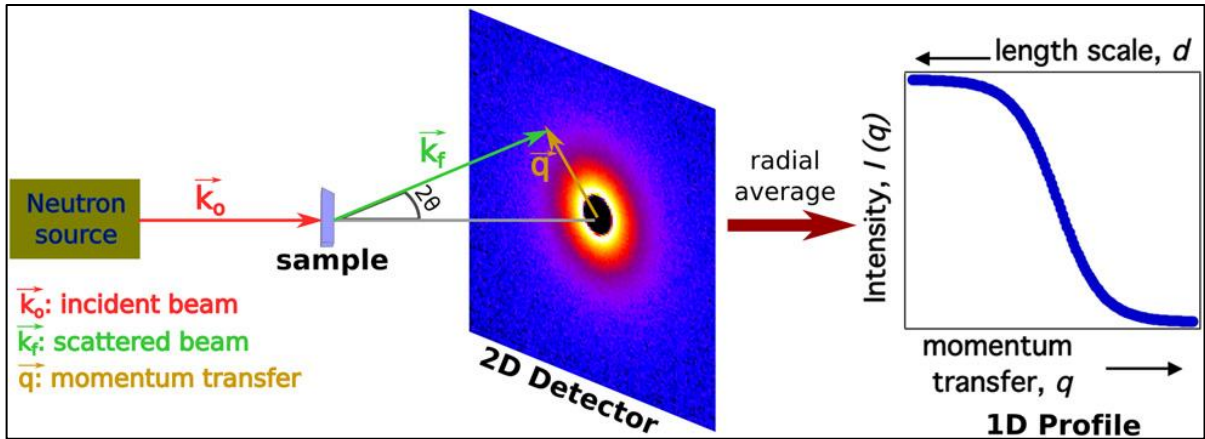
Figure I-8. Schematic of a small-angle neutron scattering setup adapted from (Castellanos *et al.*, 2017).
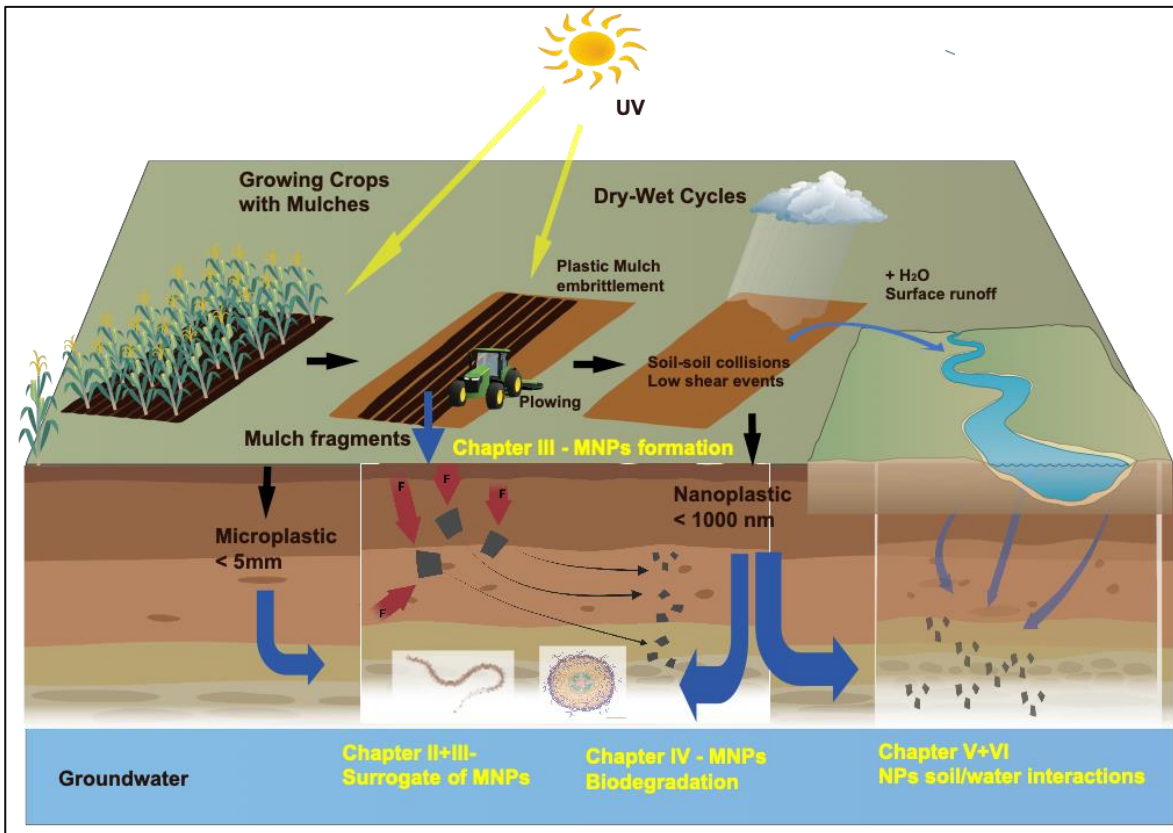
Figure I-9. Conceptual flow diagram depicting the mulch life stages starting from growing crops, tilling into the soil and the fragmentation representing the research objectives II – VI.

CHAPTER II

PROTOCOL TO FORM MICRO- AND NANO PLASTICS FROM AGRICULTRUAL PLASTIC FILMS FOR EMPLOYMENT IN FUNDAMENTAL RESEARCH STUDIES

A version of Chapter II was published in *JoVE* on July 27th, 2022:

Citation

Authors

Anton F. Astner[1], Douglas G. Hayes[1*], Hugh M. O'Neill[2], Barbara R. Evans[3], Sai V. Pingali[2], Volker S. Urban[2], Timothy M. Young[3]

[1]Department of Biosystems Engineering and Soil Science, University of Tennessee, 2506 E. J. Chapman Dr., Knoxville, TN 37996-4531, USA

[2]Neutron Scattering and [3] Chemical Sciences Divisions, Oak Ridge National Laboratory, 1 Bethel Valley Road, Oak Ridge, TN 37830, USA

[3]Center for Renewable Carbon, The University of Tennessee, 2506 Jacob Dr, Knoxville, TN 37996, USA

Anton Astner's contribution the research objective, designing, and conducting the experimental tasks, processing, and interpreting the data, and drafting the paper.

Co-researchers contributions are listed as follows:

D. G. Hayes significantly helped to identify the research goal and revised and polished the paper. H. O'Neill, B. R. Evans, S. V. Pingali, V. S. Urban helped in the experimental design and adjusting of experimental parameters
T. M. Young gave advice for the statistical evaluation and revised the manuscript.

Abstract

Microplastics (MPs) and nanoplastics (NPs) dispersed in agricultural ecosystems pose a severe threat to biota in soil and nearby waterways. In addition, chemicals such as pesticides adsorbed to NPs can harm soil organisms and potentially enter the food chain. In this context, agriculturally utilized plastics such as plastic mulch films contribute significantly to plastic pollution in agricultural ecosystems. However, most fundamental studies of fate and ecotoxicity employ idealized and poorly representative MP materials such as polystyrene microspheres. Therefore, as described herein, we developed a lab-scale multi-step procedure to mechanically form representative MPs and NPs for such studies. First, the plastic material was prepared from commercially available plastic mulch films of polybutyrate adipate-co-terephthalate (PBAT) that were embrittled through either cryogenic treatment (CRYO) or environmental weathering (W) and from untreated PBAT pellets. The plastic materials were then treated by mechanical milling to form MPs with a size of 46 - 840 μm [micrometer], mimicking the abrasion of plastic fragments by wind and mechanical machinery. The MPs were then sieved into several size fractions to enable further analysis. Finally, the 106 μm sieve fraction was subjected to wet grinding to generate NPs of size 20-900 nm, a process that mimics the slow size reduction process for terrestrial MPs. Dimensions and shape for MPs were determined through image analysis of stereomicrographs, and dynamic light scattering (DLS) was employed to assess particle size for NPs. MPs and NPs formed through this process possessed irregular shapes, which agrees with the geometric properties of MPs recovered from agricultural fields. Overall, this size reduction method proved efficient for forming MPs and NPs composed of biodegradable plastics such as polybutyrate adipate-co-terephthalate (PBAT), representing mulch materials used for agricultural specialty crop production.

2.1 Introduction

In recent decades, the rapidly increasing global production of plastics and improper disposal and lack of recycling for plastic waste led to environmental pollution that has impacted marine and terrestrial ecosystems (rajuAlimba *et al.*, 2021; Jin & Dan, 2021; Kumar *et al.*, 2021). Plastic materials are essential for contemporary agriculture, particularly to cultivate vegetables, small fruit, and other specialty crops. Their usage as mulch films, high and low tunnel coverings, drip tape, and other applications aim to enhance crop yield and quality, lower production costs, and promote sustainable farming methods (Hayes *et al.*, 2019; Serrano-Ruiz *et al.*, 2021). However, the expanding employment of "plasticulture" has raised concerns about the formation, distribution, and retention of plastic pieces in agricultural environments. After a continuous fragmentation process caused by embrittlement through environmental degradation during service life, larger plastic fragments form micro-and nanoplastics (MNPs), which persist in soil or migrate to adjacent waterways via water runoff and wind (Anunciado *et al.*, 2021; Rillig & Lehmann, 2020; Viaroli *et al.*, 2022). Environmental factors such as ultraviolet (UV) radiation through sunlight, mechanical forces of water, and biological factors mainly trigger plastic embrittlement of environmentally dispersed plastics result in the breakdown of larger plastic fragments into macro- or meso-plastic particles(Hayes *et al.*, 2017; Yang *et al.*, 2022). Further defragmentation forms microplastics (MPs) and nanoplastics (NPs), reflecting particles of average size (nominal diameter; d_p) of 0.1–5000 μm and 1–1000 nm, respectively (Schwaferts *et al.*, 2019). However, the upper d_p limit for NPs (i.e., a lower limit for MPs) is not universally agreed upon and, in several papers, is listed as 100 nm (Gigault *et al.*, 2018).

MNPs from plastic waste pose an emerging global threat to soil health and ecosystem services. Adsorption of heavy metals from freshwater by MPs led to an 800-fold higher concentration of heavy metals than the surrounding environment (Naqash *et al.*, 2020). Furthermore, MPs in aquatic ecosystems pose multiple stressors and contaminants by altering light penetration, causing oxygen depletion and adhesion to various biota, including penetration and accumulation in aquatic organisms (Manzoor *et al.*, 2021). Recent studies suggest that MNPs can impact soil geochemistry and biota, including microbial communities and plants (de Souza Machado *et al.*, 2018; Jacques & Prosser, 2021; Kwak & An, 2021). Furthermore, NPs threaten the food web (Kwak & An, 2021; Pironti *et al.*, 2021; Vighi *et al.*, 2021; Wahl *et al.*, 2021). Since MNPs readily undergo vertical

and horizontal transport in soil, they can carry absorbed contaminants such as pesticides, plasticizers, and microorganisms through the soil into groundwater or aquatic ecosystems such as rivers and streams (Horton & Dixon, 2018; Panno *et al.*, 2019; Su *et al.*, 2019; Zurier & Goddard, 2021). Conventional agricultural plastics such as mulch films are made from polyethylene, which must be removed from the field after usage and disposed of in landfills. However, incomplete removal leads to substantial plastic debris accumulation in soils (Hayes, 2021; Yang *et al.*, 2022; Yu *et al.*, 2021). Alternatively, soil-biodegradable plastic mulches (BDMs) are designed to be tilled into the soil after use, where they will degrade over time. However, BDMs persist temporarily in soil and gradually degrade and fragment into MPs and NPs (Qin *et al.*, 2021; Yang *et al.*, 2022).

Many current environmental ecotoxicological and fate studies employ idealized and non-representative MPs and NPs model materials. The most used surrogate MNPs are monodisperse polystyrene micro- or nanospheres, which do not reflect the actual MNPs residing in the environment (Gigault *et al.*, 2018; Phuong *et al.*, 2016). Consequently, the selection of unrepresentative MPs and NPs may result in inaccurate measurements and results. Based on the lack of appropriate model MNPs for terrestrial environmental studies, the authors were motivated to prepare such models from agricultural plastics. We previously reported on the formation of MNPs from BDMs and polyethylene pellets through mechanical milling and grinding plastic pellets and film materials and MNPs' dimensional and molecular characteristics (Astner *et al.*, 2019). The current paper provides a more detailed protocol for preparing MNPs that can be applied more broadly to all agricultural plastics, such as mulch films or their pelletized feedstocks. Here, to serve as an example, we chose a mulch film and spherical pellets of the biodegradable polymer polybutylene adipate terephthalate (PBAT) to represent agricultural plastics.

2.2 Protocol for Micro- and Nanoplastic Formation

The protocol in the following contains an individual numbering scheme and format.

1.1   Processing of MPs from plastic pellets through cryogenic pretreatment and milling according to the flow diagram depicted in (Figure II-1).

> **Note:** This methodology is based on a procedure described elsewhere, employing a PBAT film composed of the same material used for this presented study (Astner *et al.*, 2019).

1.1.1   Weigh polymer pellets samples of ~1 g and transfer into a 50 mL glass jar.

1.1.2   Place the "rectangular delivery" tube with a 20 mesh (840 µm) sieve in the slot in front of the rotary cutting mill and raise the delivery tube until it hits the stop pin.

1.1.3   Position the glass plate over the milling chamber's face and secure the glass plate with the adjustable clamp. Next, place a 50 mL glass jar under the mill outlet (Figure II-2).

1.1.4   Position the sliding side arm support on the mill (positioned on the right upper side) in the middle of the front glass and tighten with the knurled bolt. Ensure that the front glass of the mill is securely positioned (Figure II-2a).

1.1.5   Insert hopper funnel on top of the mill into opening of the upper milling chamber.

1.1.6   Plug line cord into power outlet and press cord switch to start mill operation.

> **Note:** To prevent jamming, feed only material after the mill is powered on and rotating. Also, wear eye and ear protection during the entire milling procedure!

1.1.7   Feed sample slowly into the hopper (around 10 pellets/min) to prevent slowing down or jamming. After audible noise reduces, add next batch of pellets (~10 pcs). After processing the pellets (1 g), press the cord switch to stop mill operation for ~20 minutes to cool down. Use wooden plunger to feed sample and prevent particles.

> **Caution:** The optimal feed rate varies depending on the type of processing material. Immediately turn off the mill if processing speed decreases due to particle friction in the cutting chamber, and track of molten polymer is on the glass plate to prevent overheating and further melting of the polymer particles.

1.1.8   Remove the 20 mesh, 840 µm delivery tube and replace it by the 60 mesh (250 µm) delivery tube upon completion of the first batch (Figure II-2b).

1.1.9   Reintroduce collected material into mill hopper. Follow steps 1.1 and 1.7 for the 250 µm milling fraction.

1.1.10 Refeed the collected 250 µm fractions up to three times.

1.1.11 Recover remaining particles in chamber and add them to the collected main fraction.

1.2   Processing of plastic films by cryogenic pretreatment and milling

1.2.1   Retrieve film from roll and cut film into strips of ~120 mm x 20 mm (machine direction) with paper cutter.

1.2.2   Presoak fragments (~1 g) in 800 mL in deionized (DI) water for 10 min in the 1000 mL glass beaker. This step improves embrittlement for the subsequent cryogenic cooling procedure by presoaking the polymer.

1.2.3   Slowly add 200 mL of liquid nitrogen (N_2) to a cryogenic container.

1.2.4   Transfer presoaked film particles carefully into the cryogenic container with steel tweezers—Presoak for 3 min in liquid N_2.

1.2.5   Transfer frozen film fragments into a 200 W, 14-speed blender

1.2.6   Process frozen material at speed level 3 for 10 s to break frozen glass film structure. To promote further size reduction, add 400 mL DI water and blend the film-water slurry for 5 minutes.

1.2.7   Transfer slurry into Büchner funnel with filter (1 µm mesh) and apply vacuum for at least 1 h.

1.2.8   Vacuum-dry solid particles at 30 °C at least 48 h in aluminum dish.

1.2.9   Feed dry particles into mill with tweezers. For milling, follow section sub steps 1.1 – 1.11.

1.3   Processing of plastic films pretreated through environmentally weathering and milling

1.3.1   Lay out plastic film fragments recovered from the field on a smooth surface (lab bench). Carefully remove absorbed soil particles and plant remnants with the soft-bristle brush.

1.3.2   Cut film with scissors into ~4 cm^2 square samples of ~1.0 g.

1.3.3   Add film fragments into a 1000 mL beaker filled with 500 mL DI water. Stir at a rate of 300 min^{-1} with 20 mm stirring bar for 1 hour.

1.3.4 Remove dissolved soil particles by decanting and reintroducing DI water under slight agitation of the beaker into sink or plastic bucket. Repeat this step three times. Continuous agitation keeps soil particles dispersed in water and can be easier decanted.

1.3.5 Transfer samples from beaker into aluminum dish. Air-dry plastic samples for 12 h and transfer and dry samples in vacuum oven for 24 h at 30 °C. For milling, follow sub steps 1.1-1.11.

1.4 Sieving procedure through cascaded sieves

1.4.1 Stack sieves, 3" diameter starting with the pan at the bottom, then stack the finest sieve #325 (45 µm), followed by increasingly coarser sieves such as #140 (106 µm) and #60 (250 µm), where the coarsest sieve #20 (840 µm) and the lid are placed on top.

1.4.2 Mount all four sieves on the shaker by inserting four pins in the openings of the sieve shaker.

1.4.3 Transfer individual fractions collected in either of the main steps 1, 2, or 3 above on top of the four cascaded sieves. Shake for 10 min at 300 min^{-1}.

1.4.4 Recover fraction of larger (top) fraction separately, which will be subjected to further milling.

Note: Adjust shaking speed on the shaker as needed. Alternatively, shaking sieves by hand is possible. Use only one sieve at a time, starting with the mesh #20 sieve, then holding the bottom and lid firm against the sieve by hand, and shake axially and horizontally for 5 minutes

1.4.5 Reintroduce sieved particles $d_p > 106$ µm to the rotary cutting mill as described in sub-steps 1.6 - 1.10.

1.4.6 Recover bottom fractions from pan and reintroduce particles to the next smaller sieve size. Repeat the procedure until 106 µm particles represent the main fraction.

1.4.7 Merge collected 106 µm fractions and store particles in a dry area (desiccator or air-sealed plastic bag).

Note: The 45 µm fraction is part of the 106 µm fraction; however, the former fraction was not isolated and separately analyzed since the yield is generally very low. Yield recoveries and particle size fractions of individual fractions can be determined by gravimetric measurements in wt % for each sieving fraction (mesh #20 – mesh #325) in relation to the initial feeding fraction using a high-precision microbalance.

1.5   Preparation of an aqueous NP slurry for wet grinding

1.5.1   Prepare a slurry of MPs dispersed in DI water by adding 800 mL of distilled water into the 1000 mL glass beaker and insert stirring bar (diameter = 8 mm, length = 50.8 mm).

1.5.2   Introduce 8 g (1 wt% of the water) of 106 µm plastic fraction as received from steps 1 or 2 or 3, and sieving step 4.

1.5.3   Place glass beaker on stirring plate and stir magnetically for 24 h at 400 min-1 to allow soaking particles in water to promote particle softening.

1.5.4   Transfer particles into 1000 mL plastic container.

1.5.5   Fill an additional two 1000 mL plastic containers with DI water, which will be used to rinse off adhering particles on the grinder's hopper during the grinding process.

1.6   Preparation of the wet grinding machine for NPs production

1.6.1   Place stones with 46-grain size (grit of a grinding stone 297-420 µm) in the wet friction grinder and fasten the center nuts hand-tight with a 17 mm wrench.

1.6.2   Add hopper on top and fasten the three nuts and bolts with the 17 mm wrench.

1.6.3   Place collection 1 L plastic jar under the outlet of the collider. Place a second empty 1 L bucket next to the outlet, which will be used for exchanging while processing.

1.6.4   Adjust the gauge clearance + 1.0, corresponding to a positive 0.10 µm shift from zero position.

1.6.5   Switch the power on and turn the adjustment wheel carefully clockwise until hearing that the grinding stones touch. Then, adjust flexible measurement ring to zero and turn wheel counterclockwise immediately. By default, the speed is adjusted at 1500 min^{-1}.

   Note: Avoid "dry-grinding" of the stones since this creates excessive heat on the grinding stones.

1.6.6   Turn adjustment wheel clockwise until stones touch and gently fill water-NPs slurry into hopper. Decrease the gap continually to a clearance gauge of -2.0, corresponding to a negative 0.20 µm shift from the zero position after the slurry was introduced. Plastic particle-water slurries between the two stone disks promote transformation from MPs into NPs and avoid direct friction between the grinding stones.

1.6.7   Collect slurry by exchanging the collection buckets once filling level exceeds the 0.5 L in the bucket.

1.6.8 Collect and reintroduce particles into the grinder between 30 - 60 times; higher passes (numbers of reintroduction) result in smaller particle sizes.

1.6.9 Wash adhering particles on the hopper with the prepared DI water bottle to allow suitable slurry mixing while processing.

Note: Collection of intermediate samples during the process is possible by holding 20 ml glass vials into the outlet stream. The individual steps will assess the particle fragmentation mechanisms while process severity (number of passes) increases. Recover slurry and stir for 4 hours at 400 min-1 at 25 ºC to allow well mixing; let it stand for 48 h to stabilize the slurry.

1.7   Recovery and drying of NPs from slurry

1.7.1 Isolate the bottom fraction (or phase with the highest NP concentration) if multiple layers in the slurry are observed by slowly pouring the slurry into an additional 1000 mL glass beaker.

1.7.2 Transfer fractions into centrifugation vials (50 mL) and centrifuge for 10 min (relative centrifugal force, $[RCF] = 20 \times 10^2$ g). The RCF (also termed g-force) is the generated radial force as a function of the rotor radius and rotor speed, which causes the separation of the heavier particles and water of the slurry.

1.7.3 Remove the transparent top layer by decanting it into a separate aluminum pan.

1.7.4 Transfer the remaining bottom layer (containing an NP slurry) into an additional aluminum dish and place it in vacuum oven. Dry for 48 h at 30 °C in a vacuum oven.

1.7.5 Recover dried material with spatula under a fume hood or glove box while wearing a respiratory mask. Transfer dried content into 100 mL glass container and seal with lid.

1.7.6 Contain NPs in a vial and stored in an airtight, dry, and cool place (desiccator).

Note: MNPs released into the environment during the manufacturing process (here, either during the wet-grinding process or as dried particles) may pose a severe threat to aquatic and terrestrial ecosystems. In particular, regulatory measures are designed to minimize risk for their production and use for engineered nanomaterials (Rist & Hartmann, 2018). Therefore, the formation of MNPs requires specific precautional steps such as material handling in a fume hood or glove box. Furthermore, aqueous waste solutions formed during the isolation of NPs (sub step 6.7-6.9) will be subject to an end-of-life disposal procedure performed through our **"Environmental Health and Safety Department."**

1.8   MP imaging via stereo microscopy

1.8.1   Disperse ~20 mg of particles (collected in sieving step 4) on an area of ~4 cm2. Spread white or translucent MPs on a dark surface and spread black or dark-colored MPs on white background (paper sheet) to maximize background contrast.

1.8.2   Adjust the microscope to the lowest magnification to capture the largest possible Area (middle of the particle area). Next, direct the external lamp to the focus center to attain illumination on the regions of interest.

1.8.3   Apply magnification which allows the detection of > 50 particles in the middle of the field of view. This amount is recommended to obtain robust statistical evaluation results.

1.8.4   Focus on areas with no or minor particle overlap and good color contrast.

1.8.5   Capture at least five representative images by focusing on the outer particle shapes. The local computer used for imaging saves high-resolution images as a bitmap in the software.

1.8.6   Save the stereomicroscope recorded images in a file format recognized by ImageJ software (bitmap, tiff, or jpeg) for the following quantitative data analysis.

Note: Take one reference image at the exact magnification settings for which the main image was taken using a ruler or any other reference object recorded in the image. This procedure will allow easy calibration of the images when preparing and analyzing through ImageJ software.

1.9   Image analysis through ImageJ software

1.9.1   Open ImageJ software (Schneider *et al.*, 2012) and prepare file import by entering (CTRL + L) to open Command finder > enter Bio-Formats on the right lower corner.

1.9.2   This function activates the menu path File > Import > Bio formats (> refers to navigation steps within the software). Search for directory of stored image files.

Note: If the Bio-Formats package does not appear in the **Command finder**, search online under **Bio-Formats ImageJ.** Follow instructions for downloading and installation of ImageJ. The Bio-Formats importer allows for simple handling of importing-exporting of picture files within ImageJ and searching for commands.

1.9.3   Open image (alternatively Bio-Formats import as described in sub step 9.1) by clicking File > Open > select particle image at file location collected in sieving sub step 4.7 and the ruler-reference image described in 1.6. Creating a duplicate image is

recommended by clicking Shift + Command + D for comparison to the original image while adjusting the threshold settings of the copy image).

Note: File > Open command opens various formats natively supported by ImageJ as described in sub step 8.7. Alternatively, select the image location on the computer and **drag and drop** the File on the main ImageJ window status bar. The image file will open automatically in a separate window.

1.9.4   Zoom in and out to the image using CTRL + and CTRL −, respectively.

1.9.5   Set measurements by Analyze > Set Measurements, then select Area and Shape Descriptors as default values.

1.9.6   Define the scale bar by drawing a line Straight over the length of the scale bar using the ruler reference image as described in step 8 and press Analyze > Set Scale > enter under Known distance the numerical value of the bar length, enter unit of the corresponding length.

1.9.7   Visualize scale bar on image by Analyze > Tools > Scale Bar, adjust settings such as showing crisp contrast on image. Select a position on the image where the scale bar should be placed for scale bar settings. Select Width to adjust the bar in calibrated units, Height of the bar in pixels, and Font Size of the scale bar label. Select background to adjust the filling color of the label text box.

Note: for micrometers, the entry of **μm** is sufficient, the program adapts μm automatically in the data output.

1.9.8   Transform the image into an 8-bit image by selecting Image > Type > 8-bit.

1.9.9   Convert copied image to 8-bit by Image > Type > 8bit.

1.9.10 Adjust Image > adjust > threshold > Set (compare size to the original image).

1.9.11 Determine which measurements to take by Analyze > Set Measurements.

1.9.12 Select Analyze particles > 0-infinity, click Display results, and in situ show.

1.9.13 Store ROI (.zip) results under Save measurements and Select Folder.

1.9.14 Save Results (*.csv) under File > Save as > Select Folder.

1.10   Particle diameter (d_p) and shape factor calculation in spreadsheet software

Knowledge of particle diameter and shape factors are essential for particle behavior (fate, transport) in the environment and the determination of surface area. Therefore, geometry is essential when MPs are used for environmental studies. For example, different interaction

mechanisms with soil were observed depending on MPs' sizes and shapes, such as MPs-MPs and MPs-soil agglomerations, which influences particle movement in soil (de Souza Machado *et al.*, 2018; Raju *et al.*, 2020). Therefore, to determine d_p-particle size distribution and geometrical parameter, the following steps are suggested:

1.10.1 Import the corresponding *.csv file obtained and saved from ImageJ analysis (step 9.13) into the spreadsheet software

Note: the numerical values in each column line reflect individual calculations for each particle according to equation (1) and equation (2).

1.10.2 Evaluate the average shape parameter values such as circularity (CIR) and aspect ratio (AR) by entering = average (x,y) at the bottom of each column where x represents the first line and y last line of the column, then press Enter. The CIR values describe the relationship between the projected Area and the perfect circle with an individual particle's CIR =1 (equation 1). The AR represents the particle length/width ratio described by equation (2).

$$Circularity = 4\pi * \frac{[Projected\ area]}{[Perimeter]^2} \qquad (1)$$

$$Aspect\ Ratio = \frac{[Length\ of\ Major\ Axis]}{[Length\ of\ Minor\ Axis]} \qquad (2)$$

1.10.3 Convert the "Area Column" received from the ImageJ output into the particle diameter d_p under consideration of the AR, reflecting the length/width ratio using **equation (1)** and **equation (2).**

1.10.4 Analyze, if AR < 2.5 then use **equation (3),** if AR ≥ 2.5, then use **equation (4)** to calculate d_p. **Equation (1)** calculates d_p based on round shaped, **equation (2)** on rectangular shaped particles

Note: Selection of the **AR** threshold values **≥ 2.5** represent more rectangular-shaped particles, whereas **AR < 2.5** reflect more round-shaped particles. This selection allows for minimizing the $\boldsymbol{d_p}$ calculation error derived from the **Area** measured by microscopy and determined through ImageJ.

$$Particle\ diameter\ (d_p) = \sqrt{\frac{Projected\ area * 4}{\pi}} \qquad (3)$$

$$Particle\ diameter\ (d_p) = \sqrt{\frac{Projected\ area\ *\ Particle\ width}{Particle\ length}} \qquad (4)$$

1.11 Statistical analysis for MPs and NPs

1.11.1 Open the *.csv data file with the statistical software by File > Open > Select file location of the corresponding file as created in sub step 9.13.

> **Note:** Alternatively, the table can be directly transferred through copy-paste feature into the statistical software. Refer to Table of Materials for the brand and version of the statistical software Edit > Paste with Column Names.

1.11.2 Evaluate the d_p data by selecting Analyze > Distribution.

1.11.3 Select d_p, which reflects the column's data, and drag and drop into Y columns, press the OK button. This feature creates a histogram including a statistical output including Summary Statistics including Mean and Std Dev values in a separate window.

1.11.4 Evaluate if the histogram follows a normal distribution (or the best fit for d_p) with the best fit curve by selecting the triangle next to d_p > Continuous Fit and then select the curve received as the best fit (for example, Fit Normal). This step superimposes the histogram with a normally distributed fit.

1.11.5 Determine and report the Mean and Standard Deviation values from the Summary Statistics output of the average shape parameter values of circularity (Cir), aspect ratio (AR), Roundness (Round), and Solidity (Sol).

> **Note:** A statistical significance level of $\alpha = 0.05$ is recommended and was employed for all evaluations. The significance level is the probability of rejecting the null hypothesis when it is true when comparing numerical results.

1.12 Best fit of d_p size distribution and particle shape factors

1.12.1 Load data set into statistical software and use the same *.csv data set for the distribution of d_p as calculated in step 10.

1.12.2 Select Analyze > Reliability and Survival > Life Distribution.

1.12.3 Drag the d_p -*column* to Y, "Time to Event" field, and select "OK". This feature creates an output with a probability plot as a function of d_p.

1.12.4 Determine the optimum distribution under Compare Distributions by checking Nonparametric, Lognormal, Weibull, Loglogistic, and Normal.

1.12.5 Evaluate the quality of the model fits by the lowest numerical values for the Akaike's and Bayesian information criteria (AICc and BIC, respectively) in the Statistics Model Comparison Table below the graph by the lowest BIC numbers. The best fit model is presented in the first row by default.

1.12.6 Parametric or nonparametric estimates output fields for each distribution evaluation are located below the Compare Distributions graph.

1.12.7 Save output script to data table by selecting the red pull-down triangle on the upper left corner by Save Script > To Data Table. Next, save the original Data Table in the desired file location by selecting File> Save as > *.jmp.

1.13   Dimensional characterization of NPs through dynamic light scattering

1.13.1 Start the dynamic light scattering (DLS) software by double-clicking on the desktop icon. Select File > New > SOP. Add sample name   and select material refractive index to 1.33 for distilled water and 1.59 for polymers (Caputo *et al.*, 2021) in the DLS software under sample setup. Select material in the pull-down menu then click "OK".

   Note: Clicking the **pull-down** menu opens the **Materials Manager,** which offers to add new samples or modify existing samples by changing the **Refractive index** and **Absorption.** Select as dispersant **Water.**

1.13.2 Select the proper cell under Cell > Cell Type and select Reports to determine which output will be presented after each measurement.

1.13.3 Start the instrument by closing the instrument lid and switching on the system by closing the lid (if open) and pressing the "ON" button. Wait after the first Beep and wait around 30 minutes to allow stabilization of the beam.

1.13.4 Wait until the Initialization routine is completed and wait for a second Beep sound indicating that the pre-set temperature (generally 25 °C) is reached.

1.13.5 Prepare a sample slurry of NPs (as received in step 7) and DI water in a 15 mL vial at ~0.1 wt % concentration by magnetically stirring ~ 1 h to allow well mixing.

1.13.6 Shake the slurry before transferring ~1.0 mL into the 4.5 mL quartz cuvette and open the lid. Then, carefully insert the sample cell into the sample holder of the DLS instrument.

Note: Prepare three samples from the same slurry batch at the same concentration as described in step 13.5.

1.13.7 Perform three measurements (selection in the DLS software) for each sample. Between measurements, remove the sample cell and gently shake the samples for 5 s to allow mixing of the sample.

1.13.8 Extract and export data through the DLS software, transfer the dataset into the spreadsheet software and create histograms for MPs and NPs as described in sub step 11.5.

1.13.9 Copy from the Records View Tab either a Table or Graph by selecting Edit-copy, which can be pasted into another application such as the spreadsheet software.

1.14   Chemical analysis of MNPs using Fourier Transformation Infrared Spectrometer FTIR-ATR (attenuated total reflectance)

Chemical analyses of MNPs by Fourier transformation infrared (FTIR) and nuclear magnetic resonance (NMR) spectroscopies are well-suited tools to assess the impact of wet grinding on chemical bonding properties and the relative amounts of major components and the polymers' monomeric constituents, respectively (Brodhagen *et al.*, 2017). In addition, thermal properties and stability of MNPs' polymeric constituents can be assessed through differential scanning calorimetry (DSC) and thermogravimetric analysis (TGA), respectively (Astner *et al.*, 2019).

1.14.1 Clean the detection system (ATR crystal surface) with ethanol and a lint-free cloth.

1.14.2 Start software and press Background Button in the command bar to perform a Background Scan in the air by clearing the instrument beam path. The background spectrum is displayed shortly after collection.

1.14.3 Enter Sample ID and Sample Description in the instrument settings toolbar.

1.14.4 Adjust spectral wavenumber between 4000 cm-1 and 600 cm-1 and select a resolution of 2.0 cm-1 in absorbance mode, select 32 scans per spectrum and start.

1.14.5 Place plastic sample (~20 mg or ~ 1-3 mm3) of MPs (106 µm) and NPs (~300 nm) inside of a steel washer with an inner diameter of ~10 mm, or equivalent, on the crystal surface.

Note: The washer prevents dispersion on crystal when the sample holder compresses the sample, resulting in material inhomogeneities and data bias due to inconsistent

measurements. Place washer in the center of the ATR crystal and add the polymer sample into the middle of the washer opening with a spatula.

1.14.6 Swing sample lever above the into the center of the sample and turn the know clockwise by monitoring the Force Gauge force between 50-90. The sample shows the preliminary spectra. Press the Scan button a second time to collect the spectrum.

1.14.7 Collect between 8 - 10 spectra by clicking the Scan button and mix samples carefully after each measurement with a spatula to allow the collection of representative results.

1.14.8 Click on the Sample View folder in the Data Explorer to display all collected samples superimposed in the viewing area. First, remove significantly deviating spectra representing outliers. Next, select either Absorbance or Transmittance mode in the toolbar.

1.14.9 Save spectra by selecting the Sample View folder containing the spectra and selecting from the file menu Save As. The dialog window enables the file name, destination directory, and the default location change for all spectra.

Note: Alternatively, the spectra can be saved as a *.sp file by selecting a spectrum and right-clicking to display the Binary option. Select Save Binary and browse the final Save location. Perform baseline correction and mean normalization by selecting a single spectrum in the Data Explorer by menu selection Process > Normalization in the menu either through the software or in the next step. Mean normalization compensates for spectral errors due to the thickness or material variation in the sample.

1.14.10 Clean crystal area with ethanol and the lint-free cloth upon completion of the data collection

1.14.11 Interpret differences between MPs and NPs according to assigned FTIR vibration bands, assigned and evaluated in a previous publication(Hayes *et al.*, 2017).

2.3 Representative Results

To validate the experimental procedure method and analysis, MPs and NPs were formed from pellets and film materials and compared by size and shape using microscopic images. The method described in (Figure II-1) efficiently formed MPs and NPs from biodegradable plastic pellets and films was achieved through cryogenic cooling, milling, and wet-grinding and characterization. The former step was unnecessary for environmentally weathered films because weathering induced embrittlement (Astner et al., 2022; in preparation). Pellets were also directly subjected to milling

without cryogenic pretreatment. After milling, particles were fractionated through sieving into four size fractions: 840 μm, 250 μm, 106 μm, and 45 μm, as described in protocol step 4. The latter three fractions consist solely of MPs. Subsequently, particle characterization for each fraction was assessed by determining the distribution of size (d_p) and shape factors (i.e., circularity and aspect ratio) of collected stereomicroscopic images using ImageJ software as given in the protocol 8.1 – 8.6. Examples of images obtained by a stereomicroscope for the 106 μm sieving fraction for PBAT pellets and the 250 μm sieve fraction (Figure II-3 a,c).for unweathered PBAT film treated with cryogenic exposure (Figure II-3b,d). A representation of the fragmentation steps into MPs using pellets and cryogenic treated PBAT film particles is depicted in (Figure II-3a,c), respectively.

The statistical analysis of particle dimensions indicated an average d_p that was 41 μm smaller than the nominal sieve size (106 μm) for the PBAT pellets and 137 μm smaller for the PBAT film (250 μm nominal size), suggesting that the smaller sieve fraction represents a more homogenous particle size distribution (Table II-1). This observation was also confirmed by a larger value in circularity and lower aspect ratios (suggesting more round-shaped particles) for the processed pellets compared to the film material, which may be attributed to the different properties (density) of the starting materials. A normal distribution was the best model for describing the particle size distribution for both fractions. However, for determining circularity and aspect ratio, the Weibull and Lognormal models were optimal (Figure II-4, a-d; Table II-1). For both feedstocks, a wet grinding process applied to the 106 μm MP sieve fractions formed NPs, and their particle size distribution was measured via DLS. The numerical analysis revealed a bimodal particle size distribution for NPs produced from both feedstocks. The main particle populations for NPs from PBAT pellets were at ~80 nm, and 531 nm, corresponding number density frequency (NDF) values at 25 % and 5 %, respectively. On the other hand, NPs derived from PBAT films possessed size maxima at ~50 and 106 μm, with corresponding NDF values of 11 % and 10 %, respectively. The observations suggest that NPs from PBAT pellets yielded more uniform d_p values (~50-110 nm) than PBAT films; however, a particle subpopulation between 300 and 700 nm, with a maximum at 531 nm, also coexisted (Figure II-5).

The chemical bonding properties of the PBAT film were evaluated by FITR spectroscopy. They showed only minor changes due to milling for MPs and wet-grinding for NPs in the regions between 1300 and 700 cm^{-1}. However, a significant decrease in the C-O stretching of starches

reflecting the absorbance of the starch component (Hayes *et al.*, 2017) was observed for the mulch film. However, minor changes were observed for the bands representing PBAT, such as C-H and C=O stretching, between 1800 cm^{-1} and 1230 cm$^{-1,}$ suggesting insignificant changes in structure for the polyester attributed to the wet grinding process

2.4 Discussion

This method describes an effective process initially described in a previous publication (Astner *et al.*, 2019), to prepare MNPs sourced from pellets and mulch films for environmental studies. The size reduction process involved cryogenic cooling (for film only), dry-milling, and wet-grinding stages, to manufacture model MNPs. We have applied this method to prepare MNPs from a wide range of polymeric feedstocks, including low-density polyethylene (LDPE) polybutyrate adipate-co-terephthalate (PBAT), and polylactic acid (PLA) (Astner *et al.*, 2019). However, for LDPE, only pellets could serve as feedstocks; mulch films could not be processed due to a reinforcement grid incorporated into the film during its extrusion, as described in a previous publication (Astner *et al.*, 2019).

Critical steps within the protocol involve **a) cryogenic pretreatment**, providing embrittlement of the generally flexible film, **b) milling** to simulate the mechanical impact through agricultural practices (plowing, tilling), and **c) wet-grinding** mimicking the environmental shear events between MPs-soil collisions. MNPs formed through this method are more likely to represent MPs occurring in agricultural soils than polystyrene micro-and nanospheres. However, the latter are frequently employed as engineered model materials in environmental studies investigating the impact on soil microbial communities (Abbasimaedeh *et al.*, 2021; Ding *et al.*, 2022; Xu *et al.*, 2021), plants (Li *et al.*, 2021) and soil fauna (Sobhani *et al.*, 2021).

Various methods have generated surrogate NPs, including cryogenic milling, and grinding using rotary and ball mills (Ducoli *et al.*, 2022; Dümichen *et al.*, 2015; Lionetto *et al.*, 2021; Robotti *et al.*, 2016). In addition, milling in combination with liquid nitrogen was frequently employed to form MNPs (Ducoli *et al.*, 2022; Dümichen *et al.*, 2015; Eitzen *et al.*, 2019; Ekvall *et al.*, 2019; El Hadri *et al.*, 2020; Robotti *et al.*, 2016). In contrast, an ultracentrifugally dry milling procedure (without cryogenic treatment) in combination with wet ball milling was used to generate MPs and NPs (Lionetto *et al.*, 2021), respectively. In contrast, the method described in this paper

47

uses an inexpensive combination of cryogenic soaking-blending-milling-grinding to generate MNPs from plastic films to mimic environmental impacts such as weathering and mechanical shear forces. Therefore, a recent study compared the mechanical and chemical property changes between cryogenically formed environmentally weathered agricultural plastic films. Results showed statistically significant differences in geometrical features and physicochemical properties of the formed MNPs. A limitation of the mechanical-cryogenic milling method is the relatively low sieving yield after the first milling pass (~10 wt%) of fractions < 840 μm, which requires two more passes resulting in a longer processing time compared to the larger fractions of > 840 μm (Astner *et al.*, 2019). Since the 46 μm fraction yields are between 1 and 2 wt %, the 106 μm particle fraction was used for the wet-grinding procedure to form NPs. In addition, the friction during the milling process can lead to overheating of the processing chamber, which results in the agglomeration and thermal degradation of particles or film fragments during the milling process, as described in other studies (Astner *et al.*, 2019; Caldwell *et al.*, 2021). A further restriction of the cryogenic milling method described in this paper is the limited application for plastics such as LDPE films or PBS pellets with poor thermal properties (i.e., low glass transition temperatures). The former plastics were impossible to comminute due to the fibrous structure of LDPE films. In addition, the latter clogged up the mill as mechanical shear increased the temperature in the milling chamber. In contrast, LDPE pellets were easy to process through milling without the employment of cryogenic cooling. The comparison of the MP-d_p's shows a larger deviation for the 250 μm fraction from the nominal sieve size than the 106 μm d_p fraction. However, both sieving fractions followed a monodisperse normal distribution (Figure II-3e,f; Table II-1), suggesting similar breakdown mechanisms for film or pellets feedstocks. In contrast, NP size analysis resulted in a bimodal distribution for PBAT films, similarly to a previous publication (Astner *et al.*, 2019) and PBAT pellets with representative distribution peaks at 50 nm and 107 nm. However, the pellets show peaks at around 80 nm and 531 nm, suggesting that the breakdown occurs less uniformly than in films. The significance of the previously established method lies in the efficient and inexpensive combination of processing steps such as cryogenic pretreatment, milling, and wet grinding. Particle size distributions for NPs from PBAT film in this study are similar to a preliminary study conducted on NPs formation of biodegradable plastics (Astner *et al.*, 2019), which is characterized by a bimodal distribution with particle sub-populations peaking at ~50 nm

and ~200 nm; however, the latter resulted in slightly smaller particles (106 nm) as depicted in (Figure II-5) based on the more passes (60) in this present study, compared to 27 as performed previously by Astner *et al.* (2019). This study suggests that NPs formation derived from PBAT films follows the preliminary study results.

Further proof of the robustness of this method is that the chemical composition did not change significantly due to cryogenic treatment, milling and wet grinding (Figure II-6). In addition, differences between feedstocks such as pellets vs. film (particle size distributions), average d_p, or shape parameters did not differ significantly (Figure II-3, and 4). Environmentally dispersed MNPs and their ecotoxic impacts on terrestrial organisms (Chi *et al.*, 2021; Zeb *et al.*, 2022) marine biota (de Alkimin *et al.*, 2022; Pires *et al.*, 2022) have been widely reported. While soils may be the most prominent global environmental reservoir for MNPs comprising translocation, degradation, and bioaccumulation, the lack of robust and uniform analytical methods for isolating these materials are available (Hurley & Nizzetto, 2018) and resulting in constructive knowledge gaps about ecological risks(Hurley & Nizzetto, 2018). Consequently, future applications of this method may involve the preparation and characterization of MNPs of newly developed plastics materials for agricultural polymer films (e.g., PBAT combined with lignin) to assess the environmental fate and ecotoxicity of MNPs before market introduction. Therefore, this protocol may serve for environmental studies as a standardized protocol for generating MPs through cryogenic milling and NPs through wet-grinding and for dimensional and chemical characterization of the resultant MNPs. In addition, derived particles may be employed in environmental studies such as fate, ecotoxicity, transportation, and biodegradation in terrestrial and marine environments.

APPENDIX II
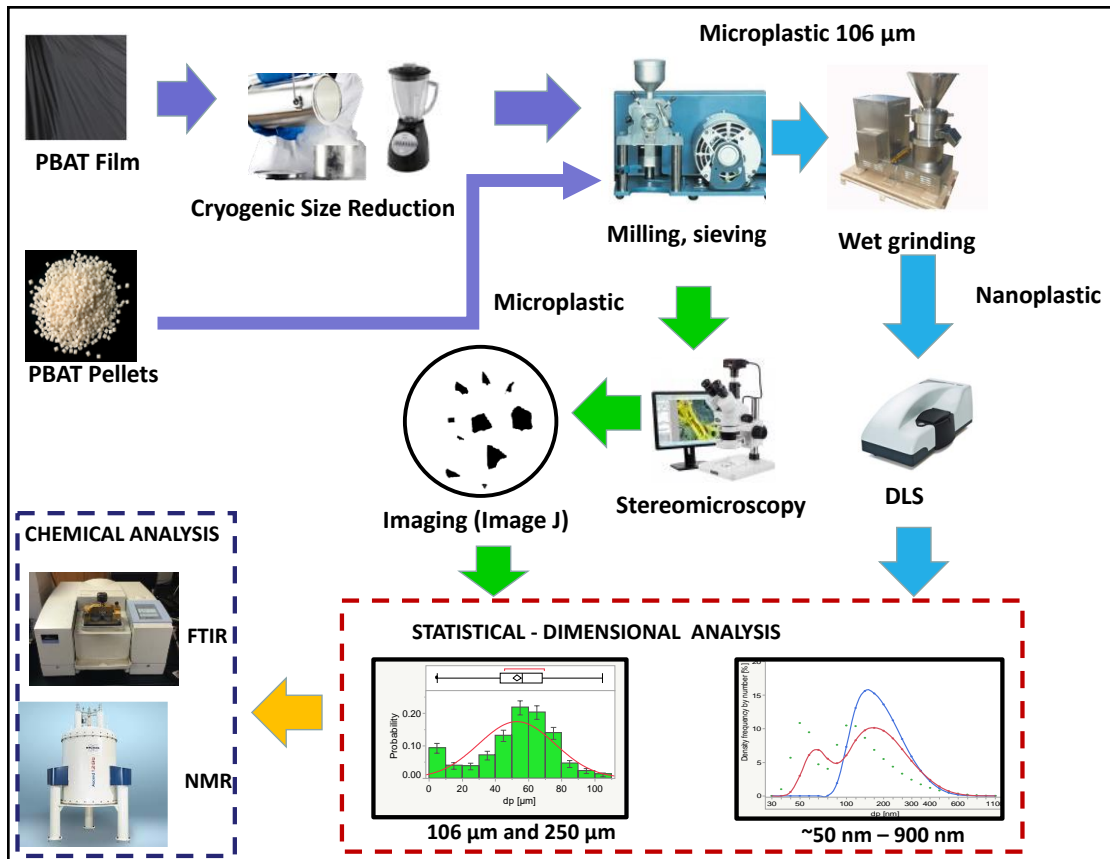
Figure II-1. Flow diagram to form and characterize micro-and nanoplastics. The representation shows the formation process and the subsequent geometrical and chemical particle evaluation. Geometrical properties were determined by combining stereo microscopy and image analysis (ImageJ), followed by a numerical statistical analysis. Chemical characterization such as chemical bonding was conducted through Fourier Transformation Infrared Spectrometer using attenuated total reflectance (FTIR-ATR). Molecular structure of polymers can be assessed by Nuclear Magnetic Resonance Spectroscopy
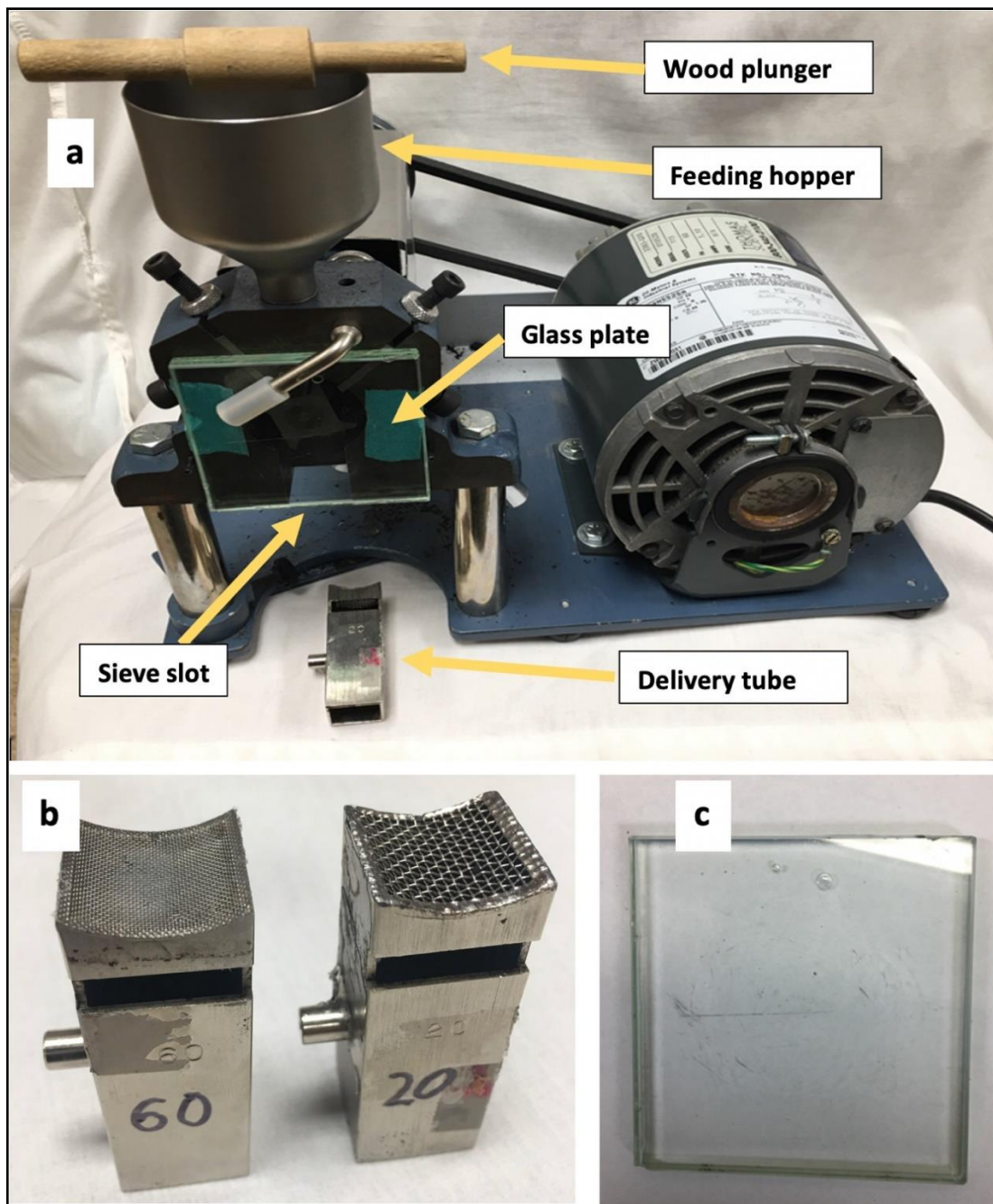
Figure II-2. Rotary cutting mill apparatus. Images of (a) the rotary mill assembly including feeding hopper, front glass plate, and sieve slot; individual delivery tubes with (b) sieve sizes #20 (840 µm) and #60 (250 µm) are fitted into the mill sieve slot starting with the coarser; and (c) double-layer glass front plate are attached to the front of the grinding chamber.
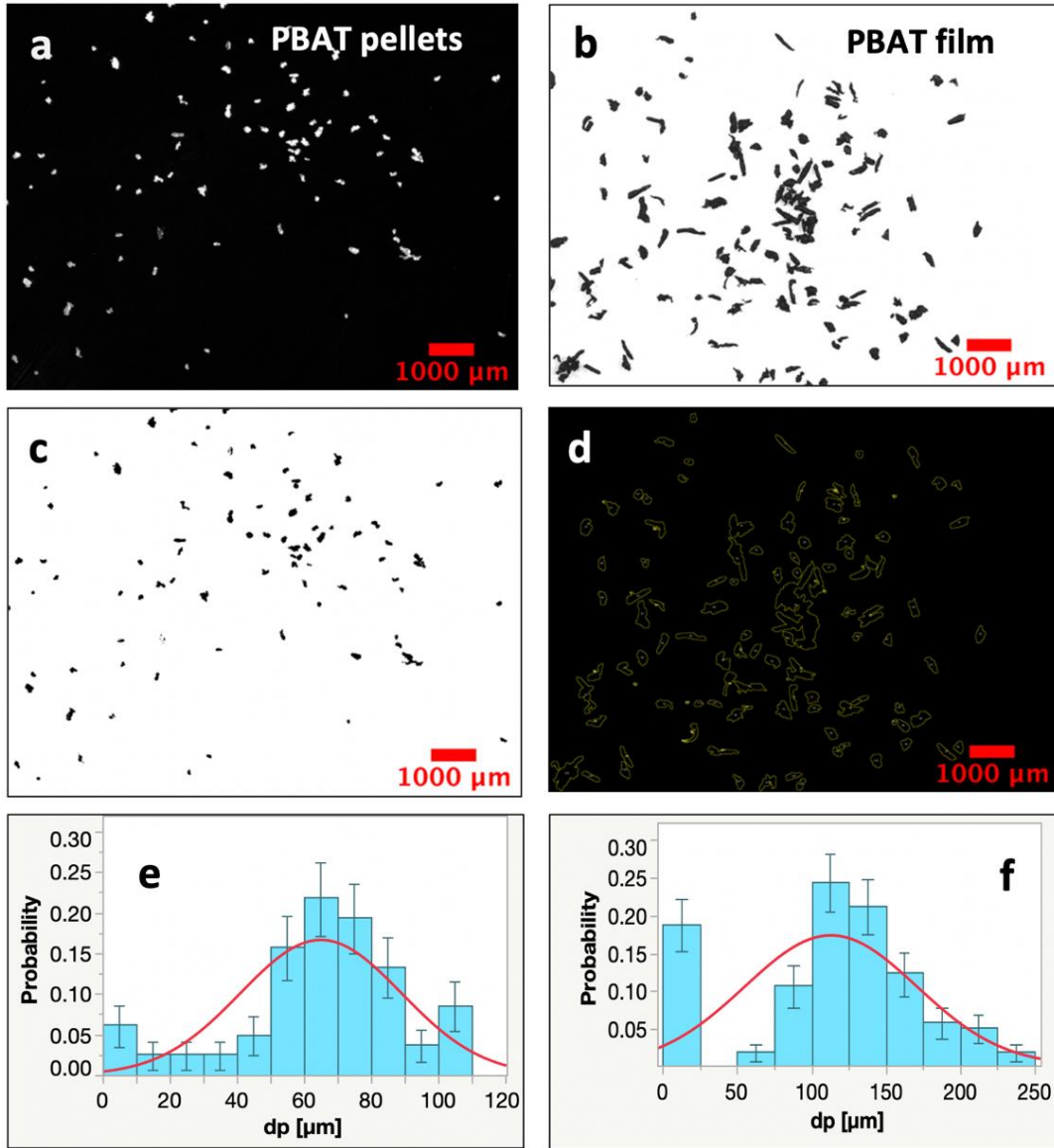
Figure II-3. Stereomicrographs of microplastics (MPs), including software processed images. The images were derived from PBAT MPs processed from (a) PBAT pellets (106 μm sieve fraction) and (b) PBAT film (250 μm sieve fraction) prepared through cryogenic exposure followed by mechanical milling. A black background was selected for imaging white PBAT particles, a white background was selected (a), and a black PBAT film (b). Corresponding images were processed by ImageJ software (Schneider *et al.*, 2012) (c) and (d), respectively. A best-fit model of d_p, depicted in histograms of particles derived from stereographs of (e) PBAT pellets and (f) PBAT film, is represented by a normal distribution. Error bars reflect one standard deviation. A stereomicroscope collected stereomicrographs with an integrated camera head.
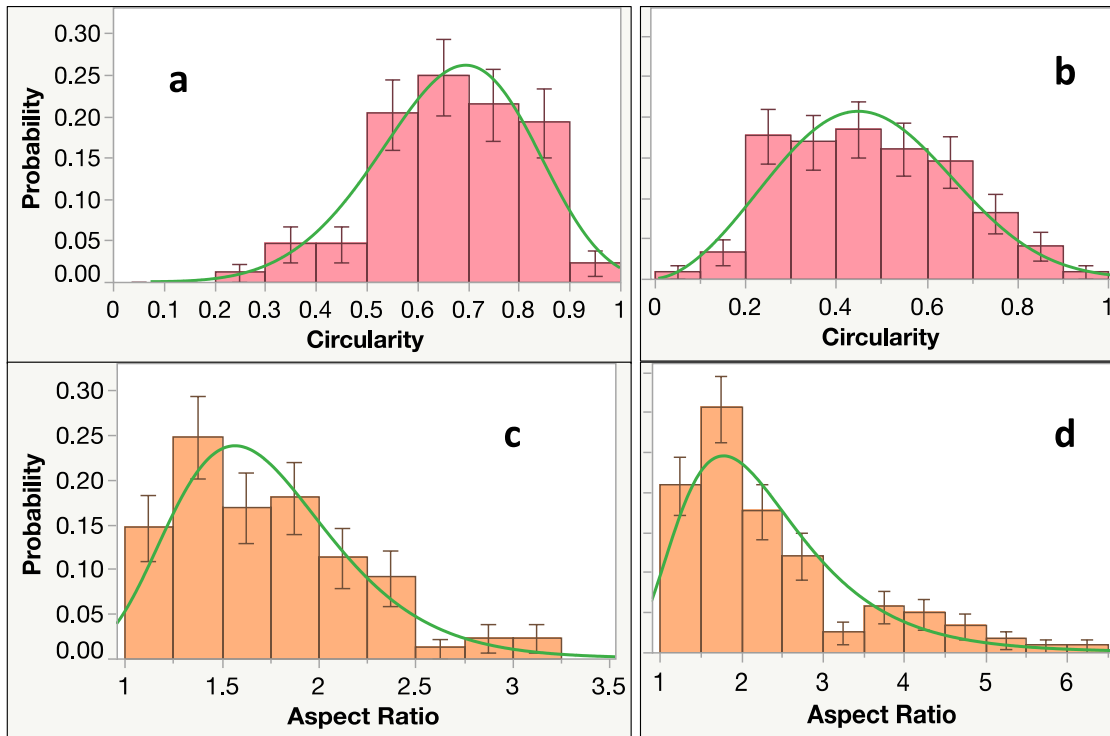
Figure II-4. Particle shape factor distribution histograms with superimposed best curve fitting. The image represents MPs: (a) circularity and (c) aspect ratio for PBAT pellets and (b) circularity and (d) aspect ratio for PBAT film, based on ImageJ analysis (Schneider *et al.*, 2012). Stereomicrographs are based on two sieve fractions particles of PBAT pellets (106 μm) and PBAT BDM MPs (250 μm). Numerical analysis was performed in the atistical software, V 15. Stereographs and histograms represent the corresponding images.
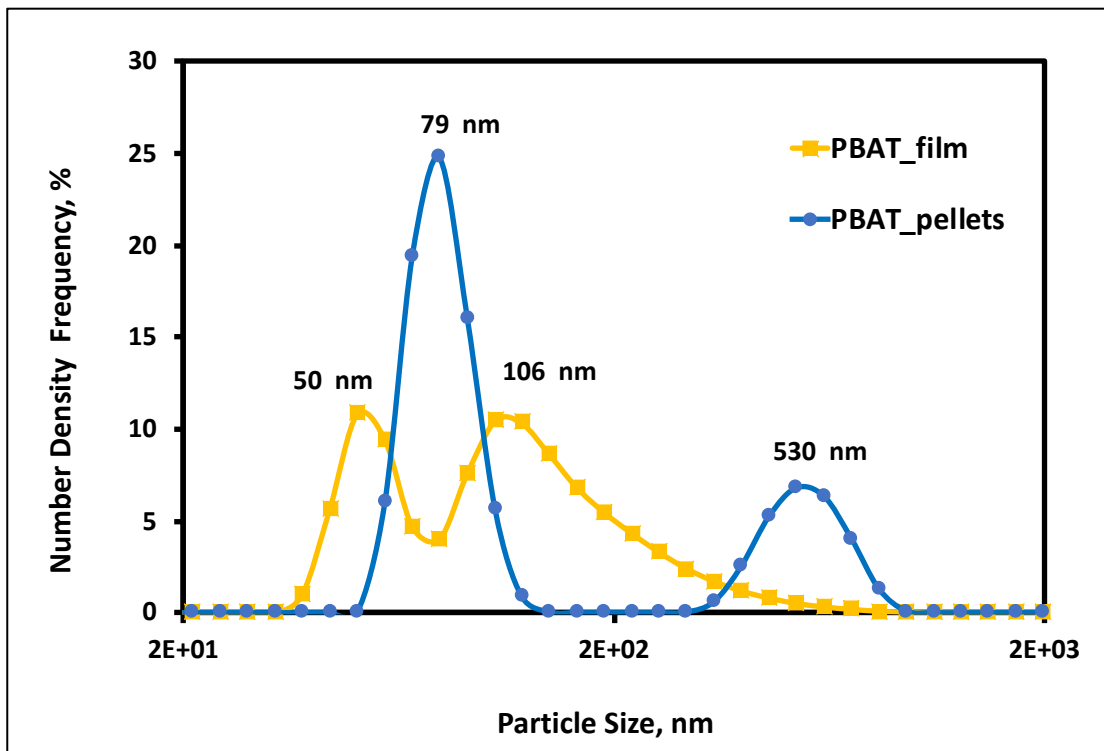
Figure II-5. Histograms of particle size (d_p) for NPs. The figures represent particle distributions derived from PBAT film and PBAT pellets formed from the wet-grinding treatment of the 106 μm MP sieve fraction. Curves represent two-parameter Weibull model fits to size distribution, conducted using JMP 15.2.0 software (SAS Institute Inc., Cary, NC). Data measurement was performed using dynamic light scattering.
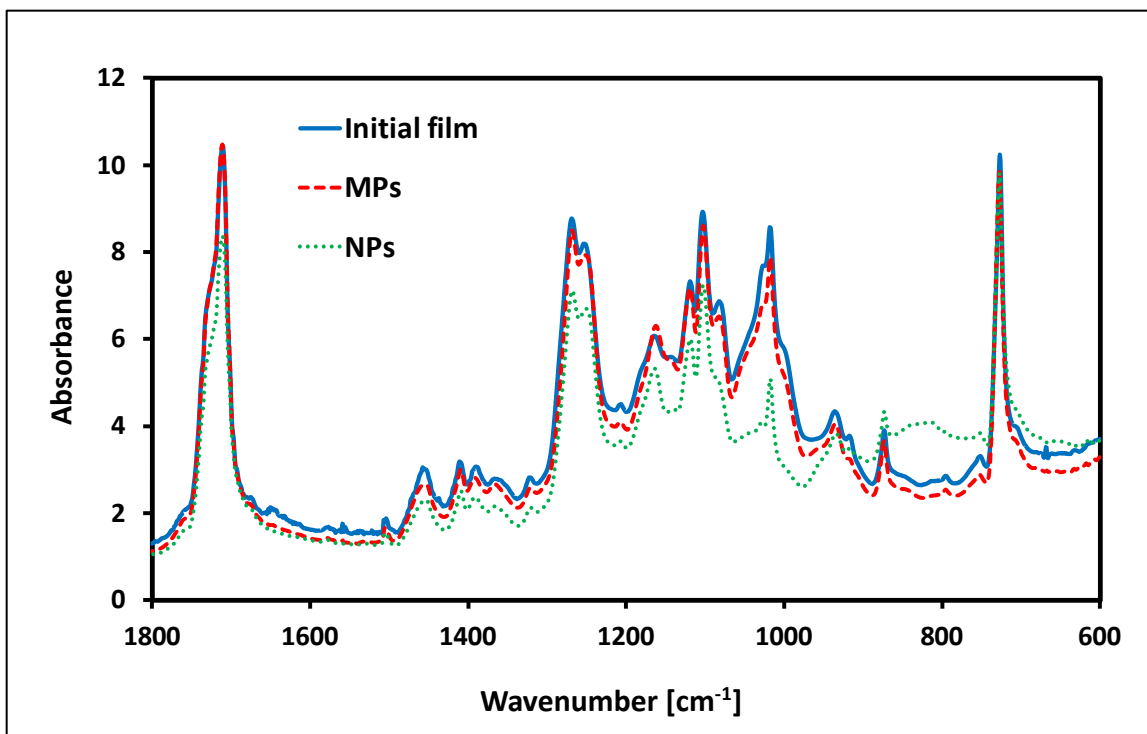
Figure II-6. Representative FTIR spectra of MNPs comparison among different processing steps. The figure depicts the comparison among the initial conditions of the PBAT film, PBAT-MPs, PBAT-NPs, plastic films, and their MPs and NPs. The PBAT film was cryogenically treated prior to mechanical milling MPs consisting of the 106 µm sieve fraction of dry milled plastics; NPs were produced via wet grinding of the 106 µm sieve fraction MPs after dry milling and sieving. Spectral data was collected using a spectrometer fitted with a diamond attenuated total reflectance (ATR) attachment. Spectral data analysis was performed using FTIR spectrum analysis software.

Table II-1. Representative particle size and shape parameters. Results were derived from statistical analysis for MPs processed from PBAT pellets and PBAT film depicted in Figures II-4 and II-5).

| | Polymer | |
	PBAT pellets	PBAT film
Sieve fraction, μm	106	250
Normal d_p, μm	65	113
Std Dev	24	58
Circularity	0.68	0.47
Aspect Ratio	1.73	2.33
Best fit, d_p	Normal	Normal
Best fit, Circularity	Weibull	Weibull
Best fit, Aspect Ratio	Lognormal	Lognormal
N	83	125

CHAPTER III

MECHANICAL FORMATION OF MICRO- AND NANOPLASTIC MATERAILS FOR ENVIRONMENTAL STUDIES IN AGRICULTURAL ECOSYSTEMS

A version of Chapter III was published in *Science of the Total Environmen*t on June 25th, 2019:

Citation of the paper:

"Astner A.F., Hayes D.G., O'Neill H.M., Evans B.R., Pingali S.V., Urban V., Young T.M. Mechanical formation of micro-and nano-plastic materials for environmental studies in agricultural ecosystems. *Science of The Total* Environment. 2019;685:1097-106."

Authors:

Anton F. Astner, Douglas G. Hayes
Department of Biosystems Engineering, University of Tennessee, Knoxville, TN, USA

Timothy M. Young
Department of Forestry, Wildlife and Fisheries, Center for Renewable Carbon, University of Tennessee, Knoxville, TN, USA

Hugh O'Neill, Barbara R. Evans, Sai V. Pingali, Volker S. Urban,
Neutron Scattering Division, Oak Ridge National Laboratory, Oak Ridge, TN, USA

Anton Astner's contribution to this paper includes identifying the research objective, designing, and conducting the experimental tasks, processing, and interpreting the data, and drafting the paper.

Co-researchers contributions are listed as follows:

D. G. Hayes significantly supported the identification of the research goals and provided support for the experiments and data analysis and revised the paper.

H. O'Neill, B. R. Evans, S. V. Pingali, V. S. Urban provided aid for the development of the experimental design and adjusting of experimental parameters

T. M. Young revised the manuscript and provided the experimental design guidelines.

Abstract

Release of microplastics (MPs) and nanoplastics (NPs) into agricultural fields is of great concern due to their reported ecotoxicity to organisms that provide beneficial service to the soil such as earthworms, and the potential ability of MPs and NPs to enter the food chain. Most fundamental studies of the fate and transport of plastic particulates in terrestrial environments employ idealized MP materials as models, such as monodisperse polystyrene spheres. In contrast, plastics that reside in agricultural soils consist of polydisperse fragments resulting from degraded films employed in agriculture. There exists a need for more representative materials in fundamental studies of the fate, transport, and ecotoxicity of MPs and NPs in soil ecosystems. The objective of this study was therefore to develop a procedure to produce MPs and NPs from agricultural plastics (a mulch film prepared biodegradable polymer polybutyrate adipate-co-terephthalate (PBAT) and low-density PE [LDPE]), and to characterize the resultant materials. Soaking of PBAT films under cryogenic conditions promoted embrittlement, like what occurs through environmental weathering. LDPE and cryogenically treated PBAT underwent mechanical milling followed by sieve fractionation into MP fractions of 840, 106, and 45 μm [micrometer]. The 106 μm fraction was subjected to wet grinding to produce NPs of average particle size 366.0 nm and 389.4 nm for PBAT and LDPE, respectively. A two-parameter Weibull model described the MPs' particle size distributions, while NPs possessed bimodal distributions. Size reduction did not produce any changes in the chemical properties of the plastics, except for slight depolymerization and an increase of crystallinity resulting from cryogenic treatment. This study suggests that MPs form from cutting and high-impact mechanical degradation as would occur during the tillage into soil, and that NPs form from the MP fragments in regions of relative weakness that possess lower molecular weight polymers and crystallinity.

3.1 Introduction

The rapid increase of global plastic production (322 million tons; 5% annual growth), combined with minimal recycling and improper disposal has led to increased release of post-consumer plastics into the environment (e.g., 250 million metric tonnes of plastic in the oceans projected for 2025, equivalent to 5.25 trillion plastic particles) (Alimi *et al.*, 2018; Jambeck *et al.*, 2015; Mattsson *et al.*, 2015; Wright & Kelly, 2017). The plastic materials, originally macro- or meso-plastics (average particle size [diameter], or d_p, of > 25 mm and 5-25 mm, respectively) undergo size reduction due to shear, chemical and biochemical reactions, resulting in defragmentation into micro- and nanoplastics (MPs and NPs, respectively) to produce d_p of 0.1-5000 μm [micrometer] and 1-1000 nm, respectively (Alimi *et al.*, 2018; Gigault *et al.*, 2018; Hartmann *et al.*, 2019). (A thorough discussion on the defining size range for NPs is given in (Gigault *et al.*, 2018).) Plastic litter accumulates in various environments, including marine (Alimi *et al.*, 2018) and terrestrial (Horton *et al.*, 2017; Nizzetto *et al.*, 2016; Scheurer & Bigalke, 2018) habitats. The small plastic fragments exhibit major environmental health concerns impacting marine and terrestrial environment, either directly or as carriers of pesticides, plasticizers, or other potentially harmful agents (Bouwmeester *et al.*, 2015; Koelmans *et al.*, 2013). Most studies of ecotoxicity formation and behavior of MPs and NPs have been reported for marine environments, showing potential harm to microorganisms (Eckert *et al.*, 2018; McCormick *et al.*, 2014) (including the microbiome of macroorganisms (Lu *et al.*, 2018; Oberbeckmann *et al.*, 2018; Zhu *et al.*, 2018)), fish, and other macroorganisms (Alimi *et al.*, 2018; Bouwmeester *et al.*, 2015; Horton *et al.*, 2017; Mattsson *et al.*, 2015). Recent studies have detected MPs in humans and other mammals, resulting from accumulation in the food chain (Bouwmeester *et al.*, 2015; Efsa Panel on Contaminants in the Food Chain, 2016; Lu *et al.*, 2018; Schwabl *et al.*, 2018; Wright & Kelly, 2017).

In contrast, terrestrial MPs have been investigated only to a minimal extent, despite their presence at higher amounts compared to marine plastics (Alimi *et al.*, 2018; Bläsing & Amelung, 2018; Horton *et al.*, 2017; Nizzetto *et al.*, 2016), and the detection of terrestrial NPs have not been reported in the literature to the best of our knowledge (although they are likely to occur (Ng *et al.*,

2018)). Recent studies reported that MPs harm soil-dwelling organisms, earthworms, and collembolans (hexapods) and microorganisms (Huerta Lwanga *et al.*, 2017; Zhu *et al.*, 2018).

The occurrence MPs and NPs on farmland is of particular concern, due to the potential harm to cropping and animal systems, which could lead to loss of agricultural productivity or accumulation of MPs and NPs in foods (Nizzetto *et al.*, 2016). A major source of terrestrial plastic fragments are agricultural plastics, employed as coverings for high tunnels, silage film, drip tape, seed casings, plant trays, and bags, and row covers (Hussain & Hamid, 2003; Scarascia-Mugnozza *et al.*, 2011). The most extensive application of agricultural plastics is mulch film (Steinmetz *et al.*, 2016), used in the production of vegetables and other specialty crops as covering on the soil to reduce weeds, control soil temperature, and prevent evaporative loss of soil moisture and erosion (Kasirajan & Ngouajio, 2012; Steinmetz *et al.*, 2016). The global market for agricultural plastic films was 4 million tons ($10.6 million) in 2016, and is projected to grow at a rate of 5.6% per year through 2030 (von Moos *et al.*, 2012).

Polyethylene (PE) is the most used polymer for mulch films and other agricultural plastics (Hussain & Hamid, 2003; Kasirajan & Ngouajio, 2012; Scarascia-Mugnozza *et al.*, 2011). Opportunities for recycling of agricultural plastics are minimal, and labor costs to retrieve plastic mulches after crop harvest are prohibitive to farmers (Kasirajan & Ngouajio, 2012; Miles *et al.*, 2017). Often, agricultural plastics are stockpiled on farms for a long duration, providing the opportunity for fragmentation. Furthermore, agricultural plastics become embrittled due to environmental weathering during their service life, with ultraviolet radiation being the most significant factor (Hayes *et al.*, 2017). Therefore, hand-retrieval of plastics would likely not remove all plastic fragments, resulting in the dispersal of the plastics into soil and watersheds. In addition, PE is poorly biodegradable, allowing for its long-term retention in the environment (de Souza Machado *et al.*, 2017; Kasirajan & Ngouajio, 2012; Nizzetto *et al.*, 2016; Steinmetz *et al.*, 2016). In summary, improper disposal of agricultural plastics, exacerbated by embrittlement via environmental weathering, leads to the dispersal of the plastic fragments into agricultural soils.

To address the problems associated with PE mulch, biodegradable plastic mulches (BDMs) have been developed. These films, containing biodegradable polymeric blends that mimic the desirable mechanical properties of PE (e.g., high tensile stress and elongation, as possessed by blends enriched in polybutyrate, i.e., polybutylene adipate-co-terephthalate [PBAT]), are designed

to be plowed into the field after the harvesting of the crop, where they should be fully biodegraded by soil-borne microorganisms into CO_2 and water within a ~2-year period (Hayes *et al.*, 2019; Kasirajan & Ngouajio, 2012; Steinmetz *et al.*, 2016). Therefore, since the biodegradation rate in the soil is slow, MPs and NPs may reside in the soil for several months, and we have detected MPs from BDMs in the soil at 20-40 kg/ha (M. English and S.M. Schaeffer, personal communication).

Mild operating conditions of milling and wet grinding were chosen (e.g., minimization of residence time to reduce friction-induced thermodegradation) so that artifacts in the chemical nature of the polymers such as oxidation or cross-linking would not occur. Exposure to cryogenic conditions followed by mechanical milling is well known to induce size reduction of polymeric materials (Dümichen *et al.*, 2015; Goedecke *et al.*, 2017; Jonna & Lyons, 2005; Poulose *et al.*, 2016; Robotti *et al.*, 2016; Saba *et al.*, 2015). A few recent studies have employed milling procedure to prepare model MPs from several different polymeric materials (e.g., polystyrene, polypropylene, PE and PBAT) for environmental research (Corradini *et al.*, 2019; Eitzen *et al.*, 2019; Guo *et al.*, 2018; Kühn *et al.*, 2018; Xu *et al.*, 2018; Zuo *et al.*, 2019). The majority of these studies produced MPs of size > 200 μm. (Guo *et al.*, 2018) prepared MPs of PE, polypropylene, polystyrene, and polyvinylchloride of size ~10-40 μm, but used harsher mechanical grinding conditions that may have produced thermal degradation. Eitzen *et al.* (2019) performed a similar low temperature milling and sieving approach to that employed herein, and obtained MP of sizes 5-100 μm. However, the cited study employed polystyrene, an inherently brittle polymer that possesses lower impact strength than the polymeric materials employed herein and is not commonly employed in agriculture. The current study probes deeper than the previous studies in terms of the size distribution and physicochemical-related properties. A unique aspect of this paper is the preparation of NPs from the MPs via wet grinding. Wet grinding is frequently employed to induce size reduction to the nanoscale (Elkharraz *et al.*, 2003; Ravishankar *et al.*, 2018; Schmidt *et al.*, 2012; Schmidt *et al.*, 2017; Watano *et al.*, 2015; Wilczek *et al.*, 2004; Zhang *et al.*, 2018). Wet grinding is believed to better simulate the low-energy degradation of plastics in the environment than milling (Ravishankar *et al.*, 2018). To the authors' knowledge, there are no commercially available sources of environmentally relevant NPs other than monodisperse polystyrene spheres employed to calibrate laser light scattering and related techniques.

The objective of this study is therefore to develop a procedure that produces MPs and NPs from agricultural plastics (a mulch film composed of biodegradable polymer polybutyrate adipate-co-terephthalate (PBAT) and low-density PE [LDPE]) and to characterize the resultant materials in terms of size, size distribution, and physicochemical properties. The methodology developed herein may also be useful to better understand the size reduction process that occurs in nature, from mesoplastics to MPs (as would occur during plastics' tillage into the soil) and from MPs to NPs (as would simulate the low-impact shear events such as MP-soil collisions).

3.2 Experimental

3.2.1 Materials

BioAgri, a black-colored biodegradable mulch film prepared from Mater-Bi® (Grade EF04P), a starch-copolyester blend containing PBAT as its major constituent, was kindly provided by BioBag Americas (Dunevin, FL, USA). The film referred to as "PBAT" in this paper, possesses an apparent density of 22.81 ± 0.411 g*m^{-2} thickness of 29 ± 1.2 μm, peak load of 12.05 ± 0.586 N and an elongation of 295 ± 30 % at maximum tensile stress, in the machine direction (Hayes *et al.*, 2017). Other physicochemical properties are given in the cited reference. The original film was provided as a 1.22 m-wide roll and stored at 20.6 ± 2.1 °C and 61.8 ± 10.6% relative humidity. LDPE beads, with a nominal diameter of 3 mm and particle density of 0.923 g*cm^{-3}, were purchased from Dow Chemical (Midland, MI, USA). Chloroform (HPLC grade) was obtained from Fisher Scientific (Pittsburgh, PA, USA) and Acros Organics (Geel, Belgium), respectively. Deionized water was used throughout all experiments.

3.3 Size Reduction Process to Prepare MPs and NPs

3.3.1 Cryogenic treatment of PBAT

PBAT films were cut with a paper cutter into strips with dimensions of ~120 mm (machine direction) x 20 mm (cross direction; Figure III-B1). The fragments (~1.0 g) were presoaked in water (800 mL) for either 0, 5, or 10 min, recovered and transferred to a cryogenic container filled with liquid nitrogen (200 mL) and soaked for either 0, 5, or 10 min. The frozen PBAT film fragments (1.0 g) were transferred into an Osterizer type blender (Oster Accurate Blend 200, Boca

Raton, FL, USA), and dry-comminuted for 10 s to break down the solidified glass-like structure of the plastic. Water (400 mL) was added to the PBAT fragments to form a slurry, and then the blender was operated at a fixed duration (5 or 10 min) at an angular velocity of $2x10^{-3}$ or $10x10^{-3}$ min^{-1}. After blending, the slurries were filtered under vacuum through a paper membrane filter (1 µm mesh) using a Büchner funnel apparatus. Solid PBAT particles (depicted in Figure III-B1) were then air dried for 48 h to reduce moisture to < 1%. A randomized experimental design was used to evaluate cryogenic processing conditions on d_p achieved.

3.3.2 Microplastic (MP) formation through milling and sieving

Cryogenic-treated PBAT fragments or untreated LDPE pellets (~1.0 g) were fed to a rotary mill (Model 3383-L10 Wiley Mini Mill, fitted with screen, Arthur H. Thomas Co., Philadelphia, PA, USA) by using sieve sizes of 20 mesh (840 µm) for the first pass and 60 mesh (250 µm) for the second pass through the mill. The residence time for milling was 20 min per pass. The MP particles recovered from milling (~1.0 g of PBAT or LDPE) were then fractionated via a cascade of four sieves (W.S. Tyler, Cleveland, OH, USA) with mesh sizes of #20 (840 µm), #60 (250 µm), #140 (106 µm), and #325 (45 µm). Enhanced uniformity of the particle size distribution was achieved by sieves mounted on an Eppendorf thermomixer 5350 (Hamburg, Germany) and shaken for 30 min at 300 rpm. The % recovery for each sieving fractions was determined gravimetrically for three replicate experiments.

3.3.3 Nanoplastic (NP) formation through high-performance wet grinding

An aqueous slurry (4.0 L) containing 1.00 wt % of MPs was prepared, which underwent stirring for 24 h to allow for a homogenous distribution. For this process, the 106 µm-size MP-fraction was used rather than the to the smallest size MP fraction (45 µm) because the yield on the latter fraction was too small to provide enough material. After stirring, slurries were subjected to the wet-grinding process using a "supermass colloider" (MKCA6-2, Masuko Sangyo, Tokyo, Japan) at a speed of 1500 rpm and 27 subsequent passes (collection of particles and reintroduction into the colloider) to provide a uniform particle size reduction. The slurry recovered from wet grinding was transferred to a 1000 mL beaker and magnetically stirred for four h (300 rpm at 25ºC). The resultant particles were dried at 40ºC for 48 h and are referred to as "NPs" herein. Analyses of NPs were conducted using aliquots collected from the middle height position of the

slurry so that NPs flocculating at the top and settling at the bottom of the slurry were not included. The final concentration of the slurry aliquots was 0.37 (wt)% and 0.28% for PAT and LDPE, respectively.

3.3.4 Particle size analysis

PBAT MPs formed via cryogenic treatment (Figure III-B1) were scanned by a flatbed-scanner (MX 490 by Canon, Tokyo, Japan) and the particle dimensions were analyzed by ImageJ software (Schneider *et al.*, 2012). PBAT and LDPE MPs belonging to each of the four MP sieve fractions identified in Figure III-A5 were analyzed via a stereomicroscope and images were analyzed using ImageJ software. Examples of images produced by ImageJ vs. the corresponding stereomicrographs are presented in Figure III-A3. The average MP diameter, d_p, was estimated using the Image J's "analyze particles" algorithm. The distribution of d_p derived from Image J analysis was fit by several different models using JMP® Pro 14.0 software (SAS Institute, Cary, NC, USA). Furthermore, the CO_2 profiles of the biodegradation experiment were subjected to exponential curve fitting, resulting in a model which was used for the biodegradation prediction of MPs and NPs. The corrected Akaike's and Bayesian information criteria (AIC and BIC, respectively) were used to compare the quality of model fits. All statistical evaluations employed a significance level of $\alpha = 0.05$. The size and size distribution of NPs was determined using dynamic light scattering (DLS) at 25 ℃. A detailed description of the procedures employed for determination of size distribution of MPs and NPs is given in the Appendix III-B.

3.3.5 Chemical and thermal analyses of the original plastics, MPs, and NPs

Chemical and thermal analyses were performed on the original polymeric materials, MPs (250 μm sieve fraction, and NPs (produced after wet grinding) for both PBAT films and LDPE pellets. (For PBAT, samples were subjected to cryogenic treatment according to optimal conditions prior to milling and sieving). Analyses consisted of FTIR spectroscopy (chemical bonding properties), gel permeation chromatography (GPC; number- and weight-averaged molecular weight [M_n and M_w, respectively] and polydispersity index [$PDI; M_w/M_n$]), differential scanning calorimetry (DSC; properties), and thermogravimetric analysis (TGA; thermal stability). The instrumentation and detailed procedures are given in the Appendix III-B and are nearly identical to those employed previously by the authors (Hayes *et al.*, 2017).

3.4 Results and Discussion

3.4.1 Effects of cryogenic treatment on the size reduction on PBAT mesoplastics

For efficient size reduction of a biodegradable agricultural mulch film (PBAT), cryogenic treatment was applied to induce embrittlement, leading to size reduction (Figure III-B1). In the absence of cryogenic exposure, the PBAT film did not undergo size reduction upon mechanical milling (data not shown). A randomized design was used to evaluate the effect of cryogenic treatment processing conditions (duration of pre-soaking in water and soaking in liquid nitrogen, and the blending speed, time, and presence vs. absence of water) for the minimization of d_p. Factor levels were selected based on observations from preliminary blending experiments performed with PBAT films, the experimental matrix was designed accordingly (Table III-A1).

A more detailed analysis of the d_p distribution is given in Table III-B1. Results showed that increased severity of processing conditions significantly enhanced size reduction to d_p = 1- 2 mm (Table III-A1, runs 4-6). Particularly runs 4-6 shared the longest soaking time in liquid N_2 (10 min), indicating that it is the most influential factor for size reduction. Similarly, a recent study focusing upon polystyrene MPs found that the yield of MPs increased with residence time during a pre-cooling step (Eitzen *et al.*, 2019). Blending time and speed were also influential factors, but to a lesser extent than soaking time.

Further evaluation of data by prediction profiler statistical software confirmed the trends discussed above that liquid nitrogen soaking time was the most influential factor, followed by blending time and speed (Figure III-B2). Also, the statistical analysis demonstrated that no interaction within processing factors was observed, suggesting that increased levels for processing parameters will result in a more effective reduction of d_p (Figure III-B2). The inclusion of water resulted in a well-blended mixture, leading to a slight reduction of d_p (Figure III-B2). The software predicted that under optimal conditions, an average d_p value of 1.15 mm could be achieved (Figure III-B 2), which is slightly lower than the minimal value of d_p achieved, 1.43 mm (Table III-A1).

A representative histogram for d_p of PBAT MPs produced by cryogenic treatment is shown in Figure III-A4, and histograms and particle count for all runs of Table III-A1 are depicted in Figure III-B3 and Figure III-A5, respectively. The smallest size fraction of, 0-0.5 mm, served as the most prominent fraction, and as the average d_p for fractions increased, the population size slowly

decreased. Several different size distribution models were evaluated for the quality of the fit to the data: log-logistic, Frechet, lognormal, and two-parameter Weibull. The latter distribution provided the best fit (followed by lognormal), exhibited by the lowest AIC and BIC values obtained for the fit. The two-parameter Weibull model is described by:

$$f(x, \alpha, \beta) = \begin{cases} \dfrac{\beta}{\alpha} \left(\dfrac{x}{\alpha} \right)^{\beta-1} \exp\left(-\left[\dfrac{x}{\alpha} \right]^{\beta} \right) & x \geq 0 \\ 0 & x < 0 \end{cases} \tag{1}$$

where $\beta > 0$ is the shape parameter and $\alpha > 0$ is the scale parameter of the distribution. The two-parameter Weibull model is a flexible distribution model that is applied to a broad range of applications such as bioproduct development (Varga *et al.*, 2001), terrestrial sediments (Allen *et al.*, 2015), quality engineering for material strength data distribution (Young *et al.*, 2015), two-phase materials in metallurgy (Fang *et al.*, 1993; Lynch & Rowland, 2005), aerosols (Dunbar & Hickey, 2000), seed sizes (Domoradzki & Korpal, 2005), and wind speed distribution in aerodynamics (Seguro & Lambert, 2000). Of relevance to this study, the two-parameter Weibull model has also been demonstrated to be the most effective size distribution model to describe soil particles (Bayat *et al.*, 2015; Esmaeelnejad *et al.*, 2016).

The average d_p values obtained through the Weibull model fit, α and β values, and information on the quality of the fit (AIC and BIC) are given in. Run 4, which provided the lowest d_p, also experienced the best fit of the two-parameter Weibull model to its size distribution data, evidenced by the minimization of AIC and BIC (Table III-A1). In general, β values (~1.0) did not change appreciably with cryogenic conditions and are reflective of a broad distribution with a maximum skewed toward the lower end of the distribution function) (Table III-A1 and Figure III-A4).

3.4.2 Effects of mechanical milling on MP formation

The use of mechanical milling led to the formation of PBAT and LDPE MPs that were isolated into four different sieving fractions (Figure III-A3): 840 µm, 250 µm, 106 µm, and 45 µm (Figure III-A6). More detailed information on the particle size distribution is given in Figure III-B2.The mass recovery and d_p values for the two smallest sieve fractions, 106 µm, and 45 µm, were nearly

equal for both plastics with a mass recovery of 2 wt% and 1 wt%, respectively, and d_p values were nearly equal to the nominal sieve sizes For 250 µm fractions, the recovery was lower for PBAT (11%) than for LDPE (18%), and d_p was lower for the former plastic (and less than the nominal size). These results reflect that mechanically milled PBAT contains a larger amount of course, less geometrically uniform, particles than milled LDPE, likely a result of PBAT being a softer and less dense polymeric material. The same trend serves as the underlying cause of the larger variability in d_p for PBAT for the 840 µm and 250 µm sieve fractions (Figure III-A6). In summary, shear force via milling (supported by additional degradation via cryogenic treatment for PBAT) produced MPs at low-to-moderate yields. Similar to PBAT MP particles obtained by cryogenic treatment, the size distribution of d_p was the best fit by a two-parameter Weibull model for all MP sieve fractions produced by milling (Figure III-A6 and Figure III-B5). Parameters related to the fit of the Weibull model are given in Table III-A2, while particle count vs. d_p is depicted in

Figure III-B6. The fit of the Weibull model improved as the sieve size of the fractions decreased, noted by a decrease of AIC and BIC (Table III-A2). Unlike the distribution obtained for cryogenic-treated MPs, which was skewed toward the lower end of the d_p distribution (i.e., β≈ 1.0; Table III-A1), for all sieve fractions, the distributions were slightly skewed in favor of higher d_p values (β> 8; Table III-A2). The narrowest size distribution occurred for the 45 µm MP sieve fractions and LDPE fractions compared to PBAT fractions (i.e., highest β value), the latter trend reflecting coarser and less geometrically uniform particles for PBAT as discussed above. The production of NPs was not detected, noting that the smallest size sieve fraction, 45 µm, provided MP particles of size (d_p) ≥36 µm. Moreover, it is unlikely that mechanical tilling of plastic mulch films will directly produce NPs.

3.4.3 Effects of wet-grinding on NP formation from MPs

Wet grinding was applied to the 106 µm MPs fraction of both plastics to produce NPs, with d_p measured by DLS. Both materials yielded NPs with similar bimodal distributions, with the major and minor fractions (I and II, respectively, with being ~2.5-fold higher in intensity than II) possessing maxima at d_p values of ~500 nm and ~60 nm, respectively (Tables III-A3 and A7). The size of fraction I is ~15-fold smaller than that of the initial 106 µm sieve fraction (Table III-A2 and Figure III-A6a,c). Average d_p values for PBAT and LDPE NPs (i.e., both fractions combined)

69

were 366.6±6.5 nm and 389.4±10.7 nm (error bars reflect standard deviation), respectively, and spanned the range ~40-1300 nm, with the range of LDPE being slightly broader (Figure III-A7 and Table III-A3). These results suggest that degradation due to low shear may occur through two steps, one of which reduces size 15-fold and the other further reducing size by an additional factor of 10. For each fraction, lower d_p values were observed for LDPE, despite the original LDPE material possessing a higher d_p (Table III-A3a,b). However, the aqueous solution of LDPE NPs produced by wet grinding contained a significant fraction of particles that flocculated on top that was not included in the sample analyzed by DLS. The flocculation is due to the density of LDPE being lower than that of water and the polymer's hydrophobicity. Another possible cause is the creeping of the NPs in the upward direction due to adhesion with the glass container walls, a phenomenon recently reported for polystyrene NPs (Eitzen *et al.*, 2019). The same study reported that adhesion was lessened when the polystyrene NPs were oxidized by ozone (Eitzen *et al.*, 2019). Environmentally-weathered PE is known to undergo oxidation, forming polar functional groups on its surface, such as hydroxyls and carboxylates (Hayes *et al.*, 2017). It is likely that the flocculation of NPs formed from weathered LDPE would be lessened. In contrast, PBAT NPs were evenly dispersed throughout the slurry, even in the absence of stirring.

The size distribution model that fit the two NP fractions for each polymeric material was the two-parameter Weibull model (Figure III-A7). The smaller, ~60 nm –sized fractions (I) were narrower in the width of their size distributions than the larger size fraction (II), noted by the larger shape factor, β (Table III-A3), and both distributions were narrower than the original starting material, the 106 mm sieve fraction (Table III-A2). Future research is needed to better understand the relationship between wet grinding conditions and the resultant sizes and size distributions of the NP products.

3.4.4 Effect of size reduction on chemical and thermal properties of plastics

Chemical and thermal analyses of MPs and NPs were compared to the original plastic feedstock to determine if size reduction promoted any changes in properties. MP samples consisted of the 250 mm sieve fraction of dry milled plastics, while NPs were produced via wet grinding of the 106 µm MPs sieve fraction. The thermal stability of MPs and NPs was examined by analysis of TGA curves (Figure III-A9a,b) and differential thermograms (DTGs) (rate of heat loss vs.

temperature; c,d). For the PBAT-rich film, the first major heating stage was found at temperatures between 300˚C and 318˚C, representing the decomposition of starch, while the second, largest, stage (~400˚C) represents the decomposition of PBAT (Hayes *et al.*, 2017). The mass remaining at the maximum temperature, 600˚C, reflects minor components such as binders and fillers, and perhaps gels (Hayes *et al.*, 2017). No weight loss was observed for temperatures <200°C, suggesting the absence of water and volatiles. The formation of MPs led to a slight shifting of both major heating stages to lower temperatures (Figure III-A9a,c). Upon further size reduction to NPs, the heating stages for starch and PBAT are shifted more significantly to lower temperatures. For LDPE, while TGA curves were nearly identical for the original material and MPs, the curve for NPs was slightly shifted to lower temperatures, to a much lesser extent than PBAT (Figure III-A9b,d).

The loss of thermostability by starch, PBAT, and LDPE may be due to either a decrease of crystallinity or molecular weight. To address, crystallinity (Figure III-A9) (X_c) was determined from the enthalpy of melting measured using DSC (discussed in the Appendix III-B). For both polymeric materials, cryogenic exposure followed by mechanical milling increased X_c nearly two-fold, and NPs and MP possessed similar values (Table III-A4). An increase of crystallinity was also observed during embrittlement caused by environmental weathering (Hayes *et al.*, 2017), suggesting the underlying cause of the increase of X_c was cryogenic exposure. DSC analysis demonstrated that the melting and glass transition temperatures of PBAT and LDPE underwent slight changes (discussed in Appendix III-B). Therefore, the loss of thermostability is likely a result of depolymerization, a hypothesis supported by GPC analysis of PBAT. Depolymerization occurred slightly during the formation of MPs (i.e., cryogenic treatment followed by Wiley milling), noted by the 27.6% decrease of M_w; but size reduction of MPs to NPs did not decrease M_w appreciably, 1.4% (Table III-A4). In contrast, the molecular weight distribution was narrower (i.e., PDI lower) and M_n slightly higher for MPs compared to the original polymeric film, and for NPs compared to MPs, suggesting the lower-molecular-weight polymers were removed during milling and wet grinding (Table III-A4). These trends may reflect the selective degradation of local regions that are weaker in strength (e.g., amorphous morphological regions), where lower molecular weight polymers would be expected to reside. In contrast, smaller particles recovered from wet grinding of plastics typically undergo a slight decrease of M_n and M_w and a minor increase

of PDI (Ravishankar *et al.*, 2018). Herein, NP samples were taken from the middle layer of the slurry, such that smaller particles, which flocculated near the top layer, were less likely to have been contained in the sample.

TGA also provides the relative proportion of components, such as PBAT and starch. Size reduction to MPs decreased the starch content from 16.8% to 13.0%, and further size reduction to NPs further reduced the starch content to 8.3% (Figure III-A9a,c). In contrast, the PBAT content of the original film and MPs were nearly identical (71.6 and 70.6%, respectively) and NPs possessed a 12% lower PBAT content (62.2%; Figure III-A9a,c). These results demonstrate that the size-reduced starch was readily leached away from MPs and NPs, while the slight loss of PBAT upon the formation of NPs is due to both leaching away of lower-molecular-weight polymers and the formation of a gel-like material, noted by the increase of mass remaining at 600 °C (Figure III-A9a,c). FTIR analysis also reflected the reduction of starch content upon size reduction, the occurrence of hydrolysis and the absence of oxidation-reduction reactions on the surface (e.g., the absence of cross-link formation or new functional surface groups; discussed in Appendix III-B).

3.5 Conclusions

In this study, a simple and effective size reduction process was developed to prepare MPs and NPs from prominent agricultural plastics, PBAT-rich biodegradable mulch films, and LDPE, that are likely to represent MPs and NPs occur at higher levels in agricultural soils, in contrast to monodisperse polystyrene beads and other commonly employed model materials in fundamental studies. The protocol consisted of cryogenic treatment (to mimic the embrittlement caused by environmental weathering), followed by mechanical milling (to prepare MPs of nominal sizes 45 μm, 106 μm, 250 μm, and 840 μm, mimicking the impact of cutting and high-impact mechanical degradation that occur during tillage of plastics into soil). The 106 μm MP fraction was subjected to wet grinding, a process that mimics low-impact shear as would occur between MPs and soil particulates or water (Ravishankar *et al.*, 2018), to produce NPs. The latter's size distribution was bimodal, with the average size of the two populations being 15- and 150-fold smaller than the original 106 μm MP fraction. The size distribution of MPs and the two NP subpopulations was described effectively by the two-parameter Weibull function, and the former was quite broad. Degradation occurred at locally weaker regions possessing lower crystallinity and average

molecular weight and was assisted by the leaching away of polar and lower molecular weight components, such as starch from the PBAT-rich film. The procedure described herein can be applied to several plastic materials, including residual plastic film fragments or debris, to form representative terrestrial MP and NPs materials for future environmental studies, such as ecotoxicity screening and the transport and fate of MPs and NPs in soil ecosystems. The methodology described herein can be employed to investigate the formation of MPs and NPs, such as the kinetics and time course of size reduction, the effect of environmental parameters such as temperature, salinity, or the presence of soil particulates.

APPENDIX III - A
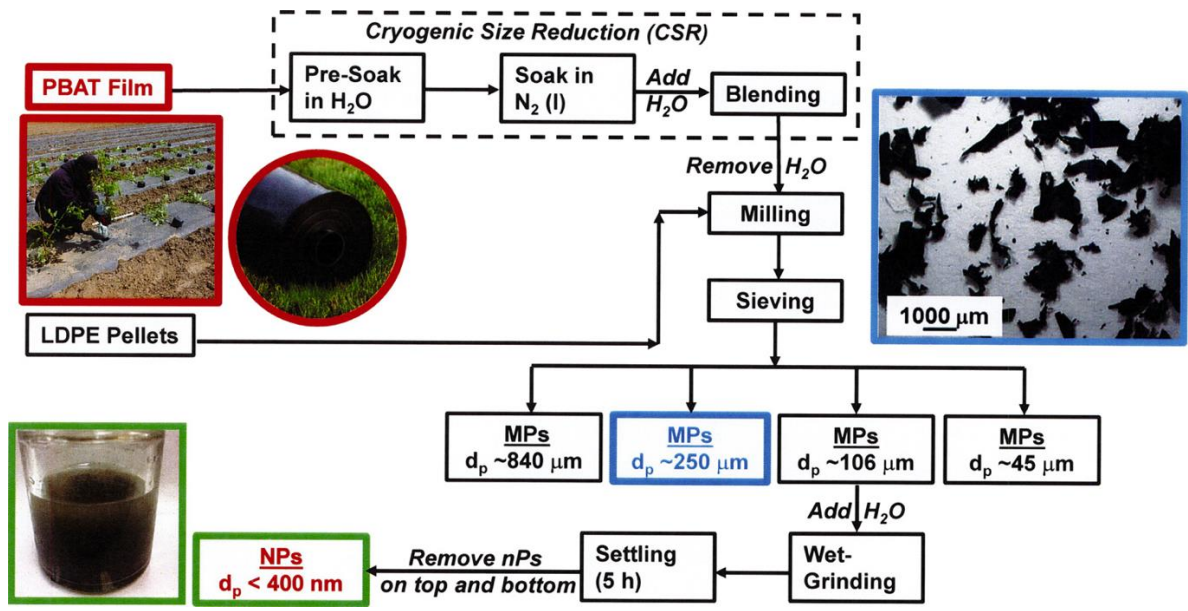
Figure III-A1. Flow diagram of plastic film processing into micro and nanoplastics through mechanical milling and wet-grinding processes
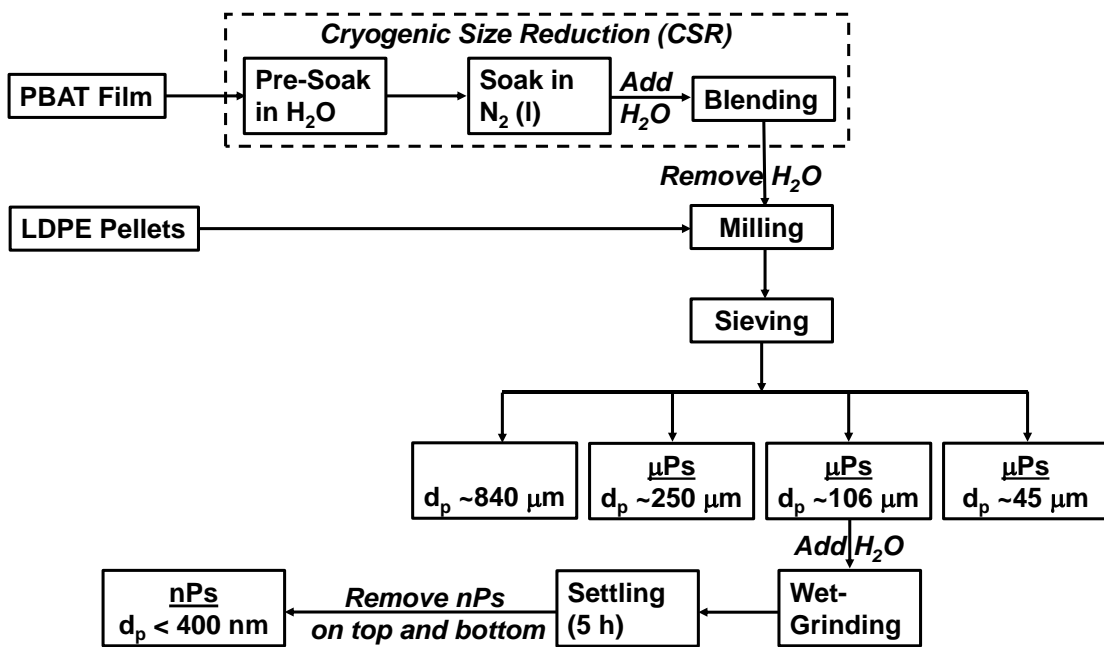
Figure III-A2. Flow diagram for processing of micro- and nanoplastics (MPs and NPs, respectively).
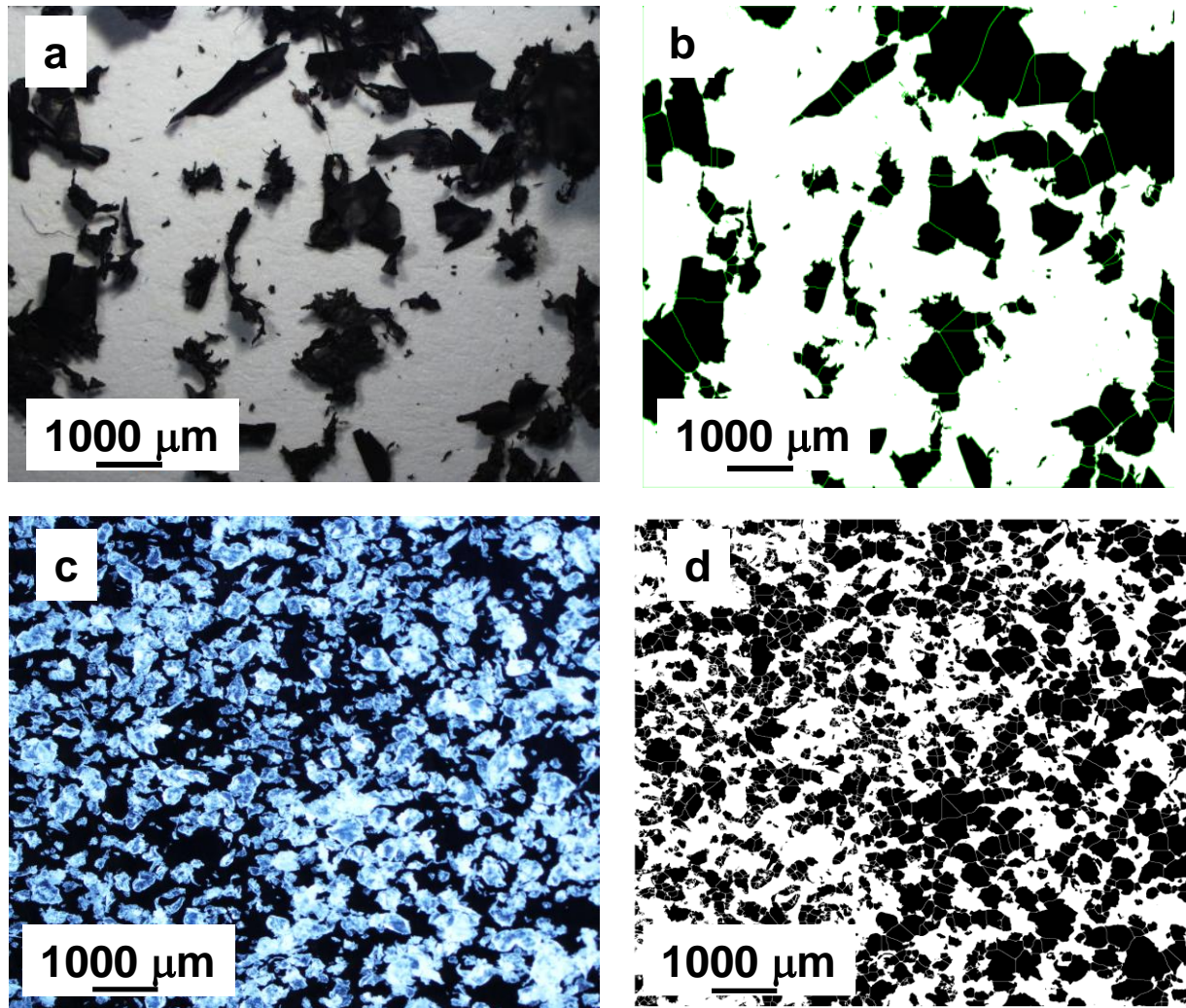
Figure III-A3. Stereomicrographs of MP (250 µm fraction resulting from milling followed by sieving; cf. (a) PBAT and (c) LDPE, and (b) and (d) the corresponding images produced by Image J software using for the watershed function. Before milling, PBAT film samples underwent cryogenic treatment according to the conditions of Run 4 of Table III-A1.
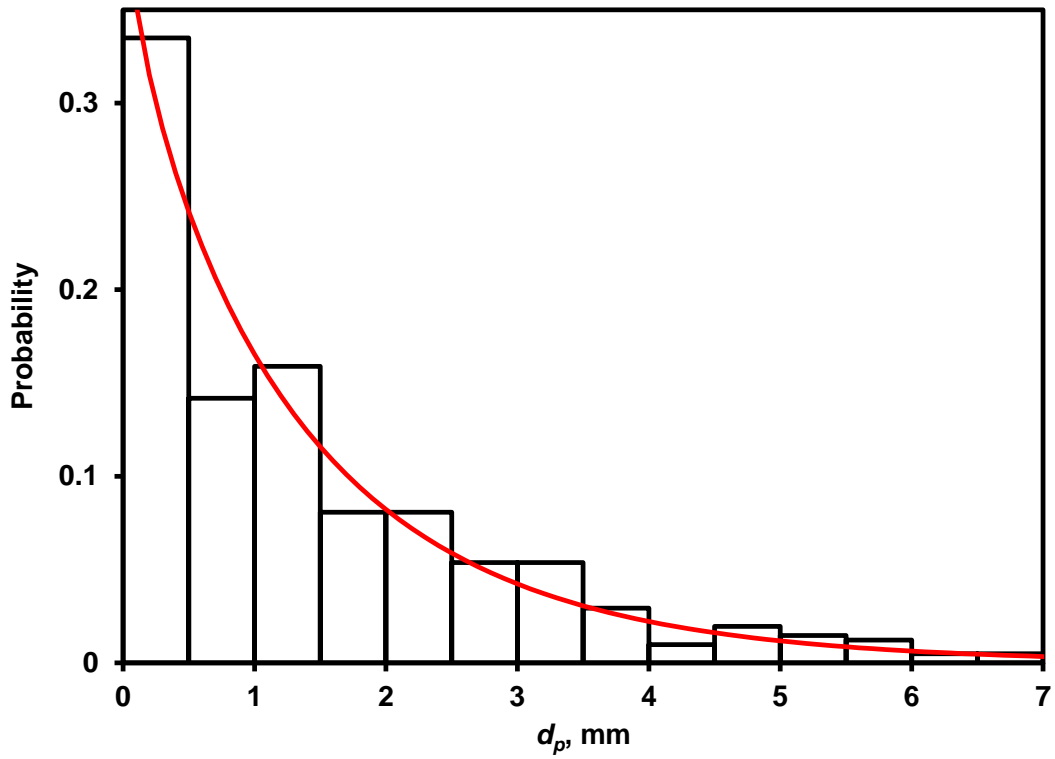
Figure III-A4. Particle size distribution of PBAT resulting from the cryogenic treatment represented by Run 4 of Table III A1. The red curve represents the fit of the two-parameter Weibull model (Eq. 1) to the data.
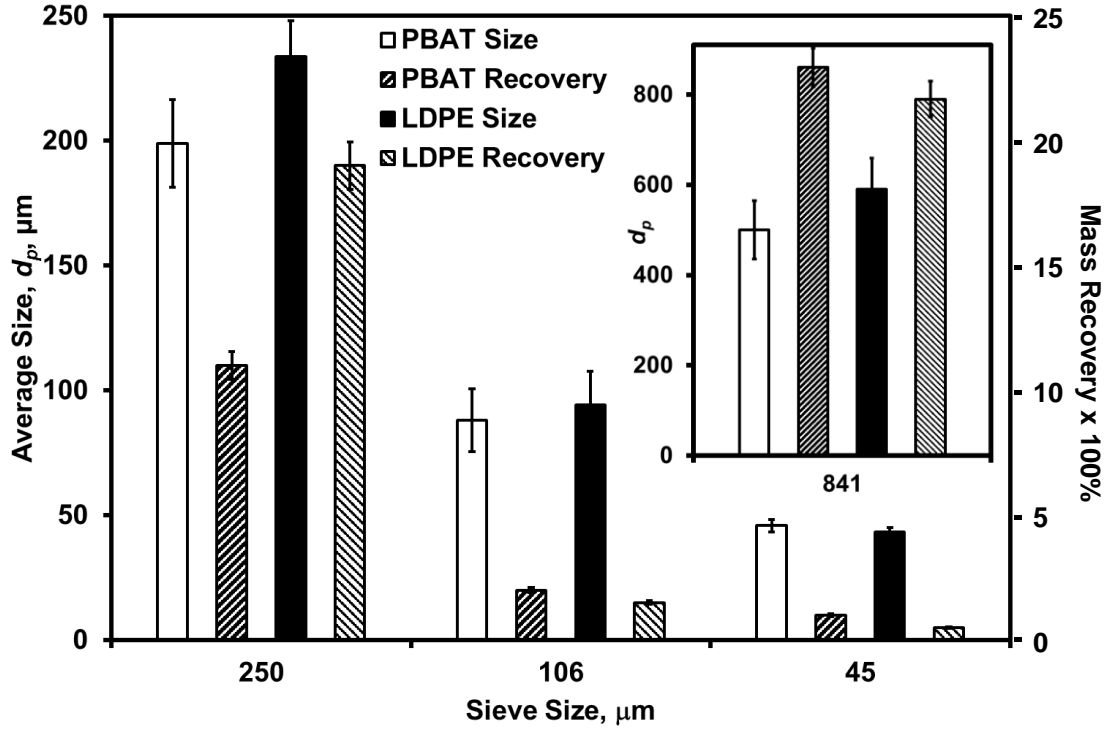
Figure III-A5. Average particle size (d_p) and % recovery of mass for PBAT and LDPE MPs obtained via dry milling (840 µm and 250 µm sieves for the first and second pass) of 1g of feed, followed by sieving. Sieve sizes are indicated by solid black bars in the figures. d_p was determined by Image J.
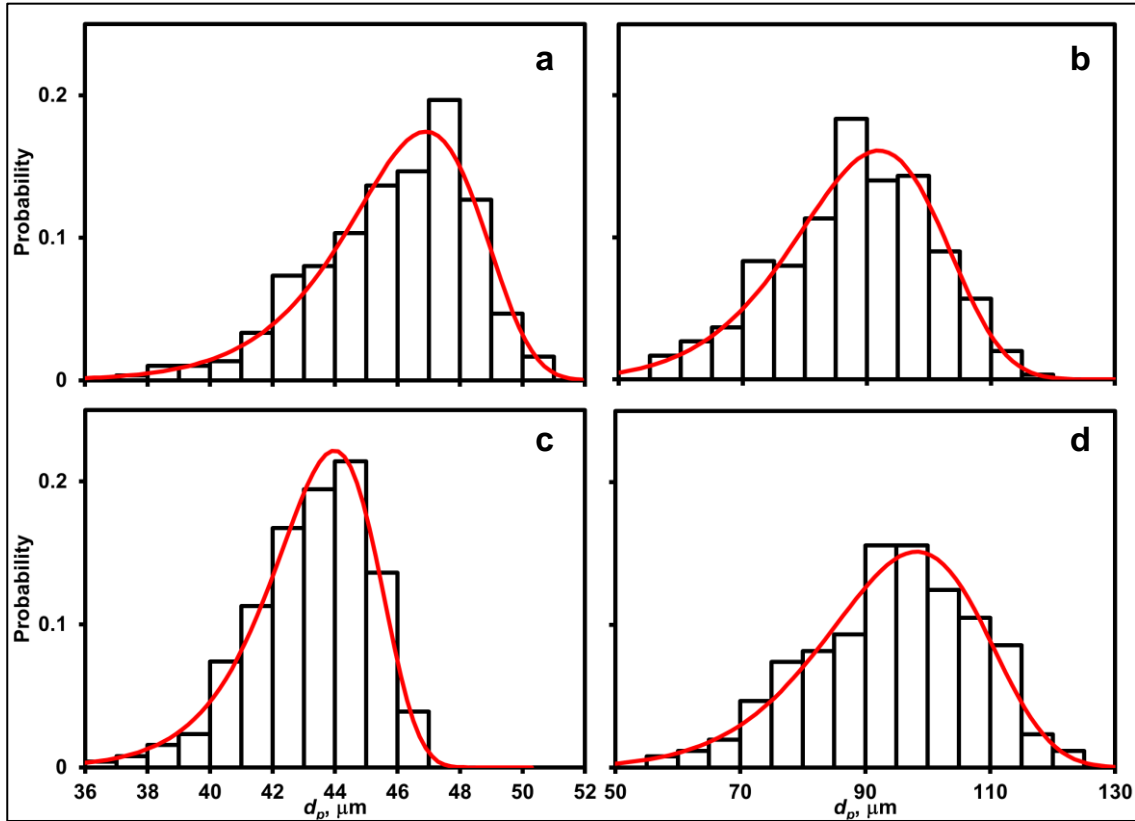
Figure III-A6. Particle size distributions of (a,b) PBAT and (c,d) LDPE for the (a,c) 45 µm and (b,d) 106 µm nominal MP sieve fractions (after mechanical milling), with superimposed two-parameter Weibull model (Eq. 1).
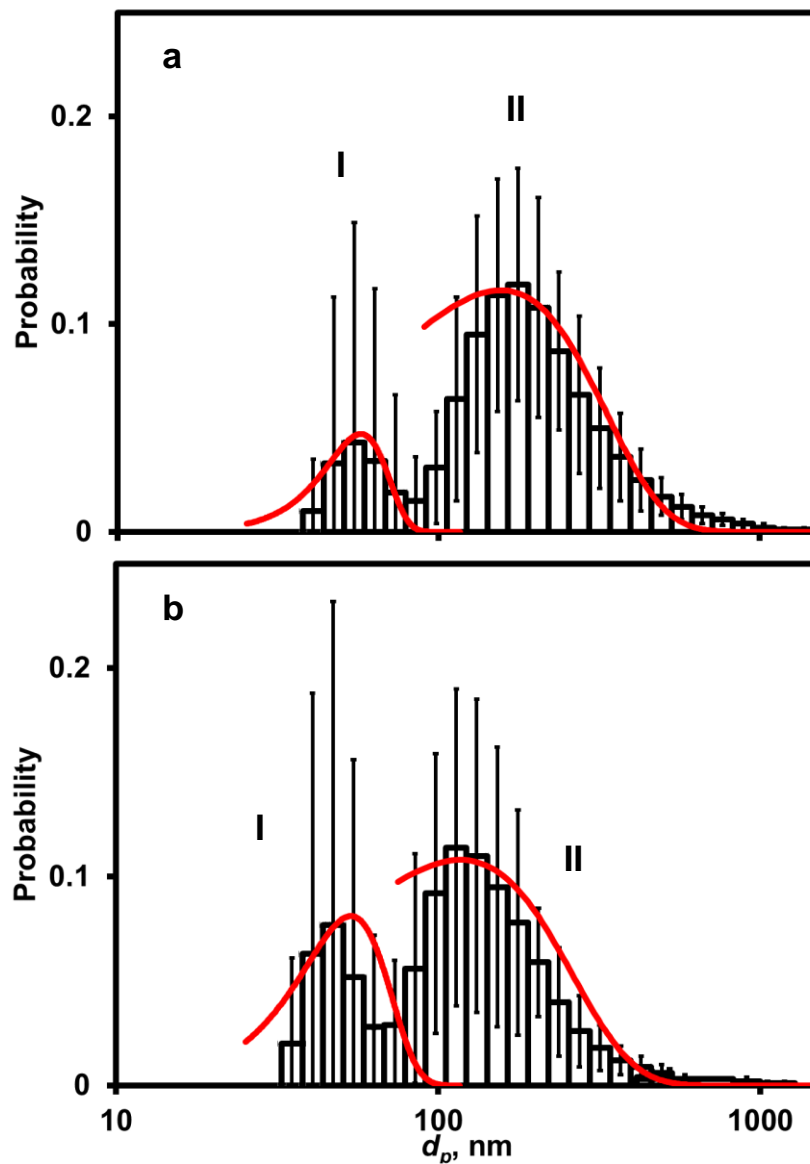
Figure III-A7. Histograms of particle size (d_p,) for (a) PBAT and (b) LDPE NPs, formed from the wet-grinding treatment of the 106 μm-MP sieve fraction. The error bars represent the ±one standard deviation of the dataset. Curves represent the two-parameter Weibull model fits fractions I and II, as listed in Table III-A3.
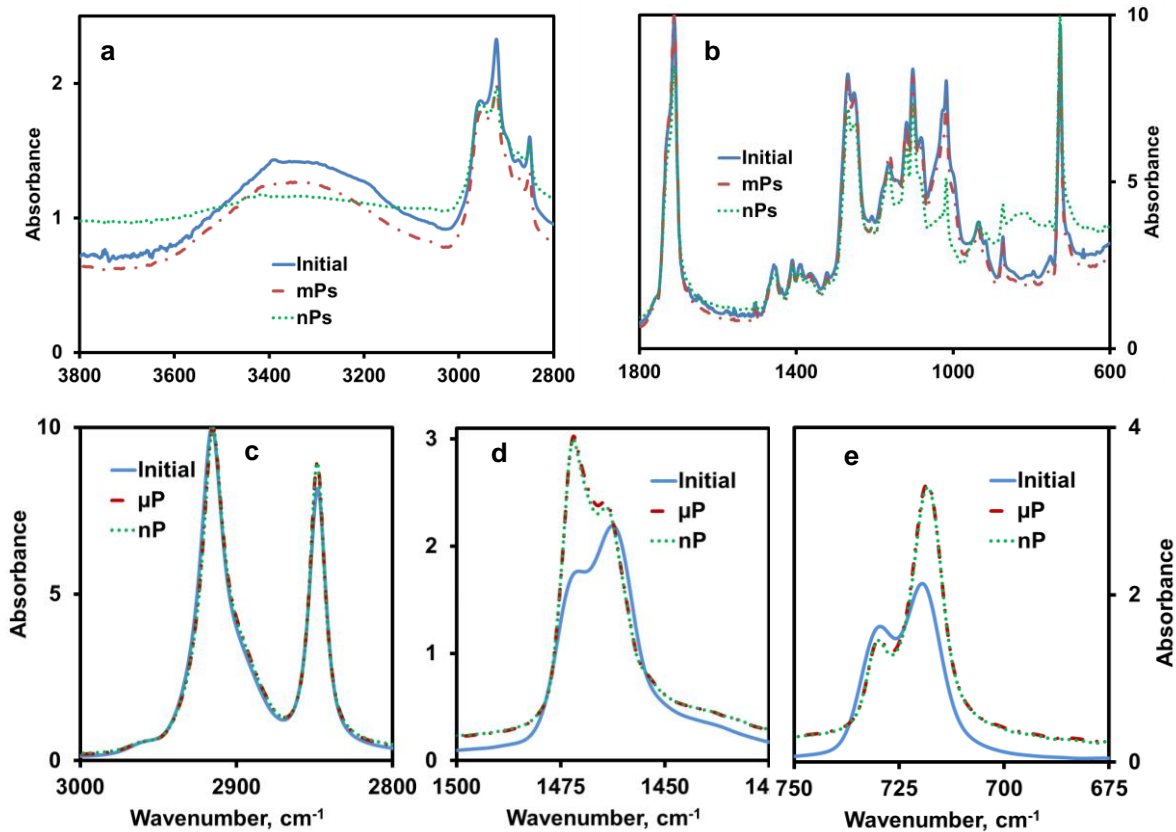
Figure III-A8. Comparison of FTIR spectra for (a,b) PBAT and (c-e) LDPE between the original plastic starting materials and their MPs and NPs. MPs consist of the 250 µm sieve fraction of dry milled plastics (cryogenic treatment applied to PBAT according to the optimal conditions: Run 4 in Table III-A1); NPs, produced via wet grinding of the 106 µm sieve fraction MPs after dry milling.
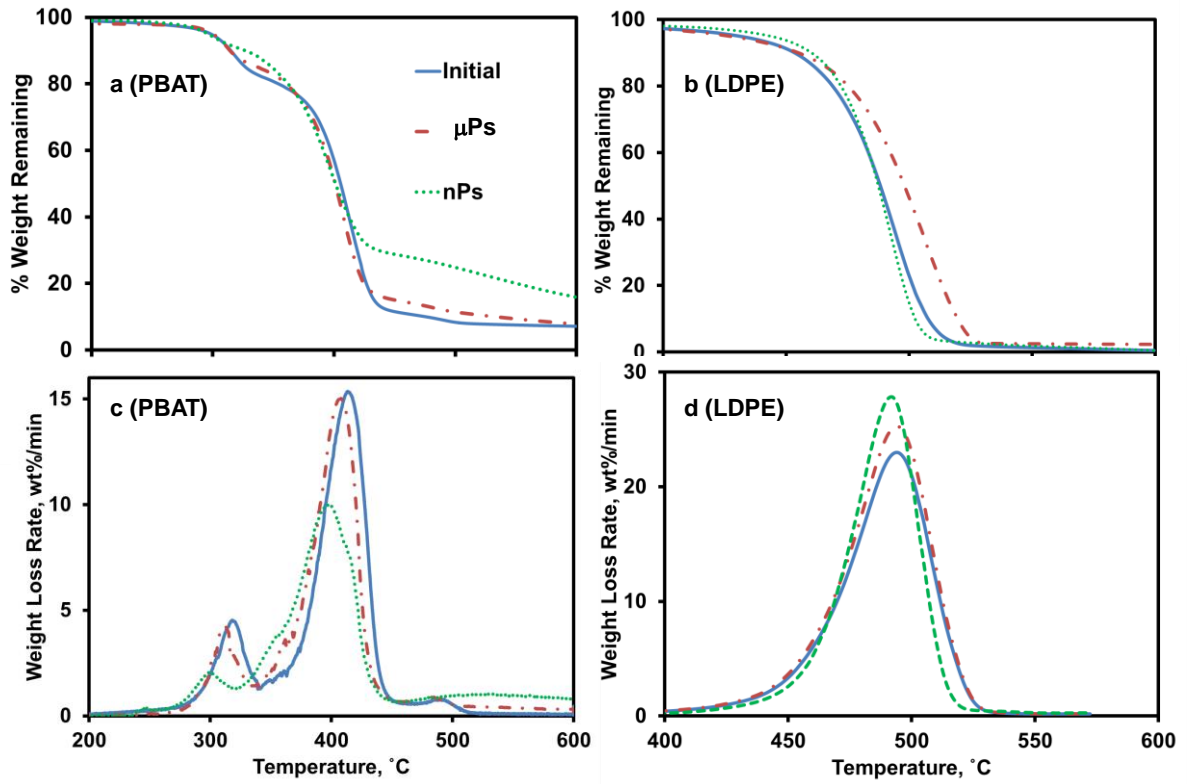
Figure III-A9. (a,b) TGA and (c,d) DTG curves before processing initial polymer, after dry-milling (MPs) and wet grinding (NP) of (a,c) PBAT and (b,d) LDPE.

Table III-A1. Effect of operational parameters for cryogenic size reduction of PBAT films on the average particle size for particles achieved (d_p) and the fitting of the particle size distribution by the two-parameter Weibull model [1]

Run #	H_2O presoaking time	N_2 soak time	Blending time	Blending speed	d_p (measured)	d_p (Weibull)	a [4]	b [5]	AIC [6]	BIC [7]
	[min]	[min]	[min]	[min^{-1} x 1000]	[mm] [2,3]	[mm]				
1	0	0	5	2	9.30 ± 4.53	9.29	8.71	0.878	2628	2636
2	0	5	2	2	3.17 ± 1.29	3.3	2.31	0.63	1621	1629
3	5	10	10	10	4.21 ±1.54	4.19	4.53	1.3	1960	1968
4	5	10	10	10	1.47 ± 0.45	1.42	1.43	0.946	1132	1140
5	10	10	10	10	1.58 ± 0.63	1.58	1.53	0.931	1194	1202
6	10	5	2	2	1.68 ±0.68	1.69	1.6	0.894	1239	1247
7	10	5	2	2	3.22 ±1.47	3.22	3.28	1.051	1777	1785
8	5	5	10	10	3.64 ± 1.57	3.65	3.31	0.835	1856	1864

[1] Cryogenic treatment conditions: presoaking in H_2O (400 mL; except for Runs 1 and 2), followed by soaking in N_2 (200 mL) for cryogenic cooling, followed by blending of the resultant mesoplastics with water (400 mL), and then air-drying.

[2] Determined by ImageJ analysis of stereomicrographs from two images per sample.

[3] error bars represent one standard deviation.

[4,5] Weibull model parameters (Eq 1).

[6] Akaike's information criterion

[7] Bayesian information criterion

Table III-A2. Particle size distribution data for PBAT and LDPE MPs obtained via dry milling (840 μm and 250 μm sieves for the first and second pass) of 1g of feed, followed by sieving, as determined by the Weibull model (Eq. 1) [1]

Polymer	Sieve Fraction [μm]	d_p (Weibull) [μm]	a	b	AIC	BIC
PBAT	840	500.7	527.2	9.58	3328	3335
	250	198.9	206.6	13.56	2553	2561
	106	88.1	93.4	8.18	2364	2372
	45	45.9	47	22.47	1375	1383
LDPE	840	591	619.7	10.58	2883	2890
	250	233.9	240	20.83	2062	2069
	106	94.2	99.8	8.23	2060	2067
	45	43.2	44	26.92	1058	1065

[1] Column headings described in Table III-A1.

Table III-A3. Size (d_p) and size distribution data for NPs of produced by wet-grinding of PBAT and LDPE MPs (106 µm sieve fraction) via Dynamic Light Scattering (DLS) analysis [1,2,3]

Polymer and Fraction	PBAT I	PBAT II	PBAT I+II	LDPE I	LDPE II	LDPE I+II
d_p range [nm]	37.7 - 91.3	91.3 - 1281	37.7 - 1281	32.7 - 91.3	91.3 - 1357	32.7 - 91.3
d_p (mean) [nm] [4]	63.8±13.7	536.8±151.8	366.0±6.5	60.9±17.8	485.7±123.6	389.4±10.7
a (Weibull) [nm]	59.8	243	-	58.3	190.5	-
b (Weibull)	5	1.81	-	3.71	1.75	-
AIC	129.5	1036	-	273.5	796.9	-
BIC	130	1041	-	276.1	801.2	-

[1] Size distributions and column headings described in Figure III-A7.
[2] Row headings defined in Table III-A1.
[3] For PBAT, cryogenic exposure was employed per the conditions of Run 4 in Table III-A1.
[4] error bars represent one standard deviation.

Table III-A4. Comparison of molecular weight-related and thermal properties of PBAT and LDPE plastics and the derived MPs and NPs [1,2].

Sample	M_n [kDa]	M_w [kDa]	PDI	Xc x100% [3]
PBAT, Initial	89.7 ±0.4	289 ± 15	3.22 ± 0.18	21.5 ± 0.6
PBAT, MP	98.0 ± 2.0	209 ± 6	2.13 ± 0.01	39.7 ± 0.9
PBAT, NP	110 ± 1.8	205 ± 2	1.87 ± 0.01	32.5 ± 0.7
LDPE, Initial	*nd*	*nd*	*nd*	24.2 ± 0.2
LDPE, MP	*nd*	*nd*	*nd*	41.5 ± 0.5
LDPE, NP	*nd*	*nd*	*nd*	42.9 ± 0.4

[1] MPs consist of the 250 µm sieve fraction of dry milled PBAT, treated using cryogenic treatment under the conditions described in Run 4 of Table III-A1.

[2] NPs were produced via wet grinding of the 106 µm sieve fraction MPs after dry milling; Error bars represent one standard deviation of two sample measurements; *nd* = not determined.

[3] Crystallinity of PBAT, determined from the enthalpy of melting measured via DSC analysis, and calculated as described in detail in the Appendix B.

APPENDIX III - B
SUPPLEMENTARY DATA FOR CHAPTER III

B 1. DETAILED DESCRIPTION OF PARTICLE SIZE ANALYSIS

B 2.1. Size determination for MPs undergoing cryogenic treatment

PBAT MPs formed via cryogenic treatment were scanned by a flatbed-scanner (MX 490 by Canon, Tokyo, Japan) and the particle dimensions were analyzed by ImageJ software, as described in the next sub-subsection. A representative sample of ~1 g of MPs was introduced in a clear Ziploc® bag (SC Johnson and Son, Racine, WI, USA), and evenly distributed within. The bag was transferred on the scanner glass surface, and the top lid of the scanner was closed to provide excellent image contrast. For a given set of cryogenic conditions, a single sample was analyzed using two scans.

B 2.2. Stereomicroscopy and image analysis for MPs

PBAT and LDPE MPs belonging to each of the four sieve fractions were analyzed using a model SZ 61 stereomicroscope from Olympus (Shinjuku, Tokyo, Japan) with a Digital Sight DS-Fi1 integrated camera head from Nikon (Shinagawa, Tokyo, Japan). Images analysis was performed using ImageJ software (Schneider *et al.*, 2012). Firstly, micrographs were converted into 8-bit images, (representing 28 gray levels) by a proper threshold setting (dividing the image into two or more classes of pixels) and choosing a value cutoff for matching out foreground areas using a specific pixel classification for the background areas. The adjusted image was converted into a binary file and adjacent objects were separated by the "watershed" algorithm. Examples of images produced by ImageJ vs. the corresponding stereomicrographs are presented in Table III-A3. The average MP diameter, d_p, was estimated using the Image J's "analyze particles" algorithm. The features "exclude on edges" and "include holes" of the algorithm were selected by including single particles and ignoring any void spaces. One image that was representative of the entire sample was collected and processed for each of two different samples for a given sieve fraction, and were subsequently processed by Image J.

The distribution of d_p derived from Image J analysis was fit by several different models using JMP® Pro 14.0 software (SAS Institute, Cary, NC, USA). The datasets generated for the three size classes were non-normally distributed according to the Shapiro-Wilk test. Accordingly, the Lognormal, Weibull, Loglogistic and Frechet models were used to test for the best fit. The corrected Akaike's and Bayesian information criteria (AIC and BIC, respectively) were used to compare the quality of model fits. All statistical evaluations employed a significance level of $\alpha = 0.05$.

B 2.3. Dynamic light scattering (DLS) analysis of NPs

Aliquots of slurries resulting from the wet-grinding process were placed in 1.0 cm pathlength quartz cuvettes, and then analyzed by DLS at 25ºC using a Malvern Zetasizer Nano instrument (Malvern, Worcestershire, UK). The beam of the 4 mW HeNe Laser (λ=633 nm) was aligned to pass through the sample at a vertical position 1.25 mm, measured from the bottom of the cuvette. In total, 48 measurements (12 subsamples with three replicates per subsample) for each sample were carried out. A sampling time of 60 s was selected for each measurement. The particle size distribution was analyzed by Malvern Zetasizer software 7.11.

In clinical trials or community trials, the Kaplan-Meier estimate is frequently used to measure the fraction of subjects living for a certain amount of time after treatment. The time span defined from a starting point until the occurrence of a specific event, for example death is termed as survival time. For this study, Kaplan Meier estimates were used to compare curves for different groups among the size distributions of eight sieving fractions. The gaps in these curves in a horizontal or vertical direction show the relationship between d_p (average) to the particle frequency. A larger vertical gap indicates for a specific d_p that a group includes a larger fraction at a specific particle count. A horizontal gap indicates that a larger particle amount was determined at a steady average d_p. For example, for a d_p of ~2 mm, the Run 1 shows a particle count of 100 (between 300 - 400); however, Run 4 indicates a particle count of 250 (between 150-400).
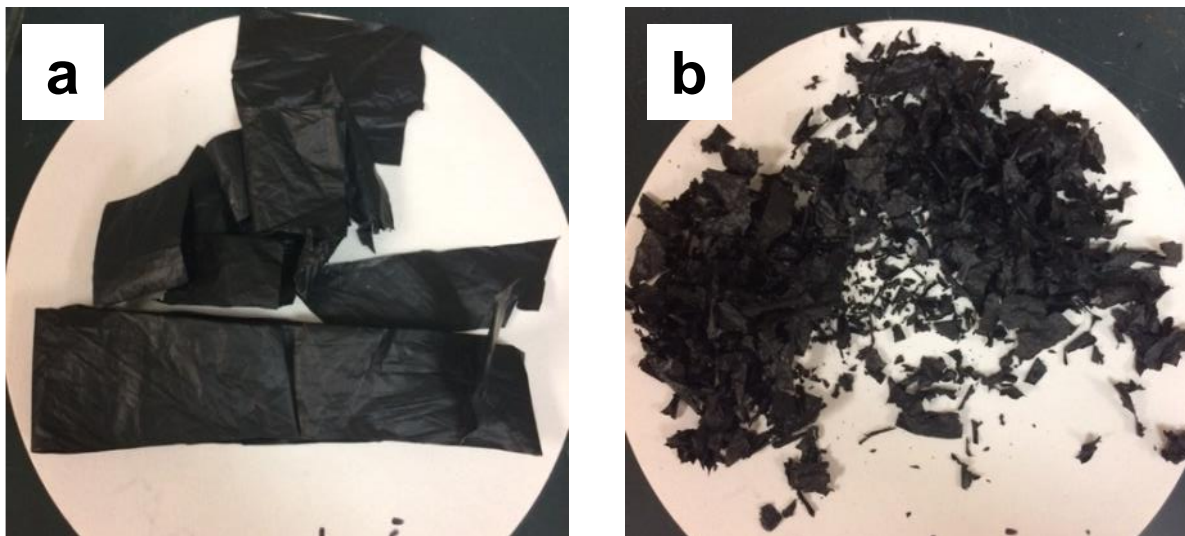
Figure III-B1. Photographs of PBAT agricultural mulch film (a) before and (b) after treatment by cryogenic size reduction. Diameter of white, circular filter paper was 5.0 cm.
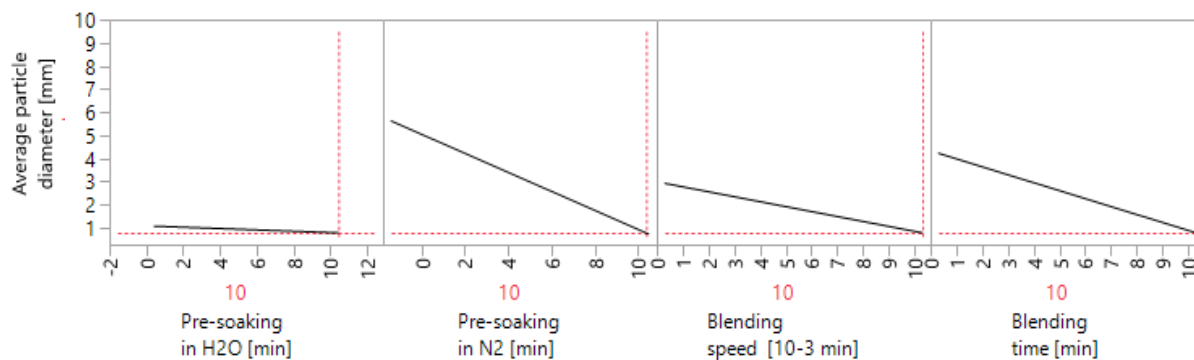
Figure III-B2. Predicted relationships for parameters involved with optimization of cryogenic size reduction, per the data given in Table III-A1, using JMP statistical software.
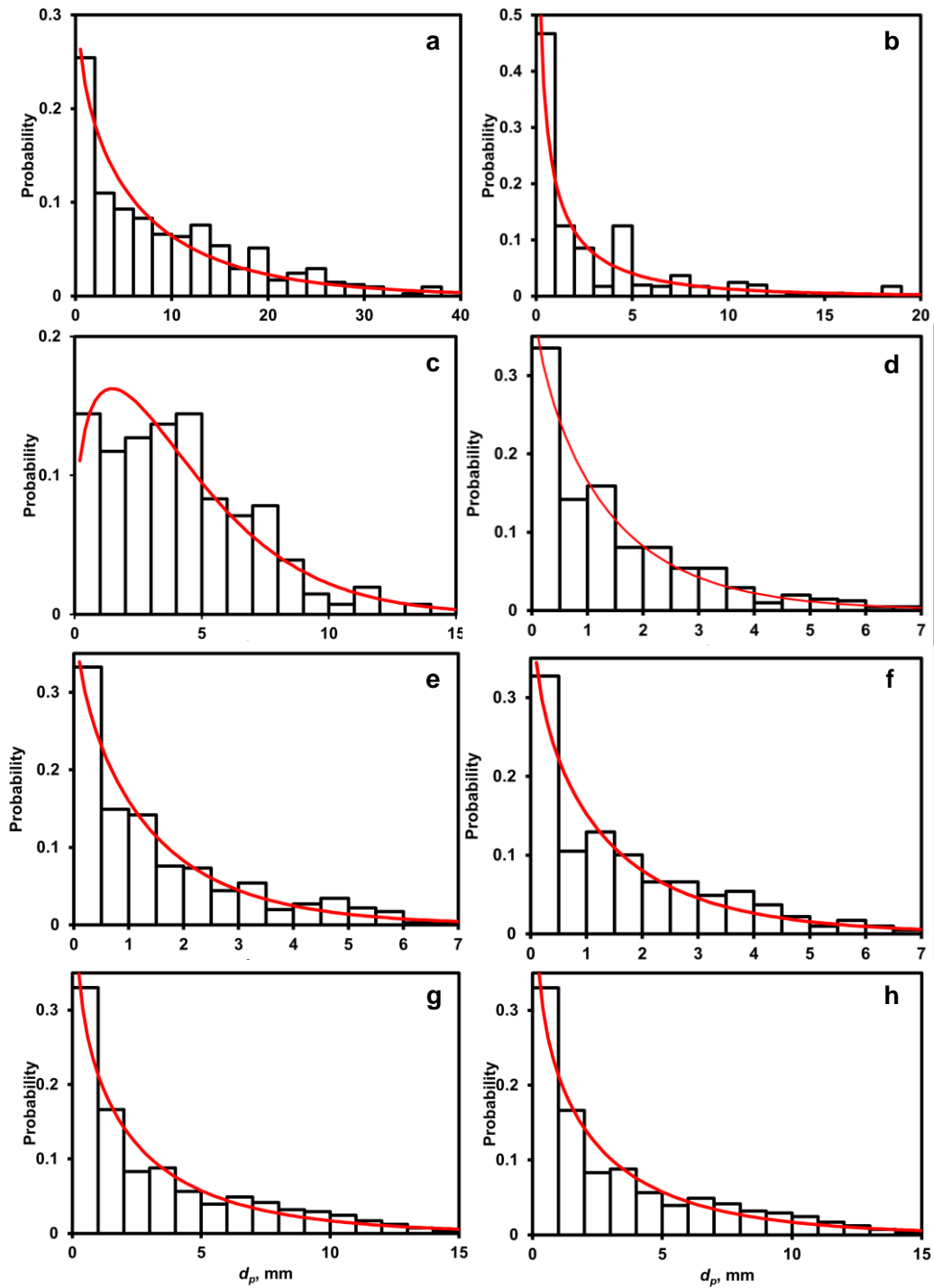
Figure III-B3. Histograms of particle size (*dp*) for cryogenic size reduction. (a), (b), ..(h) refer to Runs 1, 2, .., 8 of Table III-A1 in the Appendix A. Curves represent the fit of the two-parameter Weibull model (Eq. 1). Cryogenic treatment parameters are provided in Table III-A1.
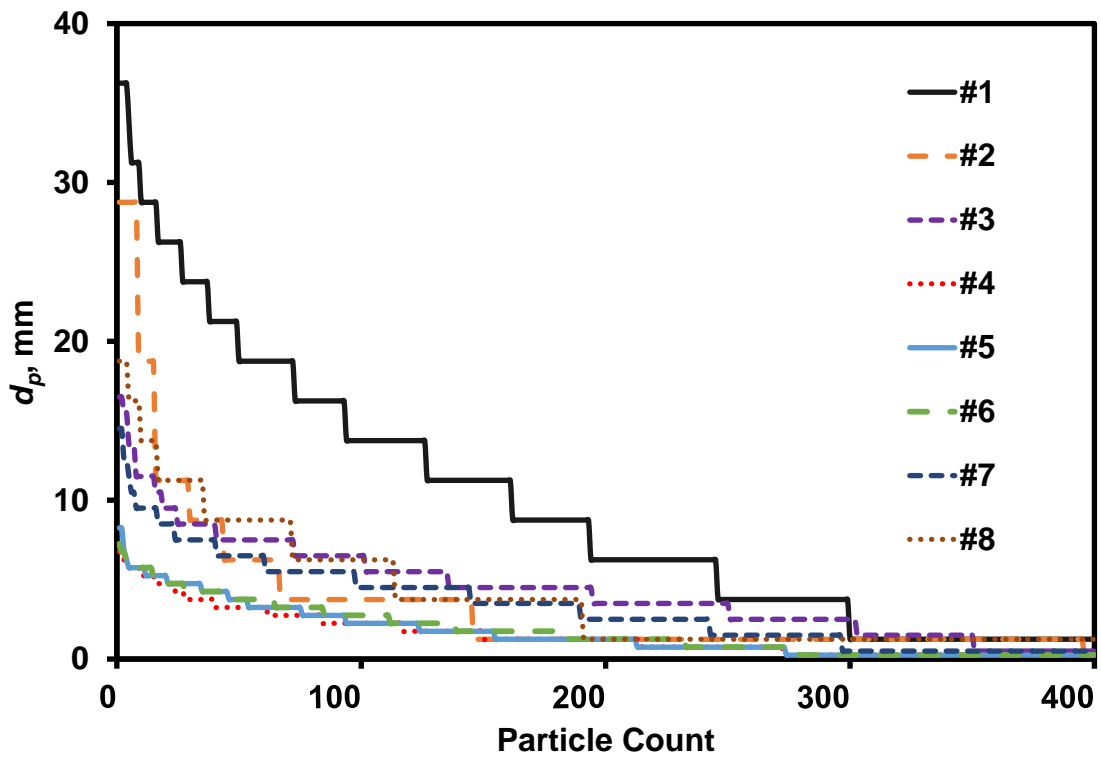
Figure III-B4. Particle count vs. d_p for PBAT treated by cryogenic size reduction. Run numbers (given in legend) correspond to run numbers given in Table III-A1.
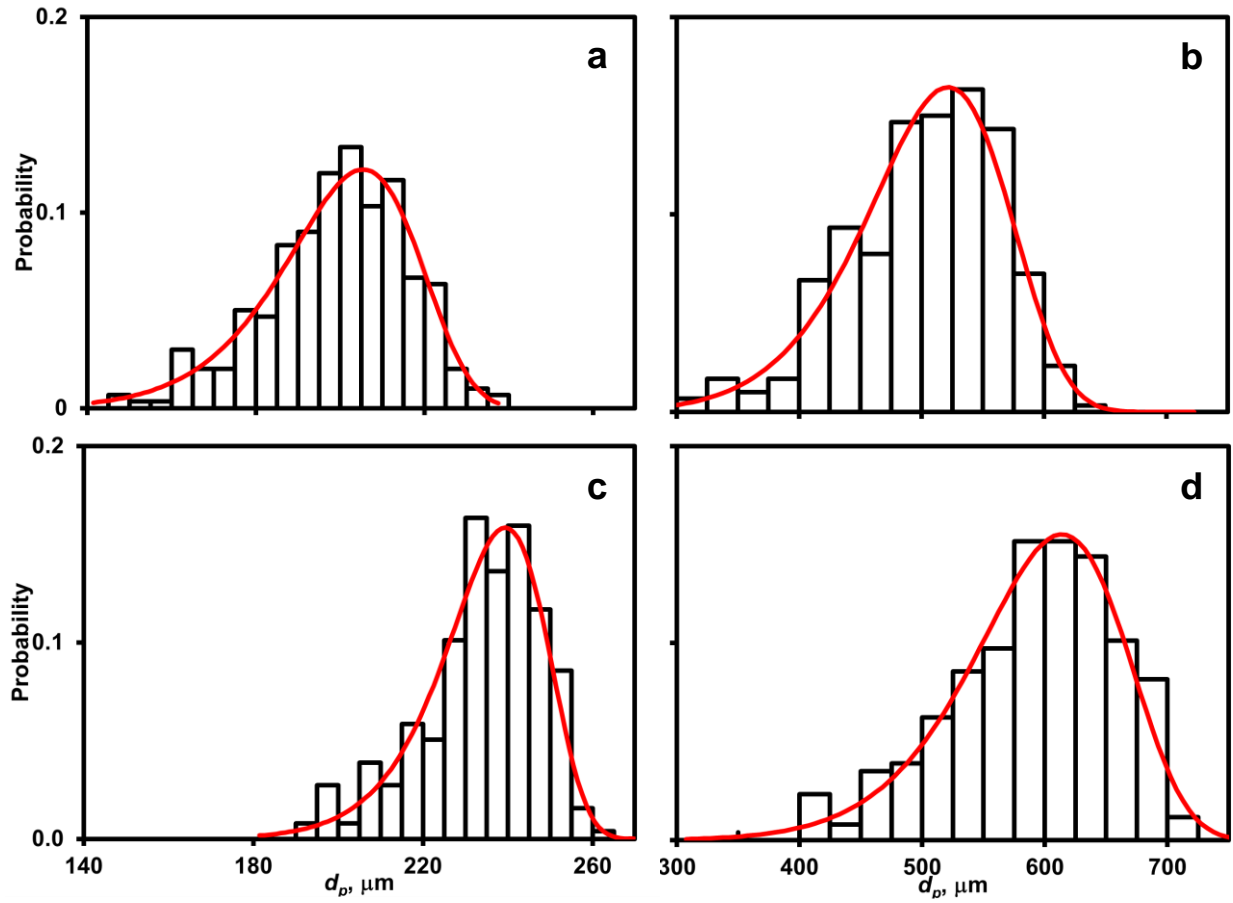
Figure III-B5. Particle size distributions of (a,b) PBAT and (c,d) LDPE of fractions received from (a,c) 250 µm and (b,d) 840 µm nominal sieve diameter, respectively, with superimposed two-parameter Weibull model fits, particles received from mechanical milling.
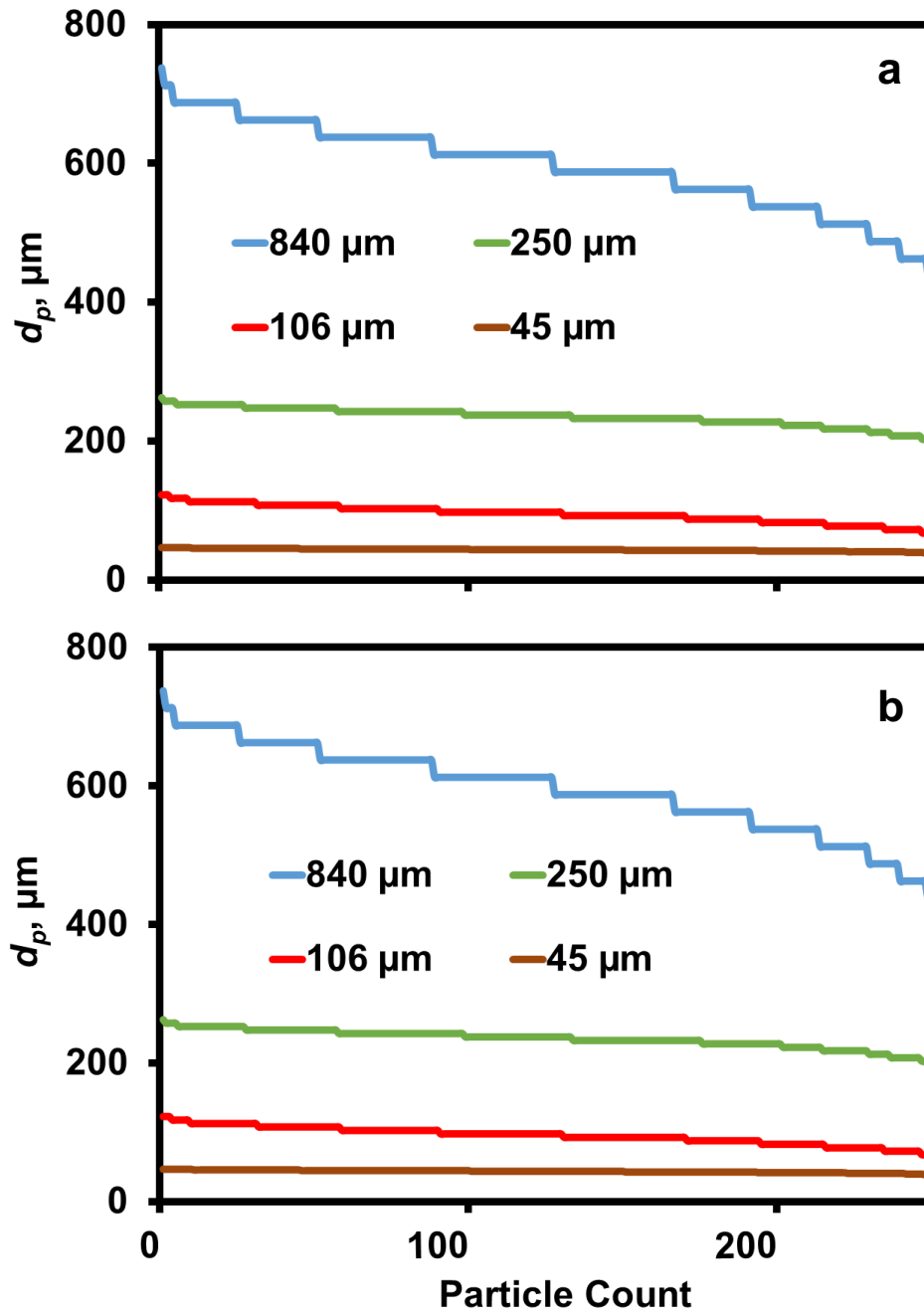
Figure III-B6. Particle count vs. d_p for (a) PBAT and (b) LDPE particle size diameters as a result of particle count of sieving fractions processed by mechanical milling.

Table III-B1. Particle size distributions of the cryogenic size reduction process for PBAT (an expansion of the data given in of the main paper)

Run #	d_p (nominal) [mm] [1]	d_p (minimum) [mm]	d_p (maximum) [mm]	d_p (upper 95%) [mm]	d_p (lower 95%) [mm]
1	9.22 ±4.25	0.21	36.71	10.04	8.38
2	3.33 ±2.15	0.03	29.53	3.84	2.81
3	4.21 ±1.53	0.14	16.76	4.51	3.91
4	1.46 ±0.71	0.04	6.96	1.6	1.33
5	1.58 ±0.80	0.06	8.16	1.74	1.43
6	1.68 ±0.81	0.04	7.26	1.84	1.52
7	3.22 ±1.38	0.08	14.3	3.49	2.96
8	3.64 ±1.99	0.09	19.99	4.03	3.25

[1] Error bars reflect standard deviation

Table III-B2. MP particle size distributions resulting from Wiley milling sieve fractionation of PBAT and LDPE (an expansion of the data given in Table III-A2).

Polymer	Nominal sieve size [μm]	d_p (mean) [μm]	d_p (minimum) [μm]	d_p (maximum) [μm]	d_p (upper 95%) [μm]	d_p (lower 95%) [μm]
PBAT	840	500.1 ± 32.5	283.9	631.7	507.5	492.7
	250	198.9 ± 8.8	141.4	238	200.9	197
	106	88.1 ± 6.3	52.8	118.8	89.5	86.7
	45	45.9 ± 1.2	37.7	51.4	46.2	45.9
LDPE	840	590.6 ± 34.2	347.5	731.4	599	582.2
	250	233.8 ± 7.1	193.5	260.2	235.5	232.1
	106	94.2 ± 6.8	44.8	122.4	95.8	92.5
	45	43.1 ± 1.0	35.8	46.8	43.4	42.9

Error bars reflect standard deviation

CHAPTER IV

ASSESSMENT OF CRYOGENIC PRETREATMENT FOR SIMULATING ENVIRONMENTAL WEATHERING IN THE FORMATION OF SURROGATE MICRO- AND NANOPLASTICS FROM AGRICULTURAL MULCH FILMS

A version of this chapter was submitted to the *Science of the Total Environment Journal* on 15th July 2022 and is currently under review.

Authors

A.F. Astner[a], D. G. Hayes[a,*], H. O'Neill[b], B.R. Evans[b], S.V. Pingali[b], V.S. Urban[b], S.M. Schaeffer[a], T.M Young[c]

[a]The University of Tennessee, Biosystems Engineering and Soil Science, 2506 E J. Chapman Dr, Knoxville, TN 37996, United States of America

[b]Oak Ridge National Laboratory, 1 Bethel Valley Road, Oak Ridge, TN 37831, United States of America

[c]The University of Tennessee, Center for Renewable Carbon, 2506 Jacob Dr, Knoxville, TN 37996, United States of America

Anton Astner's major contribution to this paper includes identifying the research objective, designing, and conducting the experimental tasks, processing, and interpreting the data, and drafting the paper.

Co-researchers contributions are listed as follows:

D. G. Hayes supported the experiments, writing, and data analysis and revised the paper.

H. O'Neill, B. R. Evans, S. V. Pingali, V. S. Urban helped in the experimental design and adjusting of experimental parameters

T. M. Young revised language and helped polishing the paper and provided the experimental design guidelines.

S.M. Schaeffer revised the document and provided information on the biodegradation analysis.

Abstract

Microplastics (MPs) and nanoplastics (NPs) from mulch films and other plastic materials employed in vegetable and small fruit production pose a major threat to agricultural ecosystems. For conducting controlled studies on MPs' and NPs' (MNPs') ecotoxicity to soil organisms and plants and fate and transport in soil, surrogate MNPs are required that mimic MNPs that form in agricultural fields. We have developed a procedure to prepare MPs from plastic films or pellets using mechanical milling and sieving, and conversion of the resultant MPs into NPs through wet grinding, both steps of which mimic the degradation and fragmentation of plastics in nature. The major goal of this study was to determine if cryogenic exposure of two biodegradable mulch films effectively mimics the embrittlement caused by environmental weathering in terms of the dimensional, thermal, chemical, and biodegradability properties of the formed MNPs. We found differences in size, surface charge, thermal and chemical properties, and biodegradability in soil between MNPs' prepared from cryogenically treated vs. environmentally weathered films, related to the photochemical reactions occurring in the environment that were not mimicked by cryogenic treatment, such as depolymerization and cross-link formation. We also investigated the size reduction process for NPs and found that the size distribution was bimodal, with populations centered at 50 nm and 150-300 nm, and as the size reduction process progressed, the former subpopulation's proportion increased. The biodegradability of MPs in soil was greater than for NPs, a counter-intuitive trend since greater surface area exposure for NPs would be expected to increase biodegradability. The result is associated with differences in surface and chemical properties and to minor components that are readily leached out during the formation of NPs. In summary, the use of weathered plastics as feedstock would likely produce MNPs that are more realistic than cryogenically treated unweathered films for use in experimental studies.

4.1 Introduction

The rapid growth of global commercial plastic production and the persistent mismanagement of plastic waste have resulted in an alarmingly high level of environmental pollution, emerging as a severe threat across various ecological systems, including terrestrial and marine biota. Over the past 70 years, the cumulative plastic production was an estimated 6300 million tons (Mt), with an

average annual growth rate of 5 % (Geyer *et al.*, 2017; Ritchie & Roser, 2018). Of that amount, around 4900 Mt (79 % of total plastic production) were discarded and accumulated in landfills and terrestrial environments (Geyer *et al.*, 2017; Jambeck *et al.*, 2015). Environmentally dispersed macro- and mesoplastic fragments of average particle size (or d_p, of >25 mm and <25 mm, respectively) undergo continuous degradation processes due to chemical reactions, sunlight exposure, rain, wind, mechanical abrasions (shear), and other environmental stressors (Hanvey *et al.*, 2017). As a result, the larger fragments undergo further size reduction and form micro-and nanoplastics (MPs, 1.0-5000 µm; NPs, <1000 nm, respectively) (Alimi *et al.*, 2018; Gigault *et al.*, 2018; Hartmann *et al.*, 2019; Redondo-Hasselerharm *et al.*, 2020). While larger terrestrial mesoplastic fragments can be easily retrieved and recycled, MPs and NPs (MNPs) persist in the environment (Strungaru *et al.*, 2019), for example, in marine sediments (Peng *et al.*, 2018), soil (Zhang & Liu, 2018), and rivers (Drummond *et al.*, 2020; Wang *et al.*, 2018), and even in remote areas of earth, such as in deep oceans (Woodall *et al.*, 2014) or alpine snow (Materić *et al.*, 2020).

The potential harm of MNPs to microorganisms, including microbiomes, and fish, in marine environments, has been reported. For example, lower reproduction, growth, and impact on microbial communities' biodiversity were found (Barría *et al.*, 2020; Lai *et al.*, 2021). Although MPs' contamination in terrestrial ecosystems is estimated to be 4-23-fold more prominent than in aquatic ecosystems (Alimi *et al.*, 2018; Horton *et al.*, 2017), research on the impact of MNPs in terrestrial ecosystems has received less attention. MPs have been detected in agricultural soils within the range of 50-500,000 items/kg (Lang *et al.*, 2022; Li *et al.*, 2023; Liu *et al.*, 2018; Park & Kim, 2022; Wang *et al.*, 2022; Wang *et al.*, 2022), 3-7 ppm (Steinmetz *et al.*, 2022; Xu *et al.*, 2022), or 50-300 kg/ha (Yang *et al.*, 2022). Currently, ecotoxicological effects of MNPs in soil are not well understood (Bläsing & Amelung, 2018). In addition, dispersed environmental MNPs are small enough to be ingested by many organisms, raising bioaccumulation and biomagnification concerns (Ma *et al.*, 2016). Therefore, environmental studies investigated the ecotoxicological impact of MPs on soil organisms such as earthworms (Wang *et al.*, 2021) and their gut (Rodriguez-Seijo *et al.*, 2017) , collembolans (hexapods) (Kim & An, 2020), and soil microorganisms (Bandopadhyay *et al.*, 2018). Also, interactions of MPs with terrestrial biota showed deleterious effects on the gut microbiome and plant growth (Büks *et al.*, 2020; Guo *et al.*, 2020; Li *et al.*, 2020; Pathan *et al.*, 2020; Wahl *et al.*, 2021; Wu *et al.*, 2020). In addition, vertical MP transport through

soil fauna within soil systems (Lwanga *et al.*, 2017; Rillig *et al.*, 2017) may pose a potential risk to groundwater contamination (Ren *et al.*, 2021).

Overall, dispersion of MNPs in agricultural soils is of particular concern due to their possible impact on soil health and the potential for entry into the food web (Iqbal *et al.*, 2020) through plants that may facilitate the uptake of NPs (Rillig *et al.*, 2018). Major sources of MNPs in agricultural soils are secondary plastics originating from plasticulture: mulch films, irrigation pipes, high tunnels, landscape fabric, silage film, and packaging (Katsumi *et al.*, 2020; Zhang *et al.*, 2020). Other secondary terrestrial MNPs sources may originate from fertilizers (Bi *et al.*, 2020; Fu *et al.*, 2018; Trinh *et al.*, 2015), sewage (Corradini *et al.*, 2019), irrigation water, and wind-carried debris (Bläsing & Amelung, 2018). Low-density polyethylene (LDPE) is currently the most used plastic mulch material in plasticulture because it is inexpensive, quickly processable, durable, and flexible (Menossi *et al.*, 2021). However, LDPE fragments are challenging to recover and are often not permitted by recyclers due to contamination with various substances, such as soil, water, and agrochemicals, particularly pesticides, insecticides, and herbicides. They can leach chemicals resulting from environmental weathering and the breakdown of polymers (Ramos *et al.*, 2015). Consequently, agricultural soils with a mulching history show elevated plastic particle concentrations (Huang *et al.*, 2020; Tian *et al.*, 2022). The higher MP concentrations impact soil microbial communities (Bandopadhyay *et al.*, 2018; Huang *et al.*, 2019; Wu *et al.*, 2022), and alter the physical and chemical soil properties (Liu *et al.*, 2014; Rong *et al.*, 2021; Steinmetz *et al.*, 2016; Wang *et al.*, 2020). As an alternative to LDPE mulches, biodegradable mulch films (BDMs) were developed that can mineralize in the field after plowing into the soil, thus eliminating film recovery and disposal (Kasirajan & Ngouajio, 2012; Menossi *et al.*, 2021). However, the biodegradability rate greatly varies based on the plastics' chemical composition and the extent of "agricultural weathering", the latter term referring to the environmental conditions they experience during their service life prior to disposal or incorporation into compost or soil, such as the intensity of ultraviolet radiation, ambient temperature, moisture, and other factors, which accelerate the depolymerization by cleavage of polymeric components. In particular, photodegradation (UV radiation) and hydrolysis are considered the most critical degradation and rate-limiting factor for environmental weathering of BDMs on the soil surface (Kasmuri *et al.*, 2022; Yang *et al.*, 2021). Furthermore, the loss of the plastics' mechanical properties results in polymeric embrittlement due

to weakening morphological regions and the availability of more low-molecular regions for subsequent microbial utilization (Chinaglia *et al.*, 2018; Hayes *et al.*, 2017). However, biodegradable mulches (BDMs) also form MNPs that will remain in the soil for several months, primarily if BDMs are used for multiple growing seasons over several years (Liao & Chen, 2021; Qin *et al.*, 2021).

Environmental studies investigating MPs and NPs require authentic (in nature occurring) agriculture polymer model materials. Due to analytical challenges, particularly the identification, and characterization of MPs and NPs, little knowledge about the life stages, formation, size reduction, and interaction of plastic fragments in agricultural soils is available (Zhang *et al.*, 2018). However, a recent study reported a detection method for NPs applied to soil samples involving a water extraction and mass spectrometry procedure (Wahl *et al.*, 2021). Furthermore, many of the recently published fundamental studies on the fate and transport of plastic particulates (Shaniv *et al.*, 2021; Zhu *et al.*, 2018) and cotransport of chemical contamination Chi *et al.* (2021) used idealized monodisperse polystyrene spheres as model material (Wahl *et al.*, 2021). However, fundamental studies about the MNPs' fate and transport, ecotoxicity, and chemical adsorption such as pesticides and plasticizers in environments require realistic plastic model systems. For environmental research, several processing techniques to form surrogate MPs were employed by cryogenic milling (Steinmetz *et al.*, 2020) to promote material embrittlement followed by or mechanical abrasion process (Seghers *et al.*, 2021), producing particle sizes > 200 μm. However, smaller MPs particle sizes (10–40 μm) of polystyrene were achieved by harsher processing conditions (Guo *et al.*, 2018). Moreover, Eitzen *et al.* (2019) achieved MPs sizes between 5-100 μm through milling and sieving steps. To form NPs, El Hadri *et al.* (2020) applied ball milling to polystyrene resulting in particles between 80-900 nm. Tanaka *et al.* (2021) employed a solvent-based precipitation method to generate NPs from polyethylene, polypropylene, polyvinyl chloride, and polystyrene, resulting in NPs sizes between ~180-460 nm aims for prospective environmental toxicity tests. Wet grinding is reported to better mimic environmental degradation of plastics than milling resulting from low-energy processes (Kefer *et al.*, 2022; Ravishankar *et al.*, 2018), as would occur for plastic fragments residing in soil. Wet grinding is effective for inducing size reduction to produce nanoparticles (Gillibert *et al.*, 2022; Sharma *et al.*, 2022).

Astner *et al.* (2019) developed a procedure to form MPs through cryogenic milling and NPs by a wet grinding procedure applied to agricultural mulch film feedstocks such as the biodegradable polymer polybutyrate adipate-co-terephthalate (PBAT) and LDPE. MP fragments produced by milling consisted of irregular shaped film fragments, similar to the fragments we retrieved from a field containing tilled-in BDMs after several months elapsed (Hayes *et al.*, 2019). Other studies reported similar geometry for mulch film fragments retrieved from soil (Liao & Chen, 2021; Park & Kim, 2022; Wang *et al.*, 2022).

In a follow-up study, Astner *et al.* (2020) employed representative PBAT-NPs (50 nm -1000 nm) in combination with vermiculite as artificial soil dispersed in an H_2O/D_2O water slurry to probe the polymer-soil interactions via small-angle neutron scattering techniques. However, it is unclear whether cryogenic treatment, employed to induce embrittlement, effectively simulates the embrittlement of plastics that occurs during environmental weathering, mainly through exposure to solar radiation. The detailed methodology of this approach is provided in (Astner *et al.*, 2022).

Moreover, for the employment of authentical model MNPs in environmental studies, deviations in shape, chemical, mechanical, and electrostatic (surface charge) properties may result in biased study results. Therefore, the main goal of this paper is to assess the performance of cryogenic treatment in mimicking the impact of agricultural weathering on the formation of MNPs from agricultural mulch films that can serve as MNP surrogates in environmental studies. The study focuses on two BDMs, one composed of polybutylene adipate terephthalate (PBAT) and the other of polylactic acid and polyhydroxyalkanoate (PLA/PHA). For MPs, geometric particle characteristics, such as particle size, polydispersity (PD), roundness, and length-to-width ratio, were characterized through image analysis. For NPs, features such as particle diameter, PD, and zeta potential (ZP) were determined, which are essential for studying environmental and biological systems' fate, behavior, and toxicity.

Furthermore, characterization of MNPs' chemical and thermal properties was performed. The second objective addresses a major research gap, a fundamental understanding of the gradual transformation from MPs into NPs in soil through low-impact shear events caused by MP-soil collisions. To address this research gap, a time series of wet-grinding runs was employed to mimic the gradual embrittlement caused by environmental weathering and transition from MPs into NPs.

This study characterizes the resultant MNPs in size, size distribution, and physicochemical properties.

4.2 Experimental Section

4.2.1 Mulch films used in experiments

Two black-colored commercially available BDMs were employed in this study. The first film, BioAgri, is a starch- polybutylene co-adipate co-terephthalate (PBAT) blend (N-type Mater-Bi® grade EF04P) polymer film, manufactured by BioBag Americas, Inc., Dunedin, FL, USA, which will be referred to as "PBAT" in this paper. The initial thickness and surface density of the PBAT film were 29 ±1.2 μm and 22.81 ±0.411 g m^{-2}, respectively. The second BDM, an experimental PLA/PHA (polylactic acid/ polyhydroxyalkanoate) film prepared from a blend of 70.9 wt% PLA and 29.1 wt% PHA, was prepared for us by Yield10 Bioscience, Woburn, MA, USA. The film's initial thickness and surface density were 37 ±1.4 μm and 27.72 ±0.379 g m^{-2}. A previous study provides more detailed information on the mulches regarding chemical composition and other mechanical and physical properties (Hayes *et al.*, 2017). PLA/PHA and PBAT mulch film rolls (1.22 m wide) were obtained in 2015 and 2017, respectively, and stored indoors in sealed moisture-resistant bags (model PM-012, Benis Co, Neenah, WI, USA) at 22 °C and 62 ±8% relative humidity. All solvents employed in the chemical analyses were high-performance liquid chromatography (HPLC) grade or higher and were purchased from Fisher Scientific (Pittsburgh, PA, USA). In addition, microcrystalline cellulose powder (d_P=50 μm, >99 % pure) was purchased from Thermo Fisher Scientific Inc., Waltham, MA, USA, and employed as a positive control in the biodegradation study.

4.3 Methods

As described below, the procedure involves preparing MNPs from environmentally weathered and untreated BDMs, as outlined in Figure IV-C1. A detailed description of the methodology is available in Astner *et al.* (2022).

4.3.1 Pretreatment through environmental weathering of plastic mulches

Environmental (field) weathering of the two BDMs took place during field trials for green pepper production from June-September 2017 (137 d) in Knoxville, TN, USA (Ghimire *et al.*, 2018). Further detail is provided in the Appendix IV-D.

4.3.2 Pretreatment through cryogenic cooling

The cryogenic cooling process mimicked environmental weathering by promoting embrittlement when applied to unweathered BDM films. First, optimal cryogenic processing conditions were employed for untreated films for maximum size reduction, as described in a previous publication (Astner *et al.*, 2019). In brief, precut BDM samples (1 g) were submerged in 800 mL deionized water (5 min), followed by soaking in 200 mL liquid nitrogen (10 min). Next, a slurry of the frozen fragments in water was introduced into an Osterizer type blender (10 min; 1.0×10^{-3} min^{-1}), and processed materials were sieved, air-dried under a vacuum, followed by mechanical milling.

4.3.3 Size reduction to form MPs - mechanical milling

Mechanical milling was applied to cryogenically treated ('CRYO') and environmentally weathered ("W") BDM samples using a rotary Wiley Mini-Mill (Model 3383-L10, Arthur H. Thomas Co., Philadelphia, PA, USA). During the milling procedure, the particles were passed through sieves of sizes 840 μm (20 mesh) for the first pass and 250 μm (60 mesh) for the second pass. The particles were recovered from the mill and air-dried for 24 h at room temperature (22±1°C). Afterward, the smaller fraction underwent a sieving procedure using a 106 μm sieve. The particles that did not pass through the mesh were reintroduced to the milling process up to three times until the particles were small enough to pass through the 106 μm sieve. The 45 μm fraction was used for gravimetrical determination only since the yield of this fraction was too low for the subsequent wet grinding process (discussed in Appendix-IV-D). For uniform particle size extraction from the sieve fractions, an Eppendorf thermomixer 5350 (Hamburg, Germany) was used at 400 rpm for 30 min. A gravimetric method with three replicate experiments was used to determine the particle % recovery for each PBAT and PLA/PHA feedstocks sieving fraction.

4.3.4 MPs size reduction for nanoplastics (NPs) through mechanical grinding

Transformation of MPs into NPs occurred through a stepwise wet grinding process, resulting in 10 individual fractions. Mechanically milled MPs (106 um) were soaked in deionized water (at a final concentration of 1 wt%) and magnetically stirred in a 1000 mL beaker at 400 min^{-1} for 24 h. NPs were formed from the aqueous MP slurry using a super mass collider (MKCA6-5JR, Masuko Sangyo Co., Ltd., Tokyo, Japan) at a rotor speed of 1500 rpm and following 60 passes (slurry collection and reintroduction). After six subsequent passes, intermittent sampling was performed to verify the gradual particle breakdown, which resulted in 10 individual sub-sample fractions. Efficient grinding was achieved with a clearance gauge of −1.0, corresponding to a negative 0.10 μm shift from the zero position, reflecting a slight contact between the grindstones. Plastic particle-water slurries were present between the two stone disks during the runtime to avoid friction between the grinding stones.

4.3.5 Dimensional and chemical analyses of MNPs

Particle size, particle size distribution (PSD), and analyses of MPs were achieved through ImageJ analysis (Schindelin *et al.*, 2012) of stereomicrographs (Figures IV-D1 to IV-D6 and Table IV-D1) of the Appendix D and discussion therein). NPs were analyzed for size and PSD by dynamic light scattering (DLS). Samples consisted of aliquots taken from the middle vertical layer of a 0.5 wt% aqueous slurry of NPs after allowing larger particles to settle for 5.0 h at 25 °C. The same samples were also analyzed for ZP. DLS and ZP measurements were replicated thrice for a given sample. Thermal analyses consisted of thermogravimetric analysis (TGA) to evaluate thermal stability and differential scanning calorimetry (DSC) to measure the degree of crystallinity for the major polymeric components of the two BDMs. Chemical analyses assessed the chemical bonding properties through Fourier transformation infrared (FTIR) spectroscopy and compositional analysis via nuclear magnetic resonance (NMR) spectroscopies. The instrumentation and procedures for dimensional, thermal, and chemical analyses described in the Supplementary Materials are nearly identical to those we employed previously (Astner *et al.*, 2019).

4.3.6 Biodegradability comparison between MPs and NPs

Biodegradability testing of cryogenically treated and weathered MPs, NPs, and microcrystalline cellulose in compost-enriched soil was performed following the standardized test method, ASTM 5988-12 (ASTM International, 2012) through measurement of CO_2 evolution. Each treatment was performed in triplicate. A detailed procedure is provided in Appendix D. Statistical assessment identified biodegradation differences between polymers, treatments, and particle sizes, detected by analysis of variance (ANOVA) using JMP (Statistical Analysis System Version 15.2.0 for Mac; SAS Institute, Cary, NC, USA). Mean differences comparison employed the Tukey honestly significant difference (HSD) at a significance level of *α=0.05*. The Wilcoxon group homogeneity test evaluated the nonparametric comparison of the live curves to determine statistical differences during the experiment duration of 154 days. Furthermore, data fitting (Specialized Modeling Platform, JMP) was performed on the CO_2 evolution profiles to describe the parameter variation over time (cumulative weight loss profile in time) corresponding to the biodegradation process expressed by discrete, exponential distributed data points. Accordingly, the CO_2 datasets were fitted through *Sigmoid (Logistic, Gompertz, and Weibull Growth)* and *Exponential Growth and Decay (Bi-exponential)* curves. The best model fits were detected by the corrected Akaike's and Bayesian information criteria (AIC and BIC, respectively) as represented by their lowest output values. Based on the best model fit, a simulation procedure using a prediction profiler estimated the complete mineralization time as a function of polymer type, particle size, and pretreatment (8 biodegradation profiles) (Table IV-D8).

The carbon content of the plastic films was determined through elemental analysis, as reported previously by Hayes et al. (2017): PBAT unweathered = 51 wt%; PBAT-W = 48% W; PLA/PHA unweathered = 47%, and PLA/PHA-W = 44%.

4.4 RESULTS AND DISCUSSION

4.4.1 Effect of film pretreatment and mass recoveries on MPs

The mechanical milling process employed for PBAT and PLA/PHA films, as described in Figure IV-C1 resulted in the formation of MPs. The mass recoveries of MP sieve fractions (251-840 μm, 107-250 μm, 46-106 μm, and ≤ 45 μm) are depicted in Figure IV-D7. Sieve fractions will be referred to by the maximum particle size, which corresponds to the nominal size of the sieve.

The mass recoveries of the 840 μm and 45 μm PBAT fractions, 79-86 wt% and 1 wt%, respectively, are consistent with the results of our previous study (Astner *et al.*, 2019) which evaluated processing and sieving only of CRYO-PBAT and LDPE materials. However, the processing conditions involved two milling passes (reintroduction of received materials) for the previous study, and the current study employed three passes to improve the size reduction effect. Lower mass recoveries of the 250 μm sieve fraction (by 41-50%) were observed for PBAT compared to PLA/PHA for CRYO- and W-films. The mass recovery of the 106 μm sieve fraction, 7-8%, was nearly independent of polymeric type and pretreatment. The mass recovery for the 45 μm size fraction was slightly higher for PLA/PHA than for PBAT. Overall, environmental weathering was slightly more effective than cryogenic treatment in forming larger amounts of smaller sieve fractions by 2 wt% (Figure IV-D7 and Figure IV-D8). The higher recovery of MPs observed for PLA/PHA may reflect softer and more flexible PLA/PHA particles that are more prone to pass through the sieves than PBAT particles. Due to the low recovery of MPs in the 45 μm sieving fraction, in subsequent experiments described below, the 45 μm sieve was removed from the cascade of sieves, i.e., the smallest sieve fraction was 106 μm.

4.4.2 Effect of film pretreatment on the particle size distribution of MPs

Differences in PSD for sieve fractions of CRYO- and W-pretreated PBAT and PLA/PHA for MPs belonging to the 106 μm and 250 μm sieving fractions are depicted by histograms of the number density frequency (NDF), referring to the accumulated number of particles found within a specific particle size range, presented in Figure IV-C2. Details about particle dimensions, counts, and shape parameters for sieving analysis of sieving fractions 106 μm and 250 μm are described in Table IV-C1. For the 106 μm fraction of CRYO-PBAT, the size distribution model fit followed a symmetrical normal-shaped distribution function, resulting in an average d_p of 55 ±10 μm (Figure IV-C2a). The highest NDF of 22 % was observed between 60 and 70 μm. In contrast, the 106 μm fraction of the W-PBAT dataset resulted in a significantly smaller average particle size of 24 ±8 μm at an NDF of 44% between the 10-20 μm range (p<0.0001). The d_p dataset for the latter sample is represented by a right-skewed lognormal PSD (Figure IV-C2b). Similar trends as described above for the PSD of the 106 μm sieve fraction were also observed for the 250 μm sieve fraction (Table IV-C1 and Figure IV-D3). These results suggest that milling more severely

105

impacted the size reduction of MP for W- than CRYO pretreatment. In addition, smaller values of d_p were observed for the 106 μm CRYO-PBAT sieving fraction compared to our previous study (88.1±6.3 μm), which likely resulted from employing three milling passes for the current study versus two passes for the previous study (Astner *et al.*, 2019).

In contrast to the observations described above, the 106 μm sieving fraction of CRYO- and W-PLA/PHA did not differ significantly in average d_p values (only 1.8 μm smaller for CRYO-) but did produce different PSDs (Figure IV-C2c,d). In particular, the PSD of CRYO-PLA/PHA followed a Weibull distribution with the highest NDF (16%) corresponding to 10-20 μm, while a lognormal distribution best described W-PLA/PHA with the highest NDF at 44%, occurring between 1 and 10 μm, and slightly lower NDFs were observed in the larger size fractions within 20-60 μm. The PSD for the 250 μm CRYO- and W-PLA/PHA sieving fractions were characterized by the Weibull PSD model, with the highest NDF occurring at 1-25 μm (NDF of 46%) and 100-125 μm (NDF of 17%), respectively (Figure IV-D4). Moreover, for 250 μm MPs derived from PLA/PHA, CRYO- pretreatment produced smaller MPs than W-, by 39 μm (Table IV-D1). The latter observation, different in trend from that observed for PBAT, may be explained by the formation of chemical bonds between PLA, PHA, and the filler contained in the mulch film (CaCO$_3$) via photodegradation reactions catalyzed by sunlight (Anunciado *et al.*, 2021; Hayes *et al.*, 2017).

Geometrical parameters, particularly the aspect ratio (AR) and circularity, followed consistent and expected trends between pretreatments and sieve fractions for PBAT-derived MPs: as the average d_p decreased, AR decreased, and the circularity increased (Tables IV-C1 and D1). In contrast, for PLA/PHA-derived MPs, AR was lower, and circularity was higher for the W-treatment, despite d_p of the 250 μm sieving fraction being slightly higher for W- than for CRYO-pretreatment, and d_p for the 106 μm sieve fraction being similar between pretreatments (Table IV-C1). Most likely, the selective cleavage of physicochemical bonds in morphological regions, which possess a low cross-linking density, during mechanical milling of W-PLA/PHA MPs served as the underlying cause.

4.4.3 Effect of wet grinding severity on NP formation

For the formation of NPs through wet grinding, the 106 μm sieving fraction of MPs underwent a decrease of average d_p of 1-2 orders of magnitude after only 6 passes, according to DLS analysis (Figure IV-C3a and Table IV-C2). Depending on the severity (number of passes) and material selection, wet grinding resulted in uni-, bi-, or trimodal distributions, represented by (I) (< 100 nm), (II) (~150-300 nm), and (III) (> 300 nm). As observed visually during the experiments, the exposure time of the plastic particles to continuous mechanical impact during wet grinding (min) is approximately equal to the number of passes divided by 2.

The mechanical impact of 6 passes of wet grinding for PBAT-MPs produced NPs with an average size of 193 nm, with d_p ranging between ~80 to ~925 nm for both pretreatments (Figure IV-C3a and Table IV-C2). Both CRYO- and W-PBAT resulted in a unimodal PSD (II), suggesting a consistent and homogenous transformation from MPs to NPs peaking at 23% NDF (W-PBAT) and 16% NDF (CRYO-PBAT) (Figure IV-C3a,c and Table IV-C2). In addition, a small PSD sub-population (III) occurred at 712 nm for W-PBAT NPs (NDF = 1%). As discussed in the Supplementary Materials, the PSD for major subpopulations of NPs formed from both mulch films subjected to both embrittlement pretreatments were well described by the two-parameter Weibull distribution, similar to our previous study (Astner *et al.*, 2019). NPs of PBAT formed via 30 passes of wet grinding resulted in a bimodal size distribution, where a new subpopulation of smaller NPs, (I), formed, with the average d_p of (I) being 68 nm and 91 nm for CRYO- and W- pretreatments, respectively, whereas the subpopulation (II) was retained (average d_p of 140-160 nm, smaller than the average size achieved for 6 passes; Table IV-C2). However, the two pretreatments differed in their relative proportions of (I) and (II), with subpopulation (I) being ~2-fold higher in NDF than (II) for W- and smaller for CRYOs- (Figure IV-C3a, Table IV-C2), suggesting a higher rate of material breakdown caused by the high embrittlement of environmentally weathered plastic films. A further increase of passes to 60 led to a further decrease of d_p for both pretreatments. Processing of CRYO-PBAT through 60 passes resulted in a bimodal PSD and a decrease of d_p for subpopulations (I) and (II) (by~50 nm and ~110 nm, respectively), while for W-PBAT, the majority of NPs belonged to subpopulation (I), centered at 90 nm and a small subpopulation at ~160 nm (II). The results indicate that a higher severity (number of passes) applied to CRYO-

PBAT resulted in multimodal distributions (Figure IV-C3a, c), whereas W-PBAT resulted in more consistent particle shapes reflected by unimodal size distributions (Figure IV-C3b, d).

The effect of pretreatment on the size reduction of PLA/PHA-derived NPs differed significantly from that observed for PBAT-derived NPs. The initial 6 passes of wet-grinding applied to CRYO-PLA/PHA MPs resulted in a bimodal distribution with d_p ranging between 90 nm and 825 nm (Figure IV-C3b).

The smaller sub-population (III) for CRYO-PLA/PHA indicated d_p values of ~530 nm (NDF of 2.27%), whereas the larger subpopulation (II) possessed an average d_p of 142 nm (NDF of 20%; Table IV-C2). In contrast, wet grinding treatment of W-PLA/PHA MP using 6 passes produced NPs of a uniform PSD centered at 825 nm, (III) (NDF of 18%), reflecting a significantly lower extent of size reduction compared to CRYO- pretreatment. An increase in the number of passes from 6 to 30 applied to CRYO-PLA/PHA resulted in the formation of new subpopulations of small-sized NPs at ~70 nm (I; NDF of 16%) and larger NPs at 164 nm [(II); NDF of 10%] (Figure IV-C3b). In contrast, the PSD for W-PLA/PHA NPs treated with 30 passes returned a unimodal PSD (III) with only a relatively small decrease of d_p observed compared to 6 passes (712 nm; NDF of 33%) (Figure IV-C3d). A further increase in the number of passes to 60 further decreased the size of CRYO-PLA/PHA NPs, shifting the average d_p of subpopulation (II) from 164 nm to 106 nm (NDF of 23%). Furthermore, a decrease in subpopulation (III) and a shift of the subpopulation's average d_p to 1000 nm (NDF of 0.5%) and an increase in the relative size of subpopulation (I) (Figure IV-C3b). The increase of wet grinding passes to 60 for W-PLA/PHA led to a modest decrease in size, with a new, smaller subpopulation forming, appearing as a shoulder in the PSD at 459 nm (Figure IV-C3d and Table IV-C2). This observation is remarkable since CRYO-PLA/PHA NPs underwent a 5.4-fold greater extent of size reduction than W-PLA/PHA NPs when increasing the number of passes from 30 to 60 (Table IV-C2). Although the larger size of the original MPs (of sieving fraction 106 μm) for environmentally weathered MPs (d_p of 48 μm and 25 μm for W- and CRYO-PLA/PHA MPs, respectively) is an underlying factor for this trend, this remarkable finding suggests that weathering resulted in NPs that were more resistant to mechanical impact. This trend may be attributed to crosslinking of the latter biopolymer when exposed to environmental weathering, as discussed above (Anunciado *et al.*, 2021; Hayes *et al.*, 2017). Overall, even mild severity (after 6 passes) applied to MPs through wet grinding resulted

in quick formation of NPs for both pretreatments, such as CRYO and W. However, the breakdown of NPs derived from weathered films occurred more uniformly, represented primarily monodisperse PSD than the CRYO, which resulted mainly in multimodal PSD. For PBAT materials, increased wet-grinding severity (number of passes) resulted in a more significant extent of size reduction and was even further enhanced by weathering. On the other hand, the opposite trend was observed for PLA/PHA materials since weathering induced cross-link formation and resulted in more resistant material against mechanical impact (Figure IV-D9).

4.4.4 Effect of wet-grinding severity on NP surface charge

The Zeta potential (ZP) of CRYO and W-NPs was evaluated as a function of surface area for PBAT and PLA/PHA NPs. The results show for all four treatments that higher severity (i.e., a greater number of passes) led to higher surface area (due to the decrease of d_p, Figure IV-C3) and magnitude of negative surface charge (Figure IV-C4). The high negative ZP values, particularly for NPs formed using a high number of passes, confer stability to the particles in solution, indicating that the NPs may remain dispersed in water for a long time. A nearly linear relationship was observed between ZP and surface area was observed for all treatments, with the linear trends extrapolating to the origin with a decrease of surface area (Figure IV-C4). The higher slopes, hence greater ZP per unit surface area, occurred for the NPs derived from weathered compared to cryogenically treated films and for PBAT compared to PLA/PHA. Similarly, while cryogenically treated films resulted in ZP values between -2 and -14 mV, ZP values for W-treated films were between -11 and -16 mV. Weathered films resulted in ~6-fold lower surface area values due to their lower overall concentrations in the aqueous slurries (Table IV-D3).

Moreover, we observed that a significantly larger fraction of W-NPs precipitated out of solution during the sample preparation compared to CRYO-NPs. The larger particle size observed for W- compared to CRYO-PLA/PHA (Table IV-C 2) also contributed to the difference in surface area. The higher ZP per surface area for PBAT compared to PLA/PHA is an inherent difference in property between the two polymers, indicating that the former is more hydrophilic than the latter polymer. In summary, the cryogenic treatment produced NPs that were significantly lower surface charges than weathered films. Moreover, the colloidal behavior of NPs prepared from cryogenically treated and weathered films will differ, affecting the fate and transport studies of

NPs in aqueous environments.Effect of film pretreatment on the thermal and chemical properties of MNPs

Thermal and chemical analyses were carried out to explore molecular-level changes for biopolymeric components resulting from size reduction to MP and further to NP for unweathered films after CRYO treatment and W-films for both PBAT and PLA/PHA. The goals are to determine if the size reduction processes induced property changes between initial films and corresponding MPs and NPs and if the cryogenic treatment was effective for mimicking films' environmental weathering in terms of MNP properties. MP samples represent the 106 μm fraction after milling and sieve fractionation, whereas the NP samples were formed via 60 wet grinding passes.

4.4.5 Changes in thermal properties (TGA and DSC analyses)

TGA was employed to determine the thermal stability of the four MP and NP fractions described in the previous paragraph. TGA and DTG thermograms are depicted in Figures IV-C5 and D11, respectively. The TGA curves represent the thermal sample decomposition as a function of temperature. The remaining mass after the 600 °C represents minor components of the films, such as fillers, binders, and gels (Anunciado *et al.*, 2021; Hayes *et al.*, 2017). The absence of weight loss below 200 °C evidenced that neither MPs nor NPs of either mulch film contained a significant amount of water or volatiles.

The first and second heating stages for MNPs derived from PBAT films, between 304-323 °C and 377-407 °C, reflect starch and PBAT, respectively. CRYO- and mechanical milling of the PBAT films led to only minor changes in the thermograms for the PBAT heating stage, while the DTG heating stage for starch was greatly decreased for NPs, similar to our previous (Astner *et al.*, 2019). Similar trends were observed for the size reduction of W-PBAT, except for more profound changes for the PBAT heating stage: a temperature shift from 398 °C to 382 °C upon formation of MPs and an increase of temperature to 392 °C for NPs, suggesting that milling reduced the thermostability of PBAT while wet grinding increased thermostability (Figure IV-C5b). As described below, these trends reflect that milling promoted hydrolysis of ester bonds, leading to depolymerization, and wet grinding induced the leaching out of lower-molecular weight oligomers from the NPs.

For PLA/PHA, the two major heating stages, observed between 262-274 °C and 306-318 °C, represent PHA and PLA, respectively. Both heating stages were broader for CRYO-MPs compared to those of the initial film, particularly for PLA, while heating stages were further broadened for NPs, and the PLA heating stage shifted to lower temperature, from 320 °C to 296 °C (Figure IV-C5c). Heating stages for W-PLA/PHA were also broader compared to those for the original weathered film, and the decomposition temperature for PLA was significantly lower (by 25°C). The weight % remaining at 600 °C (%W600) represents high-molecular-weight substances present in the film and MNPs, such as plasticizers, processing aids, inorganic fillers, adsorbed soil particles that were not removed during the cleaning procedure (for weathered films), and gels that result from cross-link formation via photodegradable or free radical reactions. For both CRYO- and W-PBAT and PLA films, (%W600) differed only slightly between size reduction treatments for a given film, within 5% (Figure IV-D11 and Table IV-D4). However, weathering resulted in higher %W600-values for PBAT by 80% for MPs and 60% for NPs, and PLA/PHA, 44% higher for MPs and 40% for NPs (Table IV-D4), reflecting increased gel formation resulting from agricultural weathering, as observed by us previously (Anunciado *et al.*, 2021).

The changes in the thermostability of polymers observed through TGA analysis may result from molecular weight or crystallinity changes. Therefore, we also examined the crystallinity of the major polymeric components, PBAT and PLA, via DSC analysis to differentiate between the two underlying factors. We found for both weathered and unweathered films that the crystallinity did not change appreciably upon size reduction to MPs and NPs. Therefore, cryogenic treatment did not change the crystallinity, nor did it fully mimic the change of crystallinity of PBAT observed for weathered films, with W-PBAT film and MNPs having a higher crystallinity than the unweathered PBAT film, and weathered PLA/PHA mulch film and CRYO-MNPs having slightly lower crystallinity for PLA compared to unweathered PLA/PHA film or CRYO-MNPs (further discussed in the Supplementary Materials; Table IV-D5). Therefore, the observed changes in thermostability reflect changes in the degree of polymerization. We did not see any significant changes in melting point temperature for PBAT or PLA due to size reduction except for the decrease of melting temperature for agriculturally weathered PBAT due to mechanical milling (Table IV-D5).

4.4.6 Changes in chemical bonding (FTIR analysis)

Changes in the chemistry of surface functional groups for BDM polymeric components upon size reduction were evaluated through FTIR analysis. The FTIR technique evaluates spectral changes of functional groups on the film surface caused by the relative extent of hydrolysis and photodegradation reactions specifically for ester linkages. The processed FTIR spectra of PBAT and PLA/PHA representing the initial unweathered and weathered films and MPs and NPs derived from them are shown in Figure IV-C6, and notable band assignments are listed in Table IV-D6 (Hayes *et al.*, 2017).

Spectra for CRYO-PBAT MPs and NPs differed from the spectrum for the untreated film: lower intensities for the C=O stretching region between 1750-1650 cm^{-1} (peak value 1710 cm^{-1}) and higher intensity for the hydroxyl stretching band (3400 - 3200 cm^{-1}), C-O stretching band (1060 - 970 cm^{-1}), representing cleavage of ester bonds via hydrolysis due to cryogenic treatment and wet grinding (Figure IV-C6a and Figure IV-D12) (Hayes *et al.*, 2017; Sintim *et al.*, 2020).

The extent of hydrolysis was slightly higher for CRYO-PBAT NPs compared to MPs. For W-PBAT, size reduction led to only minor spectral changes, with the extent of hydrolysis being slightly higher for MPs; but, one should note that the environmental weathering induced significant ester bond cleavage compared to the untreated film, thereby resulting in smaller changes during size reduction (Hayes *et al.*, 2017). The one exception where the spectral change differed significantly was the disappearance of the spectral band at 1002 cm^{-1}, which is attributable to the C=C out-of-plane bending for PBAT resulting from photodegradation (Hayes *et al.*, 2017; Kijchavengkul *et al.*, 2010). The absorbance of the latter band decreased majorly for size reduction to MPs, suggesting the C=C functional groups of the surface are easily removed by milling. FTIR spectra comparing cryogenic and environmental weathering pretreatments for MPs and NPs are similar, except that the latter pretreatment induced a greater extent of hydrolysis for both MPs and NPs (e.g., reduced COO stretching and increased CO stretching; Figure IV-C6 a,b). This trend is consistent with the lower thermostability for W-MPs and NPs compared to their CRYO-treated counterparts, as observed via TGA (Figures IV-C5a,b).

For the size reduction progression of unweathered PLA/PHA (film →CRYO-MPs → CRYO-NPs), the absorbance values of the C-O stretching (1180 – 1082 cm^{-1}) and –OH bending (1076–1000 cm^{-1}) regions increased, and the absorbance of the C=O stretching region (1800–1700 cm^{-1})

decreased, all of which reflect hydrolysis of ester bonds due to milling and wet grinding. In addition, the latter region became narrow for -W materials, with the maximum at 1760 cm^{-1} for PLA being retained and the portion of the band between 1750 and 1700 cm^{-1}, attributable to PHA, decreasing (Figure IV-C6 (d) inset), suggesting the selective hydrolysis or leaching away of the PHA over PLA on the surface.

The weathered and unweathered PLA/PHA film provide similar spectra except for a higher absorbance in the -OH bending region (1052-934 cm^{-1}) and a small but significant spectral peak at 1638 cm^{-1} (C=C stretching) for the W-film, the latter band representing a Norrish Type II photodegradation of PLA ester bonds cleavage, resulting in the formation of COOH and CH=CH$_2$ end groups (Figure IV-C6d) (Hablot *et al.*, 2014; Hayes *et al.*, 2017). The former is greatly reduced by milling, but the latter remains present for MPs, not NPs. The absorbances of bands representing the ester bond of PLA are nearly identical to the corresponding absorbances for the weathered film, suggesting that hydrolysis did not occur during milling. This result contradicts the reduced thermostability of W-MPs compared to weathered film (Figure IV-C5d). However, one must be careful when interpreting the FTIR results for W-PLA-PHA and its resultant MNPs.

Moreover, PLA, the major polymeric species, resides in two different states as a free homopolymer and as part of a cross-linked network with calcium carbonate nanofiller; it is unclear if the absorbances of both PLA populations are equivalent. Perhaps the lower thermostability observed for the PLA component of W-PLA/PHA-MPs compared to the weathered film results from the cleavage of bonds between PLA and filler. However, the FTIR results indicate that PHA was selectively cleaved compared to PLA through milling, a trend also observed for CRYO-PLA/PHA-MPs (Figure IV-C6d). The transition from MPs to NPs produced a decrease in the COO and C-O stretching regions, which would suggest that hydrolysis occurred. FTIR spectra of MPs and NPs for CRYO- and weathering treatments are different, suggesting that the CRYO treatment does not mimic the impact of environmental weathering on surface functional groups.

4.4.7 Change of biopolymeric composition (NMR)

^{1}H-NMR analysis was employed to identify the compositional changes of biopolymers resulting from the size transformation process from the initial film→ MPs → NPs for CRYO- and W-PBAT and PLA/PHA, particularly the relative proportions of adipate, terephthalate, and 1,4-

butanediol monomeric units of PBAT and the relative proportions of PLA and PHA. For both W- and CRYO-PBAT, the proportion of adipate decreased slightly due to milling and wet grinding, with the difference in adipate content between the original film and NPs being statistically significant (Figure IV-C7a). The adipate fraction for the W-film and W-MPs were 3% lower than the original film and CRYO-MPs, respectively, while W-NPs were 8% lower than CRYO-NPs. Trends involving the terephthalate content vs. pretreatment and size reduction resemble those described above for adipate. However, the differences are much smaller (Figure IV-C7a). The only statistically significant difference is the lower terephthalate content for W-NPs compared to the original weathered film. This observation suggests that the severity, a combination of wet grinding and embrittlement, impacts the chemical structure by reducing the adipate and terephthalate fractions, but with the adipate/terephthalate ratio decreasing slightly. A lower adipate/terephthalate ratio may reflect a lower proportion of amorphous morphological regions, leading to reduced biodegradability (Zumstein *et al.*, 2018). The composition change from the initial film to lower adipate fractions due to the weathering of PBAT-BDMs reflects the findings of a previous study by the authors (Anunciado *et al.*, 2021).

The proportion of PLA was significantly higher (PHA proportion lower) for MPs compared to the initial films for CRYO- and W-PLA/PHA (a trend consistent with TGA analysis; Figure IV-C5); but a further decrease in the size of NPs led to the reverse trend (Figure IV-C7b). In addition, a slight decrease of the 4-HB component within PHA was observed between the original films and MPs and between CRYO-MPs and -NPs, suggesting that the 4-HB monomer is more susceptible to hydrolysis than 3-HB during the milling and wet grinding (Figure IV-C7b). However, the only statistically significant difference in 4-HB content was between the NPs and their respective original films (by 10%); moreover, there were no differences in 4-HB content for a given particle type between CRYO- and W-pretreatments.

4.4.8 Effect of film pretreatment on biodegradation of MNPs in soil

Aerobic biodegradation of MNPs derived from cryogenically treated, and environmentally weathered films of PBAT and PLA/PHA in soil was determined by measurements of the CO_2 evolution, with the % biodegradation calculated based on an atomic balance for C atoms, as described in ASTM 5988-12. The resultant % biodegradation vs. time profiles is depicted in Figure

IV-C8, while the corresponding CO_2 evolution profiles and the profile for compost-enriched bare soil are provided in Figure IV-D15. During the first two weeks of incubation, biodegradation occurred rapidly, and after that, the biodegradation rate decreased slightly for all experiments. Biodegradation increased linearly from 14 to 45 d, and the mineralization rate increased at 66 d due to adding water at 56 d. PBAT MNPs underwent significantly higher % biodegradation than PLA/PHA MNPs, on average ($p = 0.0017$), and especially after 30d, faster than the cellulosic control, with a smaller variation among measurements observed for PLA/PHA (Figure IV-D15 b).

Statistically significantly higher biodegradation was observed during the plateau phase (128-154 d) for MPs compared to NPs for cryogenically treated and weathered forms of both polymeric materials used in this study (Figure IV-C8). Moreover, p-values of 0.0306, 0.0038, 0.0002, and 0.0001 were determined for CRYO-PBAT, W-PBAT, CRYO-PLA/PHA, and W-PLA/PHA, respectively, for this comparison. This trend contradicts the intuitive and predicted trend of an increased biodegradation rate as d_p is decreased due to the increase of surface area exposure for MNPs (Chinaglia *et al.*, 2018; Tosin *et al.*, 2019). The underlying cause of the unanticipated result is the difference in chemical properties of MPs and NPs for a given treatment. For instance, NPs derived from PBAT have a significantly lower content of starch, which is preferred as a carbon source for microorganisms over PBAT than MPs (Figure IV-C5).

Likewise, PBAT NPs possess a slightly lower adipate/terephthalate ratio compared to MPs, which may also result in lower biodegradability for NPs, as discussed above (Figure IV-C7). For weathered PLA-PHA, the higher proportion of PLA conjugated to calcium carbonate nanofiller for NPs compared to MPs, as discussed above, led to reduced availability of PLA to microorganisms, thereby reducing the biodegradability. For CRYO-PLA/PHA, the lower biodegradability for NPs compared to MPs may be related to the lower PHA content on the surface for NPs, as shown through FTIR spectroscopy (Figure IV-C6). However, the overall PHA content for NPs is larger (Figure IV-C7). Unlike the other treatments, the time course of biodegradation for CRYO-PLA/PHA was nearly identical for MPs and NPs up to 65 h. After that point, the biodegradation of MPs increased related to NPs. In summary, the results of Figure IV-C 8 teach us that biodegradation of NPs is not necessarily greater than for MPs, as would be anticipated because of changes in chemical and surface properties that may occur upon size reduction that may hinder mineralization.

The results of Figure IV-C8 and Figure IV-D15(a) clearly reflect a significant difference in biodegradability between MNPs derived from environmentally weathered and cryogenically treated films ($p = 0.0105$). For PBAT, environmentally weathering yields higher biodegradation for MNPs, but to a greater extent for NPs, resulting from the smaller particle size and lower thermostability of W-MNPs than CYRO-MNPs (Tables IV-C1). The opposite trend is observed for PLA/PHA, caused mainly by the higher proportion of cross-linkage between nanofiller and PLA in MNPs derived from weathered PLA/PHA film. These results show that cryogenic treatment does not mimic environmental weathering in the latter's impact on biodegradability. Further statistical analysis of the biodegradation results is given through Figure IV-D14, D15, D16 and a discussion is given in the Appendix D.

4.5 Conclusions

Additional information was learned about the size reduction process of plastics on the nanoscale. During the initial phase of size reduction from MPs to NPs, size reduction occurs to nearly a 10-fold extent, with the distribution being unimodal (II), between 150 and 300 nm (6 passes; Figure IV-C3). A small subpopulation resides at 500-1000 nm (III). Upon further size reduction, bimodal size distribution is observed, with a second subpopulation (I) forming at 50-100 nm, and ultimately the smaller size fraction dominates (30 and 60 passes; Figure IV-C3). The exception to the trend is W-PLA/PHA NPs, which are recalcitrant to size reduction, as described above. The presence of multiple stages during size reduction will impact the colloidal properties of NPs, hence their transport behavior in ecosystems. The results of this study will contribute to a theoretical framework for risk assessment and prediction of particle breakdown dynamics of terrestrial MPs and NPs. This study provided the surprising result that MPs were during the incubation period more biodegradable than NPs for both polymeric materials in both weathered and unweathered forms. Moreover, one would anticipate that the size reduction process would increase the exposure of plastic particles to soil microorganisms, leading to increased biodegradation for NPs. However, this hypothesis does not consider changes in structure and properties that occur during size reduction, especially to a nano-level. For example, NPs derived from PBAT films possess a lower level of starch, the preferred carbon source of microorganisms over PBAT (Figure IV-C5), due to starch being leached away during wet grinding. MPs possess a

slightly lower adipate/terephthalate ratio, both of which will hinder the biodegradation of NPs. For PLA/PHA, the lower biodegradability of NPs may be attributable to the lower PHA content on the surface for CRYO-treatment (FTIR analysis; Figure IV-C6) and to the higher proportion of cross-linked PLA for the weathered treatment. Therefore, biodegradation will not necessarily increase when biodegradable plastics undergo size reduction, particularly at the nanoscale. Therefore, changes in physicochemical and surface-related properties of particles are important factors to consider when forming hypotheses related to biodegradation. The predicted complete particle mineralization based on a non-linear mathematical modeling procedure resulted in slightly lower values (faster) for PBAT NPs than for MPs (Figure IV-19). However, for PLA/PHA NPs, a significantly longer (slower) biodegradation duration is expected based on the prediction values than for MPs (Figure IV-20).

In summary, the size reduction process, and the impact of weathering on dimensional and physicochemical properties differ greatly between polymeric materials.

Also, embrittlement by cryogenic pretreatment of unweathered films does not mimic the impact of environmental weathering on the size reduction process for biodegradable films in terms of properties. Such a difference may impact the reliability and utility of laboratory studies on MNPs' impact on soil health, ecotoxicity to soil and aquatic organisms, and transport and fate studies. The scientist must carefully consider the choice of surrogate MNPs employed for such studies and the limitations inherent to the choice of surrogate particles. Employment of environmentally weathered films as starting materials is recommended if available in sufficient quantities. Our previous study showed that artificial weathering did not effectively mimic agricultural weathering for mulch films (Hayes *et al.*, 2017).

.

APPENDIX IV - C
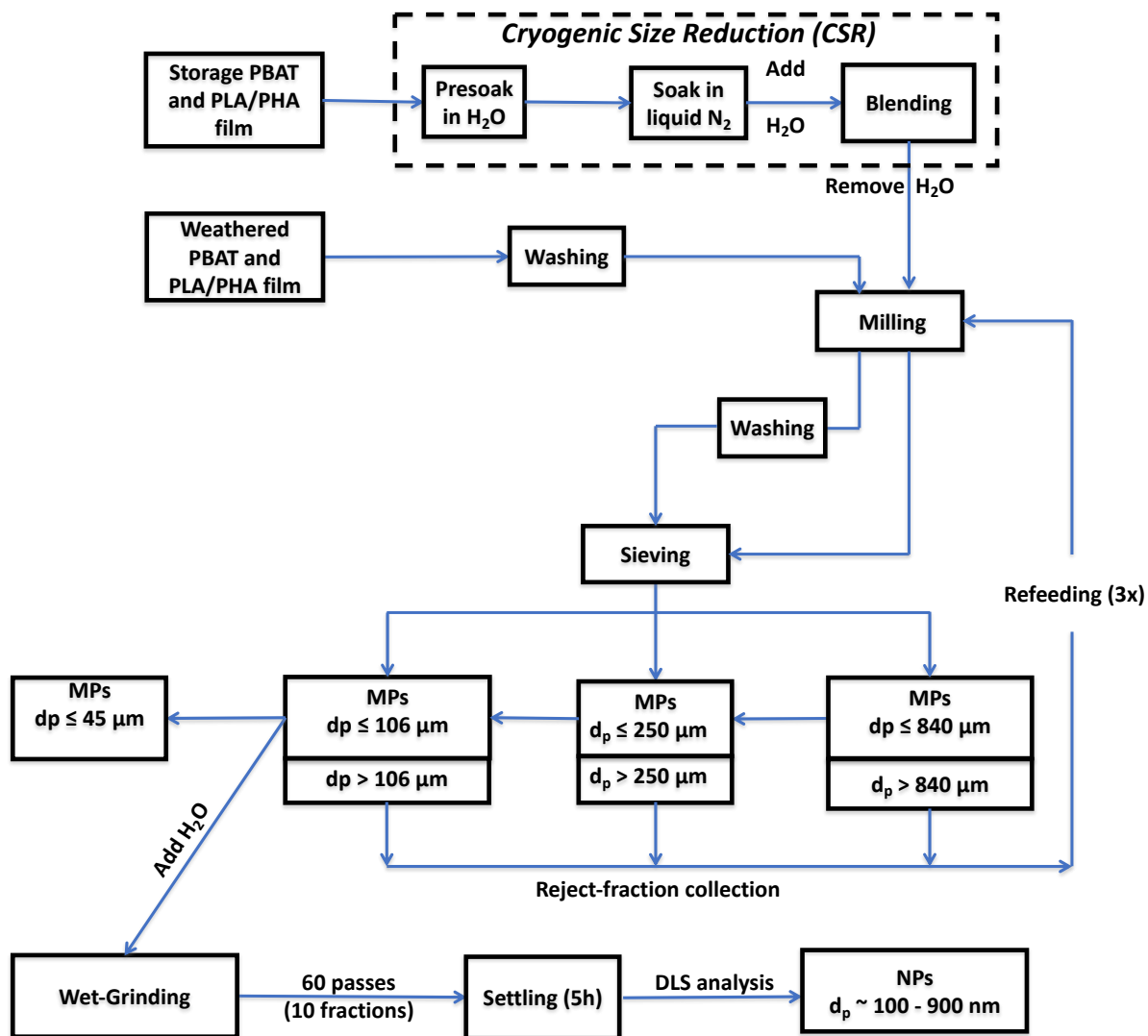
Figure IV-C1. Flow diagram of the stepwise preparation for mechanically formed micro- (MPs) and nanoplastic (NPs) process.
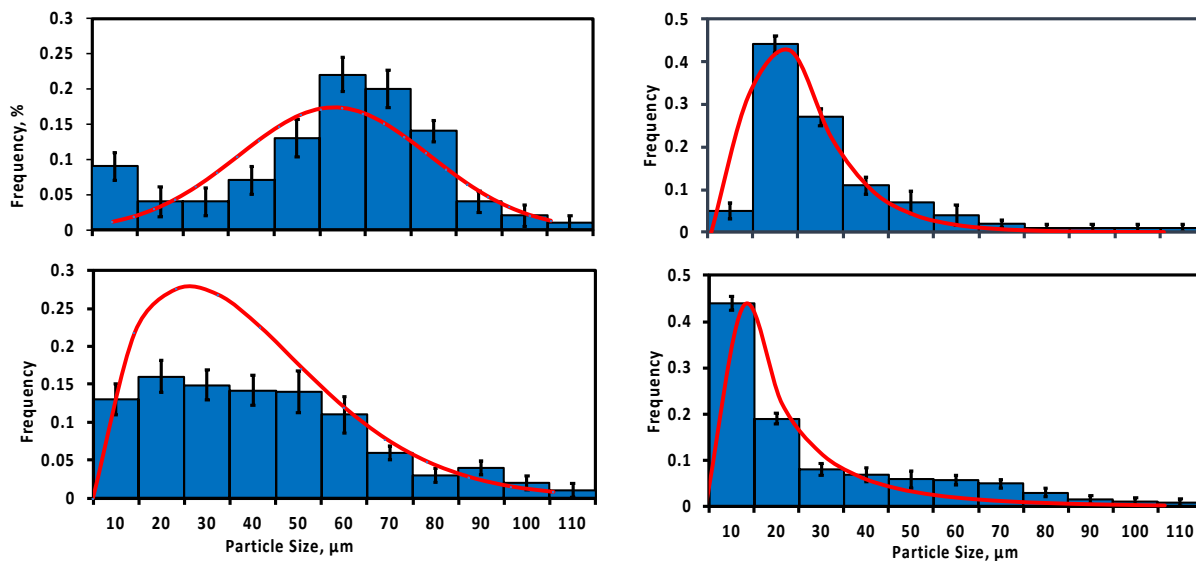
Figure IV-C2. Comparison of pretreatments, cryogenic exposure (CRYO), and environmental weathering (W) on the particle size distribution for the 106 μm MP sieve fraction for MPs, prepared according to the procedure of Figure IV-C1. Histograms: (a) CRYO-PBAT, (b) W-PBAT, (c) CRYO-PLA/PHA, and (d) W-PLA/PHA. Red curves represent the fit of the normal (Fig. a), lognormal (Figs. b,d), and Weibull (Fig. c) distributions
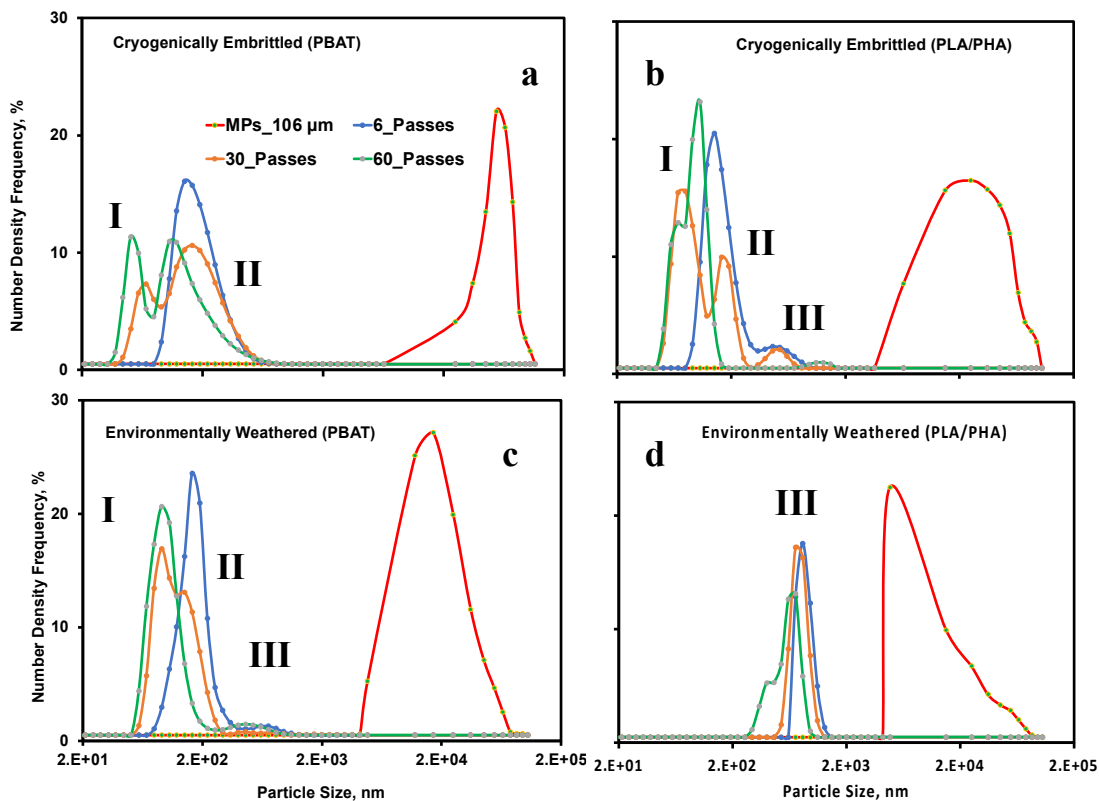
Figure IV-C3. Effect of environmental weathering vs. cryogenic pretreatment and number of passes on the size distribution of NPs formed from MPs (106 μm sieving fraction) of plastic mulch films resulting from the stepwise wet grinding process in a 1% aqueous slurry: (a) CRYO-PBAT, (b) CRYO-PLA/PHA, (c) W-PBAT and (d) W-PLA/PHA. Legend provides the number of passes during the wet grinding process. NP and MP size data were obtained through dynamic light scattering experiments and ImageJ analysis of stereomicrographs, respectively. I, II, and III refer to subpopulations of NPs with different size ranges; information on their average size and size distribution are given in Table IV-C2.
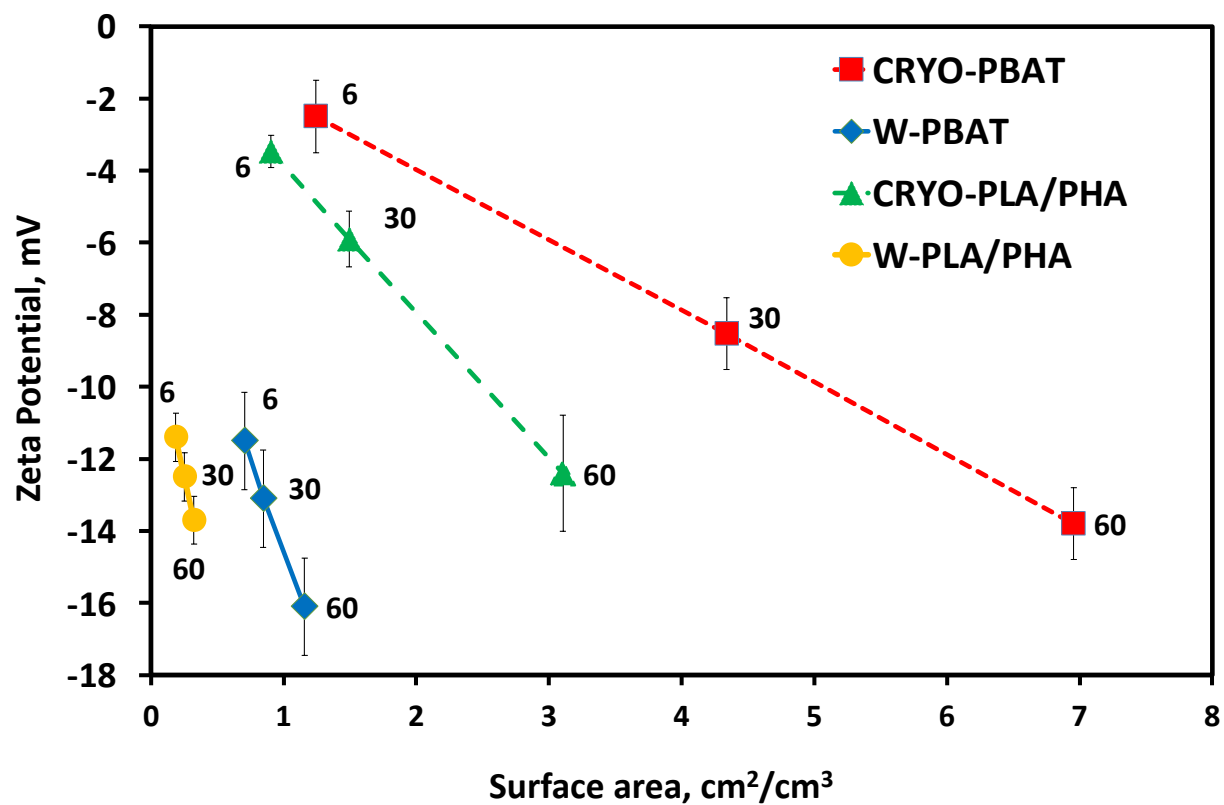
Figure IV-C4. Particle surface charge (zeta potential) for CRYO- and W-PBAT and PLA/PHA NPs dispersed in water at 22°C vs. surface area. The numbers in the figure represent the number of passes employed during wet grinding. Error bars reflect standard deviation.
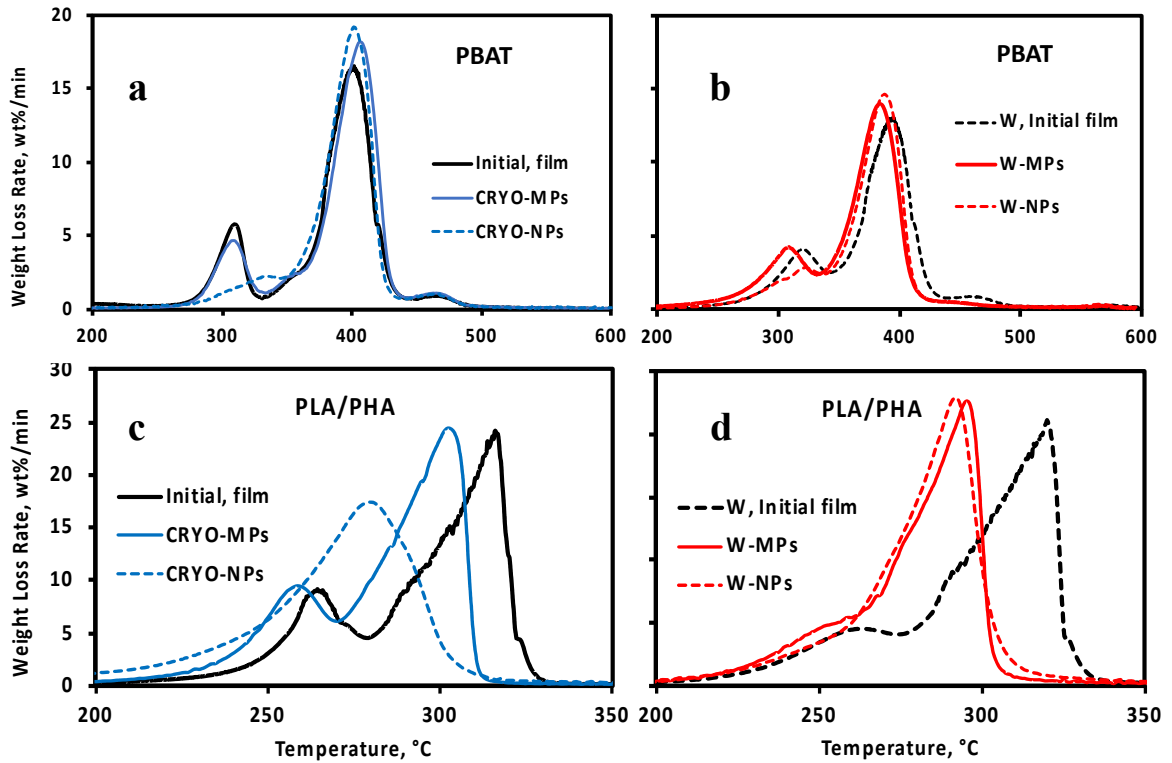
Figure IV-C5. Representative differential thermograms DTG (a, b, c, d) and corresponding TGA thermograms Figure IV-D11 (a, b, c, d) from thermogravimetric analysis (TGA) of cryogenically treated (CRYO) and environmentally weathered (W) polymers. MPs fractions, retrieved after dry-milling (MPs, 3 passes) and wet grinding (NPs, 60 passes), represented by (a, b) PBAT-MNPs, (c, d), and PLA/PHA-MNP. NPs were produced via wet grinding (60 passes) of the 106 μm MPs sieve fraction after dry milling. Maximum temperatures for each major polymeric component are identified in the DTGs. The Initial and W-Initial film data were retrieved from Hayes *et al.* (2017).
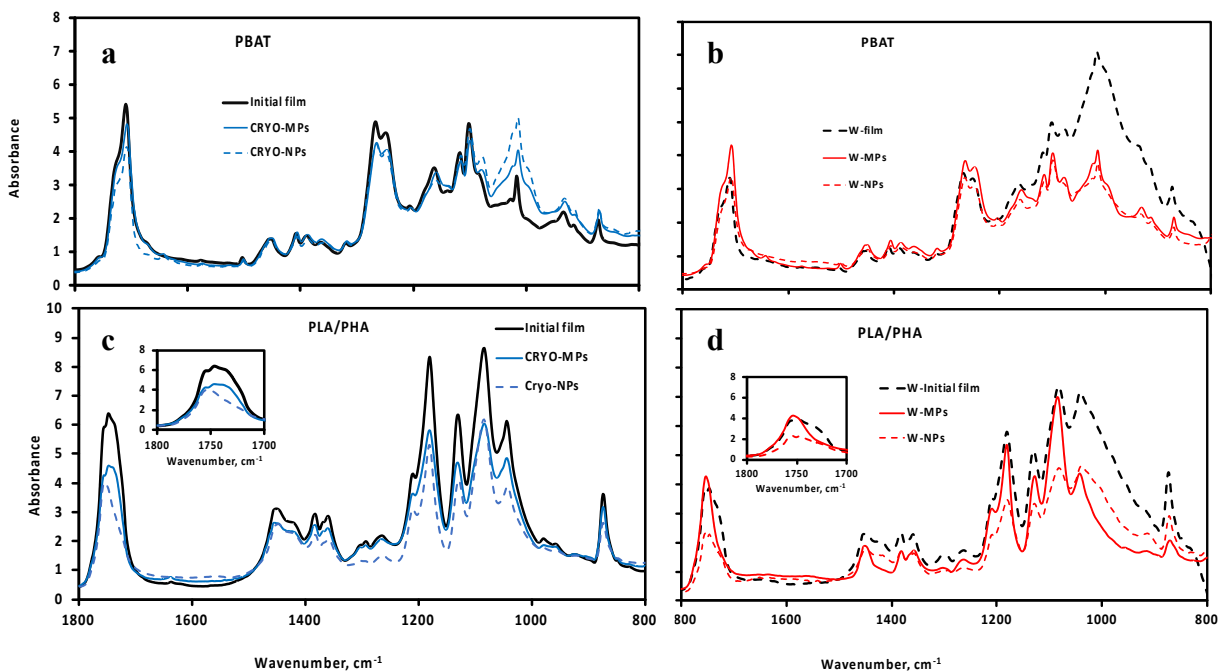
Figure IV-C6. Changes in chemical bonding of the initial (untreated) and weathered films, MNPs represented by (a, b) PBAT and (c, d) PLA/PHA between the cryogenically treated (CRYO) verus the environmental weathered (W) plastic films and their MPs and NPs. MPs consist of the 106 μm sieve fraction of dry milled plastics; NPs were produced via wet grinding (60 passes) of the 106 μm sieve fraction, and MPs were obtained after dry milling (3 passes). The "Initial" and "W-film" data were obtained from Hayes *et al.* (2017).
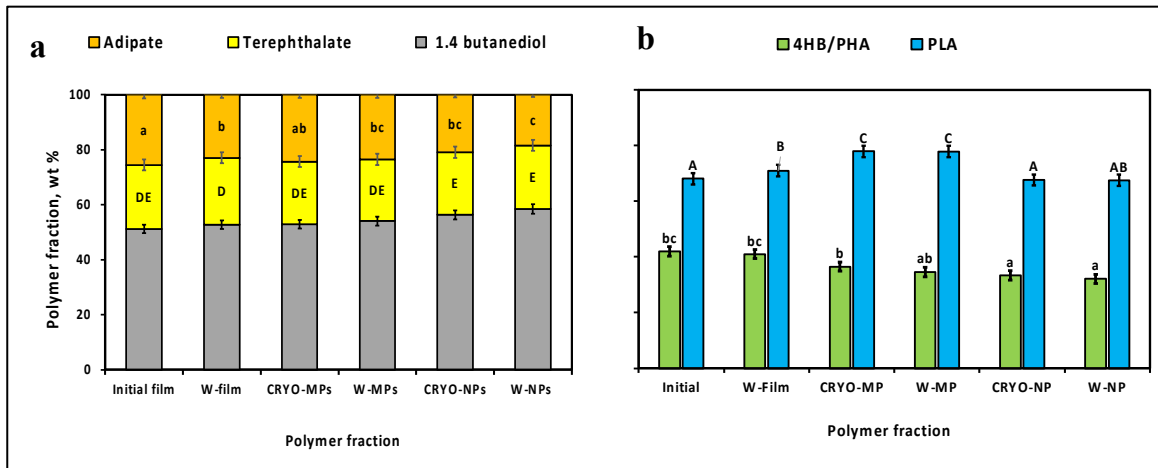
Figure IV-C7. Change of relative polymeric composition of (a) PBAT derived from (a, b) NMR spectra to assess the weight fractions for adipate, terephthalate, and 1,4 butanediol components relative to the total mass. Effect of cryogenic treatment (b) (CRYO) and environmental weathering (W) weathering polylactic acid (PLA) mass fraction among the polymers and 4-hydroxybutyrate (4HB) monomer units among polyhydroxyalkanoate (PHA) of the "Initial" PLA/PHA film based on NMR analysis. Error bars reflect standard deviation (n = 2) and means (across treatments) that do not share common capital, and lowercase letters reflect a statistically significant difference (p <0.05). "Treatment" refers to initial vs. agriculturally weathered. Data from the "Initial" mulch film were adapted from Hayes *et al.* (2017).
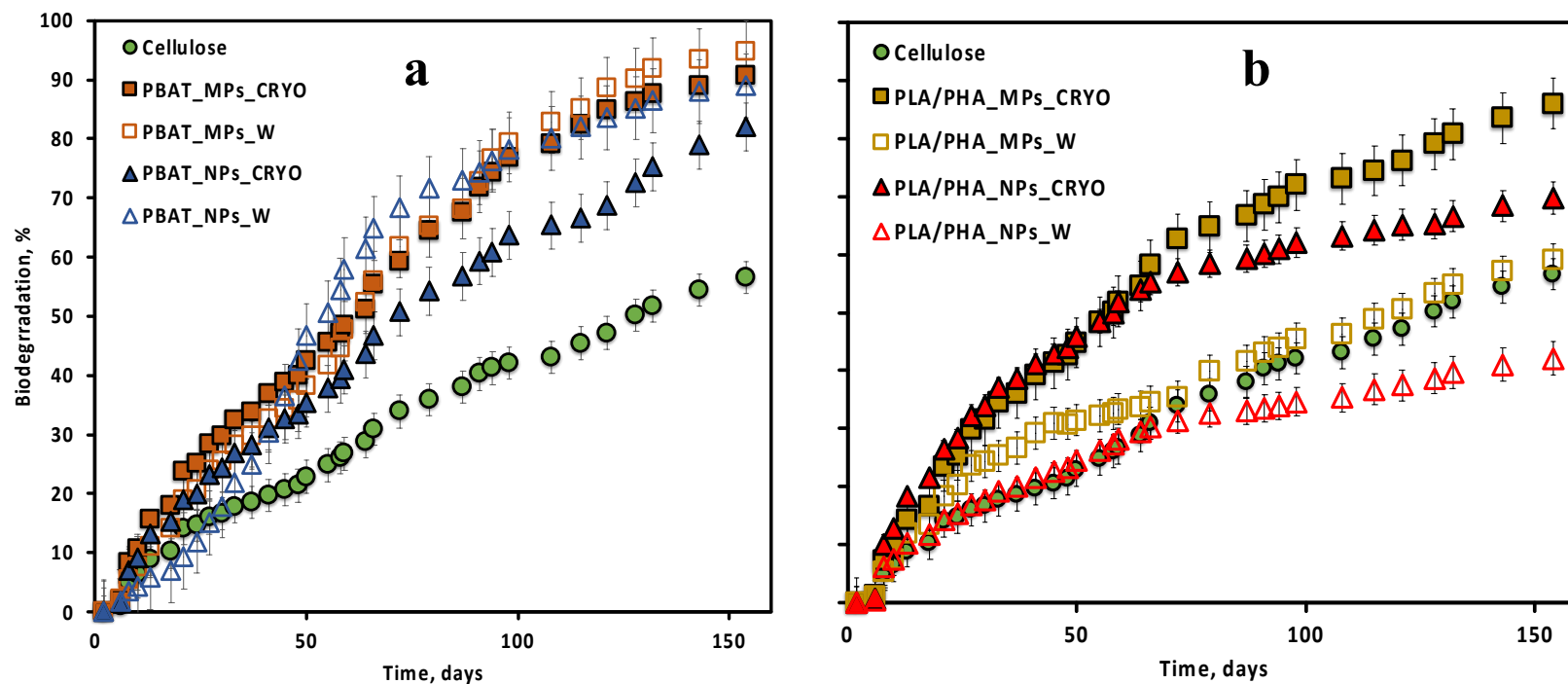
Figure IV-C8. Cumulative mineralization of weathered and unweathered BDMs during 154 days of soil incubation, according to ASTM 5988-12 standardized test conditions. CO_2 evolution data for a and b were collected simultaneously; therefore, Figure (a) and Figure (b) depict the same data for microcrystalline cellulose (positive control). Data points represent mean values, and error bars represent standard error (n = 3).

Table IV-C1. Comparison of particle size distribution, geometric and shape parameters (calculated based on Eqs. D1 and D2) for MPs prepared from PBAT and PLA/PHA via CRYO- and W-pretreatments [1,2].

Parameters	CRYO-PBAT [3]	W-PBAT [4]	CRYO-PLA/PHA [3]	W-PLA/PHA [4]
106 μm Sieving Fraction				
Average diameter [d_p, μm]	55.56 ± 0.75	24.13 ± 0.26	37.00 ± 0.60	38.80 ± 0.47
Polydispersity [PD]	0.19 ± 0.01	0.31± 0.02	0.30 ± 0.01	0.45 ± 0.03
Circularity	0.59 ± 0.01	0.82 ± 0.01	0.42 ± 0.02	0.63 ± 0.02
Aspect ratio	2.23 ± 0.02	1.74 ± 0.01	2.21 ± 0.03	2.12 ± 0.02
250 μm Sieving Fraction				
Average diameter [d_p, μm]	125.92 ± 5.19	47.52 ± 2.57	104.26 ± 5.82	143.25 ± 2.40
Polydispersity [PD]	0.17 ± 0.01	0.29 ± 0.02	0.31 ± 0.02	0.30 ± 0.01
Circularity	0.49 ± 0.01	0.70 ± 0.02	0.66 ± 0.03	0.73 ± 0.01
Aspect ratio	2.37 ± 0.04	1.83 ± 0.01	1.76 ± 0.04	1.59 ± 0.02

[1] Error bars represent standard error (SD) values; [2] further information on the calculations are given in Appendix D; [3] Cryo-film samples were prepared by soaking in 200 mL liquid nitrogen for 5 min and comminuted in a blender for 10 min; samples were recovered and soaked in liquid N_2 for a second time and 10 min and introduced into the Wiley mill, using a sieve of 840 μm for the first pass; for the second pass, a 250 μm sieve was used; [4] Environmental weathering of mulches occurred in 2017 (Jun-Sept) during mulches' use in field trials in Knoxville, TN, USA, with pepper as a test crop. Field recovered samples were cleaned with a brush and underwent a water washing in 1000 ml water beaker, stirred for 1 hour and material dried for 10 hours, then milled with Wiley Mini mill.

Table IV-C2. Effect of the number of passes for wet grinding on the particle size distribution data for PBAT and PLA/PHA NPs in a 1% aqueous slurry, as determined by Dynamic Light Scattering (DLS) analysis[1, 2]

Polymer	Passes[3]	Condition	d_p (mean) nm[4, 5]	d_p I (max.) nm[6]	Frequency I (NDF) %	d_p II (max.) nm[6]	Frequency II (NDF) %	d_p III (max.) nm	Frequency III (NDF) %	Range; I+II+III, nm
PBAT	6	CRYO	192.7 ± 30.8	142.2	15.6	-	-	-	-	78.8 - 955
	30		171.6 ± 65.7	68.1	6.8	164	10.1	-	-	43.8 - 825
	60		131.7 ± 61.7	50.7	10.8	106	10.5	-	-	37.8 - 955
	6	Weathered	193.8 ± 15.3	164.4	23.1	-	-	712	0.8	78.8 - 825
	30		144.7 ± 45.0	91.3	16.4	142.5	12.6	712	0.2	58.8 - 955
	60		122.2 ± 23.8	91.3	20.2	-	-	459	1	58.8 - 955
PLA/PHA	6	CRYO	193.8 ± 15.34	142	20	-	-	459	1.8	91.3 - 955
	30		133.2 ± 78.6	68.1	14.9	164	9.4	531	1.6	50.7 - 825
	60		114.6 ± 39.0	68.1	12.4	106.1	22.6	1110	0.05	50.7 - 955
	6	Weathered	846.5 ± 104.3	-	-	-	-	825	34.1	615 -1480
	30		775.7 ± 38.8	-	-	-	-	712	33.4	531 - 1280
	60		555.4 ± 166.2	-	-	396	9.5	712	25.2	255 - 955

[1] The Two Parameter Weibull model, described in more detail in the Appendix IV-D, was the 'Best Fit' for all distributions.

[2] PSD data provided in Fig. 3.

[3] Number of instances for reintroducing the slurry into the wet grinding machine.

[4] Number mean of d_p, determined by DLS analysis.

[5] Error bars represent one standard deviation.

[6] Particle size distribution (PSD) mean of d_p, determined for each subpopulation.

APPENDIX IV – D

D.1 INTRODUCTION

Environmental weathering of PBAT (BioAgri) and PLA/PHA biodegradable mulch films took place during the summer of 2018 at Knoxville, TN, USA (University of Tennessee [UT] East Tennessee Research and Education Center [REC], elevation 270 m above sea level (35°52′52′′N, 83°55′27′′ W) through field trials for the cultivation of 'Aristotle' peppers. The experiment consisted of 8 mulch treatments and followed a complete randomized design. Soil consisted of moderately well-drained Shady-Whitwell complex soil mainly composed of Typic Hapludult soil (shady loam). At the time of bed shaping, mulches were laid by a machine (Model 2600 Bed Shaper; Rain-Flo Irrigation, East Pearl, PA) in all plots on 24 May 2017, and residual material fragments were retrieved shortly after harvesting peppers on 18 September 2017: 117 days of environmental weathering (Ghimire *et al.*, 2018). Fragments were cleaned from adhering material and air-dried at 22 ºC.

D.2 DIMENSIONAL ANALYSIS OF MICROPLASTICS

D.2.1 Determination of size and geometry of microplastics through stereomicroscopy and ImageJ

After performing the milling and sieving steps (described in the **Methods** subsection of the main paper), the microstructure and geometry of MPs derived from PBAT and PLA/PHA films were evaluated by stereomicroscopy. Representative aliquots of plastic fragments were retrieved (1.0 g), and subsamples of around 1 mg were evenly dispersed on a paper surface. Images were collected using a stereo microscope model SZ 61 from Olympus (Shinjuku, Tokyo, Japan) with a Digital Sight DS-Fi1 integrated with a Nikon camera head (Shinagawa, Tokyo, Japan). Image analysis was performed using ImageJ 1.52q software (Ritchie & Roser, 2018) by converting micrographs into 8-bit images (representing 28 gray levels), applying a proper threshold setting using a black background to the white particles (dividing the image into two classes of pixels). Then the foreground areas were matched out using a specific pixel classification for the background areas. Then, the adjusted image was converted into a binary file, and adjacent objects

were separated by the "watershed" algorithm. A representative image of each MPs sample was collected and processed through Image J using five replicates of the stereomicroscopic images.

Examples of stereomicrographs and the images derived through ImageJ are given in Figure IV-D1 and Figure IV-D4 or MPs of the 106 μm and 250 μm sieve fraction derived from weathered and cryogenically treated PBAT and PLA/PHA films. The average diameter, d_p, was derived from the projected area using Image J's "analyze particles" algorithm to determine the particle area sizes between one μm and infinity. The features "exclude on edges" and "include holes" of the algorithm were selected by including single particles and ignoring any void spaces. One image representing the entire sample was collected and processed for each of two different selections for a given sieve fraction and was subsequently processed by ImageJ. The distributions of d_p extracted by Image J analysis were used to create histograms and perform curve fitting for d_p using JMP® Pro 15.2.0 software (SAS Institute, Cary, NC, USA). Furthermore, shape descriptors such as circularity (Circ), aspect ratio (AR), roundness (Round), and solidity of the particles were calculated as follows (Geyer *et al.*, 2017):

$$Circ = 4\pi \left(\frac{Area}{Perimeter^2} \right) \tag{D1}$$

$$AR = \left(\frac{Major\ Axis}{Minor\ Axis} \right) \tag{D2}$$

$$Roundness = 4 \left(\frac{Area}{\pi * Major\ Axis^2} \right) \tag{D3}$$

$$Solidity = \left(\frac{Area}{Convex\ Area} \right) \tag{D4}$$

Examples of histograms for the average particle size, d_p, are given in the Appendix, for the 106 μm and 250 μm sieve fraction, respectively, while MP shape data corresponding to the figures are given in Table IV-D1. Further detail on the procedures described in this section is provided in Astner *et al.* (2022).

D.2.2 Calculation of average MP diameter (d_p) from projected particle area

The particle area received from the Image J output for each stereomicrograph was converted into the particle diameter d_p based on each MP's area as described in this section. A considerable variation of particle shape types represented by round-and elongated particles is generally given in stereographic images (Figure IV-D5). These particles may all be reported (calculated) as round; however, the shape analysis differentiates and precisely shows each sub-population percentage in this mixed sample. Given that MPs' shapes are irregular, the assumption of regular geometrical shapes results in an oversimplified approximation. A single number, the diameter, describes spherical particles based on identical dimensions. Non-circular particles can be described using multiple length and width measures.

For this reason, particle assessment through techniques such as light scattering involving settling rate (Brownian motion) assume spherical or circular-shaped particles. Particle size measurement varies in complexity and depending on the particle shape. Therefore, enough numbers must be present to ensure an acceptable confidence level in the measured parameters. Additional information on particle size measurement, sample size, and data analysis in ISO 9276 (Jambeck *et al.*, 2015). Techniques like microscopy or automated image analysis describe particle size using multiple values for particles with larger aspect ratios (Geyer *et al.*, 2017). An image analysis system such as ImageJ is suitable for describing the non-spherical particle seen using the longest and shortest diameters, perimeter, projected area, or equivalent spherical diameter. The reported value of d_p is typically an equal circular diameter calculated from the particle area received from Image J. For circular-shaped particles, the size is defined by the particle diameter d_p. For analyzing MPs, various definitions of particle size exist when irregular particles are present. For this publication, the built-in standard measurements were used in the ImageJ's "Analyze Particles," assuming a circle's diameters that equal the projection area. Particle and minimal particle diameter were calculated based on previously published literature (Alimi *et al.*, 2018; Gigault *et al.*, 2018; Hanvey *et al.*, 2017; Hartmann *et al.*, 2019).

For circular particles (AR $\geq$ ~1), equation (D5) was applied to calculate d_p in the form of $d_{p,\text{Eq}}$:

$$dp_{EQ} = \sqrt{\frac{4 * Area}{\pi}}$$

(D5)

The diameter (d_{pEQ}) is equivalent to the circle diameter representing the same area as the irregular-shaped particle's projection area, as shown in Figure IV-D6a. Alternatively, the maximum and minimum diameter ($d_{p,max}$, and $d_{p,min}$, respectively) represent the longest and shortest distance between two points of a 2-dimensional particle, respectively (Figure IV-D6b). The latter two diameter measures are determined for all possible orientations (0°…180°).

For MPs of rectangular geometry (AR ≤ 2.5), $d_{p,min}$ was calculated as follows:

$$dp_{min} = \sqrt{\frac{Area * w}{l}} \tag{D6}$$

where 'w' and 'l' are the width and length of the MP particle, respectively.

When comparing the differences in d_p values calculated according to spherical and rectangular geometries, Δd_p (via Eqs. D5 and D6), the largest difference of 39 ± 0.5 % was found for the 250 µm sieve fraction of CRYO-PBAT, which corresponds to the largest AR, 2.37 ± 0.1 (Table IV-D1). When comparing CRYO- vs. W- treatments for a given sieve fraction and film type, the latter treatment resulted both in lower AR and Δd_p, suggesting weathered films result in more uniform circular-shaped MPs through milling (Table IV-D 2). These results indicate that the calculation of dp is best performed using Eq. D6 rather than Eq. D5 since AR > 1.5 for most particle fractions.

D.2.3 Fitting of particle size distribution (PSD) models to dp histogram data

The distribution of d_p derived from Image J analysis was fit by several other models using JMP® Pro 15.2.0 software (SAS Institute, Cary, NC, USA). However, the datasets generated for the three size classes were non-normally distributed according to the Shapiro-Wilk test. Accordingly, the Lognormal, two-parameter Weibull, Loglogistic, and Frechet models were used to test for the best fit. The corrected Akaike's and Bayesian information criteria (AIC and BIC, respectively) determined the quality of the model fits. All statistical evaluations employed a significance level of $\alpha = 0.05$.

Proper selection of PSD is essential since each model predicts different results, such as the number or d_p or surface area fraction of particles within a specific range size (such as particles

with a d_p of 50 μm). The particle range size determination is often critical for the detection of risk assessment of human health for air pollution (Koelmans *et al.*, 2022; Sarkar *et al.*, 2018; Sridharan *et al.*, 2021) and plants (Rillig *et al.*, 2019) and measuring the impact the germination rate of vascular plants (Pehlivan & Gedik, 2021; Yin *et al.*, 2021).

The two-parameter Weibull model is a flexible distribution model that is applied to a broad range of applications such as bioproduct development (Wang *et al.*, 2021), terrestrial sediments (Rodriguez-Seijo *et al.*, 2017), quality engineering for material strength data distribution (Kim & An, 2020). Also, in this study, the two-parameter Weibull model was applied to model soil particles and has also been demonstrated to be the most effective size distribution model to describe soil (Bandopadhyay *et al.*, 2018). The two-parameter Weibull model is defined as follows:

$$f(x, \alpha, \beta) = \left\{ \frac{\beta}{\alpha} \left(\frac{x}{\alpha} \right)^{\beta-1} exp \left(-\left[\frac{x}{\alpha} \right]^{\beta} \right) x \geq 00, x < 0 \right\} \tag{D7}$$

where β > 0 is the shape parameter, and α > 0 is the distribution scale parameter.

The Gauss function (Normal distribution) is described as follows:

$$f(x, \mu, \sigma) = \left\{ \left[\frac{1}{\sigma(2\pi)^{1/2}} \right] exp \left[-\frac{(x-\mu)^2}{2\sigma^2} \right] \right\} \tag{D8}$$

where μ is the mean of the particle diameter x and σ describes the standard deviation. The particle diameter x is replaced by its logarithm for a lognormal distribution. Generally, the PSD is represented by a cumulative curve obtained for a Gaussian model by integrating the following equations according to x:

$$F(x, \mu, \sigma) = \frac{1}{2} \left\{ 1 + erf \left[\frac{(x-\mu)}{\sigma\sqrt{2}} \right] (x > \mu) \right\} \tag{D9}$$

$$F(x, \mu, \sigma) = \frac{1}{2} \left\{ 1 - erf \left[\frac{(x-\mu)}{\sigma\sqrt{2}} \right] (x \leq \mu) \right\} \tag{D10}$$

where *erf[ ]* is the error function, which can be assessed by numerical approximation to the PSD according to (Guo *et al.*, 2020) as follows:

$$erf(x) = 1 - (03480242\,T - 0.0958\,T^2 + 0.7478556\,T^3)exp\,(-x^2) \qquad \text{(D11)}$$

where *T=1/(1+047047x)*. The models that best fit PSD data are given in Table IV-D2, along with parameter values. Normal, lognormal, and Weibull distributions described the best fit for processed MPs, producing the lowest AIC and BIC values. The fitting of models to d_p histogram data is given in Figure IV-C2, D3, and D4.

D.3 DIMENSIONAL AND ZETA POTENTIAL ANALYSES OF NANOPLASTICS

D.3.1 Experimental Procedure

Dynamic Light scattering (DLS) was used to determine the NPs' average size and size distributions at 25 °C, performed on aliquots of aqueous NP slurries containing 0.5 wt% of NPs (1 mL) originating from the wet-grinding process that were placed in 1.0 cm pathlength quartz cuvettes. In total, 120 measurements (10 subsamples from the original sequential sampling, with three replicates per subsample) were collected. The DLS instrumentation was a Zetasizer Nano model from Malvern (Worcestershire, UK). The beam of the 4 mW He Ne Laser light source (wavelength of 633 nm) was aligned to pass through the sample at a vertical position of 1.25 mm, measured from the bottom of the cuvette. A sampling time of 60 s was selected for each measurement. The particle size distribution was analyzed by Malvern Zetasizer software, version 7.11. In addition, zeta potential (ZP) was measured for the same samples and using the same instrumentation employed for DLS, along with a Smoluchowski model. The surface area per volume (SA/V) of NPs in the aqueous slurry samples (cm^2/cm^3) analyzed by DLS and ZP was estimated as a first approximation as follows:

$$SA/V = 6\,C_{NP}/(d_{p,ave}\,r_p) \qquad \text{D12}$$

where C_{NP} is the concentration of NP (g/mL; determined gravimetrically through evaporative removal of water at 105 $^{\circ}$C overnight), $d_{p,ave}$ is the average particle diameter, determined through DLS, and ρ_p the particle density (1.2 g/mL). This equation approximates the surface area per volume for NPs based on spherical geometry: $d_{p,ave}$.

D.3.2 Impact of polymer type on the PSD dispersion of nanoplastic particles

Results showed that increased passes (severity) of wet grinding processing conditions significantly enhanced size reduction by forming NPs particles with d_p's ranging from 699 nm (W-PLA/PHA) to 193 nm (CRYO-PBAT) after the first six passes (Figure IV-D9a). Interestingly, when comparing both BDMs, the particle breakdown from MPs to NPs occurred quickly for PBAT compared to PLA/PHA. However, after 30 and 60 passes, the breakdown rate was significantly higher for PLA/PHA than for PBAT. In addition, the average polydispersity index (PDI=0.82) for PLA/PHA confirms polydisperse samples, indicating particles' aggregation (Figure IV-D9b). In contrast, PBAT has a significantly lower average value (PDI=0.51), suggesting a more stable monodisperse solution of particles (Figure IV-D9b).

Compared to the size reduction throughout 60 passes, NPs for CRYO-PBAT, CRYO-PLA/PHA, and W-PBAT showed d_p's below 200 nm with relatively small standard deviations. In contrast, W-PLA/PHA showed significantly larger values ranging between 699 and 266 nm, averaging 432 nm. Comparing the unweathered conditions of both feedstocks during size reduction after the first six passes, a contribution of 42 % of the entire PSD occurs by forming NPs of CRYO-PBAT and CRYO-PLA/PHA. After 30 passes, an additional fractionation occurs for CRYO-PBAT and CRYO-PLA/PHA, respectively. Interestingly, W-PLA/PHA contributed 40% to the entire PSD diameter after six passes compared to W-PBAT with a contribution of 11% (Figure IV-D 10b). Levene's test for unequal variances was conducted and supported the assumption that the variances for W-PLA/PHA were significantly different by PSD (p-$value = 0.0367$), from which we can conclude that environmental weathering greatly influenced the breakdown of the PLA/PHA mulch film.

D.4 THERMAL AND CHEMICAL ANALYSIS OF MNPS

D.4.1 Thermogravimetric analysis (TGA) procedure

Thermogravimetric analysis (TGA) measurements were carried out on ~10 mg samples using a PerkinElmer TGA-6 thermobalance with a platinum pan under dynamic nitrogen flow (20 ml/min) heating rate of 10 °C/min starting from 25 °C up to 600 °C. Thermograms were analyzed for weight change as single-stage decomposition curves and evaluated for sample moisture content at 105˚C and characteristic decomposition temperatures between 200˚C and 600 ˚C.

D.4.2 TGA results

DTG thermograms for the original and weathered PBAT and PLA/PHA films and the MPs (106 μm sieve fraction) and NPs (60 passes) formed from them are depicted in Figure IV-D11, while differential thermograms (DTGs) are provided in Figure IV-C5 of the main paper. The weight % of films, MPs, and NPs remaining at 600ºC, i.e., at the end of the TGA run, are recorded in Table IV-D4.

D.4.3 Differential scanning calorimetry (DSC) procedure

A 3-7 mg polymer sample was evaluated with a DSC-PYRIS 1 instrument from PerkinElmer, calibrated by an indium metal. Heating and cooling cycles for non-isothermal analysis were performed under a dry nitrogen flow at 20 mL min^{-1}. Samples (the same as those listed in **Sect. S4.1**) were heated from 40˚C to 200˚C at a rate of 10˚C min^{-1} (first heating cycle), then held constant for 5 min at a temperature of 200˚C. Afterward, the sample was cooled at a rate of -10 ˚C min^{-1} until reaching -50˚C and held for 5 min. Subsequently, a second heating-cooling cycle was employed using the same parameters as the first cycle. Afterward, the temperature and melting enthalpy (T_m and ΔH_m, respectively) were determined from the first heating cycle thermogram. After that, the values of crystallinity for the films' PBAT and PLA components were calculated as follows:

$$X_c = \left(\frac{\Delta H_m}{\Delta H_m^c}\right)$$
(D13)

where X_c is the mole fraction of crystalline morphological regions, ΔH^c_m is the fusion enthalpy for a pure crystalline polymer, 114 J g^{-1}, and 293 J g^{-1} for PBAT and PLA, respectively (Pathan *et al.*, 2020; Wahl *et al.*, 2021), ΔH_m is thus proportional to PBAT's crystallinity. In contrast, the glass transition temperature (T_g) was derived from the second heating cycle.

D.4.4 DSC results

Values for the thermal properties of the PBAT and PLA/PHA are given in Table IV-D 5, which are similar to published values (Büks *et al.*, 2020). CRYO-PBAT MPs-CRYO and NPs shared similar T_m and T_g values as the original mulch film, with ΔH_m being highest for MPs, followed by NPs and then the original film. The elevated values of ΔH_m for MPs can also represent the formation of crosslinks via Norrish type II photodegradation reactions; however, FTIR spectra show no evidence of this reaction occurring, as discussed below (Wu *et al.*, 2020). For W-PBAT, T_m and T_m decreased upon the size reduction process and weathering; in contrast, ΔH_m, increased and, consequently, X_c for PBAT was highest for W-MPs, 35.2%, compared to 31.2% for CRYO-MPs (Table IV-D5).

D.5.5 Fourier transform infrared (FTIR) procedure

The effect of size reduction on chemical bonding for the samples identified in Sect. D4.1 was analyzed via FTIR spectroscopy using a "Spectrum One" spectrometer from Perkin Elmer (Waltham, MA, USA) fitted with a diamond ATR attachment, and Spectrum Image R1.7 software from Perkin-Elmer was used for spectra analysis. Spectra between 4000 and 600 cm^{-1} were collected at a spectral resolution of 2.0 cm^{-1} in absorbance mode and averaged 32 scans per spectrum. In addition, background spectra were collected in the air. Five FTIR spectra per sample were collected and normalized using the most significant absorbance value. FTIR vibration bands were assigned and evaluated based on a previous publication (Hayes *et al.*, 2017) and are listed in Table IV-D6.

D.5 BIODEGRADATION OF MNPs IN COMPOST-ENRICHED SOIL

D.5.1 Procedure for biodegradability testing

Biodegradability testing of MPs and NPs of BDMs in soil was performed following the standardized test method, ASTM D5988-12, by CO_2 evolution measurement, as described in our previous paper (Anunciado *et al.*, 2021). The soil samples were collected with a soil auger from an agricultural test field at the East Tennessee AgResearch and Education Center- μm (35.898717, -83.961297) from a depth ranging between 0-20 cm. At the exact location, environmental weathering of the PBAT and PLA/PHA mulches occurred in 2017. The C/N ratio of soil was analyzed at 10.2. Collected soil was sieved to 2 mm particle size and enriched with compost from the University of Tennessee Compost Facility, Knoxville, TN, USA. The soil moisture content was determined by drying for 24 hours at 105 $^{\circ}$C. The final soil moisture used for the biodegradation experiments was adjusted to 14.6% (about 50% of the water holding capacity). The soil pH was determined by a slurry composed of soil and deionized water at a ratio of 1:2.5 (w/v).

The CO_2 air headspace sampling was performed through 20 mm gray butyl stoppers (Millipore Sigma, Burlington, MA, USA) mounted on each lid. Amounts of MNPs used for each experiment followed ASTM 5988 recommendations (200–1000 mg carbon/100–500 g soil). Therefore, each incubation jar contained 50 g of soil well dispersed with 200 mg (100 mg of carbon) of either biodegradable MPs or NPs. Soil moisture was monitored weekly during incubation time by gravimetric analysis, and water was added when the water loss through evaporation was detected at > 1%. Incubation samples were prepared in triplicates to reduce measurement variation among jars. The incubation temperature was maintained at 27 $^{\circ}$C. An infrared gas analyzer measured the CO_2 evolution in the jar's headspace versus time in duplicates for each jar (LI-820, LiCor, Lincoln, NE, USA). Each measurement series employed CO_2 gas standards with concentrations in N_2 of 1000 ppm, 1 vol %, and 5% (Gasco, Oldsmar, FL, USA), where soda lime was used as a zero-concentration standard. The standard samples were the basis for calculating CO_2 evolution, and sampling frequency was adjusted according to the CO_2 evolution over time. For the initial weeks, three samples were taken, and lower CO_2 respiration due to decreasing microbial activity resulted in 1 measurement per week. In addition, jar venting occurred once a week, which allowed the purging of accumulated CO_2 by opening the lid. The

biodegradability experiments included two BDM polymers film materials (PBAT and PLA/PHA), two-particle sizes reflected by a d_p of 106 μm (MPs) and 300 nm (NPs), as well as two treatments CRYO (cryogenically treated) and W (environmentally weathered) and three controls: soil containing microcrystalline cellulose powder (average particle size 50 μm, Item #AC387242500, Thermo Fisher Scientific Inc., Waltham, MA, USA), a blank sample (soil only) and a technical control (air only).

D.5.2 Results: biodegradation of MPs and NPs, CO₂ evolution

The CO_2 evolution profiles from the biodegradation experiment evaluated the differences as a function of BDM materials (PBAT and PLA/PHA), particle sizes (MPs and NPs), and pretreatment (CRYO and W). The CO_2 evolution profiles (Figure IV-D15) were used to calculate percent biodegradation (Figure IV-C6) along with the measured carbon content of the films, through calculations of polymeric carbon depletion, as described in ASTM D5988-12.

D.5.3 Statistical analysis of biodegradation data

Confirmation of statistical difference was conducted through failure plots (Kaplan Meier) by evaluating the carbon consumption/day in relation to biodegradation, which revealed significant lower biodegradation values for PLA/PHA compared to PBAT (p= 0.0044) and W- compared to CRYO- (p = 0.0047) (Figure IV-D16). The degradation profiles between PBAT and PLA/PHA particles (MPs and NPs combined) indicate similar biodegradation kinetics up to 25% biodegradation. The comparison between CRYO- and W-MNPs (collectively) shows that the former particles start at higher "survival rates" compared to the latter particles up to 75% mineralization, where a reverse trend was observed (Figure IV-D16b).

For PBAT, the MP particles for CRYO (95%) and W (90%) showed similar CO_2 evolution patterns over 154 days of biodegradation, reflecting the biodegradation values of all BDMs (Table IV-D 7). A slower initial mineralization rate (initial 37 days) was observed for PBAT NPs-W (0.9%/day) than NPs-CRYO (1.2%/day). However, the biodegradation rate/day increased for the former polymer and reached a plateau after 87 days of incubation, resulting in maximum mineralization of 90%.

For PLA/PHA, the MPs-CRYO indicated fast initial biodegradation within the first 45 days, similar to the PLA/PHA NPs-CRYO fraction (Figure IV-C6b and Figure IV-D17c). However, the

140

latter experiment produced smaller mineralization (71%) than the former (89%). In contrast, W-PLA/PHA MPs underwent a slower biodegradation rate than the -CRYO fraction throughout the experiment, with 61% being the maximum value. This observation of lower biodegradation of W-PLA/PHA BDMs, particularly for MPs, may be attributed to crosslinking formation due to photodegradation during environmental weathering, as detected in previous studies (Hayes *et al.*, 2017; Katsumi *et al.*, 2020). In addition, W-PLA/PHA NPs produced substantially lower CO_2 values (43%) compared to CRYO-PLA/PHA NPs (71 %) after 154 days of incubation. This observation of lower biodegradation rates for the former may be attributed to crosslinking of PLA and $CaCO_3$, as confirmed in DLS in this study (Anunciado *et al.*, 2021). CO_2 evolution from soil remained minimal ($< 2\%$) throughout biodegradation (Figure IV-D15).

Interestingly, the average values and data variability of biodegradation were similar between PBAT and PLA/PHA BDMs during the initial 60 days. However, the mineralization values increased for PBAT as the data variation decreased. In contrast, the biodegradation values were

significantly lower for PLA/PHA, indicating a more significant data variation with advancing monthly biodegradation (Figure IV-D17c). This monthly observation suggests that PBAT MNPs biodegrade more uniformly than MNPs from PLA/PHA, independent of particle size or pretreatment, as depicted in Figure IV-C6 (main paper). The average daily CO_2 evolution profiles during the first 30 days indicate smaller values for MPs than NPs, followed by a gradual increase of mineralization rate/day for both PBAT and PLA-PHA peaking at 1.1 %/day and 0.7 %/day, respectively, within the following 30 days. After 60 days of mineralization, the daily decomposition rates of PBAT and PLA/PHA decreased, indicating similar C-depletion after ~100 days of incubation. In contrast, PBAT-NPs followed a constant average trend at 0.9 %/day throughout the first 60 days, followed by a sharp decline in mineralization rate. The peak may be attributed to adding 2 ml H_2O into each jar due to evaporation during the jar venting processes. Interestingly, PLA/PHA-NPs peaked after 30 days, followed by a gradual mineralization drop for MPs (Figure IV-D17 a). For NPs, it is interesting to note that PBAT showed constant but higher daily mineralization than PLA/PHA during the initial 60 days and resulted in a significant drop in mineralization.

D.5.3 Biodegradation time prediction for MPs and NPs in soil

The collected CO_2 evolution profiles were converted into biodegradation data fitted with nonlinear models, to provide a numerical assessment of MPs and NPs biodegradation in soil. The goodness of fit analysis of exponential distributions identified statistical models in accordance with the experimental data. Following the prediction profiler, DT50 values (time required for 50% mineralization of the initial BDM concentration) and the time for complete biodegradation 100% was estimated (Table IV-D8). According to the curve fitting procedure, three main models were detected such as *Logistic 4P*, *Biexponential 4P,* and *Cell Growth 4P*, where 4P depicts the *'four parameters'*.

The **Logistic 4P** was determined as the best fit for **all PBAT** feedstocks, except W-NPs, described as:

$$Y = c + \left(\frac{(d - c)}{1 + \exp\big(-a * (Time - b)\big)} \right) \tag{D14}$$

where Y = biodegradation, a = growth rate, b = inflection point (i.e., the point on the S shaped curve halfway between c and d); c= lower asymptote (horizontal line) the minimum value that can be obtained (i.e. what happens at 0 biodegradation), d = upper asymptote, which is the maximum value that can be obtained

The **Bi-exponential** response model was found as the best fit for all **PLA/PHA MPNs** and **cellulose** and is defined as:

$$Y = a * \exp(-b * Time) + c * \exp(-d * Time) \tag{D15}$$

where a = scale 1-parameter, which represents the 'time' until an event occurs, b = decay rate of MNPs, c = scale 2-parameter, and d = decay rate 2 of MNPs.

142

The '**Cell Growth 4P'** function represents the best fit only for **W-PBAT-NPs** and is described as:

$$Y = \left(\frac{(a * b)}{(a - b) \exp(-Time * c) + b \exp(Time * d)} \right)$$

(D16)

where a = Ymax represents the maximum value of biodegradation, b = Y0 (starting value at time 0, c = division point, d = mortality (degradation)

The data fitting results of the biodegradation profiles are reported in Table IV-D8)

In accordance with the prediction profiler, the predicted time for complete biodegradation 100% Prediction of biodegradation times range between 193 days for W-PBAT-NPs and 424 days for W-PBAT-NPs, indicative that chemical changes due to environmental weathering results.

TDT50 biodegradation occurred at a higher extent for PBAT-MNPs than for PLA/PHA MNPs ranging between 51% -70% for the former and 50%-199% for the latter feedstock.

A similar trend was observed biodegradation, whereas W-PBAT NPs are expected to fully mineralize within 199 days, whereas the W-PLA/PHA indicate a significantly longer biodegradation time of 424 days for 100% mineralization (Figures IV-D19, 20, 21) and (Table IV-D8). The prediction method identified differences of dynamic process kinetics based on particle sizes and polymeric feedstocks, providing additional information on the biodegradation process of MPs and NPs for future biodegradation experiments.
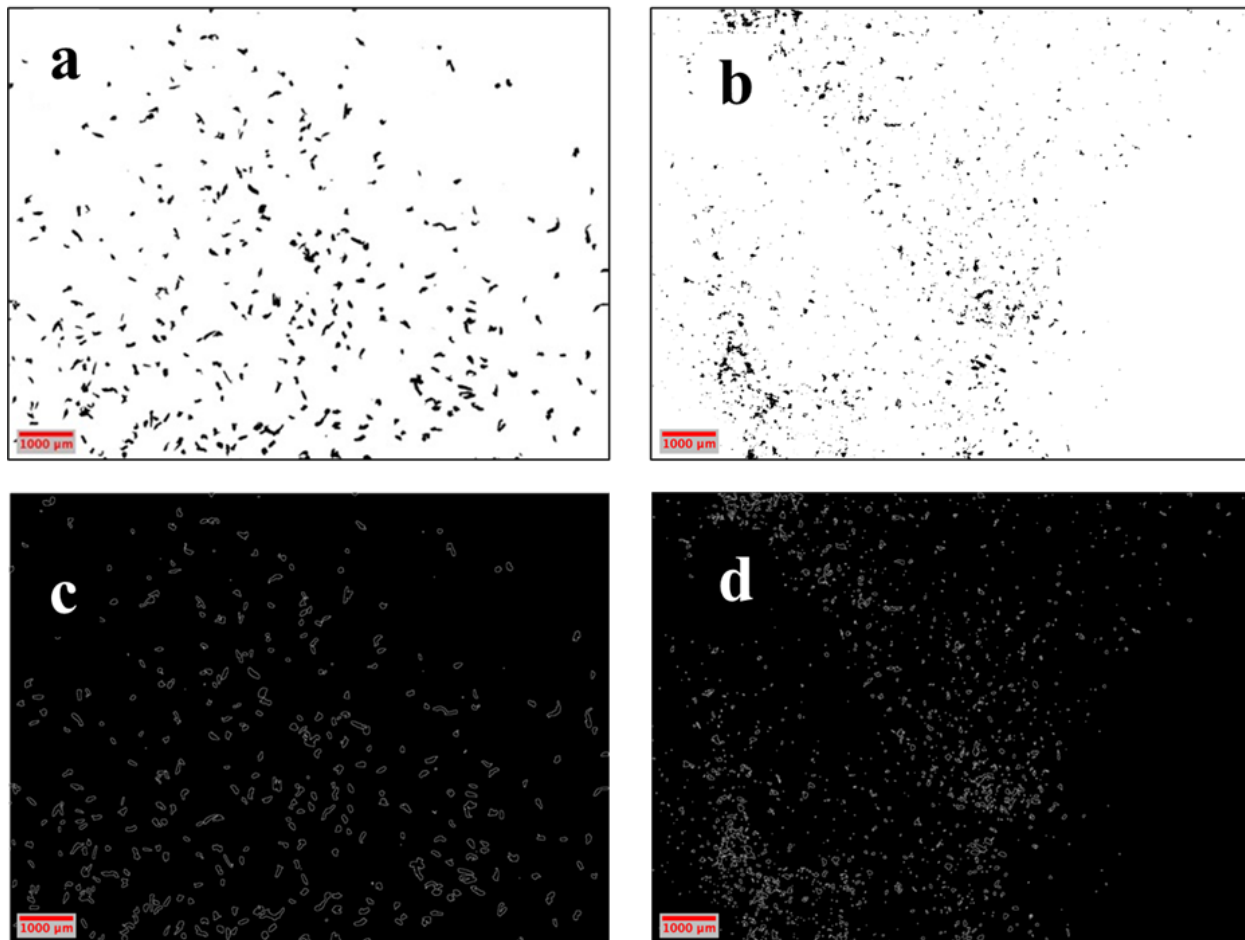
Figure IV-D1. Stereomicrographs (a,b) and derived images (c,d) obtained through ImageJ analysis for PBAT MPs, 106 μm fraction sieving fraction, Figs. a and c refer to cryogenically treated (CRYO) PBAT MPs, while Figs. b and d refer to weathered (W) PBAT MPs. The data of this figure were used to prepare the histograms of particle diameter depicted in Figure IV-C2a, b.
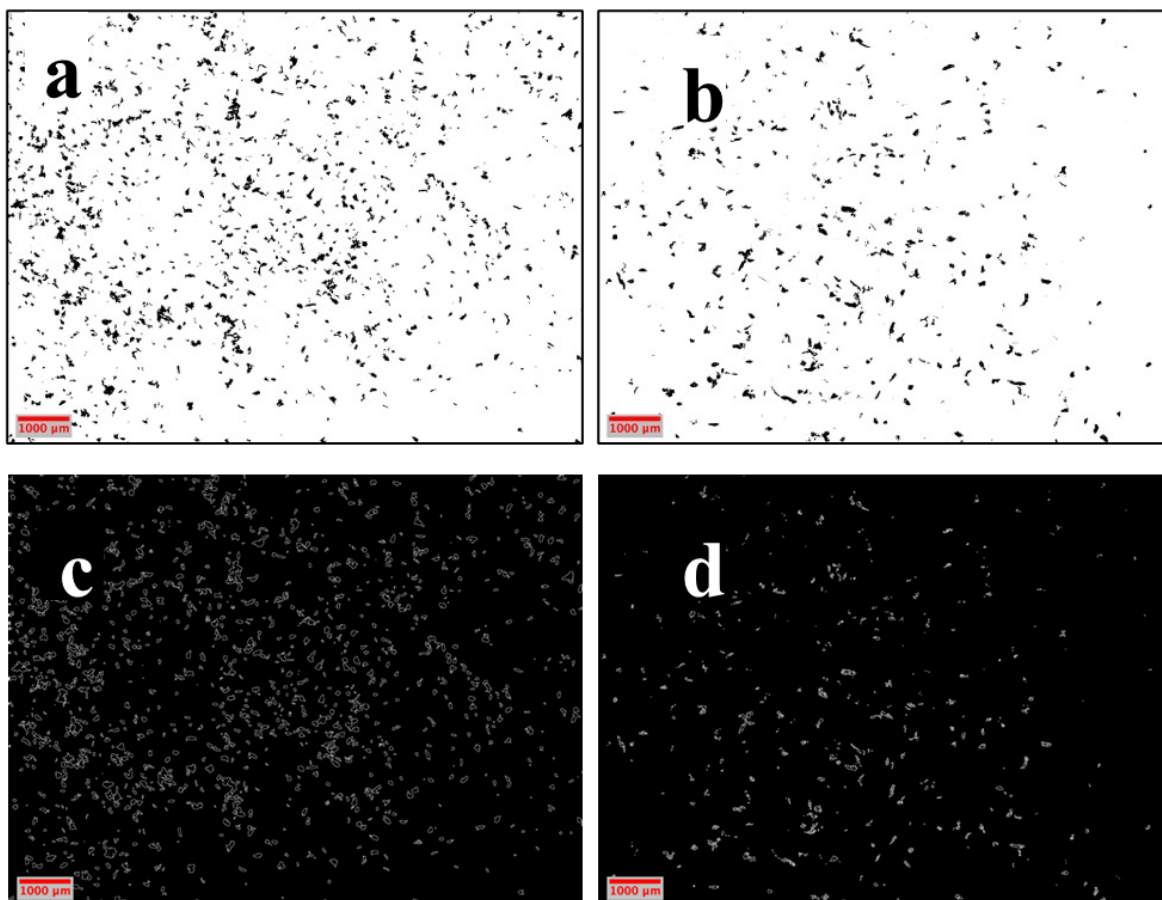
Figure IV-D2. Stereomicrographs (a,b) and derived images (c,d) obtained through ImageJ analysis for PLA/PHA MPs, 106 μm fraction sieving fraction, Figs. a and c refer to CRYO-PLA/PHA MPs, while Figs. b and d refer to W-PLA/PHA MPs. The data of this figure were used to prepare the histograms of particle diameter depicted in Figure IV-C2c,d.
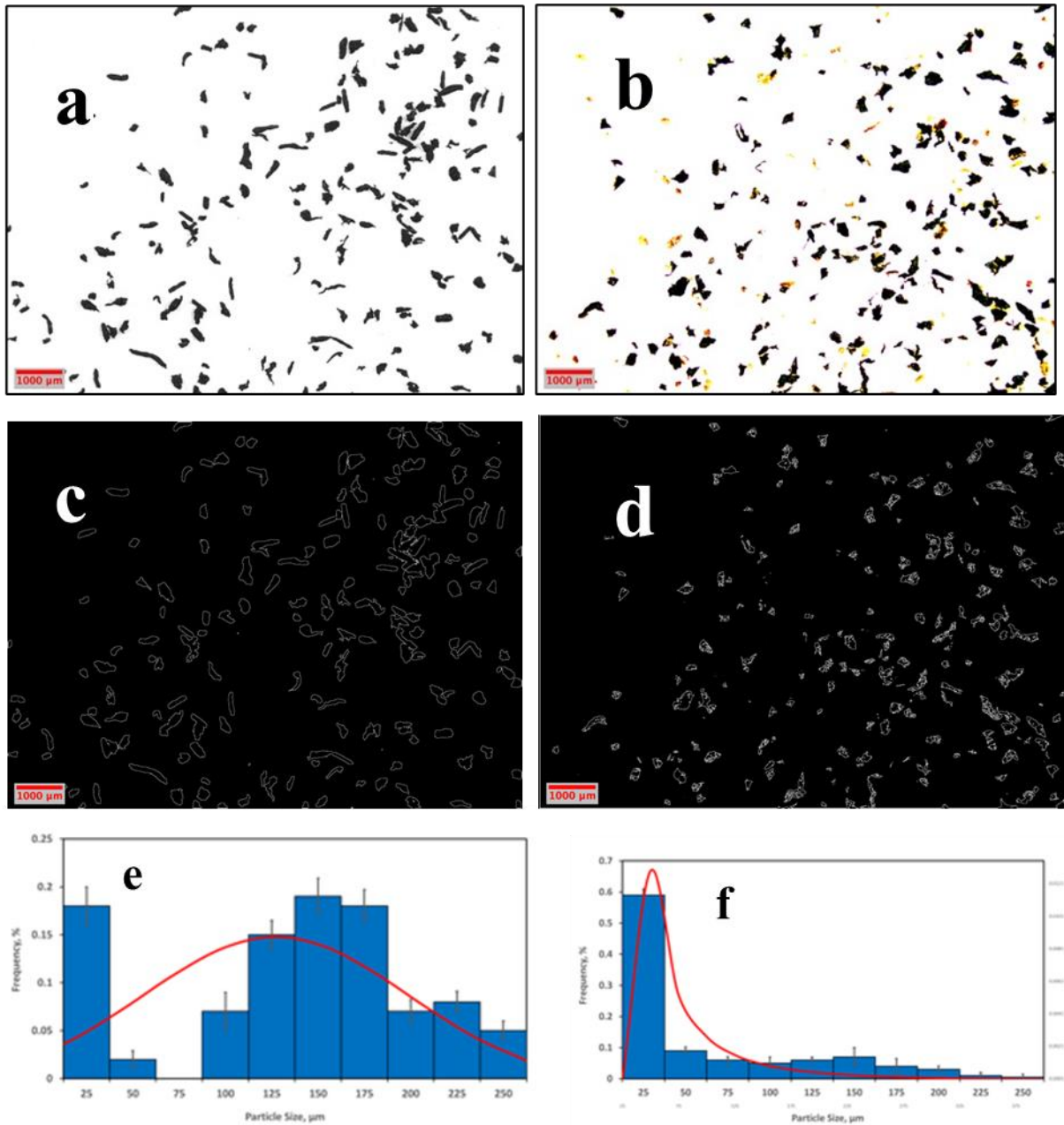
Figure IV-D3. Stereomicrographs (a,b) and derived images (c,d) obtained through ImageJ analysis for PBAT MPs, 250 μm fraction sieving fraction, Figs. a and c refer to CRYO-PBAT MPs, while Figs. b and d refer to W-PBAT MPs. Histograms of particle diameter (d_p) derived from Figs. c and d via ImageJ are given in Figs. e and f, respectively. Coplotted on the latter two figures are the best-fit models for describing the d_p distributions: normal- and lognormal, respectively. Yellow particles in Fig. b represent residual soil, which were excluded in the d_p calculation.
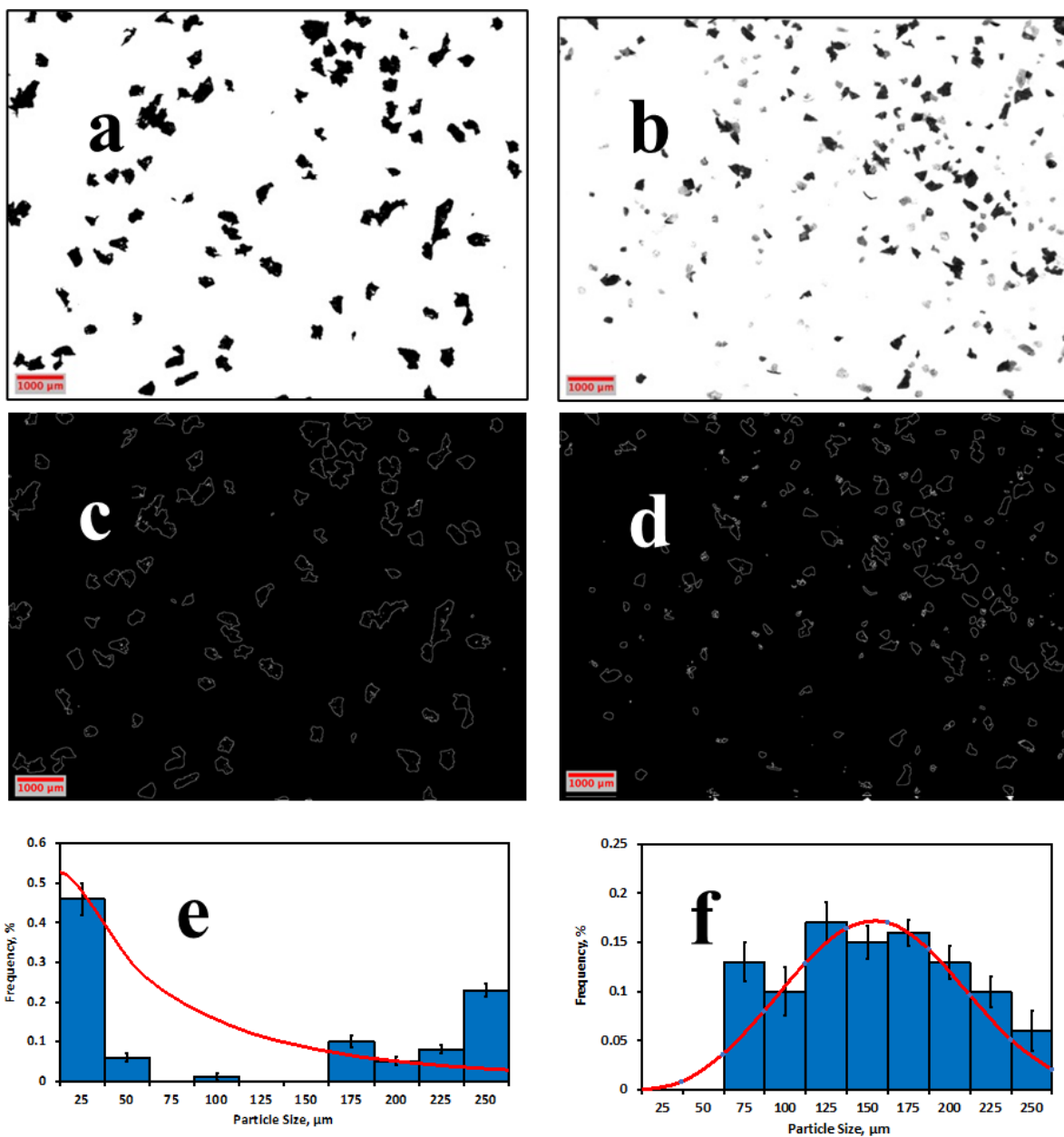
Figure IV-D4. Stereomicrographs (a,b) and derived images (c,d) obtained through ImageJ analysis for PLA/PHA MPs, 250 μm fraction sieving fraction, Figs. a and c refer to CRYO-PLA/PHA MPs, while Figs. b and d refer to W-PLA/PHA MPs. Histograms of particle diameter (d_p) derived from Figs. c and d via ImageJ are given in Figs. e and f, respectively. Coplotted on the latter two figures are the best-fit models for describing the dp distributions: Weibull. Gray particles in Fig. b represent residual soil, which were excluded in the d_p calculation.
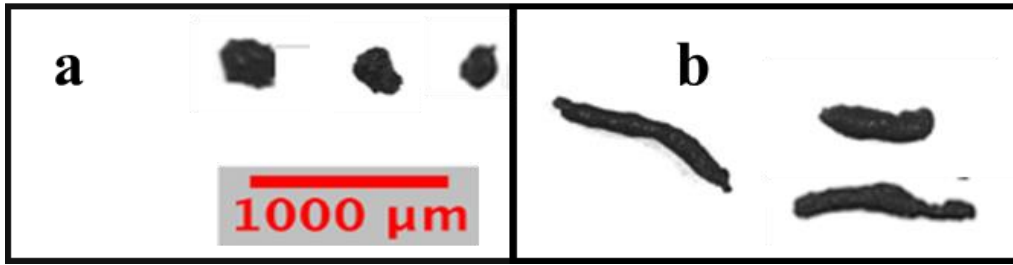
Figure IV-D5. Particle shape comparison between (a) nearly circular and (b) elongated MPs with different aspect ratios derived from the CRYO-PBAT 250 µm stereomicroscopic image.
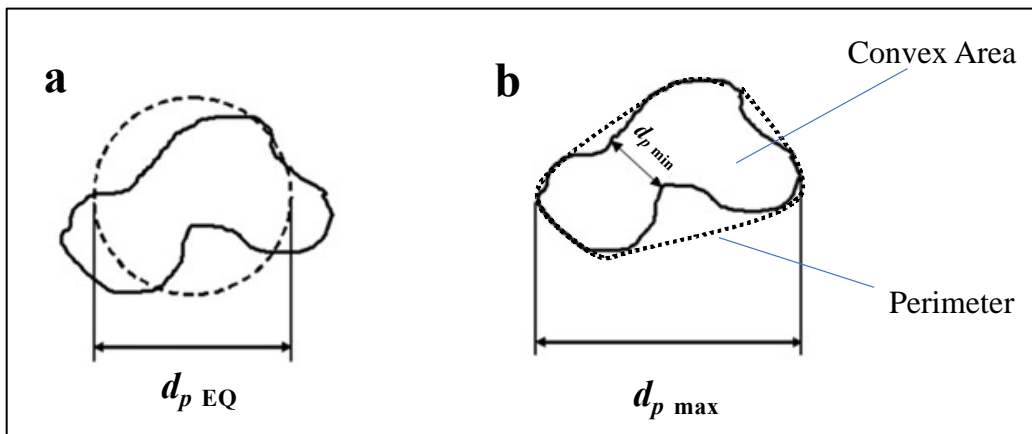
Figure IV-D6. Diameter definition (a) $d_{p\ EQ}$ =diameter of a circle of equal projection area. (b): $d_{p\ min}$ = minimum particle diameter; $d_{p\ max}$ = maximum particle diameter; image adapted from (Redondo-Hasselerharm *et al.*, 2020).

148

D3. RECOVERY AND AVERAGE SIZE OF MPs BETWEEN SIEVE FRACTIONS
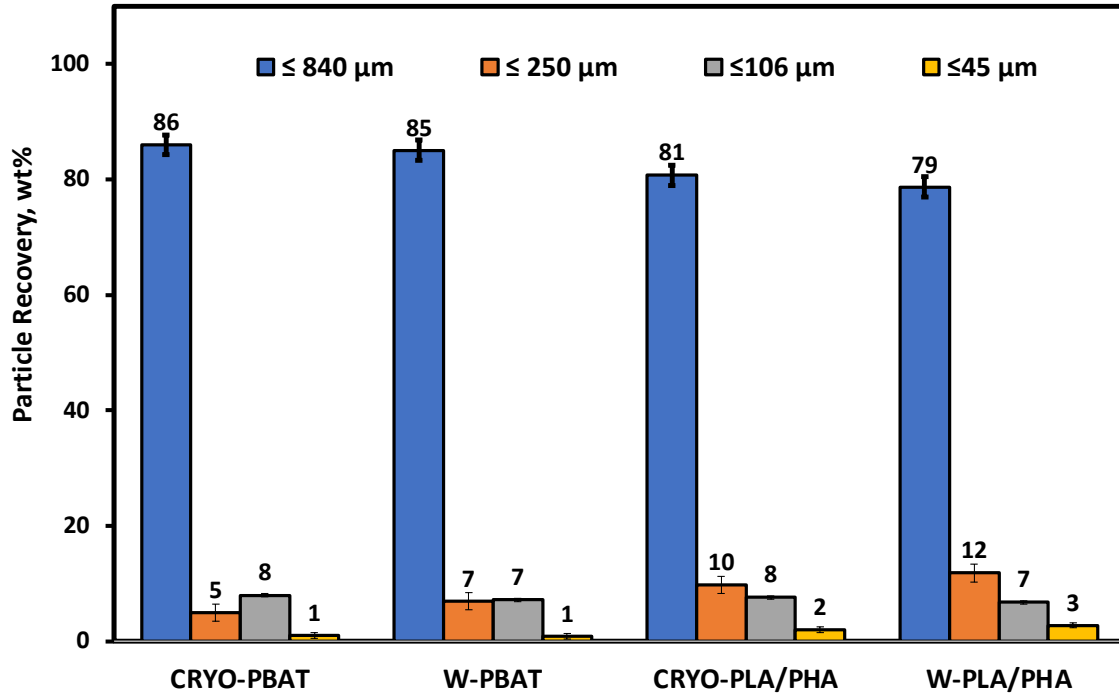
Figure IV-D7. Sieving fraction % mass recovery: comparison of cryogenically treated (CRYO-) and weathered (W) average particle size (d_p) between PBAT and PLA/PHA (fractions obtained via dry milling (≤ 840 μm, ≤ 250 μm, ≤ 106 μm, and ≤ 46 μm sieves with two replicates) of 1 g of feed, followed by sieving. For interpretation of the references to color in this figure legend. Each error bar is constructed using one standard error from the mean. (n=3; error bars reflect standard deviation)
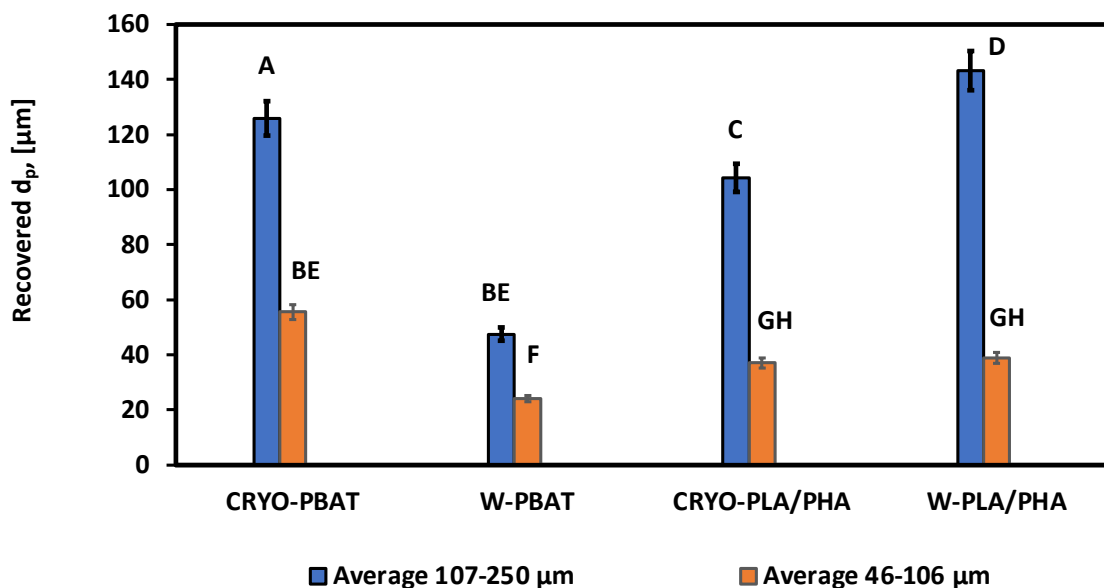
Figure IV-D8. Comparing average particle sizes (d_p) obtained from dry milling and sieving fractions (250 μm and 106 μm) according to statistical analysis for PBAT and PLA/PHA. Each error bar is constructed using one standard error from the mean. Mean values that do not share common capital letters represent a statistically significant difference.
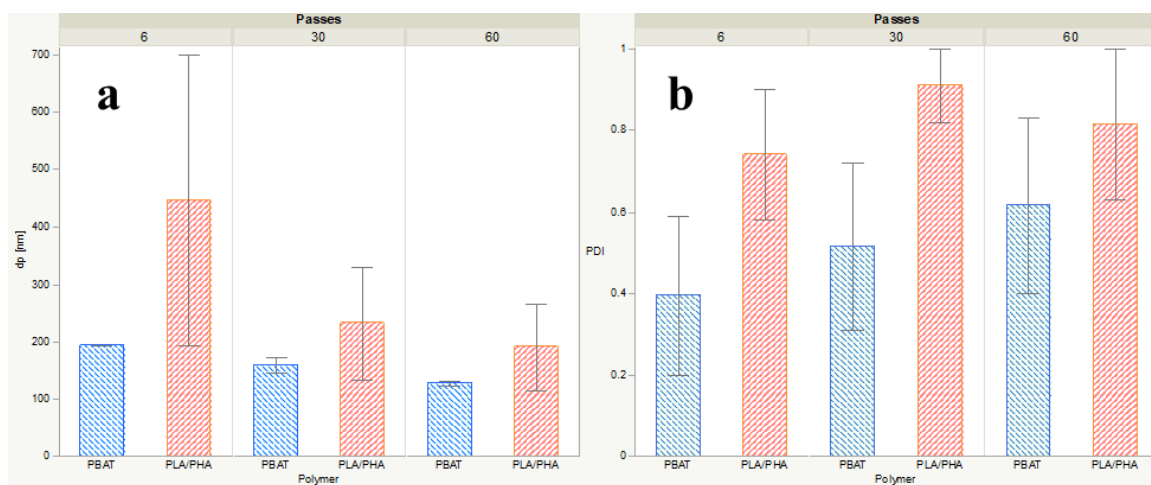
Figure IV-D9. Comparison of (a) average particle size (d_p) and (b) polydispersity index (PDI) for PBAT and PLA/PHA NPs (data from CRYO- and W- treatments pooled together). Error bars correspond to 1 standard error from the mean.
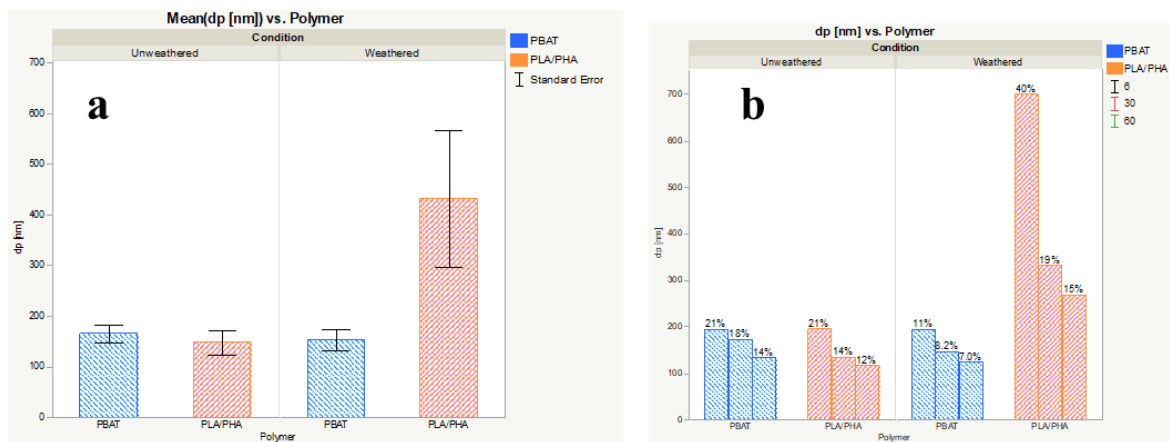
Figure IV-D10. Comparison of mean d_p values for PBAT and PLA/PHA NPs prepared from unweathered (i.e., cryogenically treated) vs. environmentally weathered films. (a) d_p values pooled together for 6, 30, and 60 passes. (b) d_p values differentiated between different numbers of passes. Error bars reflect one standard error from the mean.
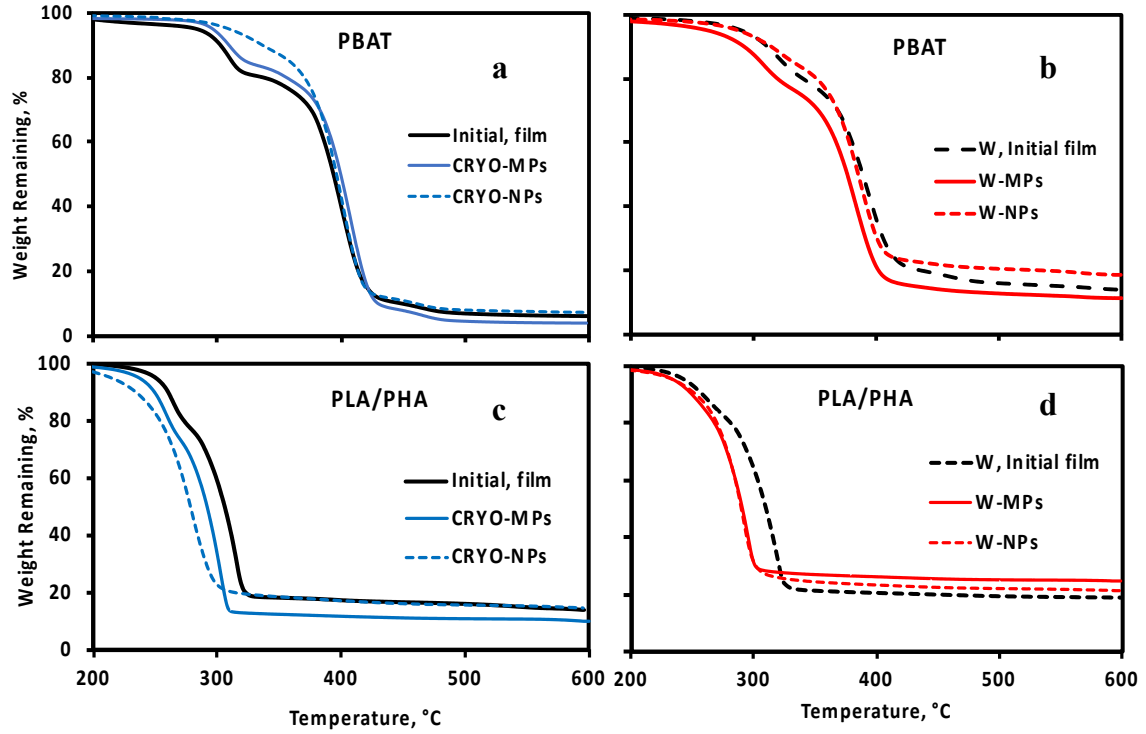
Figure IV-D11. Representative TGA thermograms of cryogenically treated (CRYO) and environmentally weathered (W) polymeric films, MPs (106 μm sieve fraction), and NPs (60 wet grinding passes of 106 μm sieve fraction) (a) CRYO-PBAT, (b) W-PBAT, (c) CRYO-PLA/PHA, and (d) W-PLA/PHA. The initial unweatehred and weathered film data were retrieved from Hayes *et al.* (2017).
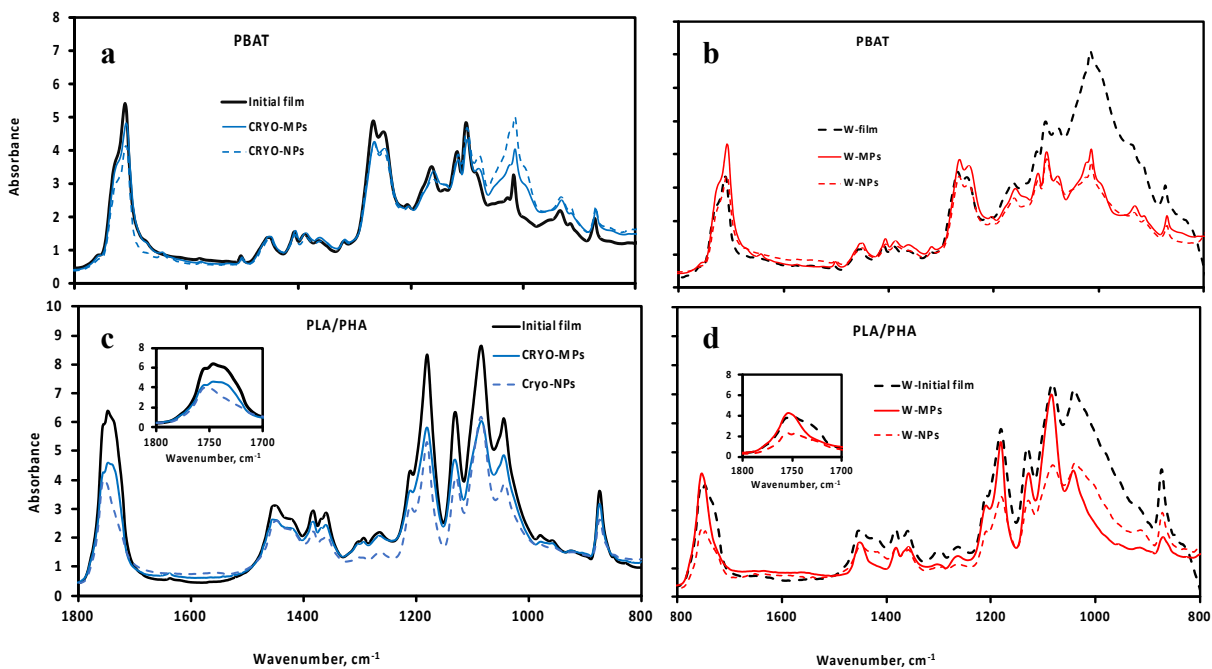
Figure IV-D12. Changes in chemical bonding of the initial (untreated) and weathered films due to size reduction into MNPs. (a, b) PBAT and (c, d) PLA/PHA; (a,c) cryogenically treated (CRYO) and (b,d) environmental weathered (W) plastic films and their MPs and NPs. MPs consist of the 106 μm sieve fraction of dry milled plastics; NPs were produced via wet grinding (60 passes) of the 106 μm sieve fraction. The "Initial" and "W-film" data were obtained from Hayes *et al.* (2017).
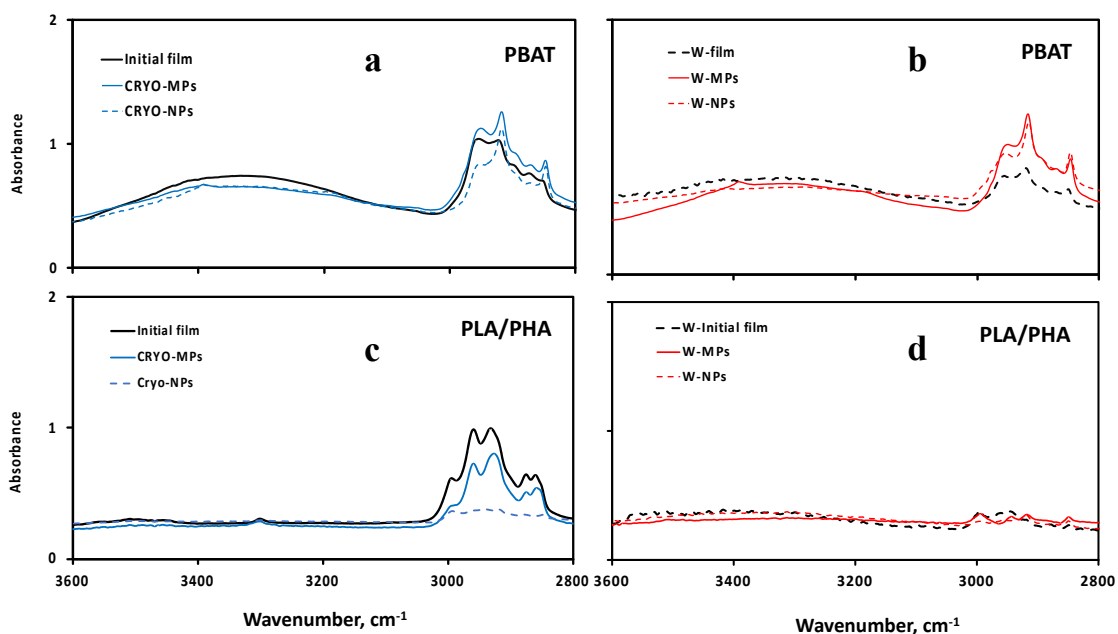
Figure IV-D13. Chemical bonding comparison of FTIR spectra (a) CRYO-
and (b)W-PBAT and (c) CRYO-PLA/PHA and (d) W-PLA/PHA between the
initial plastic mulch film materials and their MPs and NPs. CRYO represents
cryogenically milled MPs, and W- film materials underwent agricultural
weathering (150 days). The fraction of MPs reflects sieving fractions of 250
µm, and NPs represent the particle fractions after grinding 60 passes of the
106 µm MPs fraction.
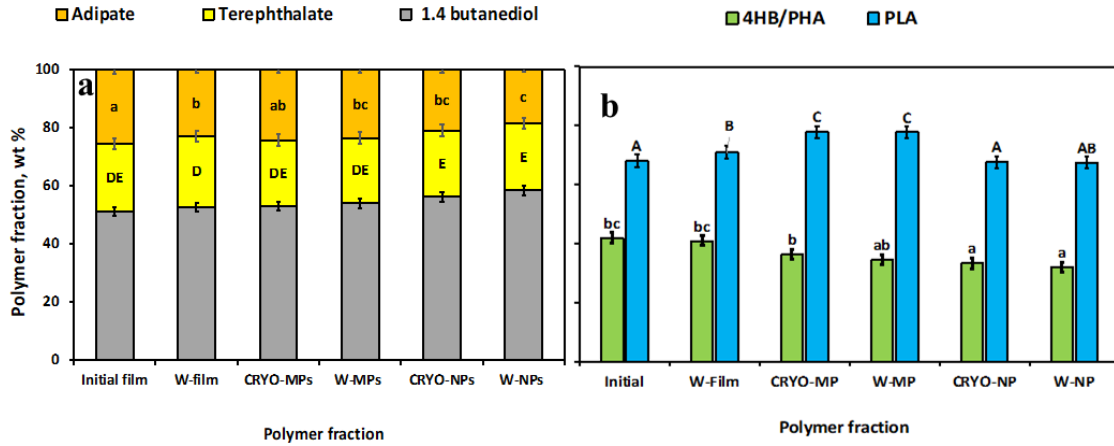
Figure IV-D14. Change of relative polymeric composition of (a) PBAT derived from (a, b) NMR spectra to assess the weight fractions for adipate, terephthalate, and 1,4 butanediol components relative to the total mass. Effect of cryogenic treatment (b) (CRYO) and environmental weathering (W) weathering polylactic acid (PLA) mass fraction among the polymers and 4-hydroxybutyrate (4HB) monomer units among polyhydroxyalkanoate (PHA) of the "Initial" PLA/PHA film based on NMR analysis. Error bars reflect standard deviation (n = 2) and means (across treatments) that do not share common capital, and lowercase letters reflect a statistically significant difference (p <0.05). "Treatment" refers to initial vs. agriculturally weathered. Data from the "Initial" mulch films was obtained from (Hayes *et al.*, 2017).
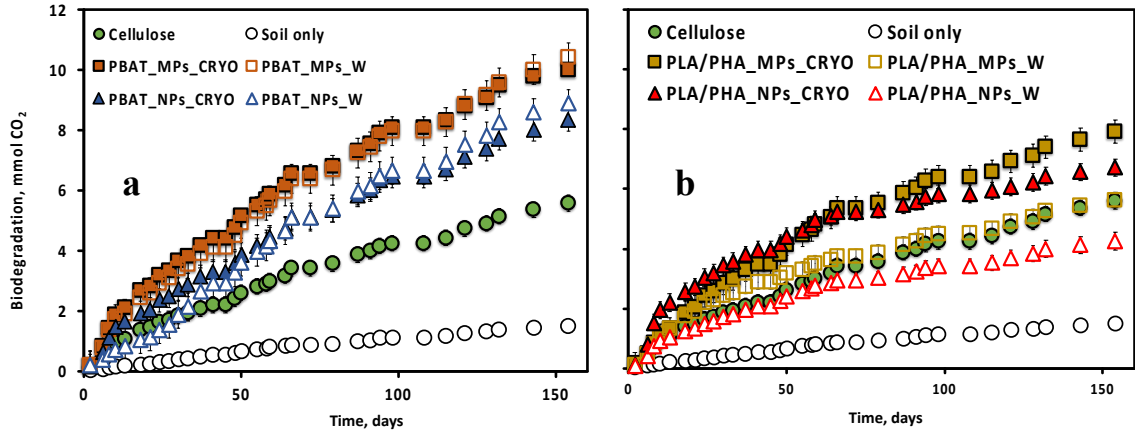
Figure IV-D15. CO_2 evolution profiles of mulches (a) PBAT and (b) PLA/PHA treatments during time-course biodegradation according to ASTM D5988 standardized test method.
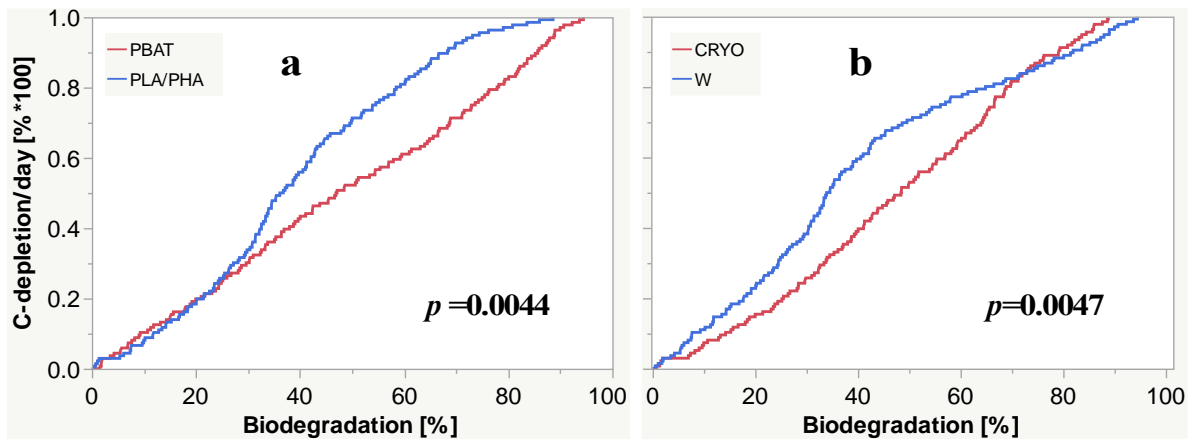
Figure IV-D16. Failure (Kaplan Meier) plot depicting the statistical comparison between (a) polymer type and (b) means of embrittlement applied to the biodegradation rate (% biodegradation /d) during the time course of biodegradation. Statistical difference was detected by employing the Wilcoxon group homogeneity test.
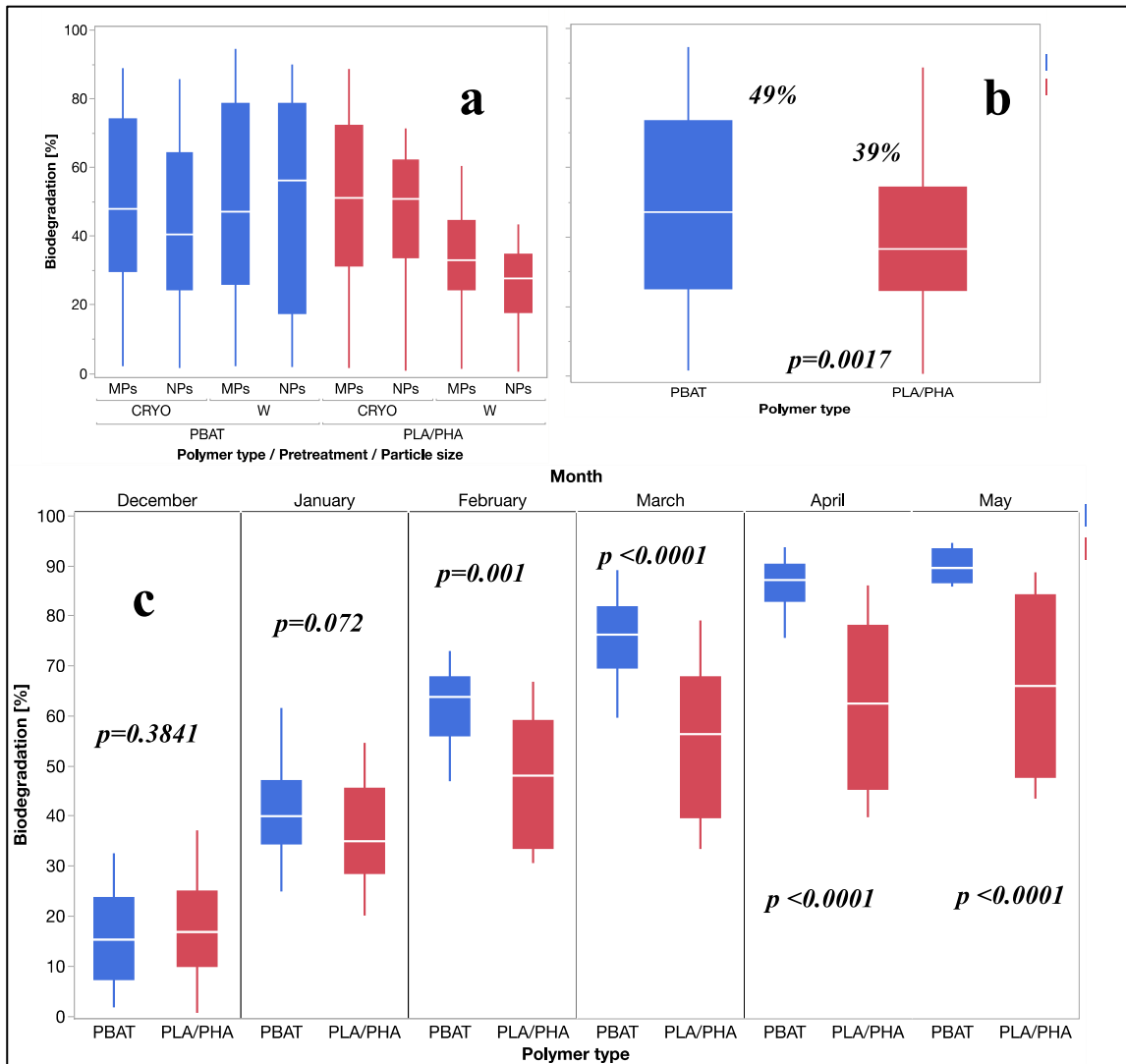
Figure IV-D17. Box plot and statistical comparison of biodegradation between (a) MPs vs. NPs and film pretreatment and (b) polymer type for cumulative biodegradation, and (c) monthly progress for biodegradation for PBAT vs. PLA/PHA-derived MNPs (data for MP and NP and CRYO- and W- for a given film type pooled).
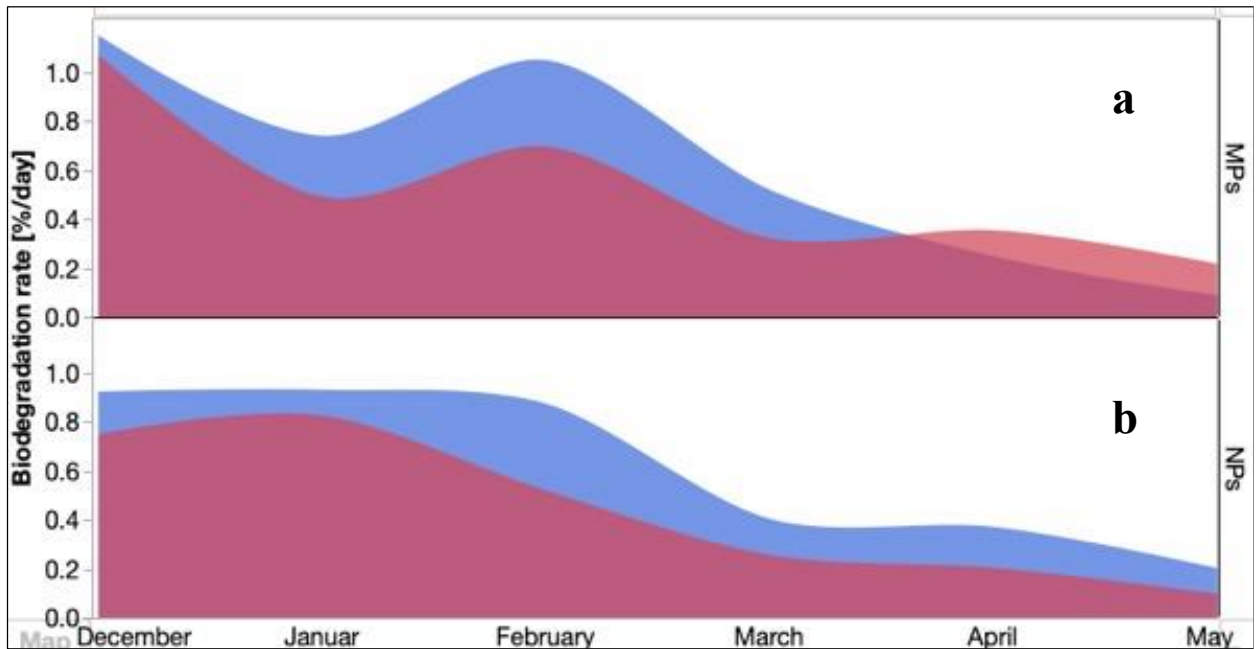
igure IV-D18. Time series plot comparing the average CO2 evolution rates %
per day MNPs derived from PBAT and PLA/PHA films. (Data for CRYO-
and W- treatments pooled together) (a) MPs and (b) NPs (n=3).
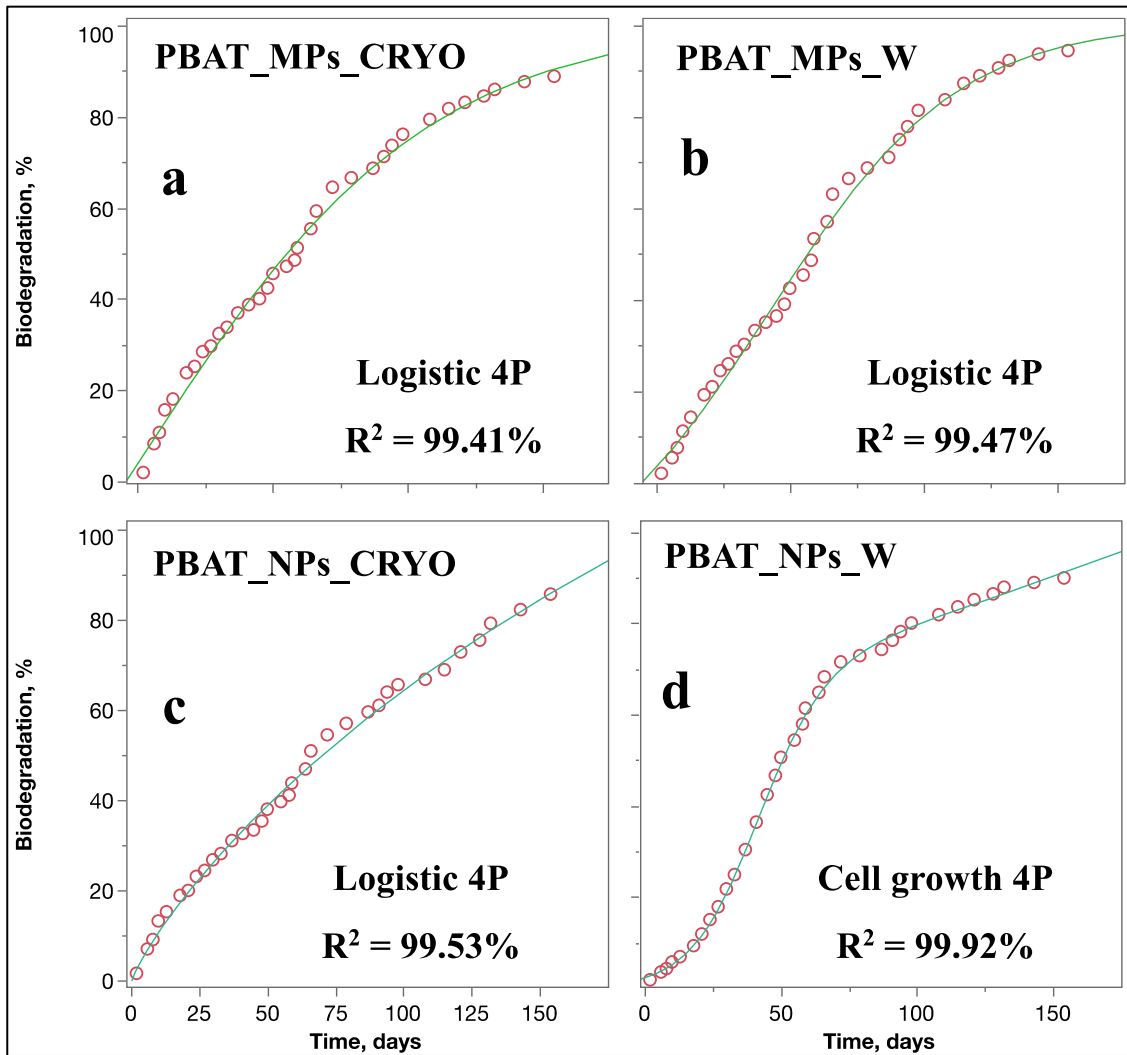
Figure IV-D19. Exponential curve fitting on the cumulative mineralization profiles of unweathered (a, b) and weathered and PBAT BDMs represend by MPs (a, b) and NPs (c, d) during 154 days of soil incubation.
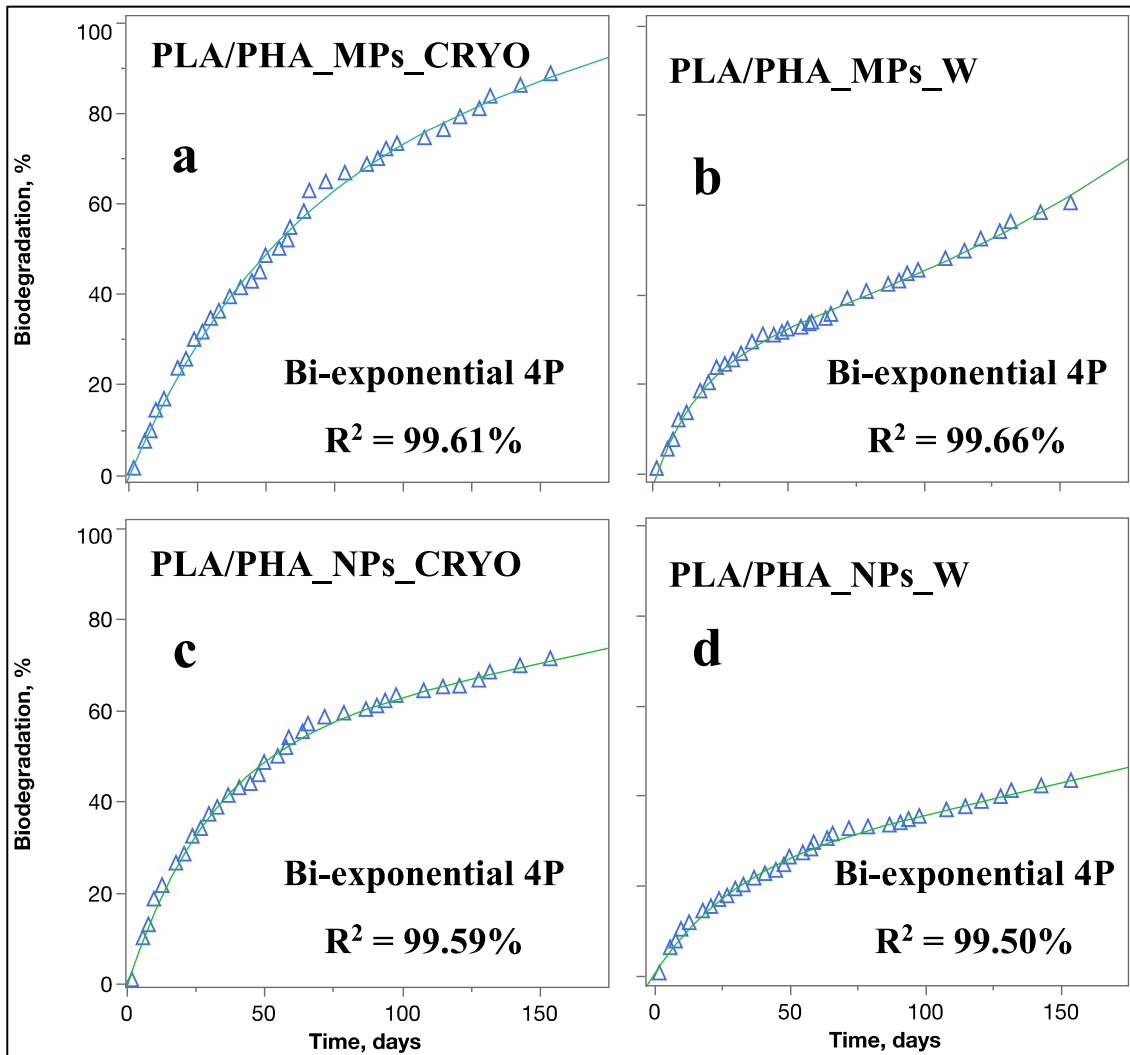
Figure IV-D20. Curve fitting diagrams of the cumulative biodegradation profiles of unweathered (a, b) and weathered and PLA/PHA BDMs represend by MPs (a, b) and NPs (c, d) during 154 days of soil incubation.
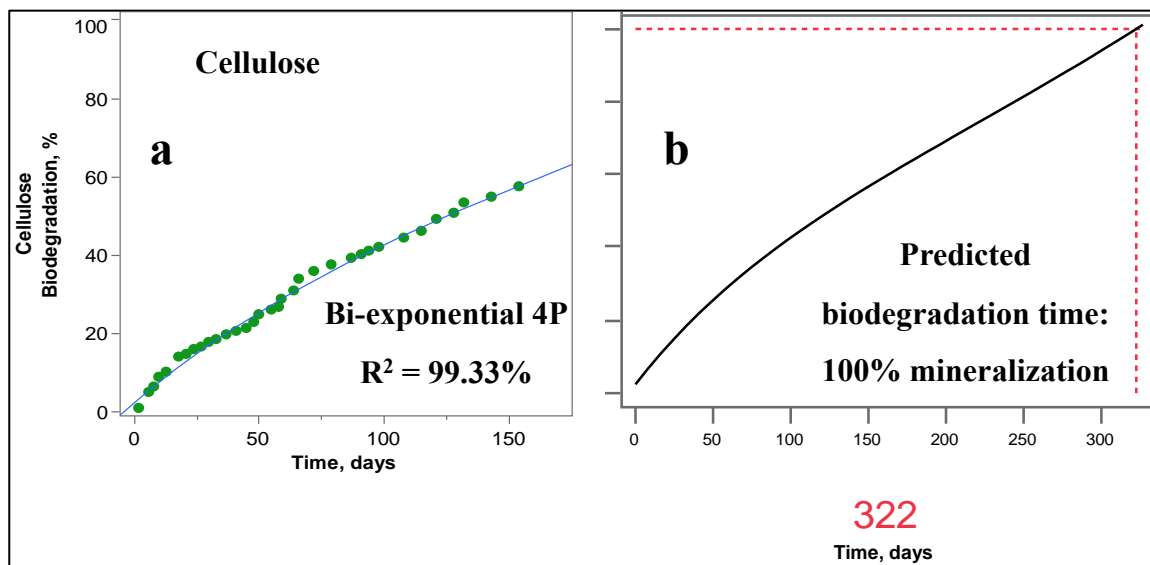
Figure IV-D21. (a) Curve fitting on the CO_2 evolution profile microcrystalline cellulose biodegradation. Cellulose was used as a positive control for the biodegradation study. (b) the '*prediction profiler*'JMP

Table IV-D1. Comparison of particle count, the projected particle area, and shape parameters between the 106 µm and 250 µm MP sieve fractions from cryogenically-embrittled (CRYO) and environmentally weathered (W) PBAT and PLA/PHA BDMs.

Parameters[1]	CRYO-PBAT	W-PBAT	CRYO-PLA/PHA	W-PLA/PHA
$d_p \leq 106$ µm				
Area [µm^2] x 10^4	0.78 ± 0.15	0.13 ± 0.01	0.37 ± 0.01	0.43 ± 0.01
Aspect Ratio (AR)	2.26 ± 0.2	1.76 ± 0.1	2.21 ± 0.3	2.10 ± 0.1
Roundness	0.53 ± 0.01	0.63 ± 0.01	0.53 ± 0.01	0.53 ± 0.01
Solidity	0.80 ± 0.01	0.84 ± 0.07	0.77 ± 0.01	0.68 ± 0.01
Δd_p [2]	37 ± 0.4	17 ± 0.2	37 ± 0.6	33 ± 0.1
$d_p \leq 250$ µm				
# of Particles	165	473	78	112
Area [µm^2] x 10^4	4.30 ± 0.13	0.99 ± 0.09	3.67 ± 0.480	3.69 ± 0.13
Aspect Ratio (AR)	2.37 ± 0.1	1.96 ± 0.1	1.76 ± 0.1	1.41 ± 0.1
Roundness	0.49 ± 0.01	0.63 ± 0.01	0.66 ± 0.02	0.68 ± 0.01
Solidity	0.77 ± 0.01	0.83 ± 0.07	0.83 ± 0.01	0.91 ± 0.01
Δd_p [2]	39 ± 0.5	34 ± 0.5	29 ± 1.0	27 ± 0.5

[1]Aspect ratio (AR), roundness, and solidity were calculated from Eqs. D2-D4, respectively; [2] geometrical size difference between calculated d_p's based on circular and rectangular particle geometric approach through AR (Eqs. D5-D6)

Table IV-D2. Model fitting [normal, lognormal, and Weibull models (Eq. D7-D11)] to the size distribution of MPs (106 µm and 250 µm sieve fractions) derived from CRYO- and W- PBAT and PLA/PHA MPs

Polymer	Pre-treatment	Sieve fraction [µm]	Scale [µ]	Shape [σ]	Mean[1] [µm]	a[1]	b[1]	AIC	BIC	Best fit
PBAT	CRYO	250	125.5	66	-			1854	1860	Normal
	W	250	3.1	1.2	-			4495	4504	Lognormal
	CRYO	106	53	23	-			3291	3298	Normal
	W	106	3	0.5	-			5318	5327	Lognormal
PLA/PHA	CRYO	250	-	-	107	86.01	0.7	871	875	Weibull
		250	-	-	143	160.5	3.1	1199	1204	Weibull
	CRYO	106	-	-	37	41.36	1.6	3187	3195	Weibull
	W	106	3.4	0.8	-	-	-	7601	7611	Lognormal

[1] Weibull distribution fit parameters

Table IV-D3. Effect of the number of passes on the concentration of NPs in aqueous slurries (C_{NP}) employed for DLS and ZP analyses [1]

Material	Number of Passes	C_{NP}, g mL^{-1} x 10^6 [2]
CRYO-PBAT	6	353 ± 35
CRYO-PBAT	30	590 ± 28
CRYO-PBAT	60	710 ± 26
W-PBAT	6	155 ± 13
W-PBAT	30	214 ± 9
W-PBAT	60	211 ± 10
CRYO-PLA/PHA	6	351 ± 25
CRYO-PLA/PHA	30	492 ± 14
CRYO-PLA/PHA	60	423 ± 8
W-PLA/PHA	6	308 ± 6
W-PLA/PHA	30	359 ± 2
W-PLA/PHA	60	296 ± 13

[1] Samples were prepared by forming aqueous slurries containing 0.5 wt% of NPs at 25 °C, allowing the slurries to settle for 5.0 h, and removing an aliquot from the middle of the slurry; [2] errors represent the standard deviation.

Table IV-D4. Percent of weight remaining at the final temperature for TGA analysis, 600 $^{\circ}$C (%W_{600}), for cryogenically treated and weathered PBAT and PLA/PHA films and derived MPs and NPs[1].

Film	Fraction	%W_{600}
PBAT	Original film	6.72
		3.68
	CRYO-MP	7.01
	Weathered film	13.83
	W-MP	17.74
	W-NP	17.12
PLA/PHA	Original film	15.69
	CRYO-MP	14.53
	CRYO-NP	12.89
	Weathered film	18.83
	W-MP	26.06
	W-NP	21.34

[1] Data for the unweathered and weathered films data were retrieved from Hayes *et al.* (2017)

Table IV-D5. Comparison of thermal properties of CRYO- and W-PBAT and PLA/PHA plastics for MPs and NPs derived via DSC analysis [1-3].

Sample	T_m, ^oC	T_g, ^oC	T_c, ^oC	ΔH_m, J/g	X_c x100%
Initial PBAT film[4]	93.84 ±0.78	-30.48 ±0.03	n.d.	30.28 ±2.62	21.50 ±0.60
Initial PLA/PHA film[4]	153.17 ±0.02	48.60 ±0.000	97.14 ±0.23	19.00 ±0.01	6.86 ±0.57
W-PBAT film[4]	108.41±0.84	-28.94 ±0.51	n.d.	42.24 ±6.23	30.17 ±2.24
W-PLA/PHA film[4]	154.83 ±0.07	49.67 ±1.28	96.55 ±0.97	19.84 ±0.38	6.11 ±0.38
CRYO-PBAT, MPs	94.21 ±0.44	-29.45 ±0.46	n.d.	30.25 ±0.73	21.62 ±0.75
CRYO-PLA/PHA, MPs	153.54 ±0.03	49.45 ±0.08	95.23 ±0.56	18.44 ±0.23	6.65 ±0.19
W-PBAT, MP	99.23 ±0.66	-29.28 ±0.89	n.d.	41.69 ±1.27	29.78 ±0.62
W-PLA/PHA, MPs	154.21 ±0.08	45.55 ±0.26	97.30 ±0.44	19.86 ±0.38	6.12 ±0.51
CRYO-PBAT, NPs	95.07 ±0.98	-30.91 ±0.49	n.d.	30.59 ±0.89	21.85 ±0.93
CRYO-PLA/PHA, NPs	153.12 ±0.07	48.27 ±0.49	96.54 ±0.93	18.91 ±0.47	6.83 ±0.51
W-PBAT, NPs	97.88 ±0.59	-29.96 ±0.44	n.d.	42.88 ±1.71	30.63 ±0.74
W-PLA/PHA, NPs	153.44 ±0.07	47.31 ±0.44	98.83 ±0.88	19.07 ±0.56	5.88 ±0.76

[1] MPs consist of the 250 mm sieve fraction of dry milled PBAT, treated using cryogenic treatment under the conditions described in Figure IV-C1 (main paper); [2] NPs were produced via wet grinding of the 106 µm sieve fraction µPs after dry milling; [2]Error bars represent one standard deviation of two sample measurements; [3] T_m, T_g, ΔH_m, and X_c refer to the temperature for the onset of melting, the melting temperature, glass transition temperature, and crystallinity of the films' major polymers (PBAT and PLA), respectively. The latter was calculated via Eq. D13. n.d. = not determined; [4] Initial film and weathered film data were adapted from Hayes *et al.* (2017).

Table IV-D6. FTIR wavenumber assignments for PBAT and PLA/PHA [1]

Wavenumber, cm^{-1}	Polymer	Contribution
3700-3000 [2]	PBAT	OH stretch
2914, 2848	PLA/PHA	C-H stretch
2956, 2920, 2876, 2840	PBAT	C-H stretch
1712 [3]	PBAT	C=O stretch
1646	PBAT	C=O stretch [4]
1464, 1472	PLA/PHA	-CH$_2$- bend
1456, 1410, 1390	PBAT	-CH$_2$- bend
1268, 1252, 1166, 1118, 1102, 1082	PBAT	C-O stretch
1076 – 1000	PBAT	OH bend
874	PBAT	C-H stretch
728	PBAT	(CH$_2$)$_4$ bend
718, 729	PLA/PHA	-CH$_2$-rocking mode

[1] Adapted from Hayes *et al.* (2017); [2] Maximum for band occurs at 3300 cm^{-1}.

[3] shoulders exist at 1728 cm^{-1} and 1756 cm^{-1}; [4] for the starch component of Mater-Bi® .

Table IV-D7. Evaluation of biodegradation (BD) (daily)

Polymer	Particle Size	Pre-treatment	Average Daily BD [% BD]	Cumulative BD [% BD]	Mean Daily BD Rate [% BD/d]	Maximum Daily BD Rate [% BD/d]	Minimum Daily BD Rate [% BD/d]
Cellulose	50 μm	-	29 ±0.9	58 ±0.8	0.38 ±0.02	1.51	0.16
PBAT	MPs	CRYO	50 ±4.4	89 ±1.4	0.59 ±0.02	2.48	0.11
		W	51 ±5.1	95 ±1.3	0.62 ±0.02	3.01	0.07
	NPs	CRYO	43 ±4.1	85 ±1.3	0.55 ±0.02	2.06	0.12
		W	50 ±5.3	90 ±1.5	0.58 ±0.01	1.98	0.09
PLA/PHA	MPs	CRYO	50 ±4.3	89 ±1.5	0.57 ±0.01	2.27	0.13
		W	33 ±2.6	61 ±2.5	0.40 ±0.02	2.19	0.03
	NPs	CRYO	47 ±3.2	71 ±2.8	0.46 ±0.01	1.98	0.09
		W	26 ±1.9	43 ±0.5	0.28 ±0.01	1.4	0.08

Table IV-D8. Curve fitting parameters and predicted biodegradation times derived from the CO_2 evolution profiles calculated through mathematical prediction modeling.

Feedstock	Particle Type	Pretreatment	Cumulative BD [%]	Best Fit Model [1]	AIC [2]	BIC [3]	Predicted 50 % [days] [4]	Predicted 100 % [days] [5]
Cellulose	50 μm	-	58 ±0.8	Bi-exponential 4P	124.6143	130.1032	125	323
PBAT	MPs	CRYO	89 ±1.4	Logistic 4P	153.6500	159.1400	54	251
		W	95 ±1.3	Logistic 4P	159.2382	164.7272	56	219
	NPs	CRYO	85 ±1.3	Logistic 4P	140.5530	146.0420	70	210
		W	90 ±1.5	Cell Growth 4P	99.5712	105.0601	50	193
PLA/PHA	MPs	CRYO	89 ±1.5	Bi-exponential 4P	137.6834	143.1724	51	217
		W	61 ±2.5	Bi-exponential 4P	99.9064	105.3954	117	236
	NPs	CRYO	71 ±2.8	Bi-exponential 4P	118.1870	123.6759	53	352
		W	43 ±0.5	Bi-exponential 4P	92.2737	94.2942	199	424

[1] Best fit obtained through exponential curve fitting performed in the JMP 15.2.0 software using the 'Specialized Modeling' platform. Details of the employed models are depicted in Appendix IV, Sect. D.5.3. Description of the nonlinear curve fitting method performed is given in the results section of Chapter IV. [2] Akaike's information criterion. [3] Bayesian information criterion.

[4] DT 50 values, representing 50% mineralization of the original feedstocks, were determined from predicted CO_2 evolution values.

[5] Predicted time for 100% mineralization determined through an extrapolation calculation using equations D1-D3, Section D.5.3 and the prediction profiler tool in JMP.

CHAPTER V

EFFECTS OF SOIL PARTICLES AND CONVECTIVE TRANSPORT ON DISPERSION AND AGGREGATION OF NANOPLASTICS VIA SMALL ANGLE NEUTRON SCATTERING (SANS) AND ULTRA-SANS (USANS)

A version of this chapter was originally published in *PLoS one Journal* on July14[th], 2020:

Citation

Authors
A.F. Astner[1], D.G. Hayes[1,*], S.V. Pingali[2,*], H. O'Neill[2], K.C. Littrell[2], B.R. Evans[2], V.S. Urban[2]

[1]*The University of Tennessee, Biosystems Engineering and Soil Science, 2506 E J. Chapman Dr, Knoxville, TN 37996*

[2]*Oak Ridge National Laboratory, 1 Bethel Valley Road, Oak Ridge, TN 37831-6106*

Anton Astner's major contribution to this paper includes identifying the research objective, designing, and conducting the experimental tasks, processing, and interpreting the data, and drafting the paper.

The co-authors' contributions are listed as follows:

D. G. Hayes significantly supported the experiments and data analysis and revised the paper.

H. O'Neill, B. R. Evans, S. V. Pingali, V. S. Urban helped in the experimental design and adjusting of experimental parameters

K.C. Littrell supported the USANS experiments at beamline 1-A at ORNL

Abstract

Terrestrial nanoplastics (NPs) pose a severe threat to agricultural food production systems by potentially disturbing soil-born micro- and macroorganisms that promote soil fertility and the ability of NPs to adsorb onto and penetrate vegetables and other crops. Very little is known about the NPs dynamics, such as dispersion, fate, and transport in soils, due to the challenges of NPs analysis by conventional microscopic techniques caused by the low NPs concentrations and absence of optical transparency. Therefore, the potential utility of small-angle neutron scattering (SANS) and Ultra SANS (USANS) probed the agglomeration behavior of NPs dispersed in aqueous soil slurries. Slurries were prepared from polybutyrate adipate terephthalate, a prominent biodegradable plastic used in agricultural mulching, in the presence of vermiculite, an artificial soil. Neutron contrast matching was employed to determine a deuteration level for water for which the SANS signal attributable to vermiculite would be minimized, thereby allowing for the isolation of NPs in the neutron beam. We determined the contrast match point for vermiculite at 66% D_2O / 33% H_2O. At this condition, the signal for vermiculite was ~50-100%-fold lower than neat H_2O or D_2O as solvent. Smaller-sized NPs (50 nm) remained dispersed in water and did not undergo size reduction or self-agglomeration nor form agglomerates with vermiculite. Larger-sized NPs (300-1000 nm) formed self-agglomerates and agglomerates with vermiculite, demonstrating their significant adhesion with soil. However, convective transport (simulated by ex situ stirring of the slurries before SANS and USANS analyses) reduced the self-agglomeration, demonstrating weak NP-NP interactions. Convective transport also led to the size reduction of the larger-sized NPs. Therefore, this study demonstrates the potential utility of SANS and USANS with contrast matching techniques for investigating the behavior of terrestrial NPs and that NPs and soil particulates undergo agglomeration.

5.1 Introduction

Increasing global plastic pollution is an emerging threat to marine and terrestrial ecosystems worldwide (Alimi *et al.*, 2018; Gourmelon, 2015). In 2015, global plastic production exceeded 400 million metric tons (MMT), from which 300 MMT plastic waste were formed (Geyer *et al.*, 2017). Approximately 79% of plastic waste generated has been dispersed into the environment through improper disposal or landfilled (Geyer *et al.*, 2017). Meso- and microplastics (average particle size, or d_p of > 25 mm and 5-25 mm, respectively) undergo further size reduction, resulting in microplastics (MPs) and nanoplastics (NPs), (d_p of 0.1-5000 μm and 1-1000 nm, respectively) (Alimi *et al.*, 2018; Alimi *et al.*, 2018; Gigault *et al.*, 2018; Hartmann *et al.*, 2019). A primary environmental concern is that MPs and NPs, due to their hydrophilicity, are likely to carry contaminants such as pesticides, plasticizers, or other potentially harmful agents that can directly impact the marine and terrestrial environment through uptake and digestion (Bouwmeester *et al.*, 2015; Koelmans *et al.*, 2013). Recent studies reported potential harm to marine biota such as macro- and microorganisms (Besseling *et al.*, 2014; Eckert *et al.*, 2018; Hüffer & Hofmann, 2016; Lu *et al.*, 2018; Oberbeckmann *et al.*, 2018) and fish and other organisms (Bouwmeester *et al.*, 2015; Chen *et al.*, 2017; Mattsson *et al.*, 2015; Nolte *et al.*, 2017; Pitt *et al.*, 2018). MP contamination has been reported in foods, including fish, bivalves, crustaceans and beverages (Barboza *et al.*, 2018). However, the effects of MPs and NPs on terrestrial environments were rarely studied (Alimi *et al.*, 2018; Horton *et al.*, 2017). Due to their smaller size than average soil particles, NPs are likely to be mobile and propagate up to higher ranks in food chains via adsorption through plant roots and uptake by livestock (Jayaram *et al.*, 2017). NPs are sufficiently small to be able to enter organs and cross the brain-blood and placental barriers (Barboza *et al.*, 2018). However, plastic plant-soil interactions are currently unknown (Ng *et al.*, 2018).

A significant secondary source of MPs and NPs in agricultural soils are plastic mulch films, which are used to produce vegetables and other specialty crops. They serve as a barrier applied to the soil surface to prevent weeds and evaporative loss of water, sustain soil temperature, reduce diseases, and pests (Hayes *et al.*, 2019; Kasirajan & Ngouajio, 2012; Steinmetz *et al.*, 2016). The most frequently used plastic mulch material is polyethylene (PE); however, there are no desirable end-of-life options. Recycling programs are mostly unavailable (Hayes *et al.*, 2019). Furthermore,

PE fragments commonly form because of their embrittlement via environmental weathering, particularly solar radiation, and persist in the environment for many years since PE is poorly biodegradable. As an alternative to PE mulches, biodegradable plastic mulches (BDMs) are designed to be tilled into soil after the crop harvest, where they are expected to ultimately be decomposed by microorganisms (Hayes *et al.*, 2019; Kasirajan & Ngouajio, 2012; Steinmetz *et al.*, 2016). The most prominent polymers used for BDMs are poly(butylene succinate) (PBS), poly(butylene succinate-co-adipate) (PBSA), and poly(butylene-adipate-co-terephthalate) (PBAT), thermoplastic starch, cellulose, polylactic acid and polyhydroxyalkanoates (Hayes *et al.*, 2019; Steinmetz *et al.*, 2016).

Although BDMs should be completely catabolized into CO_2 and water by soil microorganisms (Kijchavengkul *et al.*, 2008; Lucas *et al.*, 2008), in practice, inconsistencies in their breakdown and biodegradation were observed (Goldberger *et al.*, 2015; Hayes *et al.*, 2017; Li *et al.*, 2014). Moreover, biodegradation in the soil is typically slow: 90% biodegradation in two years via standardized lab testing is a criterion recently issued by the European Union for BDMs (European Standard, 2018). Nevertheless, MPs have been detected at 10-20 kg/ha levels in fields where BDMs were used continuously for vegetable production (English, 2019).

Also, MPs formed from BDMs may be a source of terrestrial NPs (Astner *et al.*, 2019). NPs have not been detected in soils to date, mainly due to the absence of a robust analytical approach, although they are likely to occur (Lu *et al.*, 2018). NPs derived from BDMs in soil may negatively impact soil health, fertility, and crop production and would be more likely than MPs to enter the food production system due to their small size. NPs are expected to behave differently than MPs due to their anticipated colloidal behavior, e.g., the ability to undergo Brownian motion, and differently than soil micro- and nanoparticles (which mainly occur in clays) due to their more hydrophobic nature than most soils. (But, it is noted that adsorption of hydrophobic molecules onto soils can induce hydrophobicity into soils (Doerr *et al.*, 2000).) In addition, the density of NPs for agricultural plastics would be significantly lower than soils: 0.5-1 g cm^{-3} for plastics used in mulch films versus particle densities of 2-3 g cm^{-3} for many soils (Blake, 2008; Hayes *et al.*, 2017).

For risk assessments and remediation, information about the impacts, distribution, behavior, and fate of terrestrial NPs is essential. However, their detection is difficult due to their nanoscale

174

dimensions and relatively small concentration compared to soil particulates. Microscopic detection is possible in soils for fluorescently-derivatized NPs, for instance. However, introducing a fluorophore into an N.P. may change its properties and introduce artifacts into the sample analysis. In this paper, we introduce analysis by small-angle neutron scattering (SANS) and ultra-SANS (USANS) as a potentially valuable approach to measure the aggregation behavior of NPs in solution and the presence of soil particulates. Unlike microscopy, SANS allows *in situ* measurements of size, shape, and agglomeration of NPs and soil, and neutrons are non-destructive to samples. Another advantage offered by SANS and USANS methods is the use of neutron contrast matching to isolate the behavior of one nanoscale component from that of the other components in the neutron beam.

Specifically, this investigation tests the proof-of-concept that SANS and USANS can be used in conjunction with neutron contrast matching to isolate the signal of NPs from that attributable to the soil. The contrast match point (CMP) of vermiculite microparticles, an artificial soil similar in particle size to silt (US Department of Agriculture, 1987), was determined via SANS analysis of aqueous suspensions at various H_2O/D_2O ratios. The CMP refers to the level of deuteration in solvent (water) that minimizes vermiculite's signal. Then, suspensions of NPs formed from PBAT-based BDMs and vermiculite in water at the CMP were examined to investigate their agglomeration behavior *in situ*. The effect of *ex-situ* stirring before SANS and USANS analysis was investigated to determine the impact of convective transport on agglomeration. The SANS and USANS measurements test the hypothesis that the NPs are more likely to agglomerate with soil than self-agglomerate. The agglomeration behavior may play a key role in the long-term fate, transport, and biodegradability of terrestrial NPs, especially at the water-soil interface. Particle agglomeration of NPs would also impact NPs' migration in surface waters and may explain the inability to detect NPs by flotation or leaching of soil samples.

5.2 Materials and methods

5.2.1 Materials

BioAgri, a black-colored BDM film prepared from Mater-Bi® (Grade EF04P), a starch-copolyester blend containing PBAT as its principal constituent, was kindly provided by BioBag Americas (Dunevin, FL, USA). The film referred to as "PBAT" in this paper, possesses an

175

apparent density of 22.81±0.411 g m^{-2}, a thickness of 29±1.2 µm (i.e., a specific gravity of 0.787), a peak load of 12.05± 0.586 N, an elongation of 295±30 % at maximum tensile stress in the machine direction and a contact angle of 82.5±1.1 (Hayes *et al.*, 2017). Other physicochemical properties are given in the cited reference. The original film was provided as a 1.22 m-wide roll and stored at 20.6 ± 2.1 °C and 61.8 ± 10.6% relative humidity. Deuterium oxide (D$_2$O) was purchased from Acros (Geel, Belgium). Deionized water was used throughout all experiments. Vermiculite (Mg$_{1.8}$Fe$^{2+}_{0.9}$Al$_{4.3}$SiO$_{10}$(OH)$_2$*4H$_2$O), Grade 4, mesh size 7.9 mm, was purchased from Uline (Pleasant Prairie, WI, USA). Raw vermiculite particles possessed an average particle size of 4.65 ± 2.39 mm (L/W ratio 1.39, measured with ImageJ software (Schneider *et al.*, 2012)) and were comminuted with a pestle grinder and sieved through a cascade of four sieves (W.S. Tyler, Cleveland, OH, USA) with mesh sizes of #20 (840 µm), #60 (250 µm), #140 (106 µm), and #325 (45 µm). The 45 µm sieving particle fraction was collected, and an average particle size of 38±12 µm was measured using a model SZ 61 stereomicroscope from Olympus (Shinjuku, Tokyo, Japan) with a Digital Sight DS-Fi1 integrated with a camera head from Nikon (Shinagawa, Tokyo, Japan). Soil particles of this size were selected because of their effective dispersion in water, and their high monodispersity was anticipated to simplify the interpretation of the SANS data. Vermiculite particles within the given size range mimic silt (US Department of Agriculture, 1987). Image analysis was performed using ImageJ software (Schneider *et al.*, 2012) by converting micrographs into 8-bit images (representing 28 gray levels) using a proper threshold setting (dividing the image into two or more classes of pixels). The subsequent analysis included the binary file conversion of the adjusted image. The average diameter, d_p, was estimated using Image J's "analyze particles" algorithm. A representative image of the entire sample was collected and processed through Image J using one replicate. For each particle size fraction, 250 particles were counted and averaged.

5.2.2 Production of NPs

NPs were prepared from PBAT film according to the optimized procedure (Astner *et al.*, 2019). First, the PBAT specimen (~1.0 g), cut from BDMs films to dimensions of ~120 mm (machine direction) x 20 mm (cross direction), were presoaked in water (800 mL) for 5 min, recovered, and transferred to a cryogenic container filled with liquid nitrogen (200 mL) and soaked

176

for 5 min. Next, the frozen PBAT film fragments (1.0 g) were transferred into an Osterizer-type blender (Oster Accurate Blend 200, Boca Raton, FL, USA) and dry-comminuted for 10 s. Next, water (400 mL) was added to the PBAT fragments to form a slurry, and then the blender was operated on for 10 min at 10×10^{-3} min^{-1}. After blending, the slurries were filtered under vacuum through a paper membrane filter (1 µm mesh) using a Büchner funnel apparatus and then air-dried for 48 h to reduce moisture to < 1%. The resulting MP fragments possessed a d_p of 1.47 ± 0.45 mm (ImageJ analysis of stereomicrographs) (Astner *et al.*, 2019). Next, the cryogenically embrittled PBAT MPs were fed to a rotary mill (Model 3383-L10 Wiley Mini Mill, fitted with screen, Arthur H. Thomas Co., Philadelphia, PA, USA) by using sieve sizes of 20 mesh (840 µm) for the first pass and 60 mesh (250 µm) for the second pass through the mill. The residence time for milling was 20 min per pass. MPs recovered from milling were fractionated via a cascade of four sieves (W.S. Tyler, Cleveland, OH, USA) with mesh sizes of #20 (840 µm), #60 (250 µm), #140 (106 µm), and #325 (45 µm). Uniform particle size distributions were achieved by mounting the sieves on an Eppendorf thermomixer 5350 (Hamburg, Germany) and shaking for 30 min at 300 rpm.

The 106 µm sieve fraction was suspended concentration of the slurry aliquot was 0.37 wt%. The resultant particles were vacuum dried at 40 °C for 48 h and stored in an air-sealed container. The dried NPs possessed an average d_p of 366.0±0.65 nm according to dynamic light scattering (DLS) analysis (bimodal distribution: d_p values of 536.8±151.8 nm and 63.8±13.7 nm, with each subpopulation's distribution described by a two-parameter Weibull distribution) (Astner *et al.*, 2019), and were used for SANS/USANS sample preparation. The NPs' zeta potential (in H_2O) was determined to be -22±3.6 mV through the employment of a Zetasizer Nano instrument (Malvern Instruments, Malvern, UK) using a Smoluchowski model. According to Atomic Force Microscopic (AFM) analysis, performed using a model Multimode 8 instrument from Bruker (Santa Barbara, CA, USA), NPs were irregularly shaped. They possessed an average roughness of 12.22±1.55 nm (Figure V–4). The pH (electrical conductivity) value for the 0.5% vermiculite slurry in water was determined to be 10.14±0.02 (89.57±0.28 µS cm^{-1}), and after the addition of 1% NP to the 0.5% vermiculite slurry to be 9.54±0.13 (80.03±0.29 µS cm^{-1}). in an aqueous slurry (4.0 L) via magnetic stirring at 400 rpm for 24 h, providing a 1% MPs solution. After stirring, slurries were subjected to the wet-grinding process using a "supermass colloider" (MKCA6-2,

Masuko Sangyo, Tokyo, Japan) at a speed of 1500 rpm and 27 subsequent passes (collection of particles and reintroduction into the colloider) to provide a uniform particle size reduction. The slurry recovered from wet grinding was transferred to a 1000 mL beaker and magnetically stirred for 4 h (300 rpm at 25 ºC).

5.2.3 Sample preparation for SANS and USANS experiments

SANS samples consisted of slurries containing 1.0 wt% PBAT NPs and/or 0.5% vermiculite in different H_2O/D_2O solvent ratios. In addition, ex-situ stirring was employed for several samples by mixing slurries (1.0 mL) in 7 mL borosilicate glass scintillation vials at 400 rpm (radius = 1.5 cm) for 24 h at 20 ± 1ºC using a 4-sample stirrer (Isotemp 60 Fisher Scientific, Pittsburgh, PA, USA). After stirring, samples were recovered and refrigerated before SANS/USANS analysis. Changes in d_p due to refrigeration were within 5% (DLS analysis).

5.2.4 SANS and USANS analysis

SANS and USANS experiments were conducted at 22 ± 1 ºC using the Bio-SANS and USANS instruments at Oak Ridge National Laboratory (ORNL), Oak Ridge, TN, USA. Further details on the instrumentation and its settings are provided elsewhere (Agamalian *et al.*, 2018; Heller *et al.*, 2018; Heller *et al.*, 2014). The NP/vermiculite slurries were loaded into 1.0 mm pathlength titanium cells. To obtain an even distribution of NPs and vermiculite, the cells were gently rotated *in situ* in the radial direction using a tumbling sample changer at 10 rpm and 5 rpm for SANS and USANS, respectively, to enable uniform dispersion in the path of the neutron beam (Heller *et al.*, 2014). Moreover, the tumbling speed was set to match the settling velocity of particles to ensure the particles remain mainly in the path of the beam rather than settle down. The incident wavelengths were 6.09 Å for SANS and 3.6 Å for the primary USANS beam. The higher-order neutron energies from the Bragg reflections for USANS were separated from the primary beam (3.6 Å) by time-of-flight, allowing for the elimination of a significant source of background in this class of instrument. The scattering from these samples was not sufficiently strong for the data to benefit from the additional information potentially provided by scattering from these reflections at extremely low Q. SANS experiments employed a single configuration with the main detector at 15.5 m and the wing detector at 1.4° rotation to allow for an effective range for the momentum transfer, Q (= $4 \pi \lambda^{-1} \sin[\theta/2]$, where θ is the scattering angle and λ is the wavelength

178

of incident neutrons, 6.09 Å), of 0.003 – 0.50 Å^{-1}. USANS employed a 30 m detector distance to produce a Q range of 5 x 10^{-5} – 2 x 10^{-3} Å^{-1}. Typical acquisition times were 0.5-1.0 h and 8-12 h for SANS and USANS, respectively. We did not observe the settling out of particles at any instance during the SANS or USANS experiments. Although we cannot entirely rule out that particle aggregation was induced by low *in situ* tumbling, the absence of settling gives us confidence that the impact of this event was small. Error bars shown in the *I(Q)* figures are based on counting statistics. The square root of the counts and, subsequently, error propagation were applied for any downstream corrections to the data.

SANS data (scattered intensity *I(Q)* vs. *Q*) were reduced using Mantid software and analyzed by fitting the data with a nonlinear general scattering law based on form and structure factors [*P(Q)* and *S(Q)*, respectively] through an Igor Pro macro (Kline, 2006). Next, USANS data were de-smeared using a slit height of 0.042 Å^{-1} (in units of momentum transfer) using the NIST USANS package (Igor Pro) before merging SANS and USANS data. The merge process was performed by determining the best power law line fitting for both data sets (Heller *et al.*, 2018; Kline, 2006). Then, a power law fit was applied to the linear portions of the combined SANS and USANS data (Porod region, 1/2 Q d_p >> 1).

$$I(Q) = \alpha\, Q^{-\beta} \tag{1}$$

For $0 \leq \beta \leq 3$, β is the power-law exponent and represents the mass fractal dimension (D_f). When the power-law exponent varies as $3 \leq \beta \leq 4$, then the surface fractal (D_s) varies as $3 \geq D_s \geq 2$ (D_s = 6–β). $\beta = 3$ (or $D_s = 3$) represents a rough surface, while $\beta = 4$ (or $D_s = 2$) represents a smooth surface (Schmidt, 1991).

After subtraction of Eq 1, the resultant "excess" data ($I(Q) - \alpha Q^{-\beta}$) was fitted using form factor-structure factor modeling. The structure factor, simulating particle-particle interactions, was assumed to be 1.0 due to the small volume fraction of NPs. A polydisperse sphere form factor was employed, providing the average particle radius, R, the polydispersity of the radius (based on a Schulz distribution) *pd,* and the volume fraction of dispersed phase ϕ as outputs and the scattering length densities of PBAT and water at different levels of deuteration as inputs (Kotlarchyk & Chen,

1983). $B_{incoher}$ was set equal to 0.0 since incoherent contribution was subtracted during data reduction. The average particle diameter of the NPs, d_p, is equivalent to 2R.

5.3 Results and Discussion

5.3.1 Determination of the contrast match point (CMP) for vermiculite (artificial soil)

Slurries of vermiculite (0.5%) in water consisting of various proportions of D_2O were analyzed by SANS to determine the contrast match point. As shown in Figure V-1, the scattered intensity, $I(Q)$, decreased as the D_2O fraction was increased up to 60% v/v; then, further increases of D_2O increased $I(Q)$. The data reflects a power law relationship (per Eq.1), with β decreasing from 3.4 to 2.9 as the D_2O content decreased from 100% and increases from 0%, approaching a minimum at 60% D_2O. The values of β are comparable to the values reported for small-angle x-ray scattering analysis of vermiculite (Motokawa *et al.*, 2014) and represent a rough surface.

We determined the CMP for vermiculite by plotting the square root of $I(Q)$ in the low-Q region (0.004 Å^{-1}) vs. volume fraction of D_2O in the solvent. According to this plot (Figure V-1b), the CMP is ~67% D_2O (33% H_2O), corresponding to a neutron contrast of 4.08 x 10^{-6} Å^{-2}. Figure V-1(a) contains the SANS data at the CMP. Although $I(Q)$ for vermiculite is decreased nearly 100-fold at the CMP relative to 100% H_2O and over 10-fold compared to 100% D_2O, the signal is not entirely removed. The inability to completely suppress the scattering is likely a result of the spatial heterogeneity of vermiculite's scattering length density, due to spatial heterogeneity in the particle density and chemical composition.

5.3.2 Effect of ex situ stirring and vermiculite on NP structure and agglomeration

SANS and USANS analyses at the CMP determined the impact of *ex situ* stirring (24 h) on the agglomeration of NPs in the presence of vermiculite. The addition of vermiculite led to a slight decrease of $I(Q)$, confirming that contrast matching minimized the scattering attributable to vermiculite and that NPs were removed from the neutron beam through agglomeration with vermiculite (Figure V-2(a), inset). The power-law exponent β (Eq. 1) did not change appreciably with stirring: 3.5±0.1, a value that suggests the surface characteristics of the NPs are rough (Figure V-2b). *Ex situ* stirring increased the intensity of the SANS signal of PBAT NPs, a result suggesting that convection improved the dispersion of the NPs by disrupting the formation of large

180

agglomerates. An alternate explanation would be that convection increased the extent of solvent penetration into NPs and their agglomerates. The addition of vermiculite reduced the extent of the increase for $I(Q)$.

The subtraction of the power law relationship (Eq. 1) from $I(Q)$, referred to herein as "excess" scattering, reveals the presence of scattering intensity oscillations of NPs and their agglomerates for both USANS and SANS data (Figures V-3a and b). The "excess" oscillations were fitted with spherical form factor models (Schultz distribution to account for polydispersity in the radius) as a first approximation. Values of the volume fraction of dispersed phase (i.e., of NPs; ϕ), d_p, and polydispersity (pd) are given in Table V-1. The "excess" curves at high-Q from SANS likely correspond to individual NPs, with d_p being ~51.7 nm (Table V-1). According to DLS analysis, NPs (in the absence of vermiculite) possessed a bimodal size distribution, with the smaller size subpopulation possessing d_p of ~50-65 nm, comparable to the SANS-derived value (Astner *et al.*, 2019). The absence of variance for the "excess" oscillations with *ex situ* stirring and the addition of vermiculite suggests the smaller-sized subpopulation of NPs are well dispersed in water and are unlikely to form agglomerates (Figure V-3a and Table V-1). The "excess" USANS data reflects the presence of dispersions of $d_p > 300$ nm (Figure V-3a and Table V-1), which likely correspond to the larger, $d_p = 537$ nm, sub-population of the bimodal distribution observed by dynamic light scattering (Astner *et al.*, 2019). A shoulder at low-Q (0.5-1.0 x 10^{-4} Å^{-1}) is believed to represent NP self-agglomerates of the larger sized NP subpopulation (8.5 µm = d_p). Moreover, vermiculite particles possess a d_p of ~38 µm, which would produce a USANS signal for its agglomerates at a lower Q value than available through the USANS instrument. *Ex situ* stirring diminished the low-Q "excess" shoulder, a result suggesting that convection will break apart the NP-NP attractions that lead to agglomeration (Figure V-3a).

The oscillations within the Q range of 0.2-1.4x10^{-3} Å^{-1}, likely reflecting NPs of the larger subpopulation, undergo a decrease in size and an increase of pd upon *ex situ* stirring (Figure V-3(a) and Table V-1) suggesting the NPs undergo size reduction. It is unclear if this trend may be attributable to the breakup of agglomerates composed of smaller-sized NPs by convection. The slight increase of ϕ for the smaller-sized (d_p=51 nm) NP subpopulation with *ex situ* stirring (Table V-1) suggests the latter event may occur to a small extent. Although NPs of this subpopulation decreased in size, the USANS scattering peak increased in the low-Q range (0.2-0.4 x10^{-3} Å^{-1}),

181

suggesting that *ex situ* stirring increased the effective dispersion of larger-sized NPs. The increase of ϕ (Table V-1) for the main USANS oscillation peaks supports this hypothesis. The USANS "excess" oscillations for NPs in the presence of vermiculite after *ex situ* stirring are lower than in the latter's absence (e.g., ϕ decreased 2-fold), suggesting that NPs of the larger subpopulation form agglomerates with vermiculite (particularly larger NPs thereof, noted by the decrease of d_p) (Figure V-3(a) and Table V-1). Therefore, the data demonstrate the direct interaction between NPs and soil particulates, the extent of which is modulated by convection and increases for large-sized NPs.

5.4 Conclusions

This paper describes a preliminary study to demonstrate the potential utility to employ SANS and USANS with neutron contrast matching to investigate the behavior of NPs in terrestrial systems. We determined the CMP of vermiculite, an artificial soil (67% deuteration in water), providing conditions where the scattering contribution of vermiculite would be minimized. However, the signal was not eliminated. We applied the CMP to gradable investigate the impact of soil and convective transport on NPs derived from a biodegradable plastic mulch film, composed of PBAT. Results suggest that NPs of larger size self-associate and aggregate with soil, with convection minimizing the agglomeration. The larger-sized NPs (which may be small NP aggregates) undergo size reduction under convection, while smaller-sized NPs (50 nm) remained intact. NPs are an emerging threat to soil, particularly agricultural soils, due to their involvement with producing the world's food supply and the prominence of plastic in vegetable and fruit production systems, particularly as mulch film. Their hydrophobicity is known to drive NPs' adsorption of toxicants such as pesticides and phthalate-based plasticizers, which can enter food supplies. Even biodegradable plastics, known to form MPs, will likely form NPs that will reside in the soil for several months. A fundamental understanding of terrestrial NPs and their potential impact on soil fertility, terrestrial organisms such as earthworms, and microbial communities, as well as their long-term fate and transport (including to groundwater), serves as a critical gap in knowledge. Such information is necessary to design strategies for mitigation. NPs are challenging to investigate in soils due to their low concentration and the solid-phase nature of the system. SANS and USANS, with contrast matching, may serve as a robust approach, that will allow for direct measurements of size and agglomeration behavior of NPs.

APPENDIX V
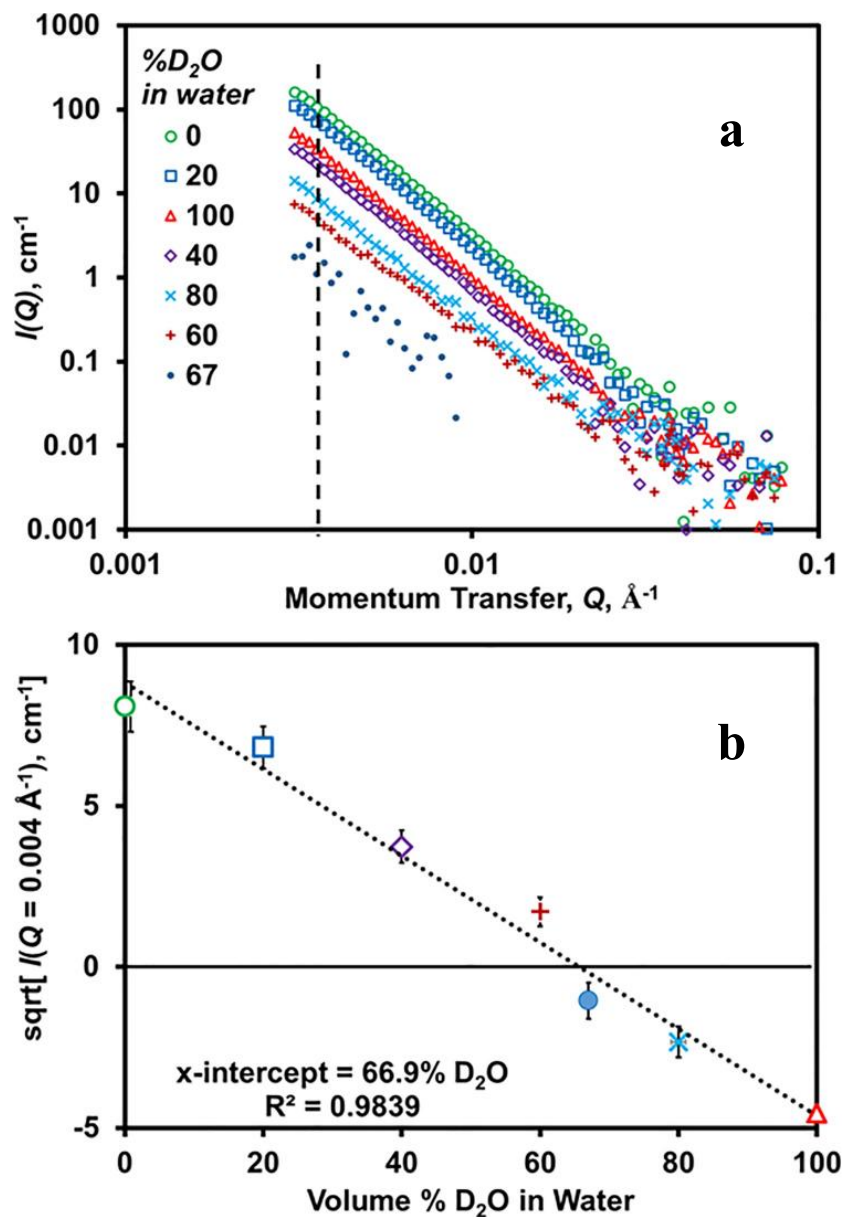
Figure V-1. Determination of the neutron contrast match point for vermiculite (0.5 wt % dispersed in H_2O/D_2O mixtures. (a) I(Q) vs Q data, (b) square root of I(Q) at $Q = 0.004$ Å^{-1} vs. D_2O volume % in water. Error bars for Figure (a) are provided in Figure V-5.
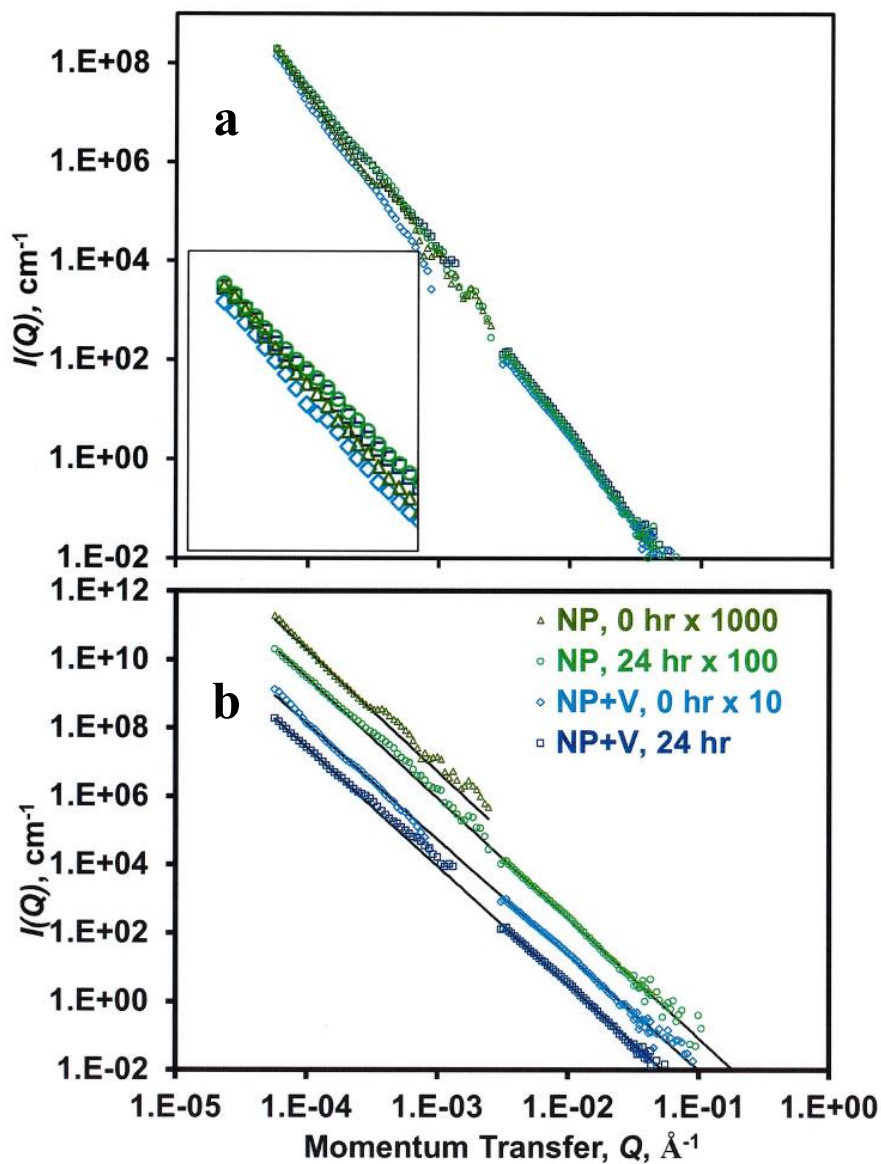
Figure V-2. Effect of pre-stirring and the presence vs. absence of vermiculite on SANS data at the contrast match point for vermiculite (67% D_2O in water; cf. (Figure V-1). The inset in (a) SANS and USANS data is expansion of the data at low Q) and (b) power law fitting (Eq. 1) of data in (a) [$I(Q) = \alpha Q^{-\beta}$, where β = 3.4-3.6].
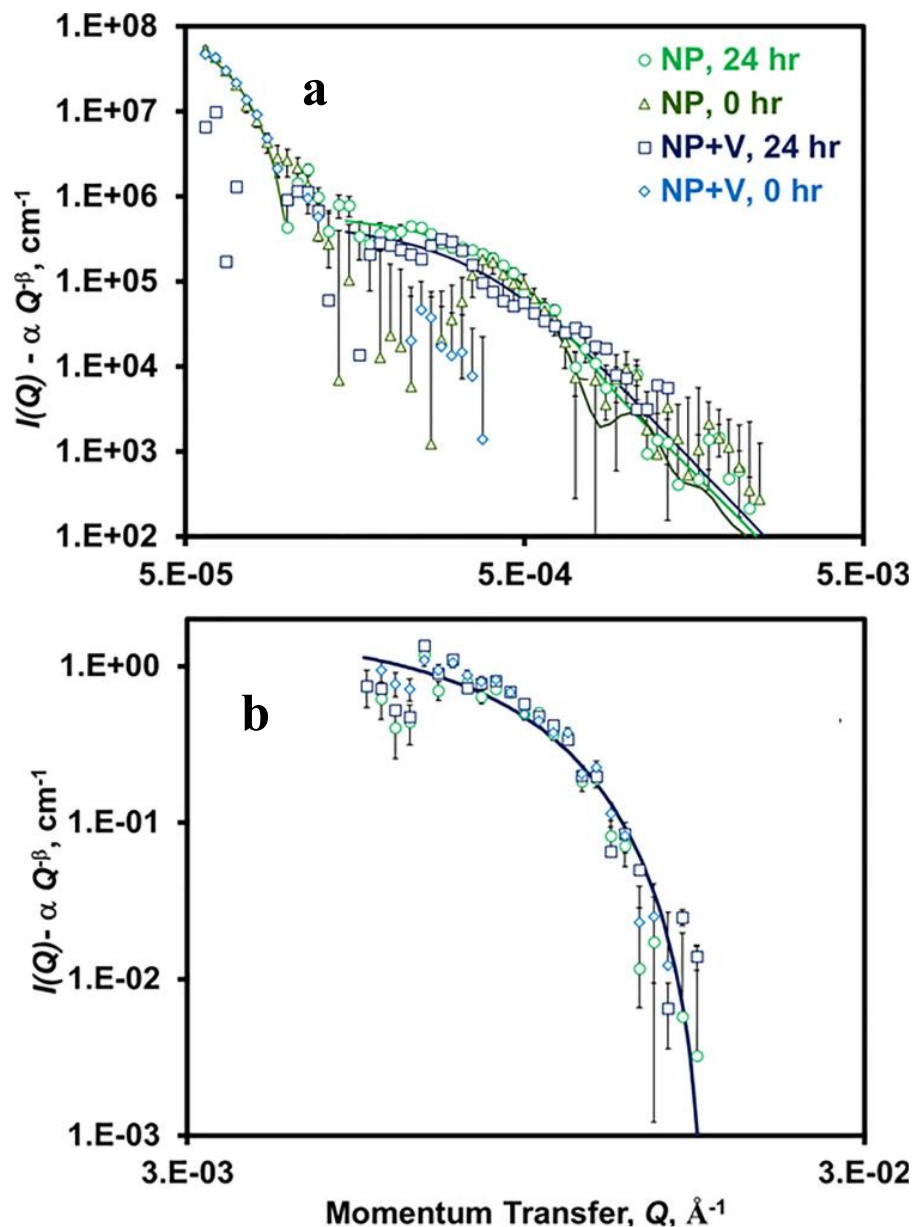
Figure V-3. Schulz polydisperse sphere model fitting of (A) USANS and (a) SANS "excess" scattering data (*I(Q)* from Figure V-2(a) minus power law fit from Figure V-2(b)). Model parameters are given in Table V-1. V and NPs refers to vermiculite and nanoplastics, respectively. Experimental condidtions are presented in Figure V-2.
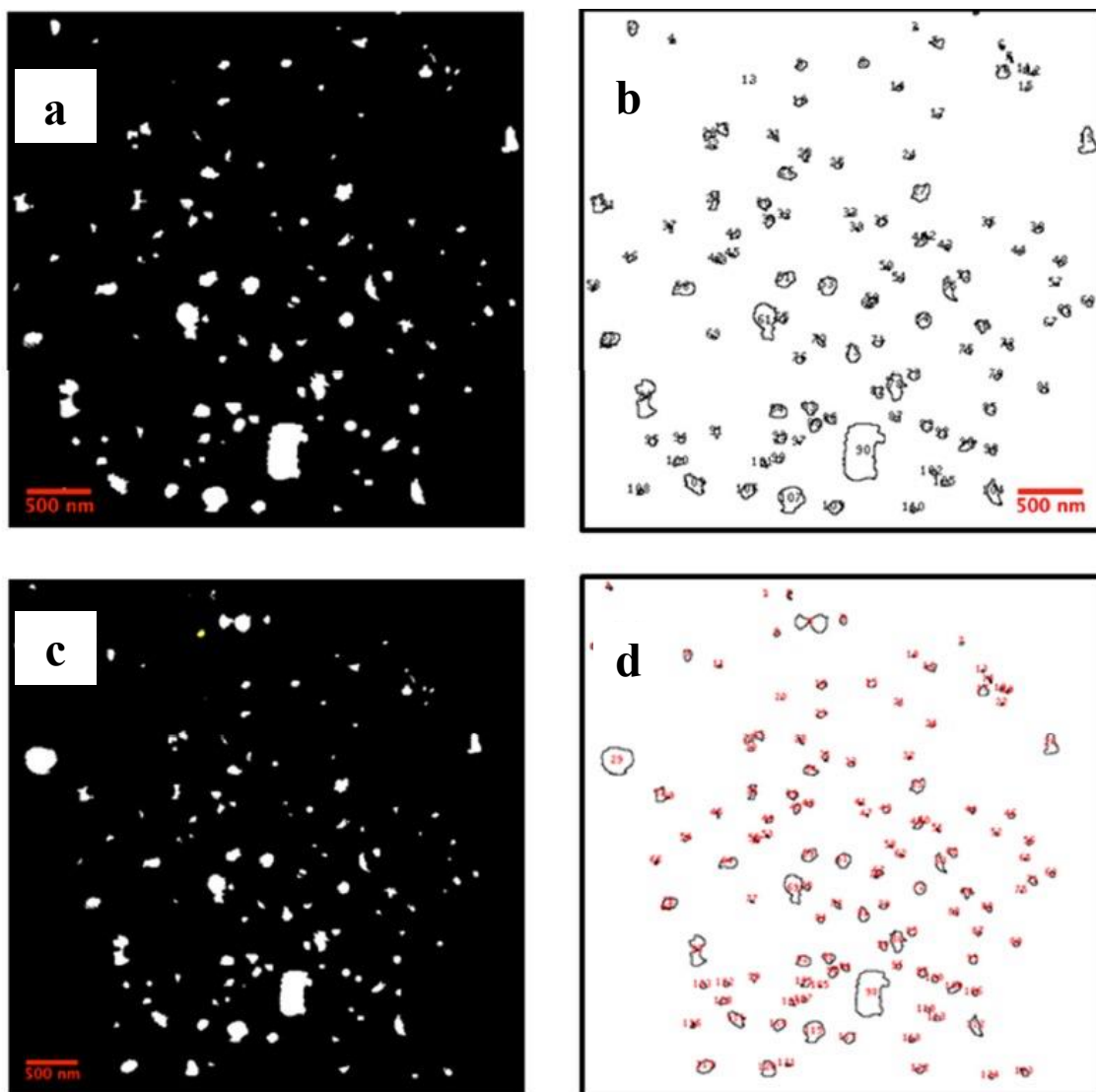
Figure V-4. AFM images of NPs used for ImageJ measurement of surface roughness for nanoplastics. (a) 400 x 400 dpi and (c) 500 x 500 dpi original images. (b) and (d) show numbering of NPs after the processing of the images for Figs A and C, respectively. AFM images were prepared using a 4 μL aliquot of 5 mg/mL slurry of NPs in water that was deposited on a mica surface and air-dried for 1 h at room temperature (22 ± 1°C) before scanning. For scanning the samples, a rectangular aluminum cantilever probe composed of an aluminum reflective coating on the backside was used. The AFM images were recorded on a scan area of 5.0 μm × 5.0 μm at a scanning speed of 1 Hz. For ImageJ analysis, the images were adjusted to 100 dpi = 1000 nm.

187
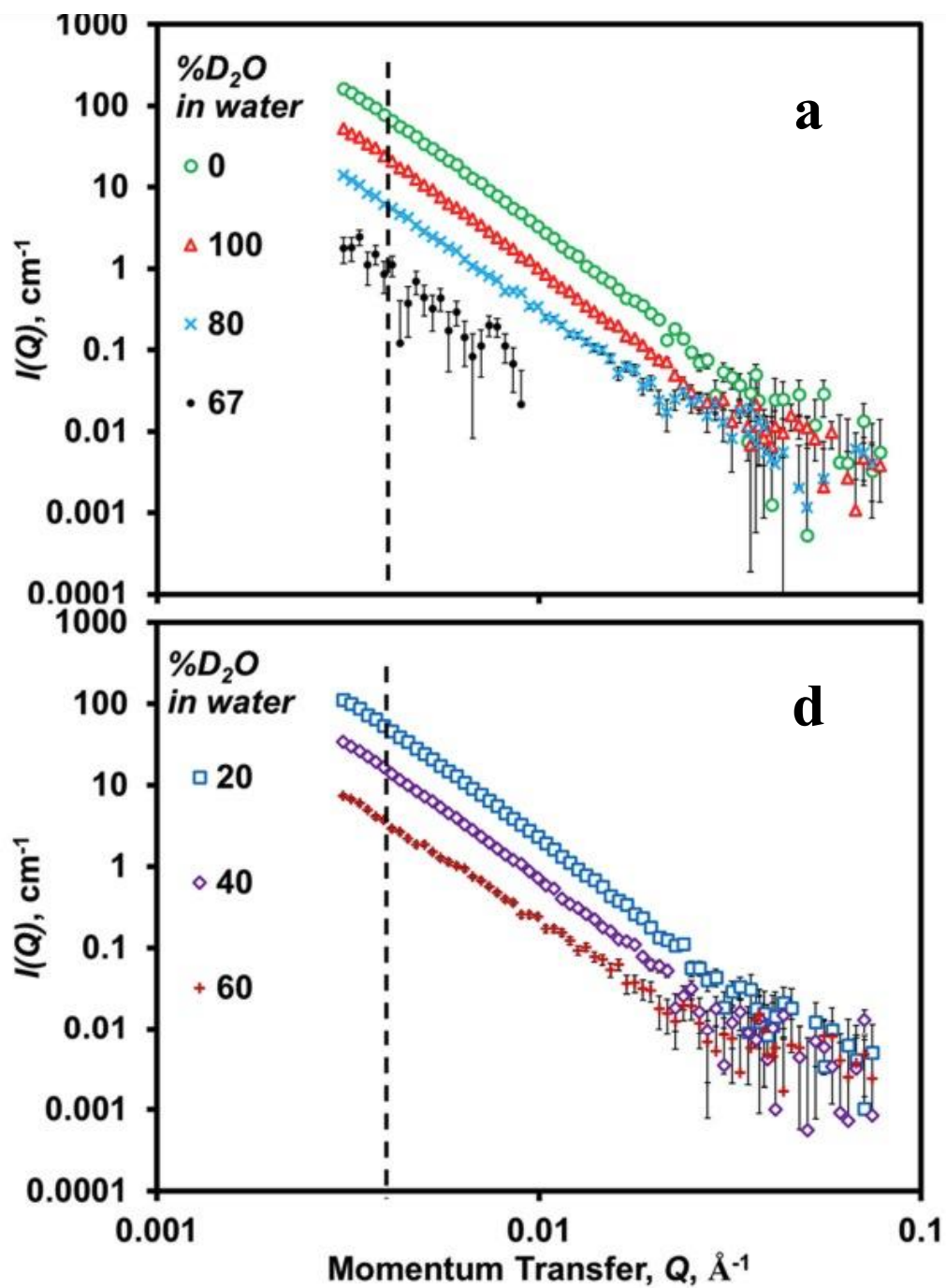
Figure V-5. Data of the main paper replotted to include error bars.

Table V-1. Results from Model Fitting of SANS+USANS "excess" data plotted in Figure V-3[a,b]

Composition[c]	Q range, Å^{-1}	f x 10^4	d_p [nm]	pd
P, 0 hr	0.5-1.0x10^{-4}	39	8500	0.01
P+V, 0 hr	0.5-1.0x10^{-4}	40	8330	0.08
P, 0 hr	0.4-2.4x10^{-3}	12	1055	0.11
P, 24 hr	0.2-1.4x10^{-3}	14	792	0.32
P+V, 24 hr	0.2-1.4x10^{-3}	7.98	287	0.84
P, 24 hr	0.5-1.7x10^{-2}	0.3	51	0
P+V, 0 hr	0.5-1.7x10^{-2}	0.39	51	0
P+V, 24 hr	0.5-1.7x10^{-2}	0.4	51	0

[a] Obtained from fitting "excess" data with a form factor based on polydisperse spheres with radii possessing a Schulz distribution. The structure factor was assumed to be ≈1.0. The scattering length density of the spheres (vermiculite) and solvent (D$_2$O/H$_2$O 67/33 v/v) were held constant at 1.60 and 4.08 x 10^{-6} Å^{-2}; the incoherent background was assumed to equal zero because all incoherent background was subtracted during data reduction; [b] column headings: ϕ and d_p are the volume fraction and average diameter of dispersed NPs, respectively; pd = polydispersity index (for radii); [c] NPs and V represent PBAT NPs (1 wt%) and vermiculite (0.5 wt%), respectively.

CHAPTER VI

PARTICLE DYNAMICS OF NANOPLASTICS AND SOIL DETERMINED BY SMALL ANGLE NEUTRON SCATTERING (SANS) AND ULTRA-SANS

Chapter VI is an article in preparation for submission. The chapter contains introduction, experimental procedure, results of preliminary data, discussion, and conclusion.

Abstract

Nanoplastics (NPs) dispersed in agricultural soils pose a severe threat by impacting soil fertility, micro- and macroorganisms, and the ability to adsorb on and penetrate crops such as vegetables. Frequent utilization of agricultural plastics and their unpredictable particle fragmentation motivated us to investigate their dispersion, aggregation, fate, and transport of NPs in soils. Therefore, the particle dynamics and dimensional changes of NPs with/without soil particles in an aqueous composite slurry were investigated. The mechanical impact was induced by pre-stirring (ex-situ) (0h, 24h, and 168h), and particle dimensions and agglomeration behavior were measured through Small Angle Neutron Scattering (SANS) and Ultra-SANS over a length scale between 50-1000 nm. The NPs were derived from polybutyrate adipate terephthalate (PBAT)-rich agricultural mulches in vermiculite particles (45 μm), used as artificial soil. The dominant signal for NPs was achieved by contrast matching techniques for vermiculite by selective deuteration of the polymer/vermiculite slurry at a ratio of 67% D_2O / 33% H_2O. Power law fitting models describe the particle dynamics and morphological changes related to structural features, including agglomeration, particle roughness, and surface fractals. The severity of ex-situ stirring caused size reduction and dispersion on NPs populations between 50-350 nm-(Pop1). In contrast, the mechanical impact was more severe on larger-sized NPs (351–1000 nm-Pop2) than on smaller NPs fractions. In addition, these particulates formed self-agglomerates and agglomerates with vermiculite. Increased severity of formed NPs resulted in the lowest particle surface roughness and size reduction effects in both populations, most significantly after 168 h pretreatments. Agglomeration effects were predominantly observed for larger NPs (Pop2) and unstirred particles; the results of this study confirmed that SANS and USANS are powerful methods to investigate NPs over a considerable length scale (50 nm to > 1000 nm) in terms of particle dynamics and size reduction behavior of nanosized plastics in combination with soil particulates.

6.1 Introduction

Terrestrial microplastics (< 5 mm) and nanoplastics (MPs and NPs, collectively MNPs) originate from the breakdown of non-biodegradable and biodegradable agricultural plastics. These small particles pose a severe environmental hazard as a contaminant to micro- and macro-organisms (Maity *et al.*, 2022). In soil, MNPs form due to mechanical, physical, and chemical influenced environmental processes, and due to their small particle size and large numbers occurring in the environment, MNPs have the potential to absorb and carry pollutants and can be toxic after being ingested by terrestrial and aquatic biota and are likely to enter the food chain (Cole *et al.*, 2011). In addition, NPs compared to MPs, represent a high surface area/volume ratio, resulting in higher mobility, chemical reactivity, and colloidal activity (Hüffer *et al.*, 2018). The surface of NPs can absorb extracellular organic molecules, leading to a surface organic layer (corona), which impacts the plastics' behavior and their interactions with organisms and soil constituents (Nasser & Lynch, 2016). The colloidal properties characterize the hetero-aggregation and stability of NPs, which is influenced by the solution's ionic strength and pH value because of the soil mineral composition and organic matter content (Gigault *et al.*, 2018) (Figure VI-1). Furthermore, studies revealed that MPs could accumulate and concentrate in the soil and change the soil's physical properties, impacting soil function and biodiversity (Rillig, 2012). Even the annual plastic release into the terrestrial environment is 4 – 23-fold higher than in aquatic ecosystems. MNPs pollution in soil and its dynamics with soil particles and biota are currently under investigation (Auta *et al.*, 2018; Horton *et al.*, 2017). The toxicity of MPs and NP to food webs is of particular concern since animals can quickly ingest these based on their small size (Zhu *et al.*, 2018). Furthermore, additives and chemicals added to improve mechanical properties such as elasticity, UV stability, and color agents may be lipophilic and penetrate the cell membranes of living organisms (Bläsing & Amelung, 2018; Pathan *et al.*, 2020). In contrast, adsorbed pollutants can accumulate in MNPs and have higher sorption levels than on adjacent surfaces (Crawford & Quinn, 2017). The biofilm matrix contains bacterial cells, proteins, extracellular DNA, lipids, and polysaccharides (Redmile-Gordon *et al.*, 2014). Plant uptake of NPs may vary between sizes between 40 -100 nm (Bandmann *et al.*, 2012). Kettler *et al.* (2014) suggested that the threshold value is 50 nm (Kettler *et al.*, 2014). However, the plant uptake of NPs is controlled by anatomical

and physiological plant and NPs properties caused by environmental impacts such as weathering and NPs surface charge and chemistry (Ng *et al.*, 2018). Terrestrial environments are ecosystems impacted by MPs and NPs that have rarely been studied (Horton *et al.*, 2017). Agricultural plastics, mainly plastic mulch films, constitute the primary source of terrestrial plastics.

Plastic mulching is a prominent practice for crop yield maximization of fruits and vegetables (4 million metric tonnes, $10.6 million in 2015). Mulches represent a barrier applied to the soil surface to reduce weeds and evaporative water loss (i.e., augments sustainable use of water via drip irrigation), reduce diseases and pests, maintain soil temperature, leading to increased fruit yield and quality, and enhance productivity (Goldberger *et al.*, 2015; Hayes *et al.*, 2017). Polyethylene (PE) is the most abundant plastic frequently used as mulch material. However, currently, there are no sustainable end-of-life options for the PE mulches after their employment (typically for a single season) due to their low biodegradability (Kasirajan & Ngouajio, 2012). In addition, very few recycling services exist, and landfilling is expensive, leading many farmers to either stockpile the thin mulch films (e.g., via burial in the ground) or (illegally) burn them, all of which lead to additional debris dispersed in the environment (Bellasi *et al.*, 2020).

The poor sustainability of PE was addressed by the development of biodegradable plastic mulches (BDMs). BDMs are polymeric blends containing components (polyesters) designed to mimic the high tensile strength and elongation of PE (e.g., polybutylene adipate terephthalate, or PBAT) and others enhance biodegradability in soil, for example, by the addition of starch. BDMs are designed to be plowed into the soil after harvest (thereby reducing labor costs), where they theoretically should undergo biodegradation. However, the adoption of BDMs by farmers as replacements for PE mulches has been hindered by observed or perceived "uncontrollable breakdown" during deployment and slow and inconsistent biodegradation in the soil.

Weathering via sunlight, moisture, and wind during their deployment on the soil surface promotes embrittlement and fragmentation, forming MP (Yang *et al.*, 2022).

As a result, biodegradable plastics may also contribute to MNP formation. The formation, distribution, and behavior of NPs in soils are crucial for risk assessments and remediation approaches involving terrestrial NPs. NPs formed by the breakdown of BDMs most likely negatively impact soil health, biota, and crop production, which may enter the food production system due to their small size. The colloidal behavior of NPs, such as the Brownian motion, will

result in different behavior than MPs due to their hydrophobicity. The nano scaled particle interactions and agglomerations behavior for risk assessment studies are challenging to detect through microscopic techniques due to their small size and low concentrations in soil. Alternatively, analysis by small-angle neutron scattering (SANS) and ultra-SANS (USANS) is a potentially suitable approach to measure the aggregation behavior of NPs in a dynamic soil/NP/water environment. NP-soil particle interactions were investigated in an aqueous slurry system involving suspended NPs and soil particles in solvents. at various H_2O/D_2O ratios. Unlike microscopy, SANS allows *in-situ* measurements of size, geometry, and agglomeration of NPs and soil, and neutrons are non-destructive to samples. Another advantage offered by SANS and USANS methods is the use of neutron contrast matching to isolate the behavior of one nanoscale component from the other components in the neutron beam. This contrast variation involving SANS and USANS methods allows the isolation of one nanoscale component by neutron contrast matching in aqueous suspensions using specific H_2O/D_2O ratios.

This study aims to gain a deeper understanding of NP-soil particle interactions when dispersed in water, as in the natural environment. For example, in vadose zones (interface between terrestrial and water bodies) and during rainfall and flooding events (Figure I-9). Specifically, the effect of *ex situ* stirring before SANS and USANS analysis was investigated to test the hypothesis that the NPs are more likely to agglomerate with soil than to self-agglomerate. The agglomeration behavior may play a vital role in the long-term fate and transport of terrestrial NPs in the NPs biodegradation associated with soil enabling more rapid biodegradation. Furthermore, particle agglomeration of NPs may also play a key role in migration in surface waters and the inability to detect NPs by flotation or leaching of soil samples.

6.2 Materials and Methods

6.2.1 Materials

Plastic feedstock characterization (unweathered) and preparation of the NPs used for SANS and USANS experiments in this study are published elsewhere (Astner *et al.*, 2019). In brief, the polymeric feedstock was biodegradable agricultural BDM, termed BioAgri, possessing a density of 22.81±0.411 g m^{-2} and a 29 ±1.2 μm thickness. The original film was provided as a 1.22 m wide roll, which was retrieved and cryogenically milled to form microplastics, followed by a highly

efficient wet grinding process to produce NPs According to the particle size analysis through dynamic light scattering, the produced PBAT NPs from the 106 possessed a bimodal distribution ranging d_p's between 37 and 1281 nm, with an average combined d_p of 366 nm (Astner *et al.*, 2022). As a model soil vermiculite was processed through a mechanical size reduction procedure using a pestle grinder. The ground material was subject to cascaded sieving to attain the final particle size. The contrast match point (CMP) was determined through an experimental design with several different H_2O/D_2O ratios for vermiculite at 67% D_2O and 33% H_2O. Chapter V provides a detailed overview of the CMP determination.

6.2.2 SANS and USANS sample preparation

The factors and associated level selections are based on the previously conducted SANS/USANS experiments (Astner *et al.*, 2019) and are described in Chapter V in more detail. Compared to the study described in Chapter V, this chapter uses an extended parameter space by using a higher NPs concentration (5 wt%) and an extended stirring time (168 h) in the presence of soil particles (vermiculite, 0.5 wt%) on particles' size reduction and agglomeration behavior. Furthermore, the same interactions were investigated for $100D_2O$ conditions, for which the NPs and vermiculite is detectable in the beam. The different polymer and vermiculite concentrations associated with the mechanical ex-situ stirring times were considered to influence agglomeration behavior, particle structure, and size (Table VI-1). The different slurry compositions were mixed and subjected to different pre-stirring times (Table VI-4) and then transferred into a titanium tumbler cell (Figure VI-2). The titanium tumbler cells were placed in a 4-sample holder. The experiments were carried out at an ambient temperature of 22 °C using titanium tumbler cells containing the composite slurry samples. The buffer solutions were composed at a ratio of 67% D_2O / 33% H_2O, representing the CMP (Table VI-4). The experimental design consisted of 18 runs, from which nine samples were prepared at the CMP and the remaining nine in 100% neat D_2O solvent. A comprehensive list of sample preparation is depicted in Table VI-4.

6.2.3 Small angle neutron scattering (SANS) experiment

The SANS measurements were performed using the Bio-SANS instrument located at the High Flux Isotope Reactor (HFIR) facility, and the USANS experiments were conducted at the beamline 1A of the Spallation Neutron Source (SNS) at Oak Ridge National Laboratory. Additional

instrumentation details are provided elsewhere (Agamalian *et al.*, 2018; Heller *et al.*, 2018; Heller *et al.*, 2014). The NP-vermiculite slurries were transferred into titanium tumbler cells adjusted with a 1.0 mm path length, resulting in a volume of 0.4 ml. An even particle dispersion was achieved by adjusting the tumbling speed during data collection.

For the SANS sample assessment, an extensive dynamic Q range was investigated, spanning from 0.003 to 0.8 Å^{-1} in a single configurational setting using 6.09 Å neutrons and a relative wavelength spread ($\Delta\lambda/\lambda$) of 15%. The main detector was located at 15.5 m from the sample position, and the wing detector array was fixed at 1.13 m from the sample at an angle of 1.4° allowing the collection of the momentum transfer as follows:

$$Q = 4\,\pi\,\lambda^{-1}\,\sin\,(\theta/2) \tag{1}$$

USANS measurements were performed at a 30 m detector distance from the sample to generate a Q-range of 5×10^{-5} - 2×10^{-3} Å^{-1}. The beam exposure times of the samples were at 0.5–2.5 h and 8–12 h for SANS and USANS, respectively. The I(Q) error bars in the figures are based on counting statistics. Data reduction of SANS and USANS data (scattered intensity I(Q) vs. Q was performed using a Python® script written and provided by instrument scientists at the Oak Ridge Laboratory.

6.2.4 Statistical evaluation of the SANS/USANS data

After merging the SANS and USANS curves, data fitting and data distribution analysis were performed employing the 'Modeling-II' tool in the IRENA package of Igor Pro (WaveMetrics, Inc., Portland, OR) software. First, data fitting occurred using form and structure factors, P(Q) and S(Q), respectively. Next, collected USANS data was de-smeared using a slit height of 0.042 Å^{-1} (in units of momentum transfer) using the Igor Pro NIST U-SANS package. Afterward, SANS and USANS data were merged by determining the best power law line fitting both data sets (Heller *et al.*, 2018). Next, linear portions of the combined SANS and USANS were subject to a power law fit. Finally, the high q region (linear portions) of the combined SANS and USANS curves was modeled to the power law function in the "Unified Fit" function. The function implemented in the IRENA package of Igor Pro software is expressed as follows:

$$I(Q) = Aq^{-P} + I_{bkg} \qquad (2)$$

where A represents the intensity scale factor P being the power law exponent, and I_{bkg} background intensity of the vermiculite in either the 67% D_2O solvent or 100 D_2O. The high Q-region was best fit to a Log-normal spherical radial distribution of polydisperse sphere, provided by the IRENA package. The best fit for low q-region curve fitting was Schulz-sphere distributions.

The (normalized) **Log-normal distribution** for the detection of the radius in the low regions given as:

$$f(R) = \frac{1}{\sigma R \sqrt{2\pi}} \exp\left[\frac{1}{2\sigma^2} (\ln(R) - \mu)^2\right] \qquad (3)$$

where $\mu = \ln(R_{med})$, R_{med} is the median radius and the polydispersity is represented by σ.

- **Log-Normal distribution equations for data fitting**

The form factor is represented by the 3rd moment of R and is normalized by the average volume:

$$\langle V \rangle = \frac{4\pi}{3} \langle R^3 \rangle = \frac{4\pi}{3} \exp\left(3\mu + \frac{9}{2}\sigma^2\right) \qquad (4)$$

Furthermore, the forward scattering cross section is determined by:

$$I(O) = N_0 \langle V^2 \rangle \Delta\sigma^2 = \frac{4}{3}\pi\emptyset\Delta\sigma^2 \exp\left(3\mu + \frac{27}{2}\sigma^2\right) \qquad (5)$$

- **Schulz spheres distribution equations for data fitting**

The best fit for the low Q-region was the Schulz sphere distribution function. The (normalized) Schulz distribution is described as:

$$f(R) = (z+1)^{z+1} \left(\frac{exp[-[z+1]x]}{R_{avg}\Gamma(z+1)}\right) \qquad (6)$$

197

Where R_{avg} is the mean radius of the sample and $x = R/R_{avg}$, z is related to the polydispersity, and σ represents the polydispersity of the distribution.

The form factor is normalized by the average volume using the 3rd moment of R:

$$\langle V \rangle = \frac{4\pi}{3}\langle R^3 \rangle = \frac{4\pi}{3}\langle R_{avg}\rangle^3 \frac{(z+3)(z+2)}{(z+1)^2} \tag{7}$$

Since there are two populations, there is no scale factor as in other models. The returned value is the differential macroscopic scattering cross-section (scattered cross-section per unit sample volume per unit solid angle) described as follows:

$$I(Q) = \left[\left(\frac{4\pi}{3}\right)^2 N_1 \Delta\, \rho_1^2 \int_0^\infty f(R_1)R^6 F^2(QR_1)dR\right] \tag{8}$$
$$+ \left[\left(\frac{4\pi}{3}\right)^2 N_2 \Delta\, \rho_2^2 \int_0^\infty f(R_2)R^6 F^2(QR_2)dR\right]$$

Where N is the total number of particles per unit volume, and $\Delta\rho$ is the difference in scattering length density.

The reduced data underwent curve fitting in Igor which allowed extraction of particle size distribution data for the two different Q-ranges, in which features on the I(Q) vs. Q diagram were observed. The distribution data were used to generate histograms and boxplots to identify the dispersion, and the peak values and dispersion were used to generate box plots (presented in the Results section). In addition, a Kruskal-Wallis test (one-way ANOVA on ranks) was performed to detect any statistical differences in mean diameters of the non-parametric distributions, whereas small p-values of less than 0.05 were considered statistically significant.

6.3 Results and Discussion

The curve fitting allowed the extraction of particle size distribution data for the two different Q ranges, in which features on the I(Q) vs. Q diagram were observed. The distribution data were used to generate histograms and boxplots to identify the dispersion, and the peak values and dispersion were used to generate box plots (presented in the Results section). In addition, the particle size distributions were statistically evaluated by ANOVA, whereas small p-values of less

198

than 0.05 were considered statistically significant. A total of 18 SANS and USANS were prepared, from which 9 samples were contrast match point samples (CMP) composed of 67% D_2O/33% H_2O, and 9 samples contained 100 % D_2O (100 D) (Table VI-4). The data reduction through a Python® script and the curve fitting in Igor software, for the experiments resulted in two distinct particle populations within similar length scale regions: where the first region (Pop 1) was determined at a length scale between ~30 nm and 90 nm and the second population (Pop 2) between ~700 – 1100 nm as depicted in Figures VI-3, 4, 5 and Tables VI-2 and 3. For all datasets, Pop 1 was best described (fitted) by a Log-Normal (Eq. 8-11) and Pop 2 by a Schulz Zimm (spheres) distribution (Eq. 12-14).

According to the ANOVA analysis, differences around the mean were detected for particle dispersion in all three experimental groups of Pop1 (NP1), (NP1+V), and (NP5+V) (Figure VI-6a). However, the evaluation on d_p for pristine NPs and NP+V did not indicate any d_p difference, based on extended convection times, suggesting that smaller particles remain stable even under extended mechanical impact. In contrast, the NP5+V samples in Pop 1 resulted in a significant drop in d_p between 0h and 168h stirring (Figure VI-6). In addition, significantly smaller particle sizes in Pop 2 were detected among all (NP1+V) and (NP5+V) samples, suggesting that the addition of vermiculite has a more severe effect on the particle stability (for Pop 2) than the variation in polymer concentration. This assumption is supported by insignificant d_p's changes among all (NP1_only) samples in Pop 1 and 2 (Figures VI-6a,b). Variation around the mean was more pronounced for Pop1 for the 5%NP concentration samples compared to the 1% NP samples and the 1% NP+V samples (Figure VI-6a). The observation that the initial d_p's were slightly larger for the initial 5% (dark gray) sample may be explained by particle agglomeration due to higher NPs concentration within the sample. For Pop 2 samples, represented by the largest particles detected by USANS, the impact through stirring combined with vermiculite was significantly different between the experiments between 0h and 168h stirring time for the P1%+V experiments (Figure VI-9).

6.3.1 Impact of convection on NPs agglomeration (CMP)

The results of the combined SANS/USANS profiles of NPs (without vermiculite) pretreatments of ex-situ particle stirring (0h, 24h, 168h) are presented in Figure VI-3 and represent

"Set A" in Table VI-2. The power law subtraction from the scattering data (referred to as "excess" scattering) resulted in scattering oscillations representing NPs and their agglomerates for both SANS and USANS experiments (Figure VI-3 c,d). In addition, the extended stirring time (168h) on the 'NPs only' in the absence of vermiculite resulted in a slight decrease of I(Q) at the high Q regime ~ 0.01 and 0.001 Å (corresponding for particles between ~50 nm and 100 nm) of SANS data and an increase at the lowest Q regime (Figure VI-3a,b).

At larger-Q range (0.1-1.5x10-3 Å^{-1}) runs (without vermiculite), stirring times of 24h and 168h indicated a more readily NPs dispersion in water, compared to the 0h stirring samples. The latter sample resulted in more distinct oscillations indicating of NPs self-agglomerations (Figure VI-3c). In contrast, evaluation of the smaller particles (high-Q region) indicated that pristine NPs remained dispersed in water when unstirred, evidenced by the minor variation. Furthermore, NPs exposure to convection did not impact the agglomeration behavior of the small particles (Figure VI-3d). Oscillations at high-Q. The presence of soil (0.5%) in the NPs slurry resulted in an increase in intensity at low-Q and a decrease of *I(Q)*, indicating that contrast matching minimized the scattering attributable to vermiculite (Figure VI-4a,b).

Furthermore, slightly lower oscillations than the pristine NPs slurry suggest that NPs form agglomerates with soil (Figure VI-4c,d).

6.3.2 Impact of convection in soil presence on NPs stability at the CMP

The particle size distributions (PSD) in Pop 1 determined by SANS revealed a slight particle size change ranging between (40nm-50nm), suggesting that the size changed insignificantly for NPs in the presence of vermiculite and water slurry. However, for the larger particle size detected by USANS, there was a significant shift between 0h, 24h, and 168h stirring time with d_p's from 1084nm, 820nm, and 658 nm, respectively (Figure VI-9 and Table VI-3). This observation reveals that the presence of vermiculite significantly changed the dimensions of larger particles (Pop 2) between all three stirring time levels. However, it did not result in a pronounced size reduction for the smaller particle-size populations (Pop1). These observations imply that the ex-situ stirring time, combined with the presence of vermiculite, increased the mechanical abrasion and particle interaction effects, resulting in significant size changes (Figure VI-9).

6.3.3 Effect of high NPs concentration (5%) on NP's stability through convection at CMP

The highest NPs concentration (5%) in combination with vermiculite resulted in lower $I(Q)$ values suggesting that contrast matching in combination with soil (vermiculite) minimized scattering because of agglomeration with vermiculite. The small oscillations in the low-Q range confirm this observation at the extended stirring time of 168 h (Figure VI-5 a-c). The high-Q region indicated very low oscillations, suggesting that stirring induced particle dispersion in the slurry (Figure VI-5). Overall, stirring changed the power-law exponent β only slightly (Eq. 2): 3.6±0.2, suggesting the "rough" surface feature of the NPs (Table VI-2).

Furthermore, the experiments for the highest polymer concentrations (5%) in combination with vermiculite showed significant changes for the 168h and 24h compared to 0h pretreatment time, resulting in d_p's 95 nm, 60 nm, and 53 nm, respectively of particles in Pop1. In contrast, the larger particle fractions (Pop 2) did not undergo significant changes upon convection. These results suggest that the mechanical impact on NPs at higher polymer concentrations is more severe on smaller particles (~20-100 nm) compared to more significant particle size fractions (900 nm-1050 nm), as observed (Figure VI-11, 12, 13 and Table VI-3). These observations suggest that the particle concentration, in combination with the mechanical impact (convection), plays an essential role in the dimensional stability of NPs.

6.3.4 Effect of pre-stirring on particle stability and agglomeration at 100% D₂O

The 100% D$_2$O experiments measured the combined impact of NPs and vermiculite on particle agglomeration and particle stability. Therefore, different results regarding NPs size patterns, such as for the CMP samples, are assumed. However, the smaller particle sizes reflected by Pop 1 showed significant differences (p > 0.001) in d_p's, indicating that the stirring time in combination with high polymer (5%) and vermiculite concentration severely impacted the structure of the NPs. In contrast, the larger particles of Pop 2 did not undergo significant changes under the influence of stirring times (Figure VI-10,11,12). Interestingly, the 5%NPs/168h run indicated a larger dp's compared to 0h and 24h stirring time. This counter-intuitive observation that more severe conditions led to an increase in dp's may originate from the fact that vermiculite particles at the original size of 45 μm underwent particle size reduction due to ex-situ stirring and resulted in an additional contribution to the neutron beam signal (Figures VI-12 and 13).

6.4 Conclusions

This study investigates the NPs particle behavior, such as reduction and aggregation, under the influence of mechanical impact and NPs concentration using SANS and USANS in combination with neutron contrast matching techniques. Therefore, NPs were derived from a commercially available biodegradable plastic mulch material (PBAT) formed through a mechanical wet grinding process. Vermiculite (V) was used as a model soil, and the CMP was determined at a solvent ratio of 67 D_2O/33% H_2O. Composite slurries of NPs, V, and solvent ratios were prepared under various pre-stirring times and particle concentrations (0%, 1%, 5%) to investigate the mechanical impact (to mimic NPs behavior in a terrestrial environment) and investigated in this study. Results found that following ex-situ stirring, larger particles (Pop 2) self-associate and aggregate with soil. In addition, a more significant size reduction was observed for the larger particle dimensions under 168h pre-stirring times compared to 0 h and 24 h pretreatment.

In contrast, the smaller-sized NPs (Pop1, ~50 nm) remained intact upon pre-stirring (0h – 24h); however, increased severity through 168h ex-situ stirring resulted in significantly smaller particles compared to the starting material (20% size reduction), suggesting that extended exposure to mechanical impact results in further fragmentation of NPs. The NP's exposure and dispersion into terrestrial environments, particularly agricultural soils, is an emerging issue, mainly through farming practices such as plastic mulching. Environmental studies confirmed that biodegradable plastics form MPs and further fragment into NPs, which may either reside in the soil for months or migrate into soil and be transferred to other environmental compartments, such as groundwater, lakes, and rivers. Currently, a fundamental gap in understanding how NPs impact soil organisms, biota and microbial communities, and transport mechanisms.

The investigation of NPs in soil environments is challenging based on their small sizes and low concentrations. However, this research contributes to a better understanding of how NPs form, aggregate, and disperse in soil environments. Therefore, contrast matching realized by SANS and USANS techniques enables the measurement of the size and aggregation behavior of NPs in environmentally relevant conditions. Future terrestrial studies on NPs and soil particulates dynamics will focus on using authentic soil components such as humic acid (organic matter) under varying concentrations.

APPENDIX VI
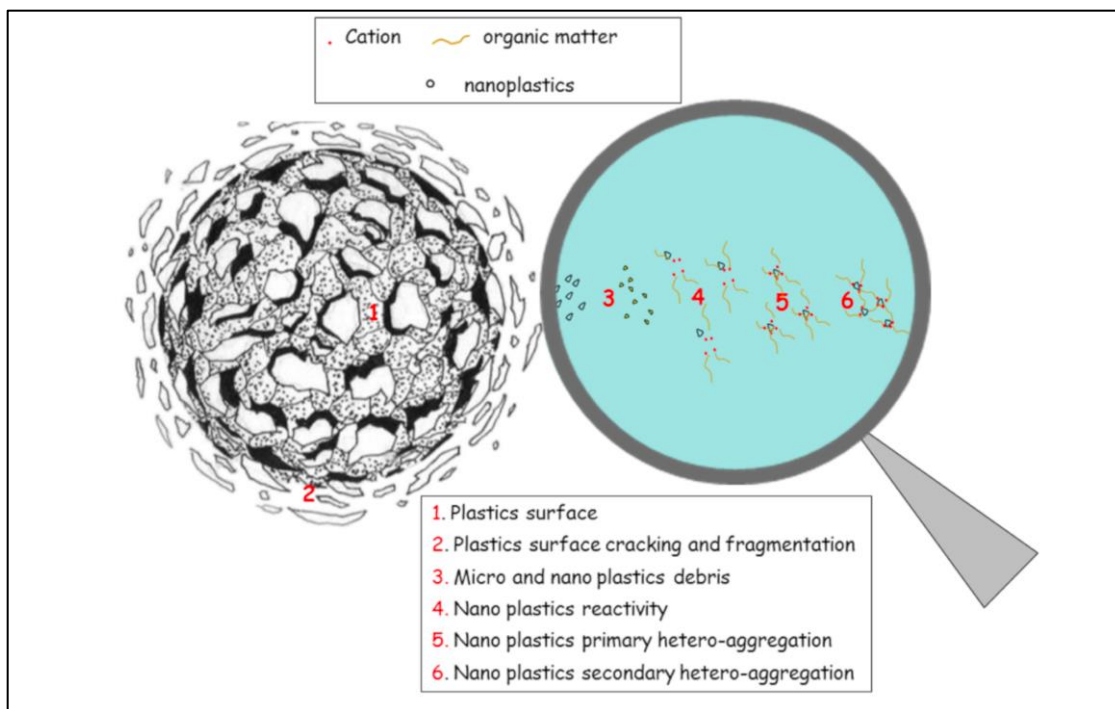
Figure VI-1. NP surface modification and hetero-aggregation process. Figure adapted from Pathan *et al.* (2020).
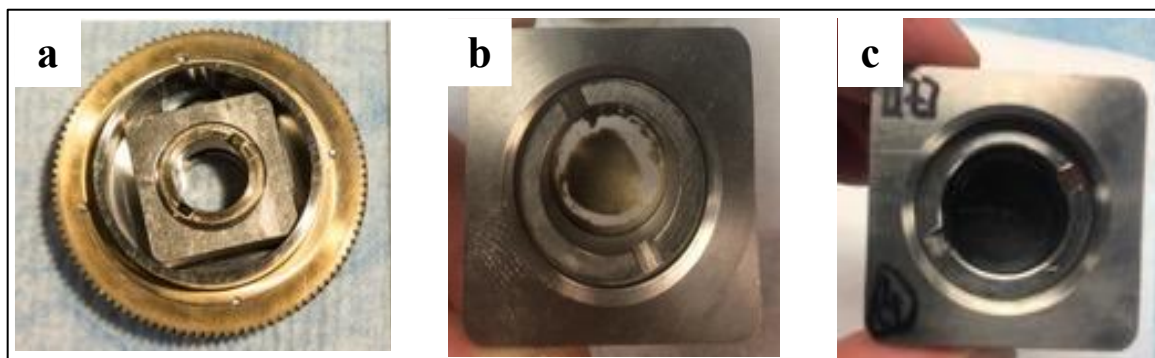
Figure VI-2. Titanium sample cell (a) in the adapter, (b) loaded with vermiculite, and (c) filled with PBAT-NPs (5 wt %) and vermiculite (0.5 wt %). Figure (a) adapted from https://neutrons.ornl.gov/eqsans/gallery
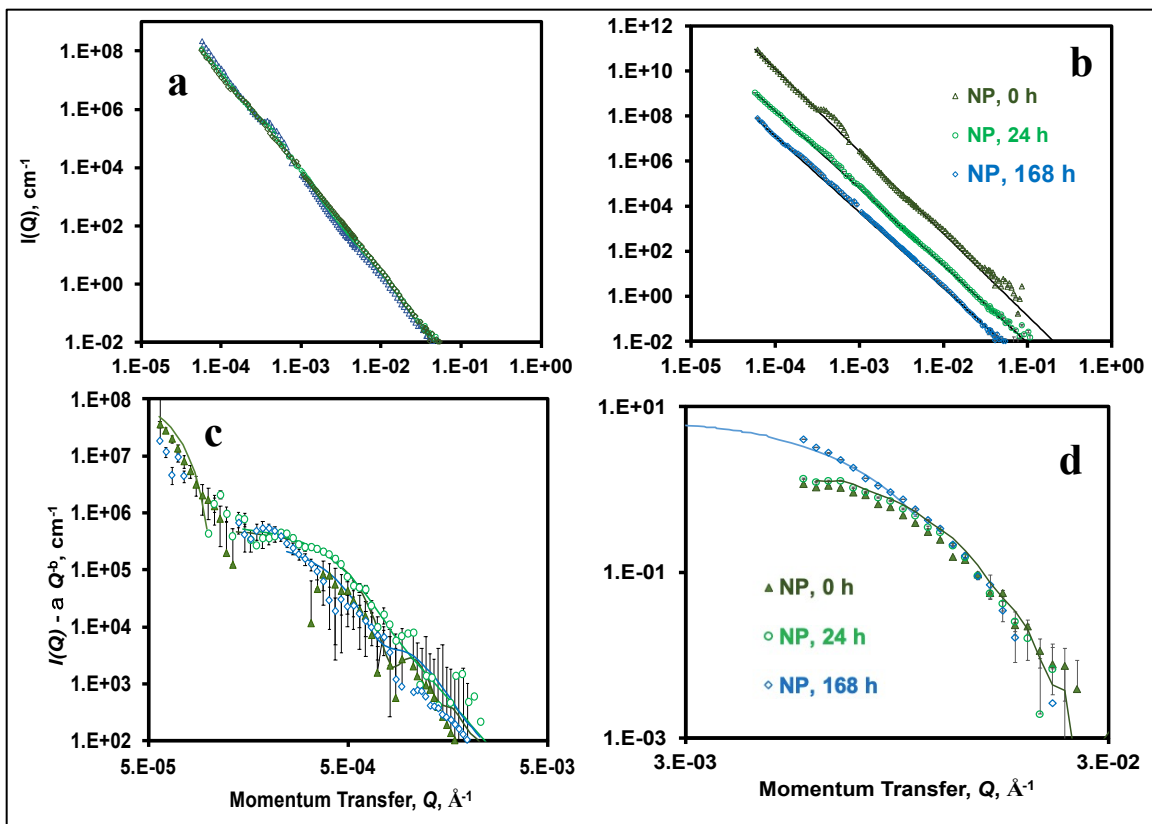
Figure VI-3. Impact of convection (ex-situ stirring) in the CMP (67% D_2O) of NPs in the absence of vermiculite investigated at 0h, 24h, and 168h pre-stirring time. (a) merged SANS/USANS data I(Q) vs. Q data, (b) power law fitting separated to improve visualization, (c) Schulz sphere model bimodal, (d) Log-Normal fitted by excess scattering data.
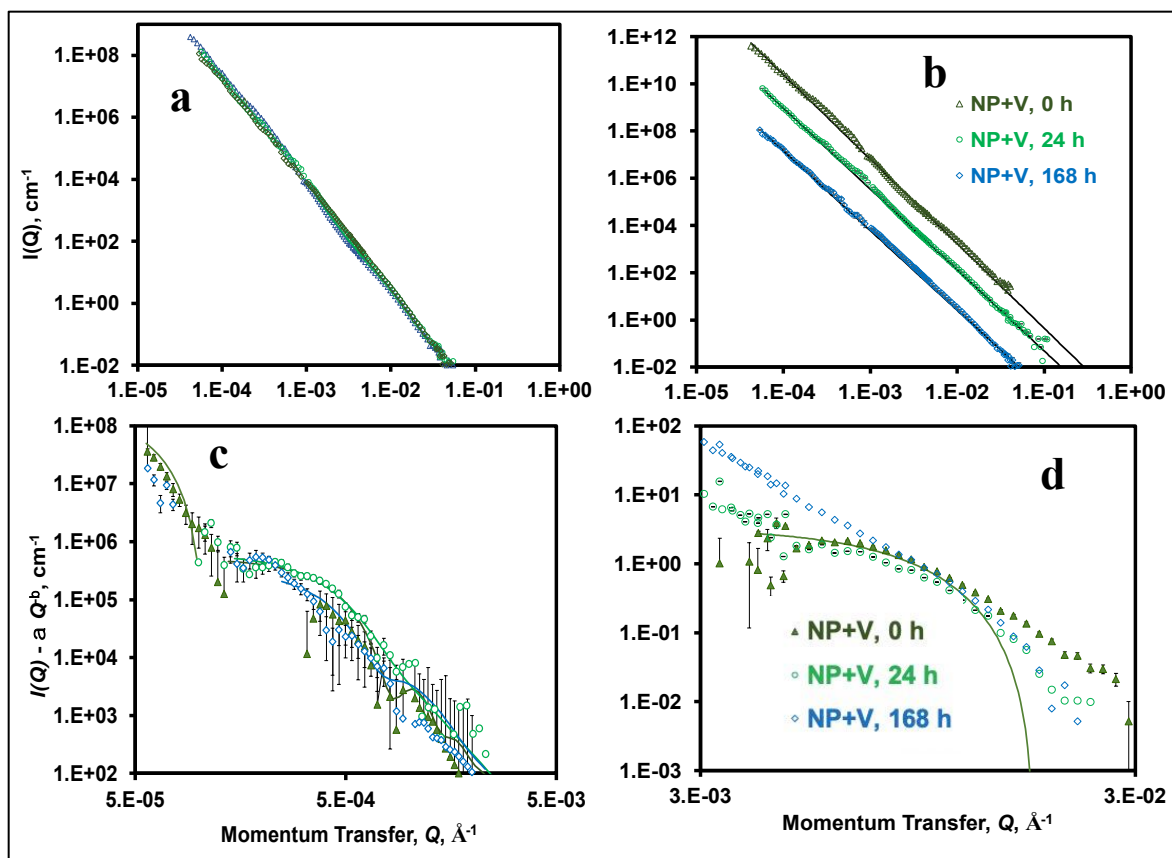
Figure VI-4. Impact of convection (ex-situ stirring) at the CMP (67% D_2O) on the agglomeration of NPs in the presence of vermiculite, investigated at three pretreatment conditions (0h, 24h, and 168h). (a) merged SANS/USANS data I(Q) vs. Q data. (b) power law fitting separated to improve visualization. (c) Schulz sphere model (bimodal) and (d) Log-Normal fitting derived from excess scattering data.
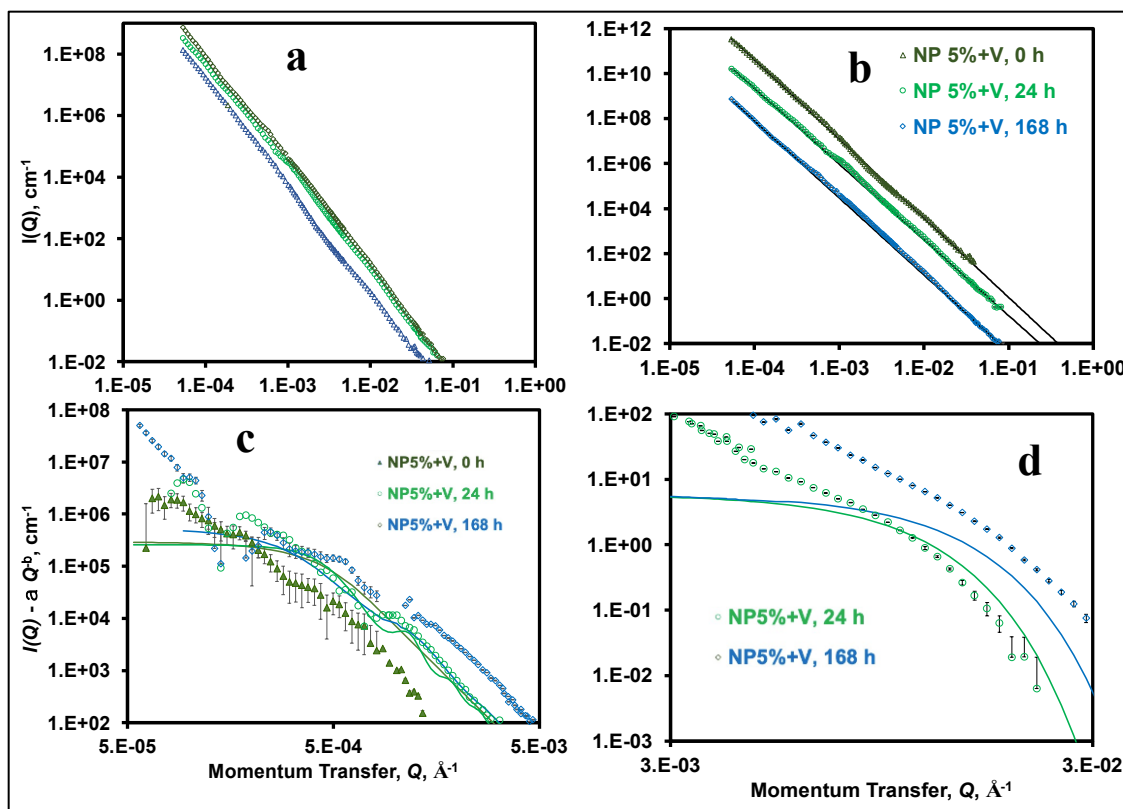
Figure VI-5. Effect of convection (ex-situ stirring) and enhanced NPs concentration (5%) on the agglomeration in the presence of vermiculite at the CMP (67% D_2O) of NPs investigated at three pretreatment conditions (0h, 24h, and 168h). (a) merged SANS/USANS data I(Q) vs. Q data. (b) power law fitting separated to improve visualization. (c) Schulz sphere model and (d) Log-Normal fitting derived from excess scattering data.
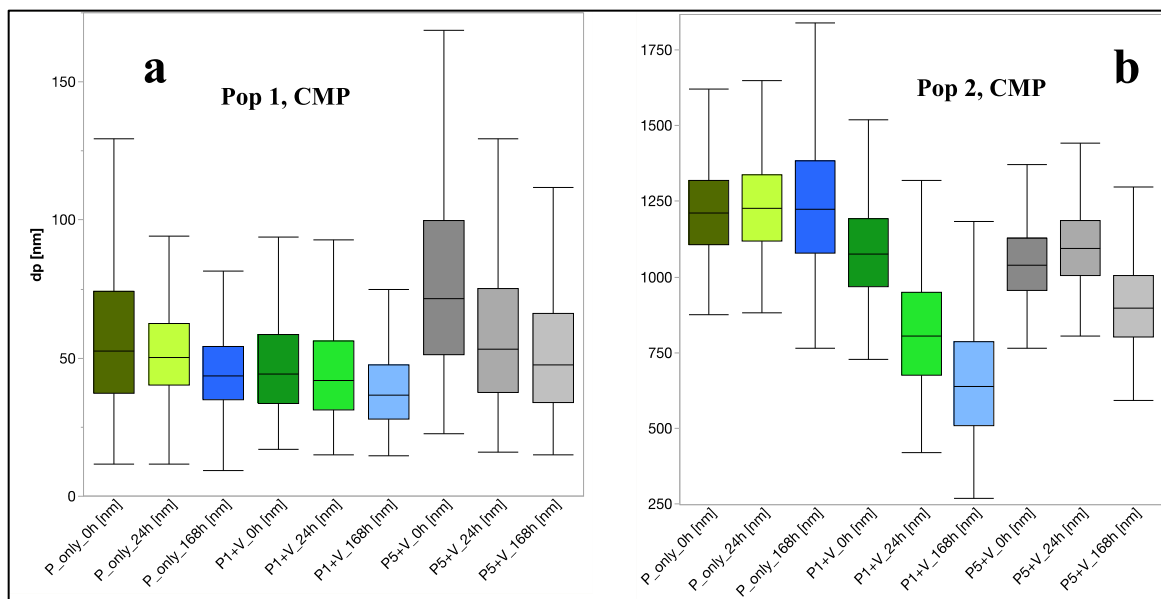
Figure VI-6. Boxplots of CMP experiments representing population 1 (Pop 1) and population 2 (Pop 2) of NPs by treatment severity (stirring times, 0h, 12h, 168 h). Size distributions derived from curve fitting of the Igor/Irena software representing average particle size variations caused by ex-situ stirring. Box plot data reflect the histograms depicted in Figures VI-8 -10.
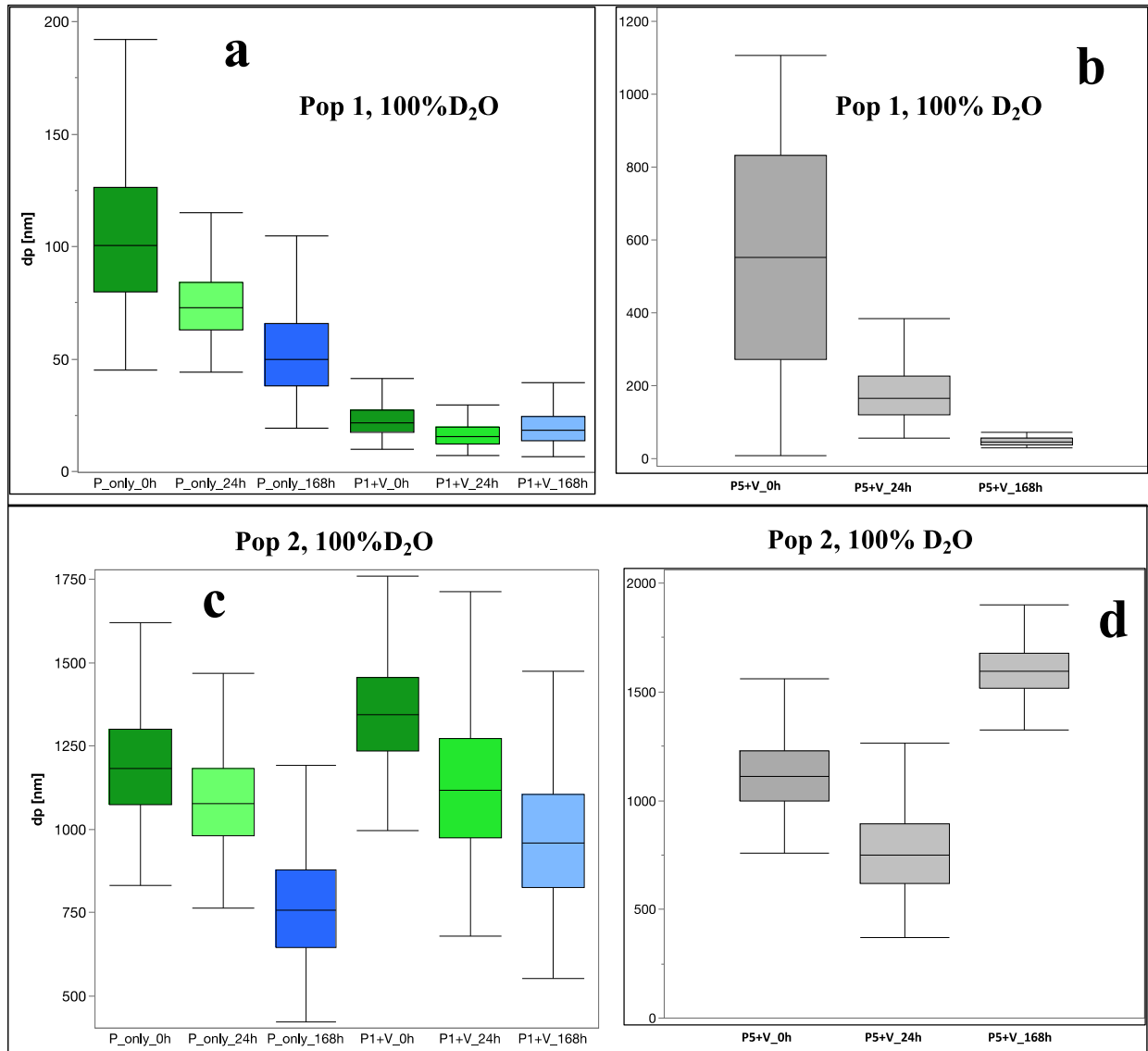
Figure VI-7. Boxplots of 100% D₂O samples representing populations 1 and 2 (Pop 1 and Pop 2, respectively) of NPs by treatment severity (stirring times, 0h, 12h, 168h). Datasets were obtained from the curve fitting procedure (Igor/Irena). Box plot data respresent the histograms depicted in Figures VI-11-13. Pop 1 represents the data collected via USANS and Pop 2 exhibits the SANS data collection.
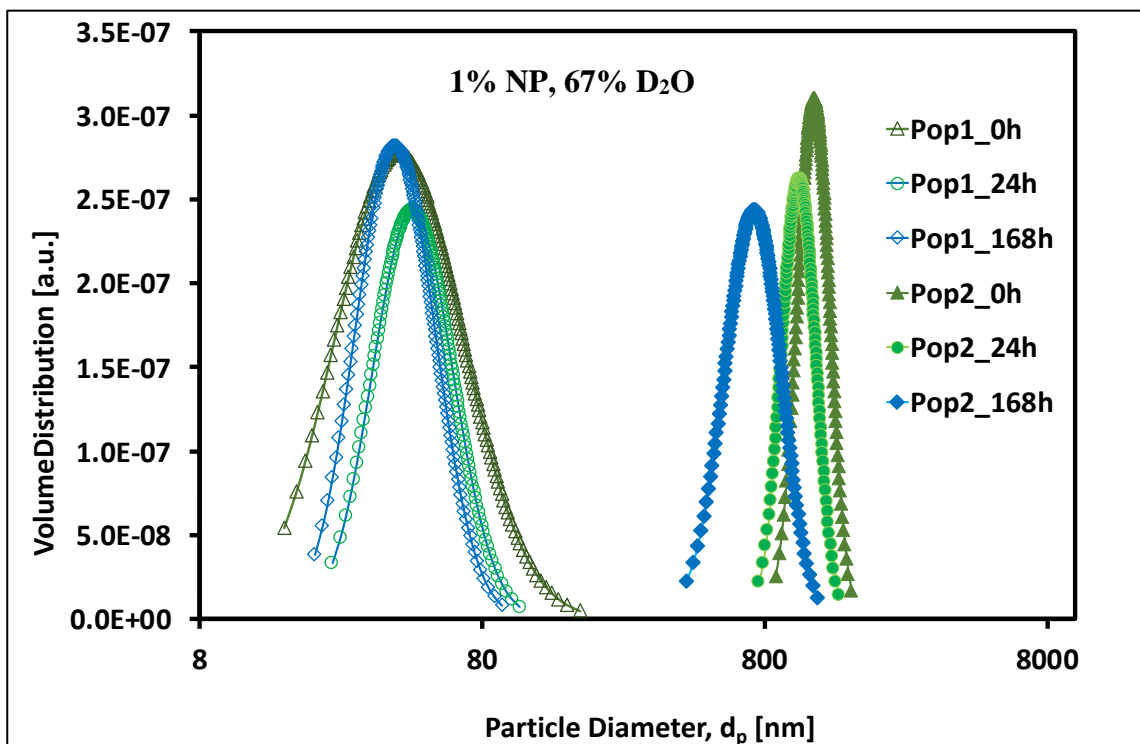
Figure VI-8. NPs only particle size distributions derived from curve fitting of the Igor/Irena software representing average particle size reduction because of ex-situ stirring. Pop 1 represents the Log-normal fit, and Pop 2 the Schulz spheres fitting. Ex-situ stirring resulted in a distinct reduction of average particle diameters for Pop 2.
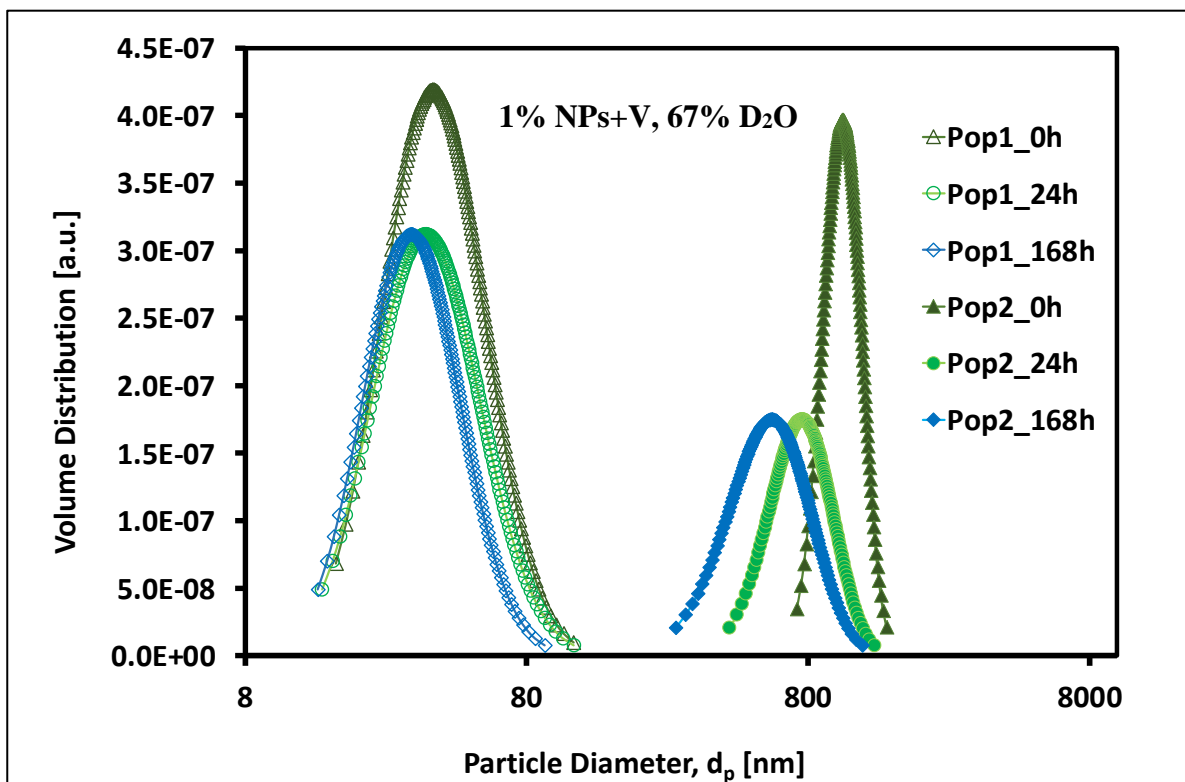
Figure VI-9. NPs size distributions derived from curve fitting of the Igor/Irena software representing average particle size reduction caused by ex-situ stirring.
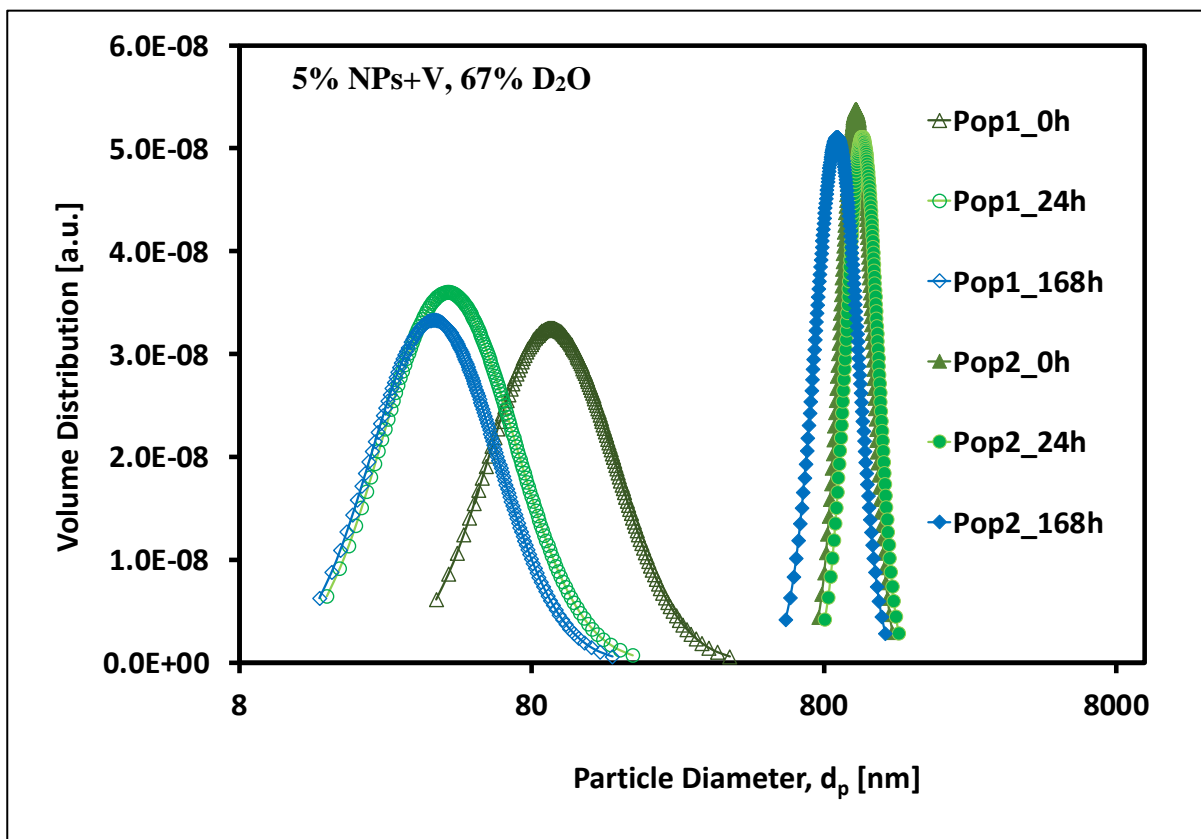
Figure VI-10. NPs (5wt%) +V: size distributions derived from curve fitting of the Igor/Irena software representing average particle size reduction because of ex-situ stirring.
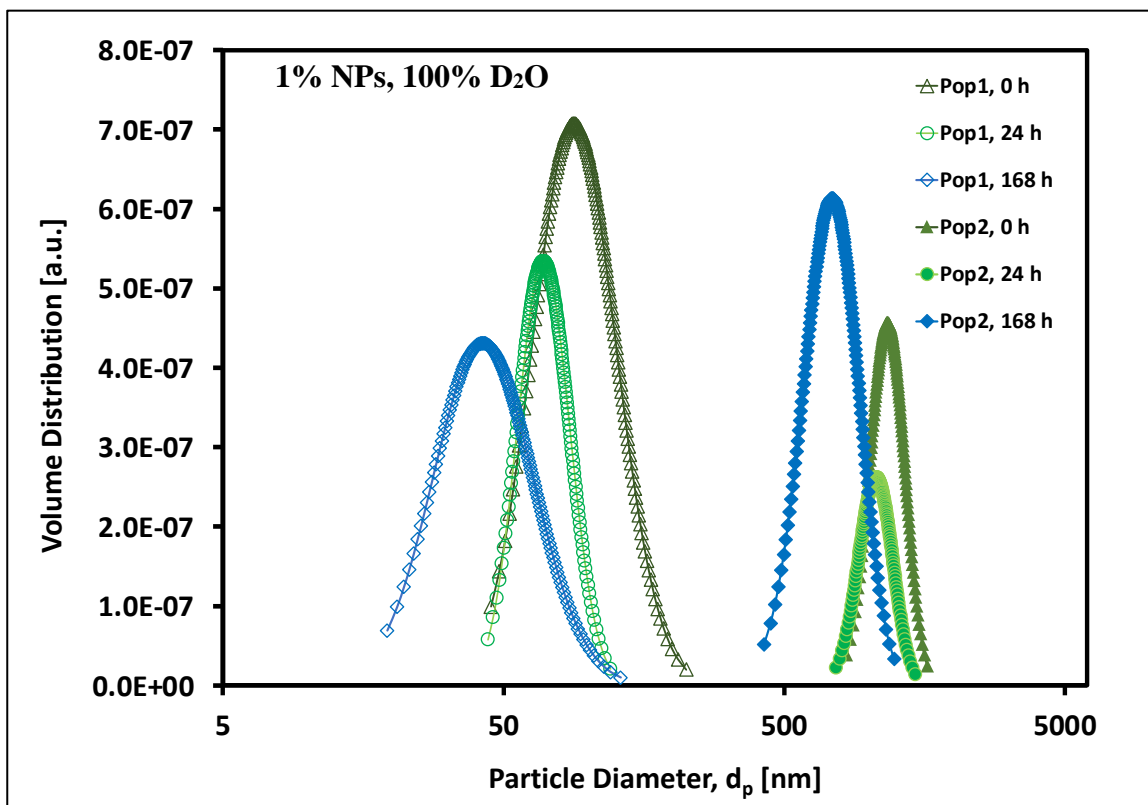
Figure VI-11. Comparison of NPs and vermiculite size distributions derived from curve fitting representing average particle size distribution because of ex-situ stirring.
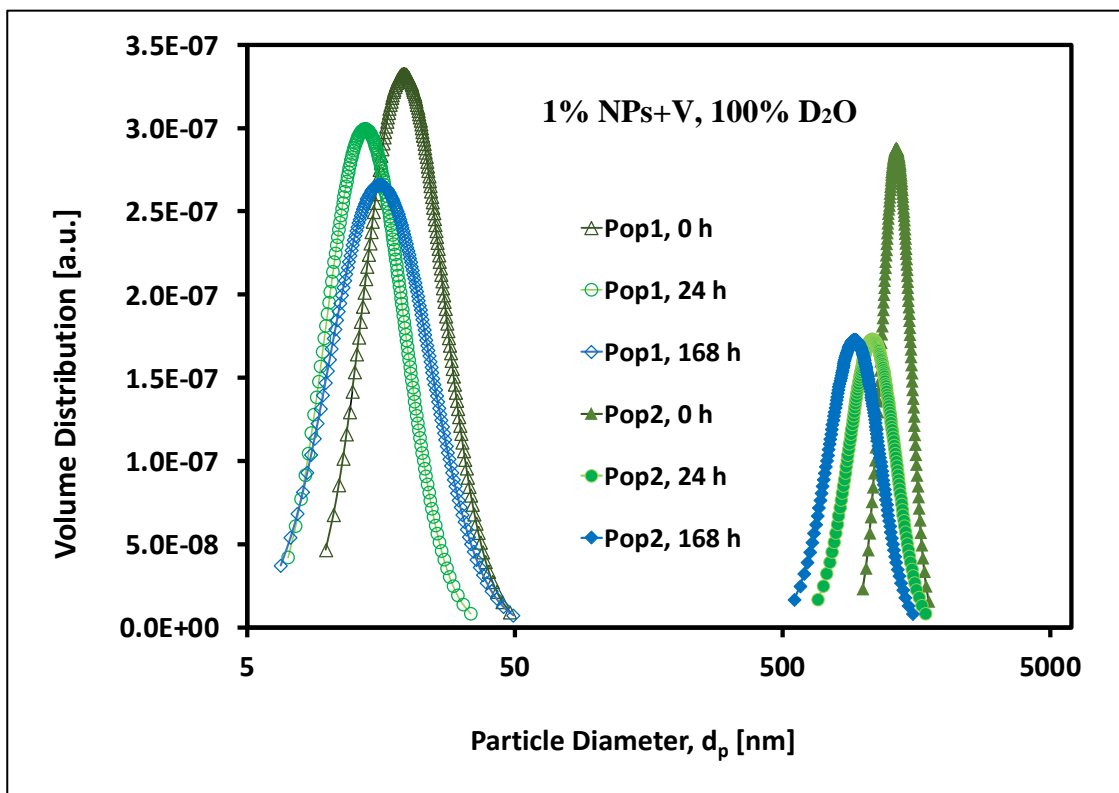
Figure VI-12. NPs and vermiculite size distributions derived from curve fitting of the Igor/Irena software representing average particle size distribution because of ex-situ stirring.
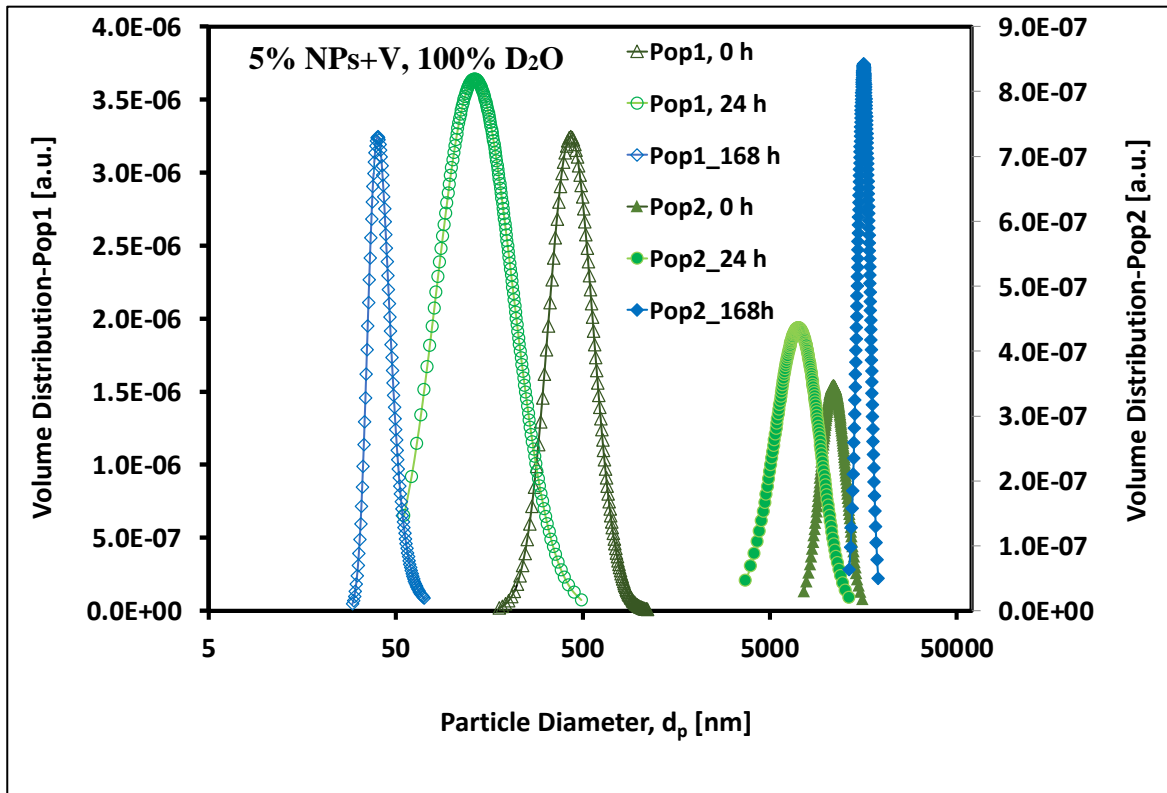
Figure VI-13. NPs and vermiculite size distributions derived from curve fitting of the Igor/Irena software representing average particle size distribution because of ex-situ stirring.

Table VI-1. Assignment of experimental factors for the SANS/USANS experiments

Design factor	Levels		
Stirring time [h]	0	24	168
Polymer concentration [wt%]	1	5	-
Vermiculite [wt%]	0	1	0.5
H_2O [vol%]	0	100	-
D_2O [vol%]	33	67	-

Table VI-2. Curve fitting parameters received from curve fitting in Igor for particle populations 1 and 2.

Run#	Set	Composition CMP[3]	Population 1[1] Mean d_p [nm]	Volume Fraction ϕ	FW-HM[4]	β[5]	Population 2[2] Mean d_p [nm]	Structure Factor	Volume Fraction ϕ	FW-HM[4]
1		NP, 0 h	54	6.58E-04	37	3.65	1180	Inteferences	6.96E-04	413.4
2	A[6]	NP, 24 h	46	4.72E-05	31	3.43	1176	Inteferences	6.85E-04	383.9
3		NP, 168 h	44	4.72E-05	30	3.37	947	Inteferences	5.59E-04	456.71
4		NP + V, 0 h	53	8.72E-05	42	3.58	1085	Dilute System	8.23E-04	397.58
5	B[7]	NP + V, 24 h	44	5.15E-05	32	3.43	814	Inteferences	4.70E-01	647.9
6		NP + V, 168 h	34	4.64E-05	24	3.37	819	Inteferences	1.07E-04	752.07
7		NP + V, 0 h	49	2.35E-05	35	3.46	840	Dilute System	1.56E-04	312.82
8	C[8]	NP + V, 24 h	47	8.55E-05	33	3.38	757	Hard Spheres	7.64E-04	425.52
9		NP + V, 168 h	41	8.55E-05	29	3.46	716	Dilute System	8.71E-04	506.68

[1+2] Populations derived from curve fitting analysis in Igor/Irena software

[3] Contrast match point samples composed of 67/33-D_2O/H_2O (vol%)

[4] Full width at half maximum of the distribution

[5] Power-law exponent describes the surface fractal, i.e. roughness of particles (-4 = smooth surface, -3 = rough surface). Form factor for all distributions: spheroids, Population 1: structure factor for all distributions = dilute system, best fit distribution = Log Normal, Population 2: best fit distribution = Schulz Zimm spheres.

[6] NPs represent PBAT NPs (1 wt%), no vermiculite added to the slurry

[7] NPs represent PBAT NPs (1 wt%) and vermiculite (0.5 wt%) added to the slurry

[8] NPs represent PBAT NPs (5 wt%) and vermiculite (0.5 wt%) added to the slurry

[1] Experimental conditions represent sets: A[1], B[2], C[3] depicted in Table VI-2

Table VI-3. Summary statistics of NPs particle diameters (d_p's) over the ex-situ stirring time series

Slurry Composition	NP [1]			NP(1%)+V [2]			NP(5%)+V [3]		
Stirring time [h]	0	24	168	0	24	168	0	24	168
Pop 1 (N = 150)									
Mean of d_p [nm]	58.8	52.5	45.4	47.9	45.7	39.3	80.1	95.5	53.1
Standard Deviation [nm]	29.3	16.6	14.4	19.5	19.8	15.3	39.2	30.6	29.9
Coefficient of Variation	50%	32%	32%	41%	43%	39%	49%	32%	56%
Std Err of of the Mean [nm]	2.4	1.4	1.2	1.6	1.6	1.2	3.2	4.5	2.1
Upper 95% Mean [nm]	49.6	55.9	48.3	51.1	48.9	41.7	86.4	64.9	57.3
Lower 95% Mean [nm]	43.2	50.4	43.6	44.8	42.5	36.8	73.8	55.0	48.9
Pop 2 (N = 150)									
Mean of d_p [nm]	1216.8	1232.6	1238.4	1084.3	820.4	658.1	1044.2	1099.1	906.5
Standard Deviation [nm]	152.3	156.8	220.9	162.3	195.9	199.7	124.1	130.7	144.9
Coefficient of Variation	13%	13%	18%	15%	24%	30%	12%	12%	16%
Std Err of of the Mean [nm]	12.4	12.8	18.0	13.2	16.0	16.3	10.1	10.7	11.8
Upper 95% Mean [nm]	1241.4	1257.9	1274.0	1110.4	852.0	690.3	1064.2	1120.2	929.9
Lower 95% Mean [nm]	1192.2	1207.3	1202.7	1058.1	788.8	625.8	1024.1	1078.0	883.1

Table VI-4. Comprehensive list of SANS and USANS experimental conditions[1]

Sample #	D₂O [vol%]	D₂O [ml]	D₂O [g]	H₂O [vol%]	H₂O [ml]	H₂O [g]	Solvent [g]	Solvent [mg]	NPs [wt%]	NPs [mg]	Vermiculite [wt%]	Vermiculite [mg]	Composition	Stirring [h]
1	67	0.67	0.74	33	0.33	0.32	1.07	1067.10	1.00	10.67	0.00	0.00	PBAT 1% only at CMP	0
2	67	0.67	0.74	33	0.33	0.32	1.07	1067.10	1.00	10.67	0.00	0.00	PBAT 1% only at CMP	24
3	67	0.67	0.74	33	0.33	0.32	1.07	1067.10	1.00	10.67	0.00	0.00	PBAT 1% only at CMP	168
4	67	0.67	0.74	33	0.33	0.32	1.07	1067.10	1.00	10.67	0.46	4.95	PBAT 1% + V at CMP	0
5	67	0.67	0.74	33	0.33	0.32	1.07	1067.10	1.00	10.67	0.46	4.95	PBAT 1% + V at CMP	24
6	67	0.67	0.74	33	0.33	0.32	1.07	1067.10	1.00	10.67	0.46	4.95	PBAT 1% + V at CMP	168
7	67	0.67	0.74	33	0.33	0.32	1.07	1067.10	5.00	53.36	0.46	4.95	PBAT 5% + V at CMP	0
8	67	0.67	0.74	33	0.33	0.32	1.07	1067.10	5.00	53.36	0.46	4.95	PBAT 5% + V at CMP	24
9	67	0.67	0.74	33	0.33	0.32	1.07	1067.10	5.00	53.36	0.46	4.91	PBAT 5% + V at CMP	168
10	100	1.00	1.11	0	0.00	0.00	1.11	1110.00	1.00	11.10	0.00	0.00	PBAT 1% at 100% D₂O	0
11	100	1.00	1.11	0	0.00	0.00	1.11	1110.00	1.00	11.10	0.00	0.00	PBAT 1% only at 100% D₂O	24
12	100	1.00	1.11	0	0.00	0.00	1.11	1110.00	1.00	11.10	0.00	0.00	PBAT 1% only at 100% D₂O	168
13	100	1.00	1.11	0	0.00	0.00	1.11	1110.00	1.00	11.10	0.46	5.15	PBAT 1% + V at 100% D₂O	0
14	100	1.00	1.11	0	0.00	0.00	1.11	1110.00	1.00	11.10	0.46	5.15	PBAT 1% + V at 100% D₂O	24
15	100	1.00	1.11	0	0.00	0.00	1.11	1110.00	1.00	11.10	0.46	5.15	PBAT 1% + V at 100% D₂O	168
16	100	1.00	1.11	0	0.00	0.00	1.11	1110.00	5.00	55.50	0.46	5.15	PBAT 5% + V at 100% D₂O	0
17	100	1.00	1.11	0	0.00	0.00	1.11	1110.00	5.00	55.50	0.46	5.15	PBAT 5% + V at 100% D₂O	24
18	100	1.00	1.11	0	0.00	0.00	1.11	1110.00	5.00	55.50	6.46	5.15	PBAT 5% + V at 100% D₂O	168

[1]A total volume of 1 ml solvent was prepared for each sample. Ratios for samples #1-9 were determined based on the contrast match point (CMP) determination as described in Chapter V. The CMP samples were composed of D₂O/H₂O 67/33 v/v and resulted in 1.07 g. Samples #10-18 contained a solvent with 100 vol%; no water was added, showing the influence of NPs and vermiculite. The CMP minimizes the vermiculite signal in water and reflects the level of deuteration in solvent (water).

CHAPTER VII

OVERALL CONCLUSIONS AND RECOMMENDATIONS

Agricultural mulch films contribute to higher crop yields but also form micro- and nanoplastics (MNPs) due to gradual breakdown after service life, posing a potential long-term hazard to terrestrial and aqueous environmental compartments and impacting soil biota and the food chain. Therefore, investigating the MNPs' interactions in soil require fundamental environmental studies using representative MNPs. In addition, generating authentic agricultural MNPs on a lab scale requires a good understanding of the stepwise formation process and dimensional and physicochemical properties of the resultant particle fractions. Furthermore, knowledge about the NPs' interactions and agglomeration behavior with soil is an inherent part of particle dynamics in soil.

This comprehensive study comprises five individual sub-studies (Chapter II-VI) presenting relevant findings about mechanical MNPs formation, their physicochemical properties, and finally, the agglomeration effects investigated by Small Angle Neutron Scattering techniques.

The first study section (Chapter II) describes detailed the formation of MNPs through stepwise size reduction procedures and characterizing methods applied to various materials in chapters II and III and as described in a previous publication (Astner *et al.*, 2019). General procedures involve cryogenically cooling (for film only), milling, sieving, wet grinding, imaging through a stereomicroscope, analyzing numerically through imaging and statistical software, and performing chemical and thermal analysis. As feedstocks, the commercially available PBAT film and PBAT pellets were used. In contrast, the cryogenic pretreatment was only applied to the film since pellets were generally easier to reduce size for generating MPs. In addition, the plastic film embrittlement (to mimic environmental weathering) was realized through cryogenic cooling before milling. Next, rotary milling was performed to simulate the abrasion by wind and mechanical machinery of field-dispersed plastic fragments. Subsequently, MPs sieving was achieved through cascaded sieves with mesh sizes ranging between 46 - 840 μm. Finally, wet grinding formed NPs (20 - 900 nm) from the 106 μm sieve fraction. For MPs, dimensional and shape analysis was performed through image analysis of stereomicrographs, and for NPs, dynamic light scattering (DLS) measured particle sizes. Overall, this size reduction method yielded similar results as discovered in previous studies (MPs and NPs were formed from PBAT films and PBAT pellets to test the robustness of these formation and characterization methods, whereas the latter feedstock was used as a starting component to form the former. However, MPs indicated a more significant deviation to the d_p for

the 250 µm fraction than the 106 µm d_p fraction concerning the nominal sieve size. Overall, the particle sizes showed similar results compared to a previous study (Astner *et al.*, 2019) (described in Chapter III), and both sieving fractions derived from film and pellets suggest similar breakdown characteristics.

In the second research section (Chapter III), we describe the successful formation of MPs and NPs derived from a PBAT film (biodegradable) and LDPE pellets (non-biodegradable).

The procedure involved a newly developed cryogenic cooling process (described in Chapter II) by employing a fractional factorial experimental design for the former feedstock. Results for both feedstocks showed that the formation process did not significantly change the physicochemical particle properties. Furthermore, the particle size evaluation after sieving experiments for both plastics resulted in unimodal MPs size distributions. Moreover, NPs indicated bimodal size distributions, suggesting similar formation behavior under similar mechanical treatment conditions. Ultimately, observations indicate that the applied size reduction process is a well-suited method for generating MPs and NPs for fundamental environmental studies without artifacts to expect from the particles compared to the initial feedstocks.

In the third research section (Chapter IV), we compared the suitability of how cryogenic pretreatment mimicked field weathering of MNPs (following the procedure described in Chapter II) derived from blends of PBAT/starch and PLA/PHA BDMs. Furthermore, we investigated the gradual size fragmentation of MPs (106 µm) into NPs after 6, 30, and 60 wet-grinding passes. Statistical software allowed particle size characterization through numerical analysis and distribution fitting of stereomicroscopic images. In addition, particle surface charges (zeta potential) of the received NPs particles were measured. Finally, a lab-biodegradation study according to ASTM 5988 was performed, mimicking soil conditions of generated cryogenically formed and environmentally weathered MPs and NPs.

Overall, MPs formed from weathered films (W-films) showed significantly higher degrees of size reduction and more prominent monodisperse size distributions. For PBAT, the formation of NPs through wet grinding resulted in smaller particles than in CRYO treatment and the starch release, as evidenced by TGA analysis. W-PBAT NPs were smaller than CRYO-PBAT NPs, showed monodisperse size distributions, had a more significant negative charge per unit surface area, and were more biodegradable in soil. Environmental weathered PLA/PHA particles

underwent crosslink formations caused by photochemical reactions of the calcium carbonate nanofiller. Interestingly, NPs formed by CRYO-PLA/PHA was significantly smaller (5-fold) compared to NPs formed by W-PLA/PHA due to the higher recalcitrance of the latter particles. In accordance, higher thermal stability and slower biodegradation of the crosslinked W-PLA/PHA NPs were observed, suggesting a lower rate of hydrolysis. Overall, W-NPs indicated lower surface charges than CRYO-NPs, implying that previous particles may form more stable aggregates than the latter. The size reduction process from MPs into NPs revealed a rapid transformation of nearly 10-fold, resulting in unimodal size distributions.

Further size reductions revealed multimodal distributions, except for NPs formed from W-PLA/PHA (crosslink formation). Interestingly, a higher biodegradability of MPs than NPs was observed for both pretreatment forms, such as cryogenically and environmentally weathered conditions. These observations indicate starch (the preferred food source for microorganisms) leaching during NPs generation. Overall, the impacts of size reduction and environmental weathering on dimensional and physicochemical show significant differences among polymeric materials. Furthermore, the embrittlement through cryogenic cooling did not mimic the effects on polymeric as it would occur through environmental weathering. Based on these observations, selecting surrogate MNPs for environmental studies requires careful consideration of multiple factors. In general, the systematic processing and characterization techniques employed in this work may serve as a basis for researchers to understand which factors to consider when generating MNPs for specific environmental research applications. However, a significant difference in particle sizes and physiochemical properties was found when environmentally weathered and cryogenically formed MPs and NPs from biodegradable mulches were compared.

The fourth study section (Chapter V) investigates the potential utility of NPs behavior in terrestrial systems using neutron contrast matching by Small Angle Neutron Scattering (SANS) and Ultra-USANS. We determined the vermiculite contrast match point (CMP) for vermiculite (artificial soil) at a 67 wt% deuteration level in the water. The CMP adjustment minimizes the vermiculite scattering contribution. Our goal was to investigate the impact of soil and convective transport on NPs formed from a biodegradable PBAT-rich plastic mulch film. Therefore, we determined the impact of convective transport (ex situ stirring for 24 h). We found that convective transport enhanced the particle dispersion of NPs exposed to the neutron beam. The observation

that larger-sized NPs (300-1000 nm) formed self-aggregates and associated with soil indicated that convection minimized the agglomeration. In addition, we observed that the larger-sized NPs (which may also represent NP aggregates) underwent size reduction by ex-situ stirring while smaller-sized NPs (50 nm) remained intact. In soil, residing NPs may severely impact soil fertility, soil biota, earthworms, and possible transport into deeper zones (eventually reaching groundwater levels). SANS and USANS techniques, in combination with contrast matching, provide a unique tool to investigate the size and agglomeration behavior of NPs in artificial soil. In addition, this study gave us a basic understanding of soil-NP interactions and dynamics regarding future environmental fate and ecotoxicity studies.

The fifth research section (Chapter VI) extends the parameter space of NPs concentration (5 wt%) and pretreatment time (168h) as described in Chapter V. This research describes particle interactions between NPs and soil (vermiculite). In contrast, the experimental conditions, such as solvent composition and ambient temperature, were constant for all experiments.

In summary, the body of research contained in this dissertation showed that we successfully formed, investigated, and characterized MPs and NPs through lab procedures suitable for environmental fate, transport, and ecotoxicity studies.

Therefore, we have developed methods to gain knowledge of MNPs' life stages in ag soils as follows:

- Preparation of surrogate MPs and NPs through a robust formation method involving cryogenic embrittlement followed by mechanical size reduction stages
- Isolation of NPs from soil particles to investigate the aggregation and size reduction behavior of NPs using SANS/USANS techniques with contrast matching techniques

The employed methods provided a deeper insight into how plastics disintegrate from meso= through micro- into nanoscale particles. The breakdown from larger fragments into MPs occurs uniformly, represented in the unimodal particle size distributions. The observations were similar among biodegradable and non-biodegradable feedstocks, which were not prior exposed to environmental weathering. The formation of MNPs through cryogenic milling and wet grinding using biodegradable (PBAT) and nonbiodegradable (LDPE) feedstocks showed comparable physicochemical property changes between polymeric materials and size fractions, indicating that

these particles may offer similar chemical and thermal properties as surrogate material for environmental studies. Furthermore, these results provide proof of a robust method to form MNPs. A comparison of MPs also confirmed this observation, and NPs started from film and pellets.

However, significant differences in size and physiochemical properties were detected when weathered environmental films were processed to form MPs and NPs and then compared to cryogenically formed MPs and NPs. The disintegration of MPs into NPs showed transformation into multimodal distributions. Higher severities promoted by the higher number of wet-grinding passes indicated the formation of different NPs particle populations. Furthermore, we observed NPs particle formation through wet grinding at low severities (6 passes). This observation suggests that MPs formed in various environmental compartments may disintegrate into NPs at early stages. For example, in the presence of aqueous compartments, as mimicked through the wet grinding process. These dispersed particles will likely degrade at different rates depending on their size and composition. For example, environmentally dispersed NPs can leach lower molecular weight components such as starch from a PBAT-rich film. This mechanism, in turn, will likely result in a lower biodegradation rate than MPs, as observed in our study.

Furthermore, our observations suggest that NPs may reside longer than anticipated in agricultural soils, which is essential for risk assessment investigating soil ecosystems.

Also, the surface polarity (charge) of environmentally weathered NPs was observed to be lower than untreated feedstocks, which may result in a more pronounced repulsive interaction with particles in the soil. The agglomeration behavior with soil and NPs-NPs interactions occur as a function of NPs particle size and concentration. Smaller particles (~30 nm-100 nm) remain dispersed in aqueous slurries, whereas larger particles (~300-800 nm tend to agglomerate with soil particles, as SANS and USANS studies revealed.

Our findings identified the life stages of MNPs derived from agricultural feedstocks and characterized their dimensional, physicochemical, biodegradation, and agglomeration behavior.

Overall, this research supports the fundamental understanding of how terrestrial MNPs may fragment in soil. Furthermore, their small size and recalcitrance (NPs of cross-linked PLA/PHA) could reside in the soil for an extended period and potentially impact terrestrial organisms such as earthworms and microbial communities. For future studies, it is essential to expand the experimental space by carefully selecting biodegradable plastic precursor materials that are readily

biodegradable. Some feedstocks form cross-links due to photodegradation reactions, as we observed for PLA/PHA film. To mitigate the impact of terrestrial MNP, future agricultural plastics may include biobased precursor components such as lignin derived from sustainable lignocellulosic feedstocks. However, besides the suitability for film manufacture, further fundamental studies will be required to identify their fragmentation, agglomeration, and biodegradation behavior when exposed to the terrestrial environment.

7.1 Future research

This dissertation covers the life stages of MNPs derived from agricultural plastic feedstocks, including their stepwise transformation and dimensional and physicochemical characterization. Furthermore, their employment in environmental studies under biodegradation and NPs defragmentation and agglomeration behavior during external mechanical impact (convection) was investigated. The evaluation and integration of mechanically formed MNPs in prospective environmental studies, future research directions will involve a broader range of agricultural plastic feedstocks, including biodegradable plastics such as composites of PBAT and Kraft lignin, PBS, and PLA feedstocks, which are promising precursor feedstocks for agricultural plastics. Lignins from woody and herbaceous lignocellulosic biomass have been previously extracted and investigated for their potential use in producing value-added chemicals and biobased polymers (Astner *et al.*, 2015; Meek *et al.*, 2016). The sorption behavior of frequently used agricultural chemicals dispersed in MNPs is essential for environmental fate studies. Absorbed chemicals onto MNPs may function as transport vectors into deeper soil layers and cause damage to soil biota (Sobhani *et al.*, 2021).

7.1.1 Chemical sorption behavior of MNPs

MNPs' chemical- and physical sorption kinetics depend on polymer-specific characteristics such as molecular polarity and electro-attractive electrostatic action forces between plastic and soil particles. MPs and even more NPs exhibit a large surface-to-volume ratio, may have a porous and rough surface, and are thus excellent sorbents and carriers for pollutants such as heavy metals and persistent organic pollutants (POPs) and may concentrate and transfer them. Furthermore, the MPs' surface area will dictate the sorption capacity based on material-specific properties. Therefore, particle diameter, shape, and topography of MPs, because of the breakdown features and the

selected plastic feedstock, will be essential for the sorption behavior of MPs. MPs processed through increased mechanical processing severity (harsher conditions) are expected to show increased adsorption kinetics through cavity formation.

7.1.2 MNPs transport in porous media

This study will determine and compare deposition and MPs and NPs during transport in porous media using dilute suspensions of MPs/NPs in soil (vermiculite), water, and changing pH levels. In addition, this investigation aims to identify if the transport of smaller particle sizes (NPs) compared to larger particle sizes (MPs) will lead to steric hindrance based on preferential attachment to the porous material of the solid-water and the air-water interfaces.

7.1.3 Agglomeration behavior of organic components in soil

Future terrestrial studies on NPs and soil particulates dynamics target using authentical soil components involving humid acid and variations of organic matter under varying particle concentrations and pH conditions. Based on the findings described in this dissertation (Chapters V and VI), SANS and USANS methods are powerful tools suitable for investigating the agglomeration behavior of NPs and vermiculite (V) in combination with authentic soil particulates such as humic acid (HA) in deuterated water (D_2O) and purified water (H_2O) at different ratios. For the investigation of the particle dynamics of organic components in the soil, the experiments are proposed as follows:

- **Contrast Match Point determination by SANS:** The contrast match point (CMP) for V+ HA (10 µg/mL H_2O) will be investigated to test if the latter component would shift the CMP of 67% D_2O as determined previously for V only (as described in Chapter V). The stirring times will involve 0 h, 24h, and 168h, and around 6 samples are required to determine the CMP.

- **Particle agglomeration investigation by SANS and USANS:** SANS and USANS samples: All samples will employ PBAT-NPs (1%, except for control), V (0.5 %) + HA (10 ug/mL H_2O), and a D_2O concentration at CMP as determined in SANS. The sample set will consist of 3 different co-suspension combinations (a) [HA]-[NPs+V]; (b) [NPs]+[HA-V] and (c) [HA, NPs] + [HA, V], all x 3 pre-stirring times (0h, 24h, and 168h), plus an empty cell: 10 samples total. The samples for SANS and USANS will be adjusted at pH 7 in a 10 mM

phosphate buffer solution to mimic soil conditions present in Tennessee. The SANS and USANS samples mentioned above will be performed at a temperature of 22 °C using the 400 µL titanium tumbler sample environment. The studies mentioned above will build on the existing framework of MNPs formation and their findings on physicochemical properties. They will also provide a comprehensive understanding of chemical sorption, transport, and agglomeration behavior using authentical plastic and soil components to mimic MNPs interactions in soil. In addition, the proposed findings will contribute to a better understanding of MNPs' environmental fate studies and risk assessment.

REFERENCES

Abbasimaedeh, P., Ghanbari, A., O'Kelly, B. C., Tavanafar, M., & Irdmoosa, K. G. (2021). Geomechanical behaviour of uncemented expanded polystyrene (EPS) beads–clayey soil mixtures as lightweight fill. *Geotechnics, 1*(1), 38-58.

Agamalian, M., Heroux, L., Littrell, K., & Carpenter, J. (2018). *Progress on The Time-of-Flight Ultra Small Angle Neutron Scattering Instrument at SNS.* Paper presented at the Journal of Physics: Conference Series.

Agamalian, M., Heroux, L., Littrell, K. C., & Carpenter, J. M. (2018). Progress on The Time-of-Flight Ultra Small Angle Neutron Scattering Instrument at SNS. *Journal of Physics: Conference Series, 1021*, 012033.

Ajioka, M., Enomoto, K., Suzuki, K., & Yamaguchi, A. (1995). Basic properties of polylactic acid produced by the direct condensation polymerization of lactic acid. *Bulletin of the Chemical Society of Japan, 68*(8), 2125-2131.

Alimba, C. G., Faggio, C., Sivanesan, S., Ogunkanmi, A. L., & Krishnamurthi, K. (2021). Micro (nano)-plastics in the environment and risk of carcinogenesis: Insight into possible mechanisms. *Journal of Hazardous Materials, 416*, 126143.

Alimi, O. S., Budarz, J. F., Hernandez, L. M., & Tufenkji, N. (2018). Microplastics and Nanoplastics in Aquatic Environments: Aggregation, Deposition, and Enhanced Contaminant Transport. *Environmental Science & Technology, 52*(4), 1704-1724.

Alimi, O. S., Farner Budarz, J., Hernandez, L. M., & Tufenkji, N. (2018). Microplastics and nanoplastics in aquatic environments: aggregation, deposition, and enhanced contaminant transport. *Environmental Science & Technology, 52*(4), 1704-1724.

Allen, P. A., Michael, N. A., D'Arcy, M., Roda-Boluda, D. C., Whittaker, A. C., Duller, R. A., & Armitage, J. J. (2015). Fractionation of grain size in terrestrial sediment routing systems. *Basin Research, 29*(2), 180-202.

Alzagameem, A., Khaldi-Hansen, B. E., Büchner, D., Larkins, M., Kamm, B., Witzleben, S., & Schulze, M. (2018). Lignocellulosic biomass as source for lignin-based environmentally benign antioxidants. *Molecules, 23*(10), 2664.

Anunciado, M. B., Hayes, D. G., Astner, A. F., Wadsworth, L. C., Cowan-Banker, C. D., Gonzalez, J. E. L. y., & DeBruyn, J. M. (2021). Effect of Environmental Weathering on Biodegradation of Biodegradable Plastic Mulch Films under Ambient Soil and Composting Conditions. *Journal of Polymers and the Environment, 29*(9), 2916-2931.

Anunciado, M. B., Hayes, D. G., Wadsworth, L. C., English, M. E., Schaeffer, S. M., Sintim, H. Y., & Flury, M. (2021). Impact of Agricultural Weathering on Physicochemical Properties of Biodegradable Plastic Mulch Films: Comparison of Two Diverse Climates Over Four Successive Years. In *Journal of Polymers and the Environment* (Vol. 29, pp. 1-16).

Arrieta, M. P., López, J., Ferrándiz, S., & Peltzer, M. A. (2013). Characterization of PLA-limonene blends for food packaging applications. *Polymer Testing, 32*(4), 760-768.

Artham, T., & Doble, M. (2008). Biodegradation of Aliphatic and Aromatic Polycarbonates. *Macromolecular Bioscience, 8*(1), 14-24.

Astner, A. F., Hayes, D. G., O'Neill, H. M., Evans, B. R., Pingali, S. V., Urban, V. S., & Young, T. M. (2019). Mechanical formation of micro- and nano-plastic materials for environmental studies in agricultural ecosystems. *Science of the total environment, 685*, 1097-1106.

Astner, A. F., Hayes, D. G., O'Neill, H. M., Evans, B. R., Pingali, S. V., Urban, V. S., & Young, T. M. (2022). Forming Micro-and Nano-Plastics from Agricultural Plastic Films for Employment in Fundamental Research Studies. *JoVE*, e64112.

Astner, A. F., Hayes, D. G., Pingali, S. V., O'Neill, H. M., Littrell, K. C., Evans, B. R., & Urban, V. S. (2020). Effects of soil particles and convective transport on dispersion and aggregation of nanoplastics via small-angle neutron scattering (SANS) and ultra SANS (USANS). *PloS one, 15*(7), e0235893.

Astner, A. F., Young, T. M., & Bozell, J. J. (2015). Lignin yield maximization of mixed biorefinery feedstocks by organosolv fractionation using Taguchi Robust Product Design. *73*, 209-216.

Auta, H. S., Emenike, C. U., Jayanthi, B., & Fauziah, S. H. (2018). Growth kinetics and biodeterioration of polypropylene microplastics by Bacillus sp. and Rhodococcus sp. isolated from mangrove sediment. *Marine pollution bulletin, 127*, 15-21.

Bandmann, V., Müller, J. D., Köhler, T., & Homann, U. (2012). Uptake of fluorescent nano beads into BY2-cells involves clathrin-dependent and clathrin-independent endocytosis. *FEBS letters, 586*(20), 3626-3632.

Bandopadhyay, S., Martin-Closas, L., Pelacho, A. M., & DeBruyn, J. M. (2018). Biodegradable Plastic Mulch Films: Impacts on Soil Microbial Communities and Ecosystem Functions. *Frontiers in Microbiology, 9*, 819.

Bandopadhyay, S., Sintim, H. Y., & DeBruyn, J. M. (2020). Effects of biodegradable plastic film mulching on soil microbial communities in two agroecosystems. *PeerJ, 8*, e9015.

Barboza, L. G. A., Vethaak, A. D., Lavorante, B. R., Lundebye, A.-K., & Guilhermino, L. (2018). Marine microplastic debris: An emerging issue for food security, food safety and human health. *Marine pollution bulletin, 133*, 336-348.

Barría, C., Brandts, I., Tort, L., Oliveira, M., & Teles, M. (2020). Effect of nanoplastics on fish health and performance: A review. *Marine pollution bulletin, 151*, 110791.

Bayat, H., Rastgo, M., Mansouri Zadeh, M., & Vereecken, H. (2015). Particle size distribution models, their characteristics and fitting capability. *Journal of Hydrology, 529*, 872-889.

Bellasi, A., Binda, G., Pozzi, A., Galafassi, S., Volta, P., & Bettinetti, R. (2020). Microplastic contamination in freshwater environments: A review, focusing on interactions with sediments and benthic organisms. *Environments, 7*(4), 30.

Besseling, E., Wang, B., Lurling, M., & Koelmans, A. A. (2014). Nanoplastic Affects Growth of S. obliquus and Reproduction of D. magna. *Environmental Science & Technology, 48*(20), 12336-12343.

Bi, S., Barinelli, V., & Sobkowicz, M. J. (2020). Degradable controlled release fertilizer composite prepared via extrusion: Fabrication, characterization, and release mechanisms. *Polymers, 12*(2), 301.

Blake, G. R. (2008). Particle density. In W. Chesworth (Ed.), *Encyclopedia of Soil Science* (pp. 504-505). Dordrecht: Springer Netherlands.

Bläsing, M., & Amelung, W. (2018). Plastics in soil: Analytical methods and possible sources. *Science of the total environment, 612*, 422-435.

Borsali, R., & Pecora, R. (2008). *Soft matter characterization* (Vol. 725): Springer.

Botta, L., Titone, V., Teresi, R., Scarlata, M. C., Re, G. L., La Mantia, F. P., & Lopresti, F. (2022). Biocomposite PBAT/lignin blown films with enhanced photo-stability. *International Journal of Biological Macromolecules, 217*, 161-170.

Bouwmeester, H., Hollman, P. C. H., & Peters, R. J. B. (2015). Potential Health Impact of Environmentally Released Micro- and Nanoplastics in the Human Food Production Chain: Experiences from Nanotoxicology. *Environmental Science & Technology, 49*(15), 8932-8947.

Brewer, A., Dror, I., & Berkowitz, B. (2020). The mobility of plastic nanoparticles in aqueous and soil environments: a critical review. *ACS ES&T Water, 1*(1), 48-57.

Briassoulis, D. (2004). An overview on the mechanical behaviour of biodegradable agricultural films. *Journal of Polymers and the Environment, 12*(2), 65-81.

Briassoulis, D. (2005). The effects of tensile stress and the agrochemical Vapam on the ageing of low density polyethylene (LDPE) agricultural films. Part I. Mechanical behaviour. *Polymer degradation and stability, 88*(3), 489-503.

Briassoulis, D. (2007). Analysis of the mechanical and degradation performances of optimised agricultural biodegradable films. *Polymer degradation and stability, 92*(6), 1115-1132.

Brodhagen, M., Goldberger, J. R., Hayes, D. G., Inglis, D. A., Marsh, T. L., & Miles, C. (2017). Policy considerations for limiting unintended residual plastic in agricultural soils. *Environmental Science & Policy, 69*, 81-84.

Büks, F., Loes van Schaik, N., & Kaupenjohann, M. (2020). What do we know about how the terrestrial multicellular soil fauna reacts to microplastic? *SOIL, 6*(2), 245-267.

Byrdson, J. (1970). Plastic materials. *Butterworth, UK, 1982) pp*, 225-279.

Cai, L., Hu, L., Shi, H., Ye, J., Zhang, Y., & Kim, H. (2018). Effects of inorganic ions and natural organic matter on the aggregation of nanoplastics. *Chemosphere, 197*, 142-151.

Caldwell, J., Lehner, R., Balog, S., Rhême, C., Gao, X., Septiadi, D., Weder, C., Petri-Fink, A., & Rothen-Rutishauser, B. (2021). Fluorescent plastic nanoparticles to track their interaction and fate in physiological environments. *Environmental Science: Nano, 8*(2), 502-513.

Caputo, F., Vogel, R., Savage, J., Vella, G., Law, A., Della Camera, G., Hannon, G., Peacock, B., Mehn, D., & Ponti, J. (2021). Measuring particle size distribution and mass concentration of nanoplastics and microplastics: addressing some analytical challenges in the sub-micron size range. *Journal of Colloid and Interface Science, 588*, 401-417.

Castellanos, M. M., McAuley, A., & Curtis, J. E. (2017). Investigating structure and dynamics of proteins in amorphous phases using neutron scattering. *Computational and structural biotechnology journal, 15*, 117-130.

Chandra, R., & Rustgi, R. (1998). Biodegradable polymers. *Progress in polymer science, 23*(7), 1273-1335.

Chen, K.-J., Galinato, S. P., Marsh, T. L., Tozer, P. R., & Chouinard, H. H. (2020). Willingness to Pay for Attributes of Biodegradable Plastic Mulches in the Agricultural Sector. *HortTechnology, 30*(3), 437-447.

Chen, Q. Q., Gundlach, M., Yang, S. Y., Jiang, J., Velki, M., Yin, D. Q., & Hollert, H. (2017). Quantitative investigation of the mechanisms of microplastics and nanoplastics toward zebrafish larvae locomotor activity. *Science of the total environment, 584*, 1022-1031.

Chi, J., Yin, Y., Zhang, W., Putnis, C. V., & Wang, L. (2021). Nanoscale imaging of the simultaneous occlusion of nanoplastics and glyphosate within soil minerals. *Environmental Science: Nano, 8*(10), 2855-2865.

Chinaglia, S., Tosin, M., & Degli-Innocenti, F. (2018). Biodegradation rate of biodegradable plastics at molecular level. *Polymer degradation and stability, 147*, 237-244.

Chu, B. (2007). *Laser light scattering: basic principles and practice*: Courier Corporation.

Cole, M., Lindeque, P., Halsband, C., & Galloway, T. S. (2011). Microplastics as contaminants in the marine environment: a review. *Marine pollution bulletin, 62*(12), 2588-2597.

Corradini, F., Bartholomeus, H., Huerta Lwanga, E., Gertsen, H., & Geissen, V. (2019). Predicting soil microplastic concentration using vis-NIR spectroscopy. *Science of the total environment, 650*, 922-932.

Corradini, F., Meza, P., Eguiluz, R., Casado, F., Huerta-Lwanga, E., & Geissen, V. (2019). Evidence of microplastic accumulation in agricultural soils from sewage sludge disposal. *Science of the total environment, 671*, 411-420.

Crawford, C. B., & Quinn, B. (2017). Microplastic collection techniques. *Microplastic pollutants*, 179-202.

Crutchik, D., Franchi, O., Caminos, L., Jeison, D., Belmonte, M., Pedrouso, A., Val del Rio, A., Mosquera-Corral, A., & Campos, J. L. (2020). Polyhydroxyalkanoates (PHAs) production: a feasible economic option for the treatment of sewage sludge in municipal wastewater treatment plants? *Water, 12*(4), 1118.

Cui, Z., Zhang, J., Xue, Y., & Duan, H. (2018). Size-dependent thermodynamics and kinetics of adsorption on nanoparticles: a theoretical and experimental study. *Langmuir, 34*(10), 3197-3206.

de Alkimin, G. D., Gonçalves, J. M., Nathan, J., & Bebianno, M. J. (2022). Impact of Micro and Nanoplastics in the Marine Environment. In *Assessing the Effects of Emerging Plastics on the Environment and Public Health* (pp. 172-225): IGI Global.

de Souza Machado, A. A., Kloas, W., Zarfl, C., Hempel, S., & Rillig, M. C. (2017). Microplastics as an emerging threat to terrestrial ecosystems. *Global Change Biology, 24*(4), 1405-1416.

de Souza Machado, A. A., Lau, C. W., Till, J., Kloas, W., Lehmann, A., Becker, R., & Rillig, M. C. (2018). Impacts of microplastics on the soil biophysical environment. *Environmental Science & Technology, 52*(17), 9656-9665.

DeVetter, L., Goldberger, J., Miles, C., & Gomez, J. (2021). *Grower acceptance of new end-of-life management strategies for plastic mulch in strawberry systems.* Paper presented at the IX International Strawberry Symposium 1309.

Ding, L., Luo, Y., Yu, X., Ouyang, Z., Liu, P., & Guo, X. (2022). Insight into interactions of polystyrene microplastics with different types and compositions of dissolved organic matter. *Science of the total environment*, 153883.

Doerr, S. H., Shakesby, R. A., & Walsh, R. P. D. (2000). Soil water repellency: its causes, characteristics and hydro-geomorphological significance. *Earth-Science Reviews, 51*(1), 33-65.

Domb, A. J., Kost, J., & Wiseman, D. (1998). *Handbook of biodegradable polymers*: CRC press.

Domenek, S., Louaifi, A., Guinault, A., & Baumberger, S. (2013). Potential of Lignins as Antioxidant Additive in Active Biodegradable Packaging Materials. *Journal of Polymers and the Environment, 21*(3), 692-701.

Domoradzki, M., & Korpal, W. (2005). Seed size dependent germination of selected vegetables. *Acta Agrophysica, 5*(3), 607-612.

Dong, Z., Zhu, L., Zhang, W., Huang, R., Lv, X., Jing, X., Yang, Z., Wang, J., & Qiu, Y. (2019). Role of surface functionalities of nanoplastics on their transport in seawater-saturated sea sand. *Environmental Pollution, 255*, 113177.

Doty, P. (1945). Classical theory of light scattering from solutions-a review. *Polym. Bull., 1*, 90.

Drummond, J. D., Nel, H. A., Packman, A. I., & Krause, S. (2020). Significance of hyporheic exchange for predicting microplastic fate in rivers. *Environmental Science & Technology Letters, 7*(10), 727-732.

Ducoli, S., Federici, S., Nicsanu, R., Zendrini, A., Marchesi, C., Paolini, L., Radeghieri, A., Bergese, P., & Depero, L. E. (2022). A different protein corona cloaks "true-to-life" nanoplastics with respect to synthetic polystyrene nanobeads. *Environmental Science: Nano*.

Dümichen, E., Barthel, A.-K., Braun, U., Bannick, C. G., Brand, K., Jekel, M., & Senz, R. (2015). Analysis of polyethylene microplastics in environmental samples, using a thermal decomposition method. *Water research, 85*, 451-457.

Dunbar, C. A., & Hickey, A. J. (2000). Evaluation of probability density functions to approximate particle size distriubitons of representative pharamaceutical aerosols. *Journal of Aerosol Science, 31*(7), 813-831.

Duval, C. (2009). *Matières plastiques et environnement: recyclage, valorisation, biodégrabilité, écoconception*: Usine Nouvelle.

Eckert, E. M., Di Cesare, A., Kettner, M. T., Arias-Andres, M., Fontaneto, D., Grossart, H.-P., & Corno, G. (2018). Microplastics increase impact of treated wastewater on freshwater microbial community. *Environmental Pollution, 234*, 495-502.

Eckert, E. M., Di Cesare, A., Kettner, M. T., Arias-Andres, M., Fontaneto, D., Grossart, H. P., & Corno, G. (2018). Microplastics increase impact of treated wastewater on freshwater microbial community. *Environmental Pollution, 234*, 495-502.

Efsa Panel on Contaminants in the Food Chain. (2016). Presence of microplastics and nanoplastics in food, with particular focus on seafood. *EFSA Journal, 14*(6), 4501.

Eitzen, L., Paul, S., Braun, U., Altmann, K., Jekel, M., & Ruhl, A. S. (2019). The challenge in preparing particle suspensions for aquatic microplastic research. *Environmental research, 168*, 490-495.

Ekebafe, L., Ogbeifun, D., & Okieimen, F. (2011). Polymer applications in agriculture. *Biokemistri, 23*(2).

Ekvall, M. T., Lundqvist, M., Kelpsiene, E., Šileikis, E., Gunnarsson, S. B., & Cedervall, T. (2019). Nanoplastics formed during the mechanical breakdown of daily-use polystyrene products. *Nanoscale advances, 1*(3), 1055-1061.

El Hadri, H., Gigault, J., Maxit, B., Grassl, B., & Reynaud, S. (2020). Nanoplastic from mechanically degraded primary and secondary microplastics for environmental assessments. *NanoImpact, 17*, 100206.

Elkharraz, K., Dashevsky, A., & Bodmeier, R. (2003). Microparticles prepared by grinding of polymeric films. *Journal of Microencapsulation, 20*(5), 661-673.

English, M. (2019). *The role of biodegradable plastic mulches in soil organic carbon cycling (MS Thesis).* (MS), University of Tennesssee, Knoxville, TN, USA.

Esmaeelnejad, L., Siavashi, F., Seyedmohammadi, J., & Shabanpour, M. (2016). The best mathematical models describing particle size distribution of soils. *Modeling Earth Systems and Environment, 2*(4), 1-11.

Espi, E., Salmeron, A., Fontecha, A., García, Y., & Real, A. (2006). Plastic films for agricultural applications. *Journal of Plastic Film & Sheeting, 22*(2), 85-102.

European Standard, E. C. f. S. (2018). *EN 17033: 2018, Plastics-Biodegradable mulch films for use in agriculture and horticultureRequirements and test methods*. Retrieved from Brussels:

Ezquerra, T. A., Garcia-Gutierrez, M. C., Nogales, A., & Gomez, M. (2009). *Applications of synchrotron light to scattering and diffraction in materials and life sciences* (Vol. 776): Springer.

Fang, Z., Patterson, B. R., & Turner, M. E. (1993). Modeling particle size distributions by the Weibull distribution function. *Materials Characterization, 31*(3), 177-182.

Fu, J., Wang, C., Chen, X., Huang, Z., & Chen, D. (2018). Classification research and types of slow controlled release fertilizers (SRFs) used-a review. *Communications in soil science and plant analysis, 49*(17), 2219-2230.

Garnaud, J. (2000). " Plasticulture" magazine: a milestone for a history of progress in plasticulture. *Plasticulture, 1*(119), 30-43.

Geyer, R., Jambeck, J. R., & Law, K. L. (2017). Production, use, and fate of all plastics ever made. *Science advances, 3*(7), e1700782.

Ghimire, S., Wszelaki, A. L., Moore, J. C., Inglis, D. A., & Miles, C. (2018). The use of biodegradable mulches in pie pumpkin crop production in two diverse climates. *HortScience, 53*(3), 288-294.

Gigault, J., Ter Halle, A., Baudrimont, M., Pascal, P.-Y., Gauffre, F., Phi, T.-L., El Hadri, H., Grassl, B., & Reynaud, S. (2018). Current opinion: what is a nanoplastic? *Environmental Pollution, 235*, 1030-1034.

Gilbert, M. (2016). *Brydson's plastics materials*: William Andrew.

Gillibert, R., Magazzù, A., Callegari, A., Bronte-Ciriza, D., Foti, A., Donato, M. G., Maragò, O. M., Volpe, G., Lamy de La Chapelle, M., Lagarde, F., & Gucciardi, P. G. (2022). Raman tweezers for tire and road wear micro- and nanoparticles analysis. *Environmental Science: Nano, 9*(1), 145-161.

Goedecke, C., Mülow-Stollin, U., Hering, S., Richter, J., Piechotta, C., Paul, A., & Braun, U. (2017). A First Pilot Study on the Sorption of Environmental Pollutants on Various Microplastic Materials. *Journal of Environmental Analytical Chemistry, 4*(1), 191.

Goldberger, J. R., DeVetter, L. W., & Dentzman, K. E. (2019). Polyethylene and biodegradable plastic mulches for strawberry production in the United States: Experiences and opinions of growers in three regions. *HortTechnology, 29*(5), 619-628.

Goldberger, J. R., Jones, R. E., Miles, C. A., Wallace, R. W., & Inglis, D. A. (2015). Barriers and bridges to the adoption of biodegradable plastic mulches for US specialty crop production. *Renewable Agriculture and Food Systems, 30*(2), 143-153.

Gourmelon, G. (2015). Global plastic production rises, recycling lags. *New Worldwatch Institute analysis explores trends in global plastic consumption and recycling.*

Guo, J.-J., Huang, X.-P., Xiang, L., Wang, Y.-Z., Li, Y.-W., Li, H., Cai, Q.-Y., Mo, C.-H., & Wong, M.-H. (2020). Source, migration and toxicology of microplastics in soil. *Environment international, 137*, 105263.

Guo, X., Pang, J., Chen, S., & Jia, H. (2018). Sorption properties of tylosin on four different microplastics. *Chemosphere, 209*, 240-245.

Hablot, E., Dharmalingam, S., Hayes, D. G., Wadsworth, L. C., Blazy, C., & Narayan, R. (2014). Effect of simulated weathering on physicochemical properties and inherent biodegradation of PLA/PHA nonwoven mulches. *Journal of Polymers and the Environment, 22*(4), 417-429.

Hanvey, J. S., Lewis, P. J., Lavers, J. L., Crosbie, N. D., Pozo, K., & Clarke, B. O. (2017). A review of analytical techniques for quantifying microplastics in sediments. *Analytical Methods, 9*(9), 1369-1383.

Hartmann, N. B., Hüffer, T., Thompson, R. C., Hassellöv, M., Verschoor, A., Daugaard, A. E., Rist, S., Karlsson, T., Brennholt, N., & Cole, M. (2019). Are we speaking the same language? Recommendations for a definition and categorization framework for plastic debris. In: ACS Publications.

Hartmann, N. B., Hüffer, T., Thompson, R. C., Hassellöv, M., Verschoor, A., Daugaard, A. E., Rist, S., Karlsson, T., Brennholt, N., Cole, M., Herrling, M. P., Hess, M. C., Ivleva, N. P., Lusher, A. L., & Wagner, M. (2019). Are we speaking the same language? Recommendations for a definition and categorization framework for plastic debris. *Environmental Science & Technology, 53*(3), 1039-1047.

Hayes, D. G. (2021). Enhanced end-of-life performance for biodegradable plastic mulch films through improving standards and addressing research gaps. *Current Opinion in Chemical Engineering, 33*, 100695.

Hayes, D. G., Amnunciado, M. B., DeBruyn, J. M., Bandopadhyay, S., Schaeffer, S. M., English, M., Ghimire, S., Miles, C., Flury, M., & Sintim, H. (2019). Biodegradable plastic mulch films for sustainable specialty crop production. In T. J. Gutierrez (Ed.), *Polymers for Agri-Food Applications* (pp. in press). Berlin: Springer Nature.

Hayes, D. G., Dharmalingam, S., Wadsworth, L. C., Leonas, K. K., Miles, C., & Inglis, D. A. (2012). Biodegradable agricultural mulches derived from biopolymers. *Degradable Polymers and Materials: Principles and Practice (2nd Edition)*, 201-223.

Hayes, D. G., Wadsworth, L. C., Sintim, H. Y., Flury, M., English, M., Schaeffer, S., & Saxton, A. M. (2017). Effect of diverse weathering conditions on the physicochemical properties of biodegradable plastic mulches. *Polymer Testing, 62*, 454-467.

Heidary, S., & Gordon, B. (1994). Hydrolyzable poly (ethylene terephthalate). *Journal of environmental polymer degradation, 2*(1), 19-26.

Heller, W. T., Cuneo, M., Debeer-Schmitt, L., Do, C., He, L., Heroux, L., Littrell, K., Pingali, S. V., Qian, S., Stanley, C., Urban, V. S., Wu, B., & Bras, W. (2018). The suite of small-angle neutron scattering instruments at Oak Ridge National Laboratory. *Journal of Applied Crystallography, 51*(2), 242-248.

Heller, W. T., Urban, V. S., Lynn, G. W., Weiss, K. L., O'Neill, H. M., Pingali, S. V., Qian, S., Littrell, K. C., Melnichenko, Y. B., & Buchanan, M. V. (2014). The Bio-SANS instrument at the high flux isotope reactor of Oak Ridge National Laboratory. *Journal of Applied Crystallography, 47*(4), 1238-1246.

Heller, W. T., Urban, V. S., Lynn, G. W., Weiss, K. L., O'Neill, H. M., Pingali, S. V., Qian, S., Littrell, K. C., Melnichenko, Y. B., Buchanan, M. V., Selby, D. L., Wignall, G. D., Butler, P. D., & Myles, D. A. (2014). The Bio-SANS instrument at the High Flux Isotope Reactor of Oak Ridge National Laboratory. *Journal of Applied Crystallography, 47*(4), 1238-1246.

Higgins, J. S., & Benoit, H. C. (1994). Polymers and neutron scattering.

Hiltunen, K., SeppÄlÄ, J. V., ItÄvaara, M., & HÄrkönen, M. (1997). The biodegradation of lactic acid-based poly (ester-urethanes). *Journal of environmental polymer degradation, 5*(3), 167-173.

Horton, A. A., & Dixon, S. J. (2018). Microplastics: An introduction to environmental transport processes. *Wiley Interdisciplinary Reviews: Water, 5*(2), e1268.

Horton, A. A., Walton, A., Spurgeon, D. J., Lahive, E., & Svendsen, C. (2017). Microplastics in freshwater and terrestrial environments: Evaluating the current understanding to identify the knowledge gaps and future research priorities. *Science of The Total Environment, 586*(1), 127-141.

Huang, M.-H., Li, S., & Vert, M. (2004). Synthesis and degradation of PLA–PCL–PLA triblock copolymer prepared by successive polymerization of ε-caprolactone and dl-lactide. *Polymer, 45*(26), 8675-8681.

Huang, Y., Liu, Q., Jia, W., Yan, C., & Wang, J. (2020). Agricultural plastic mulching as a source of microplastics in the terrestrial environment. *Environmental Pollution, 260*, 114096.

Huang, Y., Zhao, Y., Wang, J., Zhang, M., Jia, W., & Qin, X. (2019). LDPE microplastic films alter microbial community composition and enzymatic activities in soil. *Environmental Pollution, 254*(Pt A), 112983.

Huerta Lwanga, E., Gertsen, H., Gooren, H., Peters, P., Salánki, T., van der Ploeg, M., Besseling, E., Koelmans, A. A., & Geissen, V. (2017). Incorporation of microplastics from litter into burrows of *Lumbricus terrestris*. *Environmental Pollution, 220*, 523-531.

Hüffer, T., & Hofmann, T. (2016). Sorption of non-polar organic compounds by micro-sized plastic particles in aqueous solution. *Environmental Pollution, 214*, 194-201.

Hüffer, T., Weniger, A.-K., & Hofmann, T. (2018). Sorption of organic compounds by aged polystyrene microplastic particles. *Environmental Pollution, 236*, 218-225.

Hurley, R. R., & Nizzetto, L. (2018). Fate and occurrence of micro (nano) plastics in soils: Knowledge gaps and possible risks. *Current Opinion in Environmental Science & Health, 1*, 6-11.

Hussain, I., & Hamid, H. (2003). Plastics in Agriculture. In A. L. Andrady (Ed.), *Plastics and the Environment* (pp. 185-209). New York: John Wiley and Sons.

Hyon, S.-H., Jamshidi, K., & Ikada, Y. (1997). Synthesis of polylactides with different molecular weights. *Biomaterials, 18*(22), 1503-1508.

Ilavsky, J., & Jemian, P. R. (2009). Irena: tool suite for modeling and analysis of small-angle scattering. *Journal of Applied Crystallography, 42*(2), 347-353.

Iqbal, S., Xu, J., Allen, S. D., Khan, S., Nadir, S., Arif, M. S., & Yasmeen, T. (2020). Unraveling consequences of soil micro-and nano-plastic pollution for soil-plant system with implications for nitrogen (N) cycling and soil microbial activity. *Chemosphere, 260*, 127578.

Jacques, O., & Prosser, R. (2021). A probabilistic risk assessment of microplastics in soil ecosystems. *Science of the total environment, 757*, 143987.

Jambeck, J. R., Geyer, R., Wilcox, C., Siegler, T. R., Perryman, M., Andrady, A., Narayan, R., & Law, K. L. (2015). Plastic waste inputs from land into the ocean. *Science, 347*(6223), 768.

Jambeck, J. R., Geyer, R., Wilcox, C., Siegler, T. R., Perryman, M., Andrady, A., Narayan, R., & Law, K. L. (2015). Plastic waste inputs from land into the ocean. *Science, 347*(6223), 768-771.

Jayaram, D. T., Runa, S., Kemp, M. L., & Payne, C. K. (2017). Nanoparticle-induced oxidation of corona proteins initiates an oxidative stress response in cells. *Nanoscale, 9*(22), 7595-7601.

Jian, J., Xiangbin, Z., & Xianbo, H. (2020). An Overview on Synthesis, Propertiesand Applications of Poly (butylene-adipate-co-terephthalate)–PBAT. *Advanced Industrial and Engineering Polymer Research*.

Jin, Z., & Dan, L. (2021). Review on the occurrence, analysis methods, toxicity and health effects of micro-and nano-plastics in the environment. *Environmental Chemistry*(1), 28-40.

Jonna, S., & Lyons, J. (2005). Processing and properties of cryogenically milled post-consumer mixed plastic waste. *Polymer Testing, 24*(4), 428-434.

Kasirajan, S., & Ngouajio, M. (2012). Polyethylene and biodegradable mulches for agricultural applications: a review. *Agronomy for Sustainable Development, 32*(2), 501-529.

Kasirajan, S., & Ngouajio, M. (2012). Polyethylene and biodegradable mulches for agricultural applications: a review. *Agronomy for Sustainable Development, 32*, 501-529.

Kasmuri, N., Tarmizi, N. A. A., & Mojiri, A. (2022). Occurrence, impact, toxicity, and degradation methods of microplastics in environment—a review. *Environmental Science and Pollution Research*, 1-17.

Katsumi, N., Kusube, T., Nagao, S., & Okochi, H. (2020). The role of coated fertilizer used in paddy fields as a source of microplastics in the marine environment. *Marine pollution bulletin, 161*, 111727.

Kaur, R., Bhardwaj, S. K., Chandna, S., Kim, K.-H., & Bhaumik, J. (2021). Lignin-based metal oxide nanocomposites for UV protection applications: A review. *Journal of Cleaner Production, 317*, 128300.

Kawai, H., Sakurai, M., Inoue, Y., Chujo, R., & Kobayashi, S. (1992). Hydration of oligosaccharides: anomalous hydration ability of trehalose. *Cryobiology, 29*(5), 599-606.

Kefer, S., Friedenauer, T., & Langowski, H. C. (2022). Characterisation of different manufactured plastic microparticles and their comparison to environmental microplastics. *Powder Technology, 412*, 117960.

Kettler, K., Veltman, K., van De Meent, D., van Wezel, A., & Hendriks, A. J. (2014). Cellular uptake of nanoparticles as determined by particle properties, experimental conditions, and cell type. *Environmental Toxicology and Chemistry, 33*(3), 481-492.

Kihara, S., Van Der Heijden, N. J., Seal, C. K., Mata, J. P., Whitten, A. E., Köper, I., & McGillivray, D. J. (2019). Soft and hard interactions between polystyrene nanoplastics and human serum albumin protein corona. *Bioconjugate Chemistry, 30*(4), 1067-1076.

Kijchavengkul, T., & Auras, R. (2008). Compostability of polymers. *Polymer International, 57*(6), 793-804.

Kijchavengkul, T., Auras, R., Rubino, M., Alvarado, E., Montero, J. R. C., & Rosales, J. M. (2010). Atmospheric and soil degradation of aliphatic–aromatic polyester films. *Polymer degradation and stability, 95*(2), 99-107.

Kijchavengkul, T., Auras, R., Rubino, M., Ngouajio, M., & Fernandez, R. T. (2008). Assessment of aliphatic–aromatic copolyester biodegradable mulch films. Part I: Field study. *Chemosphere, 71*(5), 942-953.

Kijchavengkul, T., Kale, G., & Auras, R. (2009). Degradation of biodegradable polymers in real and simulated composting conditions. In: ACS Publications.

Kim, S. W., & An, Y.-J. (2020). Edible size of polyethylene microplastics and their effects on springtail behavior. *Environmental Pollution, 266*, 115255.

Kirste, R., Kruse, W., & Schelten, J. (1972). Die bestimmung des trägheitsradius von polymethyl-methacrylat im glaszustand durch neutronenbeugung. *Die Makromolekulare Chemie: Macromolecular Chemistry and Physics, 162*(1), 299-303.

Kister, G., Cassanas, G., Bergounhon, M., Hoarau, D., & Vert, M. (2000). Structural characterization and hydrolytic degradation of solid copolymers of d, l-lactide-co-ε-caprolactone by Raman spectroscopy. *Polymer, 41*(3), 925-932.

Kline, S. R. (2006). Reduction and analysis of SANS and USANS data using IGOR Pro. *J. Appl. Crystallogr., 39*(6), 895-900.

Koelmans, A. A., Besseling, E., Wegner, A., & Foekema, E. M. (2013). Plastic as a carrier of POPs to aquatic organisms: a model analysis. *Environmental Science & Technology, 47*.

Koelmans, A. A., Redondo-Hasselerharm, P. E., Nor, N. H. M., de Ruijter, V. N., Mintenig, S. M., & Kooi, M. (2022). Risk assessment of microplastic particles. *Nature Reviews Materials, 7*(2), 138-152.

Kotlarchyk, M., & Chen, S. H. (1983). Analysis of small angle neutron scattering spectra from polydisperse interacting colloids. *The Journal of Chemical Physics, 79*(5), 2461-2469.

Kowalski, A., Libiszowski, J., Duda, A., & Penczek, S. (2000). Polymerization of L, L-dilactide initiated by tin (II) butoxide. *Macromolecules, 33*(6), 1964-1971.

Kühn, S., van Oyen, A., Booth, A. M., Meijboom, A., & van Franeker, J. A. (2018). Marine microplastic: Preparation of relevant test materials for laboratory assessment of ecosystem impacts. *Chemosphere, 213*, 103-113.

Kumar, M., Chen, H., Sarsaiya, S., Qin, S., Liu, H., Awasthi, M. K., Kumar, S., Singh, L., Zhang, Z., & Bolan, N. S. (2021). Current research trends on micro-and nano-plastics as an emerging threat to global environment: a review. *Journal of Hazardous Materials, 409*, 124967.

Kwak, J. I., & An, Y.-J. (2021). Microplastic digestion generates fragmented nanoplastics in soils and damages earthworm spermatogenesis and coelomocyte viability. *Journal of Hazardous Materials, 402*, 124034.

Kyrikou, I., & Briassoulis, D. (2007). Biodegradation of agricultural plastic films: a critical review. *Journal of Polymers and the Environment, 15*(2), 125-150.

Lai, W., Xu, D., Li, J., Wang, Z., Ding, Y., Wang, X., Li, X., Xu, N., Mai, K., & Ai, Q. (2021). Dietary polystyrene nanoplastics exposure alters liver lipid metabolism and muscle nutritional quality in carnivorous marine fish large yellow croaker (Larimichthys crocea). *Journal of Hazardous Materials, 419*, 126454.

Lamont, W. J. (2005). Plastics: Modifying the microclimate for the production of vegetable crops. *HortTechnology, 15*(3), 477-481.

Lang, M., Wang, G., Yang, Y., Zhu, W., Zhang, Y., Ouyang, Z., & Guo, X. (2022). The occurrence and effect of altitude on microplastics distribution in agricultural soils of Qinghai Province, northwest China. *Science of the total environment, 810*, 152174.

Lendlein, A., & Sisson, A. (2011). *Handbook of biodegradable polymers: isolation, synthesis, characterization and applications*: John Wiley & Sons.

Li, C., Moore-Kucera, J., Miles, C., Leonas, K., Lee, J., Corbin, A., & Inglis, D. (2014). Degradation of Potentially Biodegradable Plastic Mulch Films at Three Diverse U.S. Locations. *Agroecology and Sustainable Food Systems, 38*(8), 861-889.

Li, J., Song, Y., & Cai, Y. (2020). Focus topics on microplastics in soil: analytical methods, occurrence, transport, and ecological risks. *Environmental Pollution, 257*, 113570.

Li, K., Jia, W., Xu, L., Zhang, M., & Huang, Y. (2023). The plastisphere of biodegradable and conventional microplastics from residues exhibit distinct microbial structure, network and function in plastic-mulching farmland. *Journal of Hazardous Materials, 442*, 130011.

Li, T., Senesi, A. J., & Lee, B. (2016). Small angle X-ray scattering for nanoparticle research. *Chemical reviews, 116*(18), 11128-11180.

Li, Y., Wang, X., Fu, W., Xia, X., Liu, C., Min, J., Zhang, W., & Crittenden, J. C. (2019). Interactions between nano/micro plastics and suspended sediment in water: Implications on aggregation and settling. *Water research, 161*, 486-495.

Li, Z., Li, Q., Li, R., Zhou, J., & Wang, G. (2021). The distribution and impact of polystyrene nanoplastics on cucumber plants. *Environmental Science and Pollution Research, 28*(13), 16042-16053.

Liao, J., & Chen, Q. (2021). Biodegradable plastics in the air and soil environment: Low degradation rate and high microplastics formation. *Journal of Hazardous Materials, 418*, 126329.

Lima, L., Aurasb, R., & Rubinob, M. (2008). Processing technologies for poly (lactic acid), Progress in Polymer Science.

Lionetto, F., Esposito Corcione, C., Rizzo, A., & Maffezzoli, A. (2021). Production and characterization of polyethylene terephthalate nanoparticles. *Polymers, 13*(21), 3745.

Liu, E., He, W., & Yan, C. (2014). White revolution'to 'white pollution'—agricultural plastic film mulch in China. *Environmental Research Letters, 9*(9), 091001.

Liu, J., Zhang, T., Tian, L., Liu, X., Qi, Z., Ma, Y., Ji, R., & Chen, W. (2019). Aging significantly affects mobility and contaminant-mobilizing ability of nanoplastics in saturated loamy sand. *Environmental Science & Technology, 53*(10), 5805-5815.

Liu, M., Lu, S., Song, Y., Lei, L., Hu, J., Lv, W., Zhou, W., Cao, C., Shi, H., Yang, X., & He, D. (2018). Microplastic and mesoplastic pollution in farmland soils in suburbs of Shanghai, China. *Environmental Pollution, 242*, 855-862.

Löfgren, A., Albertsson, A.-C., Dubois, P., & Jérôme, R. (1995). Recent advances in ring-opening polymerization of lactones and related compounds. *Journal of Macromolecular Science, Part C: Polymer Reviews, 35*(3), 379-418.

Lu, L., Wan, Z. Q., Luo, T., Fu, Z. W., & Jin, Y. X. (2018). Polystyrene microplastics induce gut microbiota dysbiosis and hepatic lipid metabolism disorder in mice. *Science of the total environment, 631-632*, 449-458.

Lucas, N., Bienaime, C., Belloy, C., Queneudec, M., Silvestre, F., & Nava-Saucedo, J. E. (2008). Polymer biodegradation: Mechanisms and estimation techniques. *Chemosphere, 73*(4), 429-442.

Lwanga, E. H., Gertsen, H., Gooren, H., Peters, P., Salánki, T., van der Ploeg, M., Besseling, E., Koelmans, A. A., & Geissen, V. (2017). Incorporation of microplastics from litter into burrows of Lumbricus terrestris. *Environmental Pollution, 220*, 523-531.

Lynch, A. J., & Rowland, C. A. (2005). *The History of Grinding*. Littleton, CO, USA: Society for Mining, Metallurgy, and Exploration, Inc.

Ma, Y., Huang, A., Cao, S., Sun, F., Wang, L., Guo, H., & Ji, R. (2016). Effects of nanoplastics and microplastics on toxicity, bioaccumulation, and environmental fate of phenanthrene in fresh water. *Environmental Pollution, 219*, 166-173.

Maity, S., Guchhait, R., Sarkar, M. B., & Pramanick, K. (2022). Occurrence and distribution of micro/nanoplastics in soils and their phytotoxic effects: A review. *Plant, Cell & Environment, 45*(4), 1011-1028.

Manzoor, S., Naqash, N., Rashid, G., & Singh, R. (2021). Plastic material degradation and formation of microplastic in the environment: A review. *Materials Today: Proceedings*.

Materić, D. a., Kasper-Giebl, A., Kau, D., Anten, M., Greilinger, M., Ludewig, E., van Sebille, E., Röckmann, T., & Holzinger, R. (2020). Micro-and nanoplastics in Alpine Snow: a new method for chemical identification and (semi) quantification in the nanogram range. *Environmental Science & Technology, 54*(4), 2353-2359.

Mattsson, K., Hansson, L. A., & Cedervall, T. (2015). Nano-plastics in the aquatic environment. *Environmental Science-Processes & Impacts, 17*(10), 1712-1721.

Matusinovic, Z., & Wilkie, C. A. (2014). Degradation, stabilization, and flammability of polymer blends. *Polymer Blends Handbook*, 1395-1430.

McCormick, A., Hoellein, T. J., Mason, S. A., Schluep, J., & Kelly, J. J. (2014). Microplastic is an abundant and distinct microbial habitat in an urban river. *Environmental Science & Technology, 48*(20), 11863-11871.

Meek, N., Penumadu, D., Hosseinaei, O., Harper, D., Young, S., Rials, T. J. C. S., & Technology. (2016). Synthesis and characterization of lignin carbon fiber and composites. *137*, 60-68.

Menossi, M., Cisneros, M., Alvarez, V. A., & Casalongué, C. (2021). Current and emerging biodegradable mulch films based on polysaccharide bio-composites. A review. *Agronomy for Sustainable Development, 41*(4), 1-27.

Merino, D., Zych, A., & Athanassiou, A. (2022). Biodegradable and Biobased Mulch Films: Highly Stretchable PLA Composites with Different Industrial Vegetable Waste. *ACS applied materials & interfaces*.

Miles, C., DeVetter, L., Ghimire, S., & Hayes, D. G. (2017). Suitability of biodegradable plastic mulches for organic and sustainable agricultural production systems. *HortScience, 52*(1), 10-15.

Motokawa, R., Endo, H., Yokoyama, S., Nishitsuji, S., Kobayashi, T., Suzuki, S., & Yaita, T. (2014). Collective Structural Changes in Vermiculite Clay Suspensions Induced by Cesium Ions. *Scientific reports, 4*, 6585.

Nair, L. S., & Laurencin, C. T. (2007). Biodegradable polymers as biomaterials. *Progress in polymer science, 32*(8-9), 762-798.

Nakamura, H., Nakamura, T., Noguchi, T., & Imagawa, K. (2006). Photodegradation of PEEK sheets under tensile stress. *Polymer degradation and stability, 91*(4), 740-746.

Naqash, N., Prakash, S., Kapoor, D., & Singh, R. (2020). Interaction of freshwater microplastics with biota and heavy metals: a review. *Environmental Chemistry Letters, 18*(6), 1813-1824.

Narayan, R. (2010). Misleading claims and misuse proliferate in the nascent. *Bioplastics Magazine, 10*(1), 38-41.

Nasser, F., & Lynch, I. (2016). Secreted protein eco-corona mediates uptake and impacts of polystyrene nanoparticles on Daphnia magna. *Journal of proteomics, 137*, 45-51.

Ng, E. L., Lwanga, E. H., Eldridge, S. M., Johnston, P., Hu, H. W., Geissen, V., & Chen, D. L. (2018). An overview of microplastic and nanoplastic pollution in agroecosystems. *Science of the total environment, 627*, 1377-1388.

Niaounakis, M. (2015). *Biopolymers: applications and trends*: William Andrew.

Nizzetto, L., Futter, M., & Langaas, S. (2016). Are agricultural soils dumps for microplastics of urban origin? *Environmental Science & Technology, 50*(20), 10777-10779.

Nolte, T. M., Hartmann, N. B., Kleijn, J. M., Garnaes, J., van de Meent, D., Hendriks, A. J., & Baun, A. (2017). The toxicity of plastic nanoparticles to green algae as influenced by surface modification, medium hardness and cellular adsorption. *Aquatic Toxicology, 183*, 11-20.

Notta-Cuvier, D., Murariu, M., Odent, J., Delille, R., Bouzouita, A., Raquez, J. M., Lauro, F., & Dubois, P. (2015). Tailoring Polylactide Properties for Automotive Applications: Effects of Co-Addition of Halloysite Nanotubes and Selected Plasticizer. *Macromolecular Materials and Engineering, 300*(7), 684-698.

Núñez-Flores, R., Giménez, B., Fernández-Martín, F., López-Caballero, M. E., Montero, M. P., & Gómez-Guillén, M. C. (2012). Role of lignosulphonate in properties of fish gelatin films. *Food Hydrocolloids, 27*(1), 60-71.

Oberbeckmann, S., Kreikemeyer, B., & Labrenz, M. (2018). Environmental Factors Support the Formation of Specific Bacterial Assemblages on Microplastics. *Frontiers in Microbiology, 8*.

Osawa, Z. (1992). Photoinduced degradation of Polymers in Handbook of Polymers Degradation. *Hamid, SH, Amin MB and Maadhaj, A, G,.(Eds), Marcel Dekker, Inc., New York*, 169-218.

Oyama, H. T., Tanaka, Y., Hirai, S., Shida, S., & Kadosaka, A. (2011). Water-disintegrative and biodegradable blends containing poly (L-lactic acid) and poly (butylene adipate-co-terephthalate). *Journal of Polymer Science Part B: Polymer Physics, 49*(5), 342-354.

Panno, S. V., Kelly, W. R., Scott, J., Zheng, W., McNeish, R. E., Holm, N., Hoellein, T. J., & Baranski, E. L. (2019). Microplastic contamination in karst groundwater systems. *Groundwater, 57*(2), 189-196.

Park, S. Y., & Kim, C. G. (2022). A comparative study on the distribution behavior of microplastics through FT-IR analysis on different land uses in agricultural soils. *Environmental research, 215*, 114404.

Pathan, S. I., Arfaioli, P., Bardelli, T., Ceccherini, M. T., Nannipieri, P., & Pietramellara, G. (2020). Soil Pollution from Micro-and Nanoplastic Debris: A Hidden and Unknown Biohazard. *Sustainability, 12*(18), 7255.

Pehlivan, N., & Gedik, K. (2021). Particle size-dependent biomolecular footprints of interactive microplastics in maize. *Environmental Pollution, 277*, 116772.

Peng, G., Xu, P., Zhu, B., Bai, M., & Li, D. (2018). Microplastics in freshwater river sediments in Shanghai, China: a case study of risk assessment in mega-cities. *Environmental Pollution, 234*, 448-456.

Phuong, N. N., Zalouk-Vergnoux, A., Poirier, L., Kamari, A., Châtel, A., Mouneyrac, C., & Lagarde, F. (2016). Is there any consistency between the microplastics found in the field and those used in laboratory experiments? *Environmental Pollution, 211*, 111-123.

Pires, A., Cuccaro, A., Sole, M., & Freitas, R. (2022). Micro (nano) plastics and plastic additives effects in marine annelids: A literature review. *Environmental research*, 113642.

Pironti, C., Ricciardi, M., Motta, O., Miele, Y., Proto, A., & Montano, L. (2021). Microplastics in the Environment: Intake through the Food Web, Human Exposure and Toxicological Effects. *Toxics, 9*(9), 224.

Pischedda, A., Tosin, M., & Degli-Innocenti, F. (2019). Biodegradation of plastics in soil: The effect of temperature. *Polymer degradation and stability, 170*, 109017.

Pitt, G. (1992). Biodegradable Polymers and Plastic. *Non-Microbial Degradation of Polyesters. Mechanisms and Modifications, ed. M. Vert, J. Feijen, A. Albertsson, G. Scott, E. Chiellini, Royal Society of Chemistry, Cambridge*.

Pitt, J. A., Kozal, J. S., Jayasundara, N., Massarsky, A., Trevisan, R., Geitner, N., Wiesner, M., Levin, E. D., & Di Giulio, R. T. (2018). Uptake, tissue distribution, and toxicity of polystyrene nanoparticles in developing zebrafish (Danio rerio). *Aquatic Toxicology, 194*, 185-194.

Poulose, A. M., Piccarolo, S., Carbone, D., & Al-Zahrani, S. M. (2016). Influence of plasticizers and cryogenic grinding on the high-cooling-rate solidification behavior of PBT/PET blends. *Journal of Applied Polymer Science, 133*(10), 43083.

Pro, I. (2011). 6; WaveMetrics Inc. *Lake Oswego, Oregon, USA*.

Proikakis, C., Mamouzelos, N., Tarantili, P., & Andreopoulos, A. (2006). Swelling and hydrolytic degradation of poly (D, L-lactic acid) in aqueous solutions. *Polymer degradation and stability, 91*(3), 614-619.

Qin, M., Chen, C., Song, B., Shen, M., Cao, W., Yang, H., Zeng, G., & Gong, J. (2021). A review of biodegradable plastics to biodegradable microplastics: Another ecological threat to soil environments? *Journal of Cleaner Production, 312*, 127816.

Raju, S., Carbery, M., Kuttykattil, A., Senthirajah, K., Lundmark, A., Rogers, Z., Suresh, S., Evans, G., & Palanisami, T. (2020). Improved methodology to determine the fate and transport of microplastics in a secondary wastewater treatment plant. *Water research, 173*, 115549.

Ramos, L., Berenstein, G., Hughes, E. A., Zalts, A., & Montserrat, J. M. (2015). Polyethylene film incorporation into the horticultural soil of small periurban production units in Argentina. *Science of the total environment, 523*, 74-81.

Ravishankar, K., Ramesh, P. S., Sadhasivam, B., & Raghavachari, D. (2018). Wear-induced mechanical degradation of plastics by low-energy wet-grinding. *Polymer degradation and stability, 158*, 212-219.

Redmile-Gordon, M., Brookes, P., Evershed, R., Goulding, K., & Hirsch, P. (2014). Measuring the soil-microbial interface: extraction of extracellular polymeric substances (EPS) from soil biofilms. *Soil Biology and Biochemistry, 72*, 163-171.

Redondo-Hasselerharm, P., Gort, G., Peeters, E., & Koelmans, A. (2020). Nano-and microplastics affect the composition of freshwater benthic communities in the long term. *Science advances, 6*(5), eaay4054.

Ren, Z., Gui, X., Wei, Y., Chen, X., Xu, X., Zhao, L., Qiu, H., & Cao, X. (2021). Chemical and photo-initiated aging enhances transport risk of microplastics in saturated soils: Key factors, mechanisms, and modeling. *Water research, 202*, 117407.

Rillig, M. C. (2012). Microplastic in terrestrial ecosystems and the soil? In: ACS Publications.

Rillig, M. C., de Souza Machado, A. A., Lehmann, A., & Klümper, U. (2018). Evolutionary implications of microplastics for soil biota. *Environmental Chemistry, 16*(1), 3-7.

Rillig, M. C., & Lehmann, A. (2020). Microplastic in terrestrial ecosystems. *Science, 368*(6498), 1430-1431.

Rillig, M. C., Lehmann, A., de Souza Machado, A. A., & Yang, G. (2019). Microplastic effects on plants. *New Phytologist, 223*(3), 1066-1070.

Rillig, M. C., Ziersch, L., & Hempel, S. (2017). Microplastic transport in soil by earthworms. *Scientific reports, 7*(1), 1-6.

Rillig, M. C., Ziersch, L., & Hempel, S. (2017). Microplastic transport in soil by earthworms. *Scientific Reports, 7*(1), 1362.

Rist, S., & Hartmann, N. B. (2018). Aquatic ecotoxicity of microplastics and nanoplastics: lessons learned from engineered nanomaterials. In *Freshwater microplastics* (pp. 25-49): Springer, Cham.

Ritchie, H., & Roser, M. (2018). Plastic pollution. *Our World in Data*.

Robotti, M., Dosta Parras, S., García Cano, I., Concustell, A., Cinca i Luis, N., & Guilemany, J. M. (2016). Attrition and cryogenic milling production for low pressure cold gas spray and composite coatings characterization. *Advanced Powder Technology, 2016, vol. 27, num. 4, p. 1257-1264*.

Robotti, M., Dosta, S., Cano, I. G., Concustell, A., Cinca, N., & Guilemany, J. M. (2016). Attrition and cryogenic milling powder production for low pressure cold gas spray and composite coatings characterization. *Advanced Powder Technology, 27*(4), 1257-1264.

Rodriguez-Seijo, A., Lourenço, J., Rocha-Santos, T., Da Costa, J., Duarte, A., Vala, H., & Pereira, R. (2017). Histopathological and molecular effects of microplastics in Eisenia andrei Bouché. *Environmental Pollution, 220*(Pt A), 495-503.

Rong, L., Zhao, L., Zhao, L., Cheng, Z., Yao, Y., Yuan, C., Wang, L., & Sun, H. (2021). LDPE microplastics affect soil microbial communities and nitrogen cycling. *Science of the total environment, 773*, 145640.

Rudnik, E., & Briassoulis, D. (2011). Comparative biodegradation in soil behaviour of two biodegradable polymers based on renewable resources. *Journal of Polymers and the Environment, 19*(1), 18-39.

Saba, N., Tahir, P. M., Abdan, K., & Ibrahim, N. A. (2015). Preparation and characterization of fire retardant nanofiller from oil palm empty fruit bunch fibers. *BioResources, 10*(3), 4530-4543.

Sadeghifar, H., Venditti, R., Jur, J., Gorga, R. E., & Pawlak, J. J. (2017). Cellulose-lignin biodegradable and flexible UV protection film. *ACS Sustainable Chemistry & Engineering, 5*(1), 625-631.

Sanders, D. C., Cook, W. P., & Granberry, D. (1995). *Plasticulture for commercial vegetables*: NC Cooperative Extension Service.

Sarkar, S., Fan, W. H., Jia, S., Blake, D. R., Reid, J. S., Lestari, P., & Liya, E. Y. (2018). A quantitative assessment of distributions and sources of tropospheric halocarbons measured in Singapore. *Science of the total environment, 619*, 528-544.

Scarascia-Mugnozza, G., Sica, C., & Russo, G. (2011). Plastic materials in European agriculture: actual use and perspectives. *Journal of Agricultural Engineering, 42*(3), 15-28.

Schelten, J., Wignall, G. t., & Ballard, D. (1974). Chain conformation in molten polyethylene by low angle neutron scattering. *Polymer, 15*(10), 682-685.

Scheurer, M., & Bigalke, M. (2018). Microplastics in Swiss floodplain soils. *Environmental Science & Technology, 52*(6), 3591-3598.

Schindelin, J., Arganda-Carreras, I., Frise, E., Kaynig, V., Longair, M., Pietzsch, T., Preibisch, S., & Rueden, C. (2012). Fiji: an open-source platform for biological-image analysis. *Nat Methods, 9*, 676-682.

Schmidt, J., Plata, M., Tröger, S., & Peukert, W. (2012). Production of polymer particles below 5μm by wet grinding. *Powder Technology, 228*, 84-90.

Schmidt, J., Romeis, S., & Peukert, W. (2017). Production of PBT/PC particle systems by wet grinding. *AIP Conference Proceedings, 1914*(1), 050003.

Schmidt, P. (1991). Small-angle scattering studies of disordered, porous and fractal systems. *Journal of Applied Crystallography, 24*(5), 414-435.

Schneider, C. A., Rasband, W. S., & Eliceiri, K. W. (2012). NIH Image to ImageJ: 25 years of image analysis. *Nature Methods, 9*, 671.

Schwabl, P., Liebmann, B., Köppel, S., Königshofer, P., Bucsics, T., Trauner, M., & Reiberger, T. (2018). Assessment of microplastics concentrations in human stool: preliminary results (United Eurpean Gastroenterology Conference, Vienna, Austria, 20-24 October 2018).

Schwaferts, C., Niessner, R., Elsner, M., & Ivleva, N. P. (2019). Methods for the analysis of submicrometer-and nanoplastic particles in the environment. *TrAC Trends in Analytical Chemistry, 112*, 52-65.

Seghers, J., Stefaniak, E. A., La Spina, R., Cella, C., Mehn, D., Gilliland, D., Held, A., Jacobsson, U., & Emteborg, H. (2021). Preparation of a reference material for microplastics in water—evaluation of homogeneity. *Analytical and Bioanalytical Chemistry, 414*(1), 1-13.

Seguro, J. V., & Lambert, T. W. (2000). Modern estimation of the parameters of the Weibull wind speed distribution for wind energy analysis. *Journal of Wind Engineering and Industrial Aerodynamics, 85*(1), 75-84.

Serrano-Ruiz, H., Martin-Closas, L., & Pelacho, A. M. (2021). Biodegradable plastic mulches: Impact on the agricultural biotic environment. *Science of the total environment, 750*, 141228.

Sha, L., Chen, Z., Chen, Z., Zhang, A., & Yang, Z. (2016). Polylactic acid based nanocomposites: Promising safe and biodegradable materials in biomedical field. *International Journal of Polymer Science, 2016*.

Shaik, A. A., Richter, M., Kricheldorf, H. R., & Krüger, R. P. (2001). New polymer syntheses. CIX. Biodegradable, alternating copolyesters of terephthalic acid, aliphatic dicarboxylic acids, and alkane diols. *Journal of Polymer Science Part A: Polymer Chemistry, 39*(19), 3371-3382.

Shaniv, D., Dror, I., & Berkowitz, B. (2021). Effects of particle size and surface chemistry on plastic nanoparticle transport in saturated natural porous media. *Chemosphere, 262*, 127854.

Shankar, S., Reddy, J. P., & Rhim, J.-W. (2015). Effect of lignin on water vapor barrier, mechanical, and structural properties of agar/lignin composite films. *International Journal of Biological Macromolecules, 81*, 267-273.

Sharma, S., Singh, A., Kaur, N., & Singh, N. (2022). Chapter 12 - Sensing of environmentally and biologically important analytes using organic nanoparticles (ONPs). In S. K. Sahoo (Ed.), *Sensing and Biosensing with Optically Active Nanomaterials* (pp. 365-399): Elsevier.

Siegenthaler, K., Künkel, A., Skupin, G., & Yamamoto, M. (2011). Ecoflex® and Ecovio®: biodegradable, performance-enabling plastics. In *Synthetic biodegradable polymers* (pp. 91-136): Springer.

Singh, N., Tiwari, E., Khandelwal, N., & Darbha, G. K. (2019). Understanding the stability of nanoplastics in aqueous environments: effect of ionic strength, temperature, dissolved organic matter, clay, and heavy metals. *Environmental Science: Nano, 6*(10), 2968-2976.

Sintim, H. Y., Bandopadhyay, S., English, M. E., Bary, A., y González, J. E. L., DeBruyn, J. M., Schaeffer, S. M., Miles, C. A., & Flury, M. (2021). Four years of continuous use of soil-biodegradable plastic mulch: impact on soil and groundwater quality. *Geoderma, 381*, 114665.

Sintim, H. Y., Bandopadhyay, S., English, M. E., Bary, A. I., DeBruyn, J. M., Schaeffer, S. M., Miles, C. A., Reganold, J. P., & Flury, M. (2019). Impacts of biodegradable plastic mulches on soil health. *Agriculture, Ecosystems & Environment, 273*, 36-49.

Sintim, H. Y., Bary, A. I., Hayes, D. G., Wadsworth, L. C., Anunciado, M. B., English, M. E., Bandopadhyay, S., Schaeffer, S. M., DeBruyn, J. M., Miles, C. A., Reganold, J. P., & Flury, M. (2020). In situ degradation of biodegradable plastic mulch films in compost and agricultural soils. *Science of the total environment, 727*, 138668.

Sobhani, Z., Fang, C., Naidu, R., & Megharaj, M. (2021). Microplastics as a vector of toxic chemicals in soil: Enhanced uptake of perfluorooctane sulfonate and perfluorooctanoic acid by earthworms through sorption and reproductive toxicity. *Environmental Technology & Innovation, 22*, 101476.

Sobhani, Z., Panneerselvan, L., Fang, C., Naidu, R., & Megharaj, M. (2021). Chronic and transgenerational effects of polystyrene microplastics at environmentally relevant concentrations in earthworms (Eisenia fetida). *Environmental Toxicology and Chemistry, 40*(8), 2240-2246.

Song, Z., Yang, X., Chen, F., Zhao, F., Zhao, Y., Ruan, L., Wang, Y., & Yang, Y. (2019). Fate and transport of nanoplastics in complex natural aquifer media: Effect of particle size and surface functionalization. *Science of the total environment, 669*, 120-128.

Sorensen, C., & Wang, G. (1999). Size distribution effect on the power law regime of the structure factor of fractal aggregates. *Physical Review E, 60*(6), 7143.

Squires, G. L. (1996). *Introduction to the theory of thermal neutron scattering*: Courier Corporation.

Sridharan, S., Kumar, M., Singh, L., Bolan, N. S., & Saha, M. (2021). Microplastics as an emerging source of particulate air pollution: A critical review. *Journal of Hazardous Materials, 418*, 126245.

Steinmetz, Z., Kintzi, A., Muñoz, K., & Schaumann, G. E. (2020). A simple method for the selective quantification of polyethylene, polypropylene, and polystyrene plastic debris in soil by pyrolysis-gas chromatography/mass spectrometry. *Journal of Analytical and Applied Pyrolysis, 147*, 104803.

Steinmetz, Z., Löffler, P., Eichhöfer, S., David, J., Muñoz, K., & Schaumann, G. E. (2022). Are agricultural plastic covers a source of plastic debris in soil? A first screening study. *SOIL, 8*(1), 31-47.

Steinmetz, Z., Wollmann, C., Schaefer, M., Buchmann, C., David, J., Tröger, J., Muñoz, K., Frör, O., & Schaumann, G. E. (2016). Plastic mulching in agriculture. Trading short-term agronomic benefits for long-term soil degradation? *Science of the total environment, 550*, 690-705.

Strungaru, S.-A., Jijie, R., Nicoara, M., Plavan, G., & Faggio, C. (2019). Micro-(nano) plastics in freshwater ecosystems: abundance, toxicological impact and quantification methodology. *TrAC Trends in Analytical Chemistry, 110*, 116-128.

Su, Y., Ashworth, V., Kim, C., Adeleye, A. S., Rolshausen, P., Roper, C., White, J., & Jassby, D. (2019). Delivery, uptake, fate, and transport of engineered nanoparticles in plants: a critical review and data analysis. *Environmental Science: Nano, 6*(8), 2311-2331.

Summers, S., Henry, T., & Gutierrez, T. (2018). Agglomeration of nano-and microplastic particles in seawater by autochthonous and de novo-produced sources of exopolymeric substances. *Marine pollution bulletin, 130*, 258-267.

Tanaka, K., Takahashi, Y., Kuramochi, H., Osako, M., Tanaka, S., & Suzuki, G. (2021). Preparation of Nanoscale Particles of Five Major Polymers as Potential Standards for the Study of Nanoplastics. *Small, 17*(49), 2105781.

Tavares, L., Ito, N., Salvadori, M., dos Santos, D., & Rosa, D. (2018). PBAT/kraft lignin blend in flexible laminated food packaging: Peeling resistance and thermal degradability. *Polymer Testing, 67*, 169-176.

Tavares, L. B., & Rosa, D. d. S. (2019). Stabilization effect of kraft lignin into PBAT: Thermal analyses approach. *Matéria (Rio de Janeiro), 24*(3).

Tian, L., Jinjin, C., Ji, R., Ma, Y., & Yu, X. (2022). Microplastics in agricultural soils: sources, effects, and their fate. *Current Opinion in Environmental Science & Health, 25*, 100311.

Tiwari, A. (2012). *Biotechnology in Biopolymers: Developments, Applications & Challenging Areas*: Smithers Rapra.

Tosin, M., Pischedda, A., & Degli-Innocenti, F. (2019). Biodegradation kinetics in soil of a multi-constituent biodegradable plastic. *Polymer degradation and stability, 166*, 213-218.

Trinh, T. H., Kushaari, K., Shuib, A. S., Ismail, L., & Azeem, B. (2015). Modelling the release of nitrogen from controlled release fertiliser: Constant and decay release. *Biosystems Engineering, 130*, 34-42.

US Department of Agriculture. (1987). Soil Mechanics Level 1 Module 3. USDA Soil Textural Classification Study Guide.

Van Soest, J., & Knooren, N. (1997). Influence of glycerol and water content on the structure and properties of extruded starch plastic sheets during aging. *Journal of Applied Polymer Science, 64*(7), 1411-1422.

Varga, E. G., Titchener-Hooker, N. J., & Dunnill, P. (2001). Prediction of the pilot-scale recovery of a recombinant yeast enzyme using integrated models. *Biotechnology and Bioengineering, 74*(2), 96-107.

Velandia, M., Smith, A., Wszelaki, A., Galinato, S., & Marsh, T. (2018). *The economics of adopting biodegradable plastic mulch films*. Retrieved from

Vert, M., Doi, Y., Hellwich, K.-H., Hess, M., Hodge, P., Kubisa, P., Rinaudo, M., & Schué, F. (2012). Terminology for biorelated polymers and applications (IUPAC Recommendations 2012). *Pure and Applied Chemistry, 84*(2), 377-410.

Vert, M., Li, S., Spenlehauer, G., & Guérin, P. (1992). Bioresorbability and biocompatibility of aliphatic polyesters. *Journal of materials science: Materials in medicine, 3*(6), 432-446.

Viaroli, S., Lancia, M., & Re, V. (2022). Microplastics contamination of groundwater: Current evidence and future perspectives. A review. *Science of the total environment*, 153851.

Vighi, M., Bayo, J., Fernández-Piñas, F., Gago, J., Gómez, M., Hernández-Borges, J., Herrera, A., Landaburu, J., Muniategui-Lorenzo, S., & Muñoz, A.-R. (2021). Micro and nano-plastics in the environment: research priorities for the near future. *Reviews of Environmental Contamination and Toxicology Volume 257*, 163-218.

von Moos, N., Burkhardt-Holm, P., & Kohler, A. (2012). Uptake and effects of microplastics on cells and tissue of the blue mussel *Mytilus edulis* L. after an experimental exposure. *Environmental Science & Technology, 46*.

Wahl, A., Le Juge, C., Davranche, M., El Hadri, H., Grassl, B., Reynaud, S., & Gigault, J. (2021). Nanoplastic occurrence in a soil amended with plastic debris. *Chemosphere, 262*, 127784.

Wang, J., Huang, M., Wang, Q., Sun, Y., Zhao, Y., & Huang, Y. (2020). LDPE microplastics significantly alter the temporal turnover of soil microbial communities. *Science of the total environment, 726*, 138682.

Wang, K., Chen, W., Tian, J., Niu, F., Xing, Y., Wu, Y., Zhang, R., Zheng, J., & Xu, L. (2022). Accumulation of microplastics in greenhouse soil after long-term plastic film mulching in Beijing, China. *Science of the total environment, 828*, 154544.

Wang, Q., Adams, C. A., Wang, F., Sun, Y., & Zhang, S. (2022). Interactions between microplastics and soil fauna: A critical review. *Critical Reviews in Environmental Science and Technology, 52*(18), 3211-3243.

Wang, W., Yuan, W., Chen, Y., & Wang, J. (2018). Microplastics in surface waters of dongting lake and hong lake, China. *Science of the total environment, 633*, 539-545.

Wang, X. W., Wang, G. X., Huang, D., Lu, B., Zhen, Z. C., Ding, Y., Ren, Z. L., Wang, P. L., Zhang, W., & Ji, J. H. (2019). Degradability comparison of poly (butylene adipate terephthalate) and its composites filled with starch and calcium carbonate in different aquatic environments. *Journal of Applied Polymer Science, 136*(2), 46916.

Watano, S., Matsuo, M., Nakamura, H., & Miyazaki, T. (2015). Improvement of dissolution rate of poorly water-soluble drug by wet grinding with bio-compatible phospholipid polymer. *Chemical Engineering Science, 125*, 25-31.

Wilczek, M., Bertling, J., & Hintemann, D. (2004). Optimised technologies for cryogenic grinding. *International Journal of Mineral Processing, 74*, S425-S434.

Winursito, I., & Matsumura, S. (1996). Biodegradability, hydrolytic degradability, and builder performance in detergent formulations of partially dicarboxylated alginic acid. *Journal of environmental polymer degradation, 4*(2), 113-121.

Witt, U., Einig, T., Yamamoto, M., Kleeberg, I., Deckwer, W.-D., & Müller, R.-J. (2001). Biodegradation of aliphatic–aromatic copolyesters: evaluation of the final biodegradability and ecotoxicological impact of degradation intermediates. *Chemosphere, 44*(2), 289-299.

Witt, U., Müller, R.-J., & Deckwer, W.-D. (1997). Biodegradation behavior and material properties of aliphatic/aromatic polyesters of commercial importance. *Journal of environmental polymer degradation, 5*(2), 81-89.

Woodall, L. C., Sanchez-Vidal, A., Canals, M., Paterson, G. L., Coppock, R., Sleight, V., Calafat, A., Rogers, A. D., Narayanaswamy, B. E., & Thompson, R. C. (2014). The deep sea is a major sink for microplastic debris. *Royal Society open science, 1*(4), 140317.

Wright, S. L., & Kelly, F. J. (2017). Plastic and human health: a micro issue? *Environmental Science & Technology, 51*(12), 6634-6647.

Wu, C., Ma, Y., Wang, D., Shan, Y., Song, X., Hu, H., Ren, X., Ma, X., Cui, J., & Ma, Y. (2022). Integrated microbiology and metabolomics analysis reveal plastic mulch film residue affects soil microorganisms and their metabolic functions. *Journal of Hazardous Materials, 423*, 127258.

Wu, X., Lyu, X., Li, Z., Gao, B., Zeng, X., Wu, J., & Sun, Y. (2020). Transport of polystyrene nanoplastics in natural soils: Effect of soil properties, ionic strength and cation type. *Science of the total environment, 707*, 136065.

Xing, Q., Ruch, D., Dubois, P., Wu, L., & Wang, W.-J. (2017). Biodegradable and high-performance poly (butylene adipate-co-terephthalate)–lignin UV-blocking films. *ACS Sustainable Chemistry & Engineering, 5*(11), 10342-10351.

Xiong, S.-J., Pang, B., Zhou, S.-J., Li, M.-K., Yang, S., Wang, Y.-Y., Shi, Q., Wang, S.-F., Yuan, T.-Q., & Sun, R.-C. (2020). Economically Competitive Biodegradable PBAT/Lignin Composites: Effect of Lignin Methylation and Compatibilizer. *ACS Sustainable Chemistry & Engineering, 8*(13), 5338-5346.

Xu, B., Liu, F., Brookes, P. C., & Xu, J. (2018). Microplastics play a minor role in tetracycline sorption in the presence of dissolved organic matter. *Environmental Pollution, 240*, 87-94.

Xu, L., Xu, X., Li, C., Li, J., Sun, M., & Zhang, L. (2022). Is mulch film itself the primary source of meso- and microplastics in the mulching cultivated soil? A preliminary field study with econometric methods. *Environmental Pollution, 299*, 118915.

Xu, M., Du, W., Ai, F., Xu, F., Zhu, J., Yin, Y., Ji, R., & Guo, H. (2021). Polystyrene microplastics alleviate the effects of sulfamethazine on soil microbial communities at different CO_2 concentrations. *Journal of Hazardous Materials, 413*, 125286.

Yang, W., Fortunati, E., Dominici, F., Giovanale, G., Mazzaglia, A., Balestra, G. M., Kenny, J. M., & Puglia, D. (2016). Effect of cellulose and lignin on disintegration, antimicrobial and antioxidant properties of PLA active films. *International Journal of Biological Macromolecules, 89*, 360-368.

Yang, W., Owczarek, J. S., Fortunati, E., Kozanecki, M., Mazzaglia, A., Balestra, G. M., Kenny, J. M., Torre, L., & Puglia, D. (2016). Antioxidant and antibacterial lignin nanoparticles in polyvinyl alcohol/chitosan films for active packaging. *Industrial Crops and Products, 94*, 800-811.

Yang, Y., Li, Z., Yan, C., Chadwick, D., Jones, D. L., Liu, E., Liu, Q., Bai, R., & He, W. (2022). Kinetics of microplastic generation from different types of mulch films in agricultural soil. *Science of The Total Environment, 814*, 152572.

Yin, L., Wen, X., Huang, D., Du, C., Deng, R., Zhou, Z., Tao, J., Li, R., Zhou, W., & Wang, Z. (2021). Interactions between microplastics/nanoplastics and vascular plants. *Environmental Pollution, 290*, 117999.

Young, T. M., León, R. V., Chen, C.-H., Chen, W., Guess, F. M., & Edwards, D. J. (2015). Robustly estimating lower percentiles when observations are costly. *Quality Engineering, 27*(3), 361-373.

Yu, Y., Griffin-LaHue, D. E., Miles, C. A., Hayes, D. G., & Flury, M. (2021). Are micro-and nanoplastics from soil-biodegradable plastic mulches an environmental concern? *Journal of Hazardous Materials Advances, 4*, 100024.

Zeb, A., Liu, W., Shi, R., Lian, Y., Wang, Q., Tang, J., & Lin, D. (2022). Evaluating the knowledge structure of micro-and nanoplastics in terrestrial environment through scientometric assessment. *Applied Soil Ecology, 177*, 104507.

Zhang, F., Wang, Z., Wang, S., Fang, H., & Wang, D. (2019). Aquatic behavior and toxicity of polystyrene nanoplastic particles with different functional groups: complex roles of pH, dissolved organic carbon and divalent cations. *Chemosphere, 228*, 195-203.

Zhang, G., & Liu, Y. (2018). The distribution of microplastics in soil aggregate fractions in southwestern China. *Science of the total environment, 642*, 12-20.

Zhang, L., Sintim, H. Y., Bary, A. I., Hayes, D. G., Wadsworth, L. C., Anunciado, M. B., & Flury, M. (2018). Interaction of Lumbricus terrestris with macroscopic polyethylene and biodegradable plastic mulch. *Science of the total environment, 635*, 1600-1608.

Zhang, L., Xie, Y., Liu, J., Zhong, S., Qian, Y., & Gao, P. (2020). An overlooked entry pathway of microplastics into agricultural soils from application of sludge-based fertilizers. *Environmental Science & Technology, 54*(7), 4248-4255.

Zhang, Y., Fei, S., Yu, M., Guo, Y., He, H., Zhang, Y., Yin, T., Xu, H., & Tang, X. (2018). Injectable sustained release PLA microparticles prepared by solvent evaporation-media milling technology. *Drug Development and Industrial Pharmacy, 44*(10), 1591-1597.

Zhu, D., Chen, Q.-L., An, X.-L., Yang, X.-R., Christie, P., Ke, X., Wu, L.-H., & Zhu, Y.-G. (2018). Exposure of soil collembolans to microplastics perturbs their gut microbiota and alters their isotopic composition. *Soil Biology and Biochemistry, 116*, 302-310.

Zimm, B. H. (1948). The scattering of light and the radial distribution function of high polymer solutions. *The Journal of Chemical Physics, 16*(12), 1093-1099.

Zumstein, M. T., Schintlmeister, A., Nelson, T. F., Baumgartner, R., Woebken, D., Wagner, M., Kohler, H.-P. E., McNeill, K., & Sander, M. (2018). Biodegradation of synthetic polymers in soils: Tracking carbon into CO_2 and microbial biomass. *Science advances, 4*(7), eaas9024.

Zuo, L.-Z., Li, H.-X., Lin, L., Sun, Y.-X., Diao, Z.-H., Liu, S., Zhang, Z.-Y., & Xu, X.-R. (2019). Sorption and desorption of phenanthrene on biodegradable poly(butylene adipate co-terephtalate) microplastics. *Chemosphere, 215*, 25-32.

Zurier, H. S., & Goddard, J. M. (2021). Biodegradation of microplastics in food and agriculture. *Current Opinion in Food Science, 37*, 37-44.

5988-12. ASTM International, Standard Test Method for Determining Aerobic Biodegradation in Soil of Plastic Materials (ASTM 5988), West Conshohocken, PA, USA, 2012. In *ASTM International*.

VITA

Anton Astner was born in Salzburg, Austria. During his undergraduate study at the Salzburg University of Applied Sciences, he joined the University of Tennessee, Knoxville, pursuing an internship, working on designing and constructing an organosolv pretreatment reactor. In his undergraduate research, he designed a "A Feasibility Study on Energy Supply Conversion to Biomass for a Dairy Plant in Piding, Germany." In 2009, he graduated from Salzburg University of Applied Sciences with a concentration in Forest Products Technology and Management. Afterward, Anton pursued a joint Master's study simultaneously at the University of Applied Sciences Salzburg and the University of Tennessee with concentration in Wood Science Technology and Biomaterials, supervised by Professor Timothy M. Young and Professor Joseph J. Bozell.

His research focused on optimizing the "Organosolv Fractionation Process" using statistical methods. In 2013, he received the prestigious "Leo Schörghuber Award for the Promotion of Wood Research" from the Technical University Munich for his unique thesis research. After working as a research associate at the Center for Renewable Carbon, he joined the team of Professor Douglas Hayes in the Department of Biosystems Engineering and Soil Science to pursue his PhD study research in the field of biodegradable plastics. He currently investigates the formation and characterization of micro- and nanoplastics in terrestrial environments.

During his research, he is collaborating with a team of scientists at the Oak Ridge National Laboratory to conduct research related to nanoplastic identification using Small Angle Neutron Scattering (SANS) and Ultra-SANS techniques. In 2020, Anton participated in the 22nd National School on X-ray and Neutron Scattering. In 2022, Anton graduated from the University of Tennessee with a PhD degree in Biosystem Engineering.

Currently, Anton works as a Postdoctoral Research Associate at the Department of Biosystems Engineering and Soil Science supervised by Professor Douglas Hayes.